Measurement of the shape of the boson rapidity distribution for $p\bar{p} \rightarrow Z/\gamma^* \rightarrow e^+e^- + X$ events produced at $\sqrt{s} = 1.96$ TeV

A thesis submitted to the University of Manchester for the degree of
Doctor of Philosophy
in the Faculty of Engineering and Physical Sciences

September 2013

Pengfei Ding
Particle Physics Group
School of Physics and Astronomy

Contents

Final word count: 21342

Abstract

Name of the University: The University of Manchester
Candidate Name: Pengfei Ding
Degree Title: Doctor of Philosophy in the Faculty of Engineering and Physical Sciences
Thesis Title: Measurement of the shape of the boson rapidity distribution for $p\bar{p} \to Z/\gamma^{*} \to e^{+}e^{-} + X$ events produced at $\sqrt{s} = 1.96$ TeV
Date: September 2013

The measurement of the shape of the boson rapidity distribution for $p\bar{p} \to Z/\gamma^{*} \to e^{+}e^{-} + X$ events at a center-of-mass energy of 1.96 TeV is presented in this thesis. Data, with an integrated luminosity of $L = 9.86$ fb^{-1}, collected with the D0 detector during the whole RunII data taking period of the Fermilab Tevatron $p\overline{p}$ collider has been used. The measurement is made for events with electron-positron mass $66 < M_{ee} < 111$ GeV. The current result gives the best precision of the boson rapidity shape at the Tevatron. It significantly reduces the uncertainty in the boson rapidity range $|y| > 2.3$. Predictions of Next-to-Leading-Order (NLO) QCD theory with CTEQ and MSTW parton distribution functions are found to agree well with the data over the full rapidity range.

Declaration

No portion of this work referred to in this thesis has been submitted in support of an application for another degree or qualification of this or any other university or other institute of learning.

Pengfei Ding
School of Physics and Astronomy
The University of Manchester
Oxford Road
Manchester
M13 9PL

Copyright

The author of this thesis (including any appendices and/or schedules to this thesis) owns any copyright in it (the ”Copyright”) and s/he has given The University of Manchester the right to use such Copyright for any administrative, promotional, educational and/or teaching purposes.

Copies of this thesis, either in full or in extracts, may be made **only** in accordance with instructions given by the Author and lodged in the John Rylands University Library of Manchester. Details may be obtained from the Librarian. Further copies (by any process) of copies made in accordance with such instructions may not be made without the permission (in writing) of the Author.

The ownership of any patents, designs, trade marks and any and all other intellectual property rights except for the Copyright (the ”Intellectual Property Rights”) and any reproductions of copyright works, for example graphs and tables (”Reproductions”), which may be described in this thesis, may not be owned by the author and may be owned by third parties. Such Intellectual Property Rights and Reproductions cannot and must not be made available for use without the prior written permission of the owner(s) of the relevant Intellectual Property Rights and/or Reproductions.

Further information on the conditions under which disclosures and exploitation may take pace is available from the head of the School of Physics and Astronomy.

Acknowledgements

First of all, I would like to thank my supervisor Professor Terry Wyatt for guiding me through the past four years, with much help and encouragement, and for the continuing help and support throughout my thesis.

Thanks to Prof. Liang Han for introducing me to the high energy physics filed and supporting me to apply this program, and to Professor Stefan Söldner-Rembold for his help and guidance throughout my PhD. My thanks also goes to to Dr. Xuebing Bu, Dr. Kostas Pertidis, Dr. Maiko Takahashi, Dr. Zhenyu Ye and Dr. Hang Yin for their continuous help. Thanks to all members of the D0 Manchester group and those D0 colleagues who helped me throughout my PhD.

My special thanks goes to my parents and my wife Chenchen Xu for their continuous support and belief in me.

Chapter 1

Introduction

This thesis presents work that was performed at the D0 experiment and consists a measurement of the shape of the boson rapidity distribution for $p\bar{p} \rightarrow Z/\gamma^* \rightarrow e^+e^- + X$ events. The measurement aims to improve the precision of the shape of boson rapidity distribution.

Chapter 2 gives a brief overview the Standard Model of particle physics. A description of the Tevatron and the D0 detector is provided in Chapter 3. Chapter 4 introduces a novel variable, the “Hits-on-Road” (HoR) variable, for electron and photon identification. The measurement of the shape of the boson rapidity distribution is documented in Chapter 5. Additionally, studies of the D0 Silicon Microstrip Tracker (SMT) clustering algorithm are included in Appendix D.

Chapter 2

Theoretical overview

2.1 The Standard Model

The Standard Model (SM) [1] is one of the most successful theories ever invented. It is a simple and comprehensive theory explaining particles and the interactions between them. It accurately predicts all observed phenomena at distances smaller than $\sim 10^{-15}$m.

2.1.1 Fundamental Particles and interactions

Fundamental particles in the SM include:

- 6 quarks (u, d, s, c, b, t),
- 6 leptons $(e, \mu, \tau, \nu_e, \nu_\mu, \nu_\tau)$,
- force carrier particles (gluon, photon, $W^{\pm}$, Z^0).

At present, there are four fundamental interactions, which are believed to sufficiently explain all phenomena in physics. These interactions are:

- the strong interactions,
- the electromagnetic interactions,
- the weak interactions,
- and the gravitational interactions.

The strong interaction, which is modeled by Quantum Chromodynamics (QCD), is the interaction among quarks. The electromagnetic and weak interactions are unified by the electroweak sector. The SM is a gauge theory of the strong and electroweak interactions.

There are two basic types of particles in the SM, fermions and bosons, shown in Figure 2.1. Particles with half-integral spin $(\frac{\hbar}{2},\frac{3\hbar}{2},...)$ are called fermions, since they obey Fermi-Dirac statistics. Those with integral spin $(0,\hbar,2\hbar,...)$ are called bosons, which obey Bose-Einstein statistics. Fermions adhere to the Pauli Exclusion Principle: only one fermion can occupy a particular quantum state. Among the fundamental particles, quarks and leptons are fermions; the force carrier particles are bosons.

The leptons are particles that do not participate in the strong interaction. For each charged lepton, there is a neutrino that is electrically neutral. Unlike charged particles that interact electromagnetically, neutrinos only participate in the weak interaction.

The quarks make up particles called hadrons. Baryons and mesons are the two type of hadrons. Hadrons with three constituent quarks (such as protons and neutrons) are called baryons, and those with a quark and an antiquark are mesons. Quarks must have color charge in addition to electric charge [2], since without color, quarks in some hadrons appear to occupy the same quantum state, which is not allowed according to the Pauli Exclusion Principle for fermions. Color charge has three "polarities" represented by the red, green, and blue. There are also "anticolors" for the antiquarks. Mixtures of a color and its anticolor or of the three separate colors or anticolors are referred to as colorless. Individual free quarks with color are not observed. The quarks seem to be confined inside colorless mesons and baryons. The top quark, the last quark to be discovered, was observed in 1995 with the D0 [3] and CDF [4] detectors at the Tevatron.

The quarks and leptons can be grouped into three generations. Each generation of quarks has an up type and a down type quark. Each generation of leptons has a negatively charged particle and a massless neutrino. The second generation contains heavier particles than the first and similarly for the third. The particles of the heavier generations are unstable and ultimately decay down to the first generation or to photons. Only particles of the first generation make up matter in the everyday world. Particles of the second and third generations can be produced with cosmic rays and in high energy particle colliders. The second and third generations appear to play no role in the everyday world. Experiments at CERN's LEP e^+e^- collider have shown that there are no more than three light or massless neutrinos [5], strongly suggesting that there are only three generations.

The force carrier particles are responsible for transmitting the fundamental interactions:

- massless gluons, described by the QCD model, mediating the strong interactions between color charged quarks;
- massless photons, well-described by the theory of quantum electrodynamics, mediating the electromagnetic force between electrically charged particles;
- massive $W^{\pm}$ and Z vector bosons, mediating the weak interactions between particles (quarks and leptons).

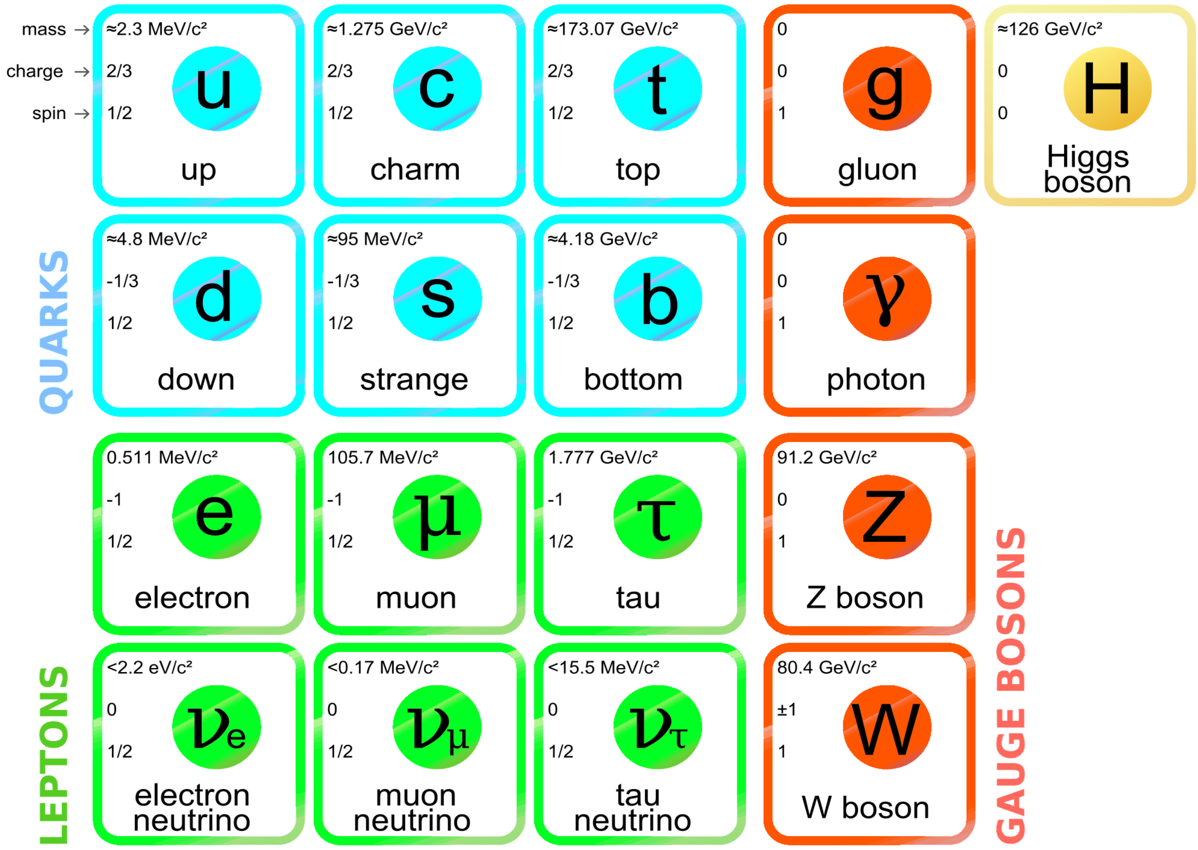

Figure 2.1: The fundamental particles in the Standard Model. [1]

2.1.2 QCD and the electroweak theory

The Standard Model is comprised of two separate theories, quantum chromodynamics (QCD) and electroweak. Electroweak unifies the electromagnetic force, described by quantum electrodynamics (QED), with the weak force. All of these theories are gauge theories in that they involve fields (mathematical constructs that represent the particles and interactions) that are invariant under a change of phase or gauge.

QED involves phase factors of $e^{i\phi(x)}$, which are members of the symmetry group $U(1)$ - unitary transformations in one dimension. For the weak force, it is convenient to group the particles into doublets,

$$\begin{pmatrix}\nu_e\\ e\end{pmatrix}_L, \begin{pmatrix}\nu_\mu\\ \mu\end{pmatrix}_L, \begin{pmatrix}\nu_\tau\\ \tau\end{pmatrix}_L, \begin{pmatrix}d\\ u\end{pmatrix}_L, \begin{pmatrix}s\\ c\end{pmatrix}_L, \text{ and } \begin{pmatrix}b\\ t\end{pmatrix}_L, \tag{2.1}$$

where the L subscript indicates that the weak interactions only affect particles in left handed helicity states. Instead of using a field for every particle, there is a two-component field for each doublet. The gauge transformations are now quite complicated since matrices are involved, and, in fact, the transformations can cause a particle to transform into its doublet partner. Such transformations belong to the $SU(2)_L$ symmetry group. For the theory to be gauge invariant, there must be three massless gauge bosons [1], W^+, W^-, and the W^0. At this stage, the electromagnetic force can be combined with the weak force by adding in the $U(1)$ group and its gauge boson, the massless and neutral B^0 which will eventually become part of the photon. This $SU(2)_L \times U(1)$ theory with the massless gauge bosons does not reflect the fact that electromagnetism and the weak forces are separate in the everyday world, and that the W and Z weak gauge bosons have mass. Therefore, the symmetry must be broken in some way.

The Higgs mechanism provides the method for spontaneously breaking electroweak symmetry by forcing one to choose a vacuum expectation value (vev) for a Higgs field. The results are that the W^+, W^-, and the neutral Z (a mixture of the W^0 and the B^0) acquire mass. The photon (a different mixture of W^0 and the B^0 bosons) remains massless. The price one pays is the introduction of a new field representing a scalar (spin zero) particle, the Higgs boson, and a new parameter in the model, θ_W, the mixing angle for relating the Z and γ to the W^0 and B^0 . The scalar Higgs couples to any particle with mass: the heavier the mass, the stronger the coupling. The triumph of the Higgs mechanism is the prediction of the masses of the W and Z weak bosons. These particles were discovered at CERN with the UA1 and UA2 detectors in the mid 1980's [6]. Their masses were measured to be right at the SM prediction. The success of the combined fits to precision EW measurements was very powerful evidence that the SM was correct,

---

[1] These massless bosons are not the same as the massive W and Z bosons described in Section 2.1.1; at least not yet.

even before the direct discovery of Higgs boson found by the ATLAS and CMS experiment at the LHC.

2.2 Phenomenology of high energy proton-antiproton ($p\overline{p}$) collisions at the Tevatron

The proton and antiproton beams, at the Tevatron, can be thought of as broadband beams of partons. The $p\overline{p}$ collision at the Tevatron might be shown schematically as in Figure 2.2. The highest energy collisions take place between a valence quark from the proton and an antiquark from the antiproton, carrying fractions x_1 and x_2 of the momentum of the incoming proton and antiproton, respectively. The energy, Q is given by $Q^2 = x_1 x_2 E_{cm}^2$ in the parton–parton centre-of-mass frame. The probability of a proton containing a parton of type i at the appropriate values of x_1 and Q^2 is given by a "parton distribution function" (PDF), $f_i(x_1, Q^2)$. The cross section for the parton-parton collision to produce a given final state is denoted by $\hat{\sigma}(Q^2)$. When determining the cross section, σ, for the $p\overline{p}$ collision to produce such a final state, summing over all possible combinations of incoming partons and integrating over the momentum fractions x_1 and x_2 is needed:

$$\sigma = \sum_{i,j=q,\bar{q},g} \int dx_1 dx_2 \cdot f_i(x_1, Q^2) \cdot f_j(x_2, Q^2) \cdot \hat{\sigma}(Q^2) \tag{2.2}$$

The PDFs cannot be calculated directly from first principles in QCD. They can, however, be constrained by experimental measurements, such as the measurement of Z/γ^* boson rapidity shape presented in this thesis.

A nice review of the phenomenology can be found in Reference [8].

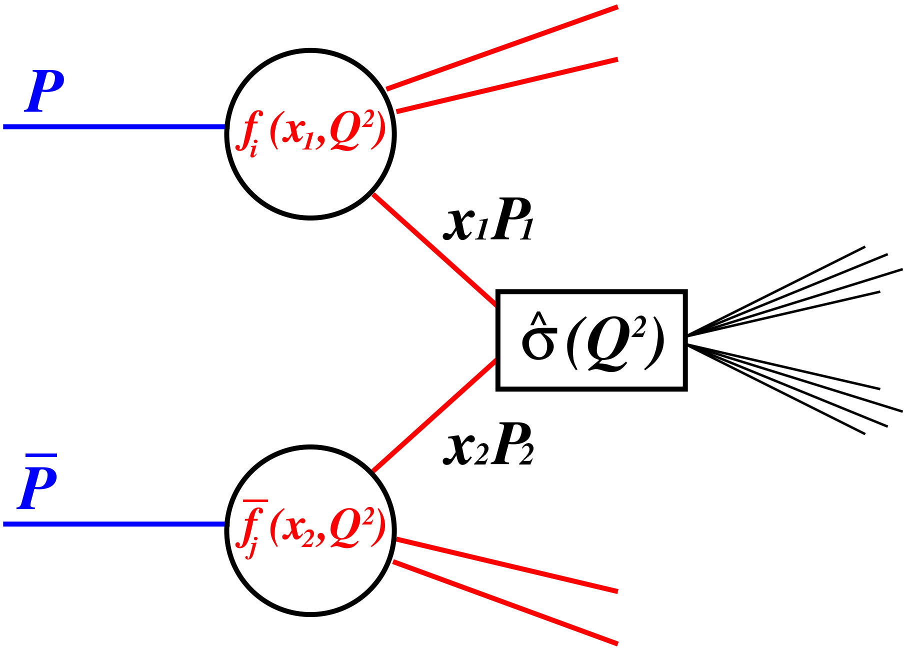

Figure 2.2: Schematic view of a high-energy $p\bar{p}$ collision [7].

Chapter 3

Experimental Apparatus

The Tevatron accelerator complex, shown in Figure 3.1, collides protons and antiprotons at a center of mass energy of 1.96 TeV.

The D0 detector is one of two general purpose detectors that record the results of these collisions. In this chapter, an overview of the Tevatron and and the D0 detector is provided.

3.1 The Tevatron Accelerator Complex

The acceleration process starts from the production of negatively charged hydrogen ions. They are injected into the Cockroft-Walton accelerator once produced. The ions are then passed through an electrostatic field and reach an energy of 750 keV, before the next injection into a linear accelerator (LINAC). In the LINAC, the ions are accelerated by means of RF fields to an energy of 400 MeV. At this stage, the hydrogen ions pass through a carbon foil, which strips off their electrons and produces a beam of protons. The protons are then transferred into the Booster synchrotron ring, which accelerates them to an energy of 8 GeV. From the Accumulator they are transferred to the Recycler, in which they are stored and cooled in preparation for further acceleration. The protons are subsequently transferred to the Main Injector, and accelerated to 150 GeV.

Bunches of protons, are extracted from the Main Injector to impact on a nickel-copper target, producing anti-protons and other secondary particles. The anti-protons get collected, bunched and accelerated to 8 GeV in the Accumulator. They are transferred to the Main Injector, traveling in the opposite direction to the proton beam, and accelerated to 150 GeV.

Both proton and anti-proton beams are extracted to the Tevatron. They are then accelerated to 980 GeV before collisions take place at the D0 and B0 interaction regions, which are the locations of the D0 and CDF detectors, respectively. A more detailed description of the Tevatron complex can be found in Reference [9].

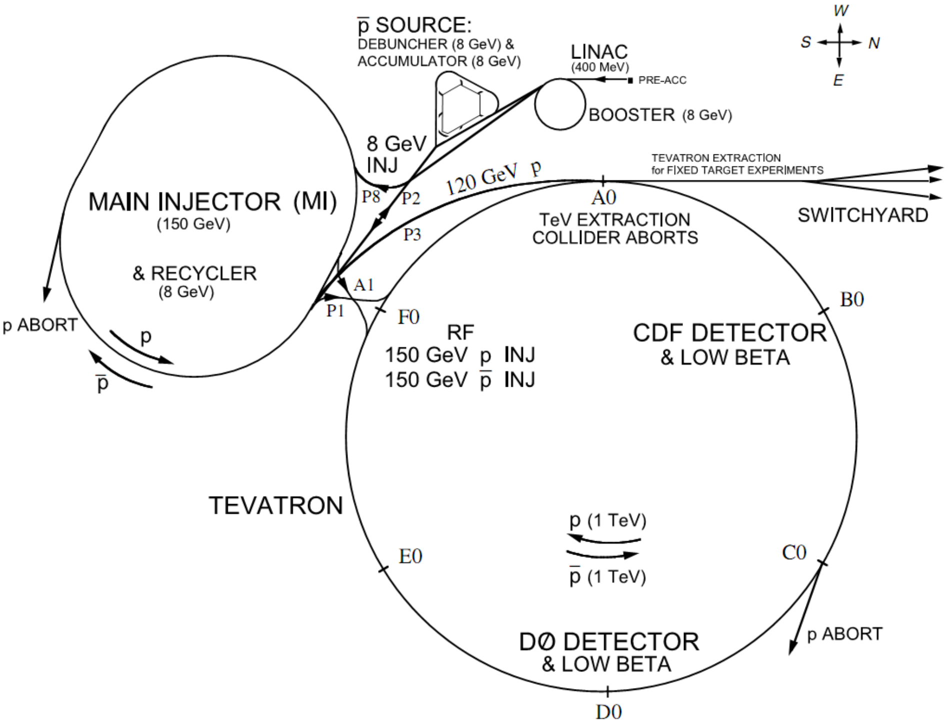

Figure 3.1: The Tevatron Complex at the Fermi National Accelerator Laboratory (FNAL), Batavia, IL, USA [9].

3.2 The D0 Detector

With the high luminosities and high energies provided by the Tevatron, the studies of many rare processes at small distance scales become accessible. The D0 detector is designed to identify high energy particles produced by these processes. An overview of the D0 detector is shown in Figure 3.2. Charged particles deposit energy in a tracking system that is enclosed in a solenoidal magnet with a field strength of 2 Tesla. The tracking system, together with this solenoidal magnet, enables the measurement of particle momenta, and thus aids in particle identification. The energies of most particles are measured by preshower detectors and a liquid-argon/uranium calorimeter. Outside of the calorimeter, a system composed of drift tubes and scintillators, as well as a 1.8 Tesla toroidal magnet, is used to identify muons and provide an additional, with lower resolution, measurement of muon momenta. Since the rate of collisions at the Tevatron is many orders of magnitude too large for all of them to be recorded, a three-tiered trigger system is designed, together with the data acquisition system, selecting which collisions to save.

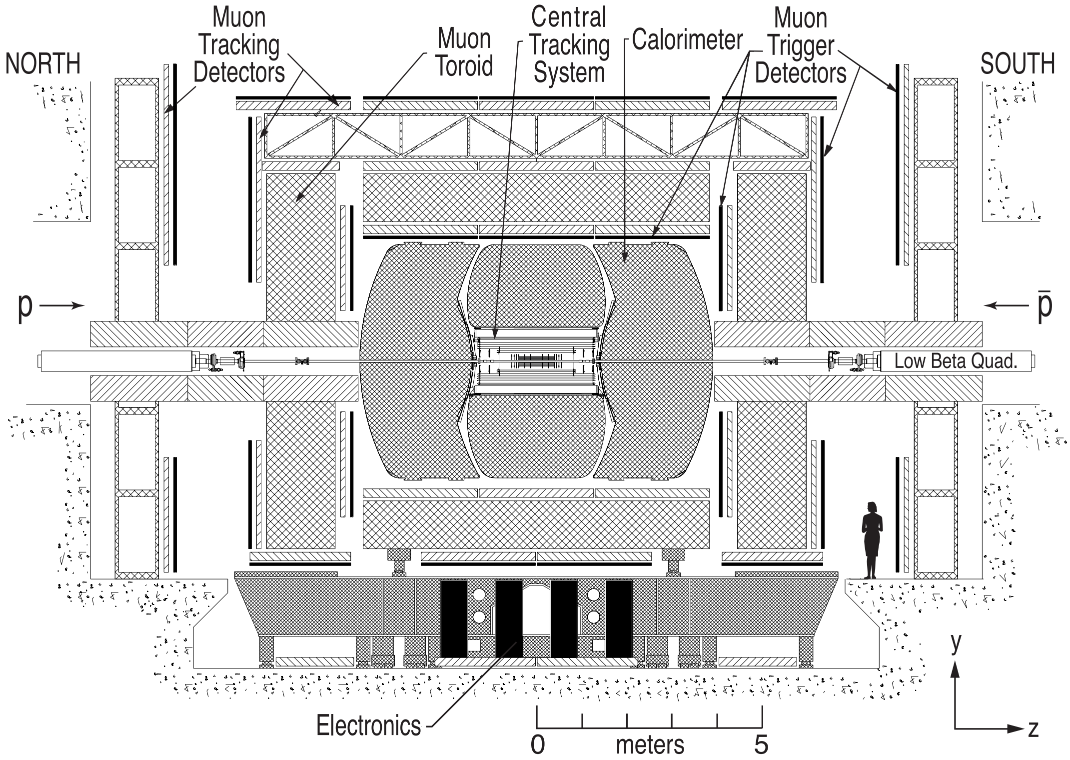

Figure 3.2: Overview of the D0 detector.

The detector, along with the low-level trigger and readout electronics, is located in an underground collision hall. The remainder of the electronics, trigger and data-acquisition systems are located in rooms that are adjacent to the collision hall.

Most of the studies presented in this thesis are only relevant to the tracking system and the calorimeter of the detector. Thus a detailed description for each of them is provided in this section. Further information on the D0 detector can be found in Reference [10] and Reference [11]. Except where noted, all information and figures in this section are taken from these references.

3.2.1 The tracking system

The Silicon Microstrip Tracker

The Silicon Microstrip Tracker (SMT) is mounted directly on the Tevatron's beryllium beam pipe. It is used for high precision track and vertex reconstruction. The SMT is composed of wafers of silicon. Each silicon wafer contains doped strips typically 50 microns in pitch, which form semiconducting traces. A charged particle traversing such a sensor generates electron-hole pairs. Electrons are collected by the anode strips deposited onto the wafer surface. The resulting electrical pulses are digitized. Double-sided sensors are created by doping strips on both sides of the wafer, with p-type strips on one side and n-type strips on the other. Stereo information is provided by double-sided sensors with strips on both sides aligned nonparallel.

An isometric view of the SMT is shown in Fig. 3.3. There are three types of sensors used in the SMT: single-sided (SS), double-sided (DS) and double-sided double-metal (DSDM) sensors. A DS sensor is two SS sensors glued together with a stereo angle of 2^o between the strips; a DSDM sensor is a “real” double-sided sensor with an angle of 90^o between strips on each side. Both of DS and DSDM sensors provide stereo information.

The detector includes 6 barrels in the central region. Each barrel consists of 5 readout layers. Layers 1 and 2 have 12 silicon ladders each (silicon modules installed in the barrels); layers 3 and 4 have 24 ladders each. Each ladder of the barrel detectors are made of two sensors. Layers 2 and 4 uses DS sensors. Layers 1 and 3 uses SS sensors for the outer barrels and DSDM sensors for the inner four barrels. Each barrel is capped with an F-disk. Forward of the barrels and F-disk is a unit of 3 F-disks and a unit of 2 H-disks on each side. Each F-disk contains 12 DS wedge detectors. Each H-disk contains 24 wedges, with two back-to-back single-sided detectors in each wedge.

An additional layer of sensors (layer 0) was installed in later after RunIIa data taking period, during which a data with an integrated luminosity of $\sim$1.5fb^{-1} was taken. Layer 0 consists of 8 barrels with 6 silicon ladders each. One SS sensor is used in each of the 8 barrels.

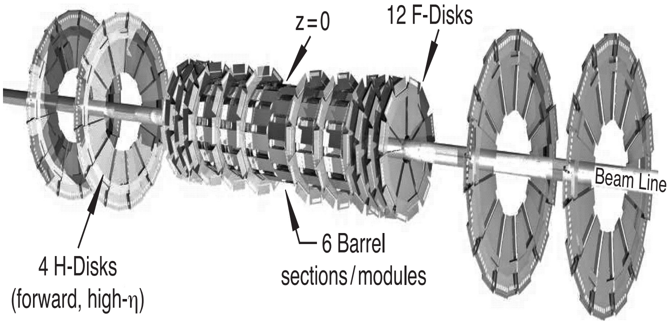

Figure 3.3: The disk/barrel design of the SMT.

The read-out chip used for the sensors is a radiation-hard 128 channel analog pipeline and 8-bit ADC. It provides channel-specific thresholds to allow real-time zero suppression, thus minimizing readout times. These chips are daisy-chained in groups of up to nine on Kapton flex circuits, which is a radiation-hard plastic. Individual channels are connected to the SMT strips. Low mass cables are used to connect the flex circuits to adapter cards outside of the calorimeter. Adapter cards are then connected by high mass cables and additional interface boards to sequencer boards on the electronics platform below the detector. The sequencers provide timing and control signals to the readout chips. They are connected by optical fibers to VME Readout Buffers (VRBs) in VME (Versa Module Eurocard) crates outside of the collision hall. The adapter card interface board chain collects data from and distributes control signals and power to the SMT sensor assemblies. This readout chain is shown in Figure 3.4.

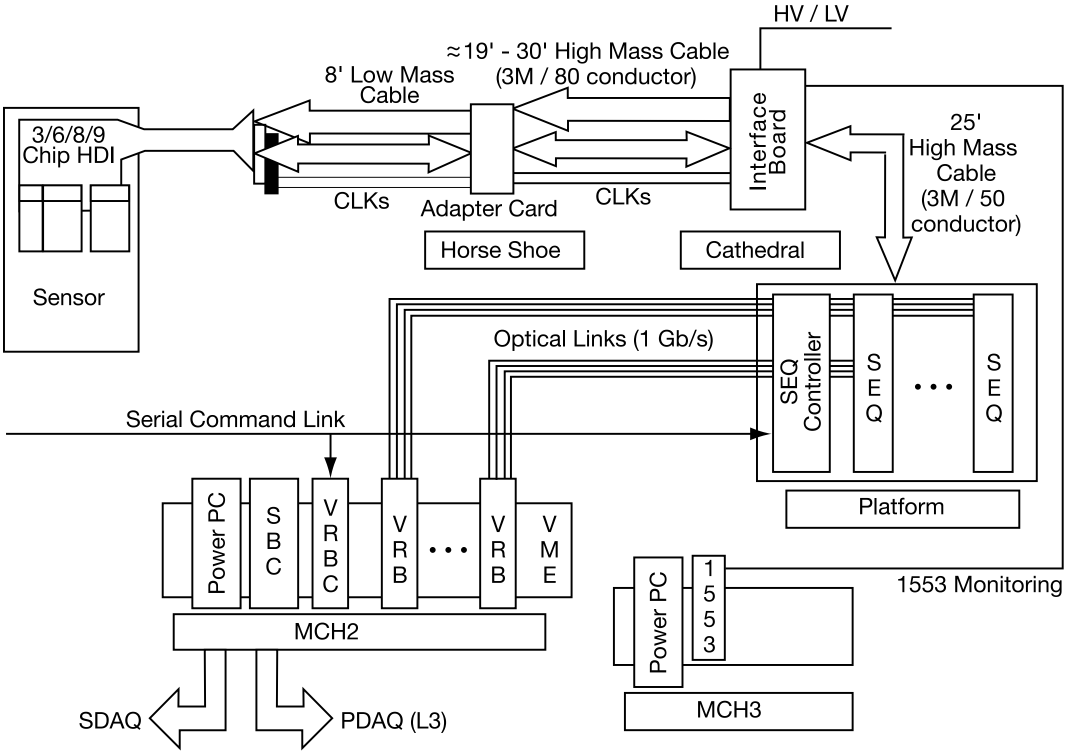

Figure 3.4: Schematic of the SMT readout.

The Central Fiber Tracker

The Central Fiber Tracker (CFT), shown in Figure 3.5, consists of 76,800 scintillator-doped fibers mounted on eight concentric cylinders surrounding the SMT. A charged particle traversing these fibers ionizes their organic molecules. The excited molecules emit photons as they return to their ground states. This light is captured by clear optical fibers attached to one end of each scintillating fiber. The end not connected to the waveguide is mirrored to increase the total light collected. Visible light photon counters (VLPCs) are used to convert these op-

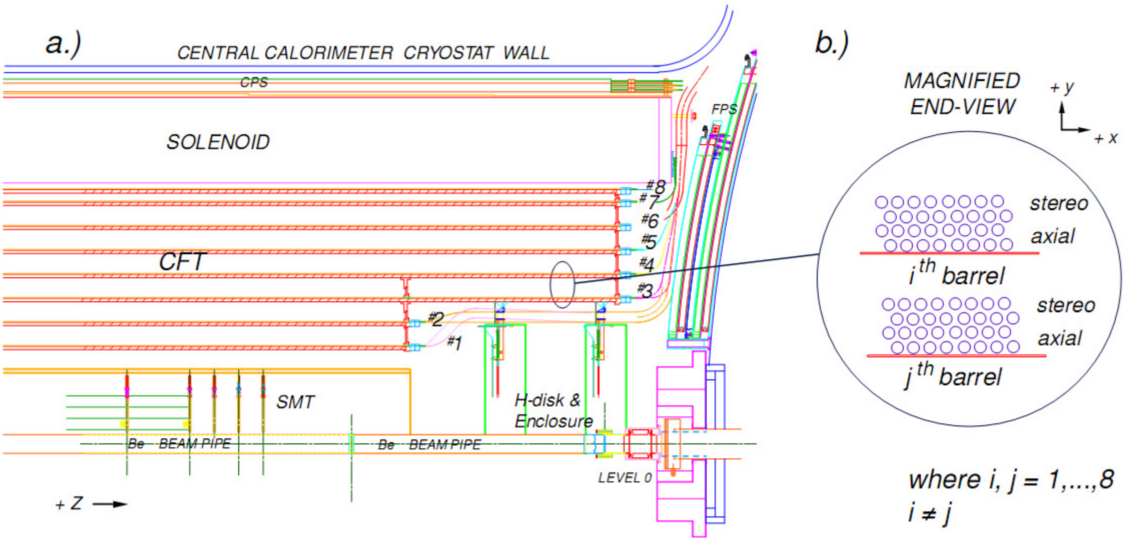

Figure 3.5: The central fiber tracker [24].

tical signals into electronical signals, which are then delivered to the trigger and data acquisition systems.

Each cylinder of the CFT consists of one layer of axial fibers immediately surrounded by another layer of stereo fibers which are at an angle of 3^o with respect to the beam axis. The sign of the angle alternates with each successive stereo layer. The innermost two layers provide coverage of up to $|\eta| < 1.6$, while the remaining layers provide coverage up to $|\eta| < 1.8$.

3.2.2 The Calorimeter

The D0 calorimeter, shown in Figure 3.6, provides energy measurement of most long-lived particles, and enables for the efficient identification of jets, electrons, and photons. It consists of a central cryostat (CC), covering $|\eta| < 1.1$, and two endcap cryostats (EC), covering $1.3 < |\eta| < 4$. Two intercryostat detectors, consisting of scintillating tiles that are read out by photomultiplier tubes, give additional coverage in the gaps between the cryostats. The cryogenic and electrical services for the solenoid as well as the cabling for the inner tracking system are routed between the CC and the ECs.

The calorimeter is composed of cells containing liquid argon, grounded absorber plates and high voltage pads. A typical cell is shown in Figure 3.7. A particle traversing the calorimeter will interact with the absorber, producing a shower of secondary particles. These secondary particles ionize the liquid argon and the resulting charge is collected at the high voltage pads, giving a measure-

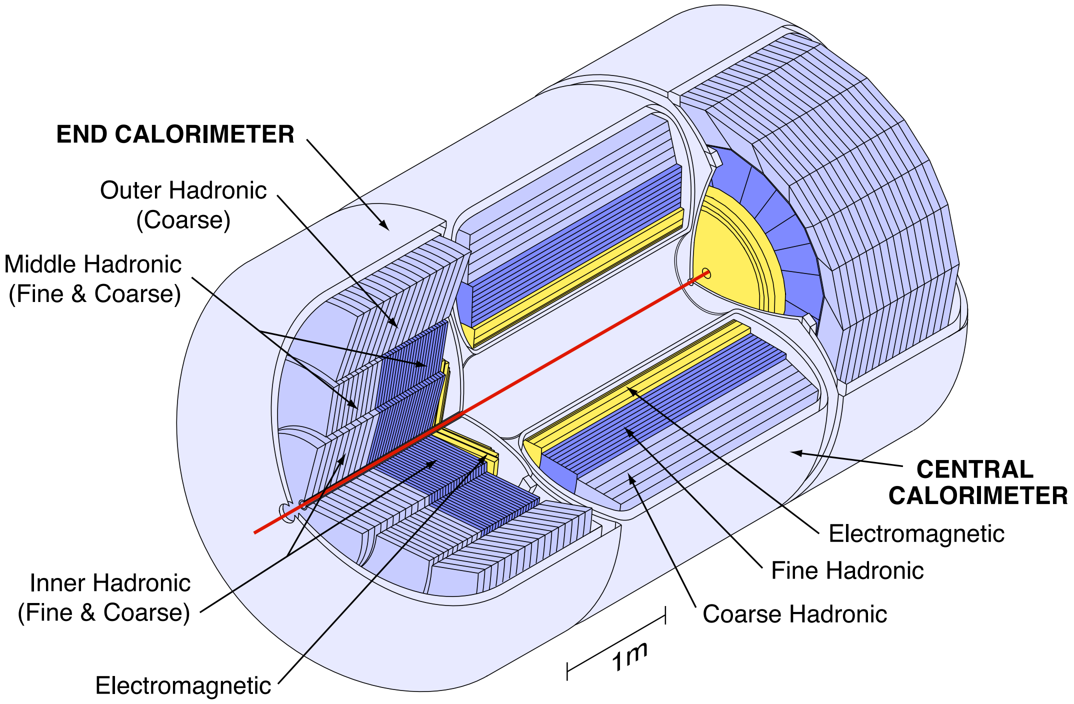

Figure 3.6: The DØ calorimeter.

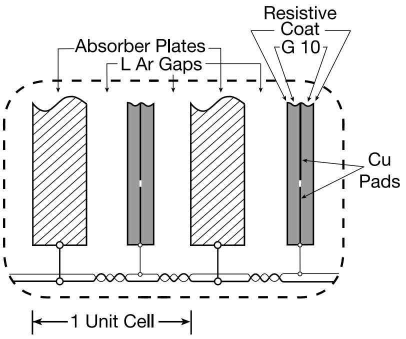

Figure 3.7: Schematic view of a typical calorimeter unit cell. The signal boards are the copper pads with resistive coats.

ment of the energy deposited in that cell.

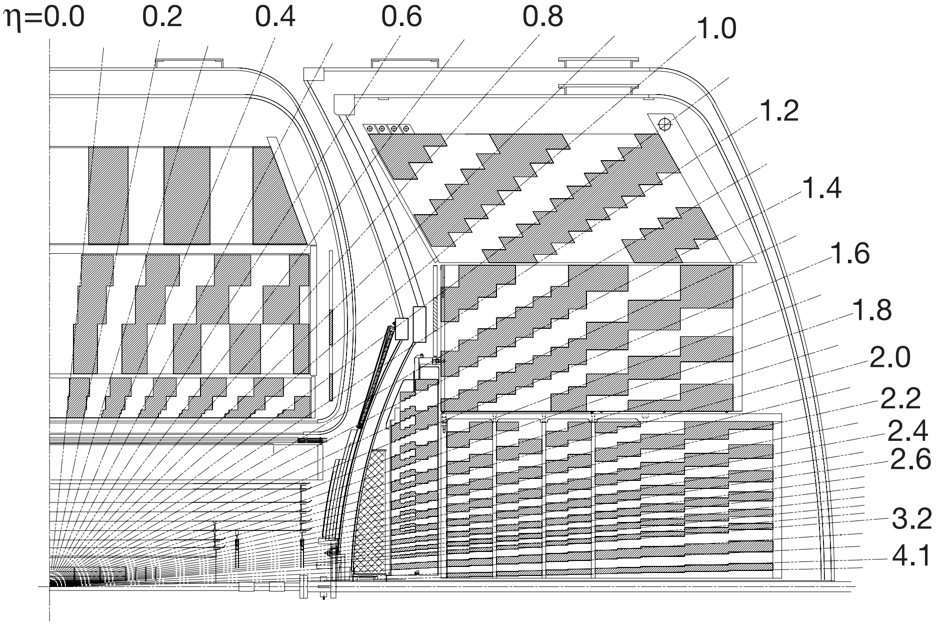

Figure 3.8: Schematic view of a part of the D0 calorimeter. Pseudorapidity intervals are indicated by the rays from the center of the detector. Groups of cells ganged together for signal readout are indicated by the shading pattern.

The calorimeter cells are arranged in four electromagnetic layers, three fine hadronic layers (four in the ECs) and one coarse hadronic layer, as shown in Figure 3.6. The four electromagnetic layers in the CC (EC) are approximately 1.4, 2.0, 6.8 and $9.8X_0$ (1.6, 2.6, 7.9 and $9.3X_0$) thick. The detector components provide approximately $4.0X_0$ ($4.4X_0$) of material between the interaction region and the first active gap in the CC at $\eta = 0$ (in the EC at $\eta = 2$). The absorbers in the electromagnetic layers are made of depleted uranium. The electromagnetic layers in CC, approximately, has a coverage of $|\eta| < 1.2$ and $1.5 < |\eta| < 3.2$ in EC. The fine hadronic absorbers are composed of a uranium-niobium alloy and the coarse hadronic absorbers consist of copper (in the CC) and stainless steel (in the ECs). The EC hadronic layers are further divided into the inner, middle and outer sections, with $|\eta|$ coverage starting from $\sim$ 1.6, 1.2, 1.0, 0.6 up to 4.1 respectively.

The showers from electrons and photons stop in the fourth electromagnetic layer with a maximum in the third layer. The finer segmentation of this layer allows a more precise measurement of the shower position. The cells are aligned in projective towers (visible in Figure 3.8) with $\eta - \phi$ dimensions of 0.2×0.2.

One thing to note is that the typical drift time of ions in the liquid argon is $\sim$ 450 ns, while the time between collisions is 396 ns. Therefore the charge collected from previous events piles up in the readout of the current event. This problem is solved by a method called baseline subtraction, in which the charge from the preceding collision is sampled and subtracted from the signal in the event being read out.

3.3 Particle Reconstruction

3.3.1 Tracks

Tracks are reconstructed by SMT and CFT hits. The reconstruction includes a pattern recognition algorithm, which reconstructs clusters by grouping signals from neighboring channels in a specific SMT or CFT layer/disk, and a track finding algorithm, which hypothesizes possible tracks from clusters [12, 13]. The tracks can be described by the following parameters:

- the curvature $\frac{q}{p_T}$, where p_T is the transverse momentum of the charged particles;
- the dip angle to a plane which is perpendicular to the magnetic filed, tanλ;
- the coordinates of the point on the track where the closest approach to the beam pipe sits.

Tracks are rarely used as individual objects but as part of electron, muon or jet reconstruction.

3.3.2 Photons and Electrons

The dense material in the layers of the calorimeter causes photons and electrons to make electromagnetic showers and deposit most of their energy within them. The first step of reconstructing photons and electrons is to from electromagnetic clusters (EM clusters) from isolated deposits in the calorimeter. Energy deposits in the four EM layers and the first hadronic layer are used for EM clusters. Calorimeter cells are grouped together with the same η and ϕ to form towers. Beginning with the highest transverse energy tower ($E_T > 500$ MeV), energies of neighboring towers in a cone of $\Delta R < 0.4$ around the highest E_T tower, where $(\Delta R)^2 = (\Delta\eta)^2 + (\Delta\phi)^2$, are added to form EM clusters in the CC. EM clusters in the EC are a set of neighboring cells with a transverse distance of less than 10 cm from an initial cell to the highest energy content in the third EM layer. The centroid of the EM cluster is computed by weighting cell coordinates with cell energies in the third EM layer of the calorimeter. To be selected as an electron or photon candidate, EM clusters must satisfy the following criteria:

- $E_T > 1.5$ GeV, where E_T is the cluster transverse energy;
- The fraction of energy in the EM layer $F_{EM} > 0.9$, where $F_{EM} = E_{EM}/E_{tot}$, E_{EM} being the cluster energy in the EM layers, and E_{tot} being the total energy in all layers within the cone;
- The calorimeter isolation $I_{cal} < 0.2$, where $I_{cal} = (E^{0.4}_{tot} - E^{0.2}_{EM})/E^{0.2}_{EM}$, $E^{0.4}_{tot}$ is the energy in the towers within a cone of $\Delta R < 0.4$ around the the cluster, summed over the entire depth of the calorimeter except the coarse hadronic layers, and $E^{0.2}_{EM}$ is the energy in the towers in a cone of $\Delta R < 0.2$ summed over the EM layers only;

EM clusters passing the above criteria can be further matched to tracks. If a track with $p_T > 1.5$ GeV is present within a window of $\Delta\eta \times \Delta\phi = 0.05 \times 0.05$ around the centroid of the EM cluster, this EM cluster will be considered as an electron candidate. Otherwise, it is considered as a photon candidate.

Further quantities are employed for electron and photon identification to reject misidentified jets and increase the purity of the selected electron and photon candidates. These quantities can be found in the following.

- **EM Shower width.** Showers induced by jets are usually wider than those from photons and electrons, thus it can be used to further reject jets for photon and electron selection.
- **H-Matrix $\chi^{2(7)}_{EM}$ and $\chi^{2(8)}_{EM}$.** The shower shape of a photon or an electron is different from that of a jet. In order to obtain the best discrimination against hadrons, longitudinal and transverse shower shapes, as well as the correlations between energy deposits in different calorimeter cells are considered together by using a covariance matrix ("H-matrix") technique [?]. The matrix in the CC (EC) is of dimension 7 × 7 (8 × 8), thus the H-matrix discriminate is denoted as $\chi^{2(7)}_{EM}$ ($\chi^{2(8)}_{EM}$).
- **Track isolation I_{trk}.** The scalar sum of the p_T of all charged tracks with $p_T > 500$ MeV, originating from the primary vertex in an annular cone of $0.05 < \Delta R < 0.4$ around the EM cluster and excluding the matched track for the EM cluster itself, is expected to be small. This variable is a sensitive discriminant for separating photon and electron candidates from jets.

- **Track match probability P_{trk}.** It is a probability of the track matching with $\chi^2_{trk} = (\Delta\phi/\delta_\phi)^2 + (\Delta\eta/\delta_\eta)^2$, where $\Delta\eta$ and $\Delta\phi$ are the differences between the track and the centroid of the EM cluster in the third EM layer, and where $\delta\phi$ and $\delta\eta$ are the resolutions of the associated quantities. The track with the highest P_{trk}, i.e. the smallest χ^2_{trk}, is taken as the matched track for the EM cluster. P_{trk} is set to -1 if there is no matched track.

- **Electron likelihood L_{EM}.** The presence of a track close to the track associated to the EM cluster or a large E_T/p_T when the *ee* pair is reconstructed as a single EM cluster might be the signature of photon conversions. Here E_T/p_T is the transverse energy of the EM cluster measured by the calorimeter divided by the transverse momentum of the associated track measured by the tracking detector. Other calorimeter quantities, including shower shape, $\chi^{2(7)}_{EM}$ or $\$chi^{2(8)}_{EM}$, F_{EM}, I_{cal}, I_{trk}, P_{trk}, number of tracks in a cone of $\Delta R < 0.4$ around the matched track and the transverse impact parameter of the matched track with respect to the primary vertex, are used to calculate the electron likelihood L_{EM}. It is a sensitive variable to discriminate electrons from photons with conversions of *ee* pairs.

Almost 100% of single electrons with transverse momenta above 30 GeV are triggered in the fiducial regions of the calorimeter with $|\eta|$ up to 2.5. For transverse momenta of $E_T = 40$ GeV, electrons can be identified with a total identification efficiency of 90% (95%), and with a 5% (3%) misidentification efficiency of jets in the CC (EC). Typically $70\% - 85\%$ of the photons in the CC and EC region can be identified, with a $2\% - 10\%$ misidentification rate of electrons or jets.

Chapter 4

The HoR method for electron and photon identification

4.1 Introduction

The cluster-track matching algorithm for an EM object serves a crucial role in the identification of electrons and photons. However this algorithm is not fully efficient in separating electron from photon candidates. A major source of fake photons comes from those electrons without any matched track or neutral pions which rarely leave information in the tracking detectors; a main factor of inefficiency of electron selection is brought by the requirement of cluster-track matching. This limitation is much more pronounced in the forward region of the detector[1], where the coverage of tracking system is much poorer. It is also more pronounced in high instantaneous luminosity environment, where the occupancy of the tracking system is higher. Therefore, in addition to the cluster-track matching algorithm, a supplementary way of using tracking information is highly desired, especially for the EC electron candidates which fail the cluster-track matching algorithm, and for the data taken in RunIIb-3 and RunIIb-4 period during which more data were taken with high instantaneous luminosity.

The supplementary way is to use the "Hits-on-Road" (HoR) discriminant. Instead of using the tracking information at the level of reconstructed tracks, as in the cluster-track matching algorithm, a lower level of tracking information is used in the HoR method. It utilizes the hit clusters (denoted as hits hereafter) in the tracking system directly.

The method was firstly developed during D0 RunIIa data taking period [15].

---

[1] To give a rough quantitive view, the tracking efficiency for electron candidates found in the CC is $\sim 90\%$, and $\sim 60\%$ in the EC.

It was developed for EM objects (clusters reconstructed in the EM layers of the D0 calorimeters) in the CC only. During D0 RunIIb, an attempt of directly extending this method to the EC EM objects was performed [16]. However, the direct extension was unsuccessful. The geometry of the tracking system needs to be considered carefully in this case. Since the hits used in this method are associated to individual layers (disks) of the SMT and CFT, the coverage of each layer would have a direct impact on the final HoR discriminant. The tracking system has a full coverage in ϕ, but a limited coverage in η. The coverage in η is wide enough for all the CC EM objects (of which $|\eta|$ is up to 1.1). Thus it does not need to be considered in for CC EM objects. However, the η coverages of each SMT layer/disk and CFT layer vary from layer to layer, and most of them are smaller than the coverage of the EM layers in the EC, where EM layers have a coverage in η up to ~ 3.2.

This chapter presents:

- an optimization of the HoR method for the CC EM objects with the aid of SMT layer 0, which was not yet installed in RunIIa when this method was first introduced,
- a new development of the method for the EC EM objects, which considers the geometry of the tracking system at the level of layer/disk.

Artificial neural network (ANN) is for the first time used in the development of the HoR discriminant for both CC and EC EM objects.

A detailed description of the HoR method can be found in Section 4.2. The step-by-step procedure for the development of the discriminant and its performance are documented in Section 4.3 (for CC EM objects) and Section 4.4 (for EC EM objects). A conclusion is also provided in Section 4.5.

4.2 Description of the HoR method

Two roads, the left road and the right road, are defined for each EM object due to the ambiguity of charge. Figure 4.1 shows a schematic view of the two roads defined for an EM object. The roads describe the expected trajectory in the tracking detector of an electron candidate or a positron candidate. Both roads originate from the primary vertex of the event, point to the EM object and have the same curvature as a track with transverse momentum equivalent to the transverse energy of the considered EM object.

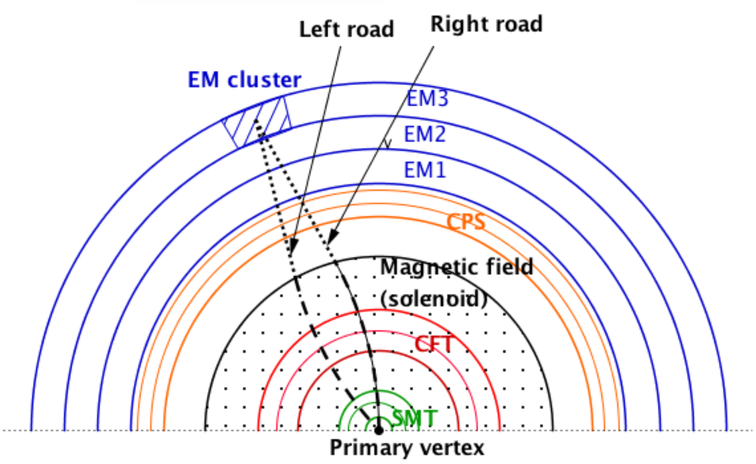

Figure 4.1: Schematic view of the left and the right road defined for an EM object.

After defining the road, we count the number of fired CFT fibers or SMT strips which are found within a certain distance (road width) around the road. The road width for each SMT and CFT layer/disk (denoted as D_i for the ith layer/disk) is estimated by using electrons from $Z/\gamma^* \to e^+e^-$ data events.

Since the central preshower (CPS) [2] has a higher position resolution than the calorimeters, the position of the matched CPS stereo cluster for an EM object, if there is one, is used to defined the roads (denote these roads as CPS roads, the other as EM roads).

Due to the different performance in each layer of the tracking system, we group the layers (disks) into four groups. These groups are: (i) SMT barrel layers (denoted as $smtB$), (ii) SMT disks (including F-disks and H-disks, only used for EC EM objects, denoted as $smtD$), (iii) CFT axial layers (denoted as $cftA$), and (iv) CFT stereo layers (denoted as $cftS$). The number of hits associated is counted separately for each group (N^{smtB}_{hits}, N^{smtD}_{hits}, $N^{cftA}_{hits}$and N^{cftS}_{hits}). Among the two roads of the considered EM object, the one with bigger N^{total}_{hits}, where $N^{total}_{hits} = N^{smtB}_{hits} + N^{smtD}_{hits} + N^{cftA}_{hits} + N^{cftS}_{hits}$, is chosen. N^{i}_{hits} ($i = smtB$, $smtD$, $cftA$, and $cftS$) for the chosen road are used as input variables to the ANN for the tuning of the HoR discriminant.

The development consists of two main steps: (i) estimating D_i, the road width in the ith layer(disk); and (ii) tuning the ANN discriminant.

Due to the geometry of the SMT and CFT detectors, the maximum number of hits, N^{i}_{max} ($i = smtB$, $smtD$, $cftA$, and $cftS$), which is also the number

---

[2] CPS sits within the EM calorimeter and outside of the tracking system. It provides higher position resolution than EM calorimeters. More information about the CPS can be found in Reference [11].

of layers or disks traversed by the road, depends on the orientation of the road. Figure 4.2 shows one example of this case, in which the road does't traverse all CFT barrel layers and SMT disks. In this case, the input variables for ANN are no longer N^i_{hits} but R^i, where $R^i = N^i_{hits}/N^i_{max}$ ($i = smtB$, $smtD$, $cftA$, and $cftS$).

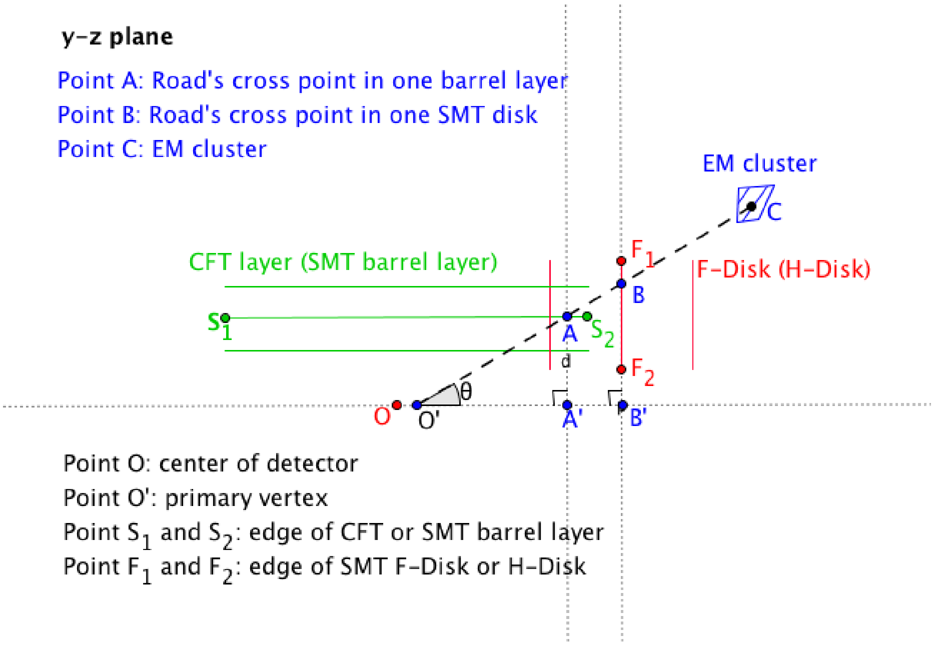

Figure 4.2: An example of road defined for an EM cluster in the EC, where the road only traverse certain CFT layers and SMT disks.

A step-by-step description of the method is provided for the EM objects in the CC and EC separately.

CC EM objects:

- Step 1. For each EM object, estimate the position of the cross point for the left and the right road in each tracking detector layer in ϕ. An example for the left road of an EM cluster is shown in Figure 4.3 as $\overset{\frown}{OB} + \overline{BC}$.

  Point O, B and C are the primary vertex, cross point of the trajectory on the solenoid boundary and the EM cluster in the third EM layer, respectively. Point A is the cross point of the road in the jth layer of the tracking detector. Point D is on the x-axis. Point A's position in ϕ is calculated by $\phi_A = \phi_1 + \phi_2 + \phi_3$, where ϕ_1 is the angle $\angle DOC$, ϕ_2 is the angle $\angle COB$ and ϕ_3 is the angle $\angle BOA$. The radius of the road within solenoid is the radius of $\overset{\frown}{OB}$, i.e. $R_{road} = \overline{O_1O} = \overline{O_1B}$. It can be calculated by $R_{road} = E_T/(0.003 \times B_z)$, where R_{road} is in the unit of cm, E_T (in MeV) is the transverse energy of the EM cluster and B_z (in T) is the z-component of the magnetic filed in the solenoid. Note that $\angle OBO_1 = \angle BOO_1 = \phi_1 + \phi_2$, thus

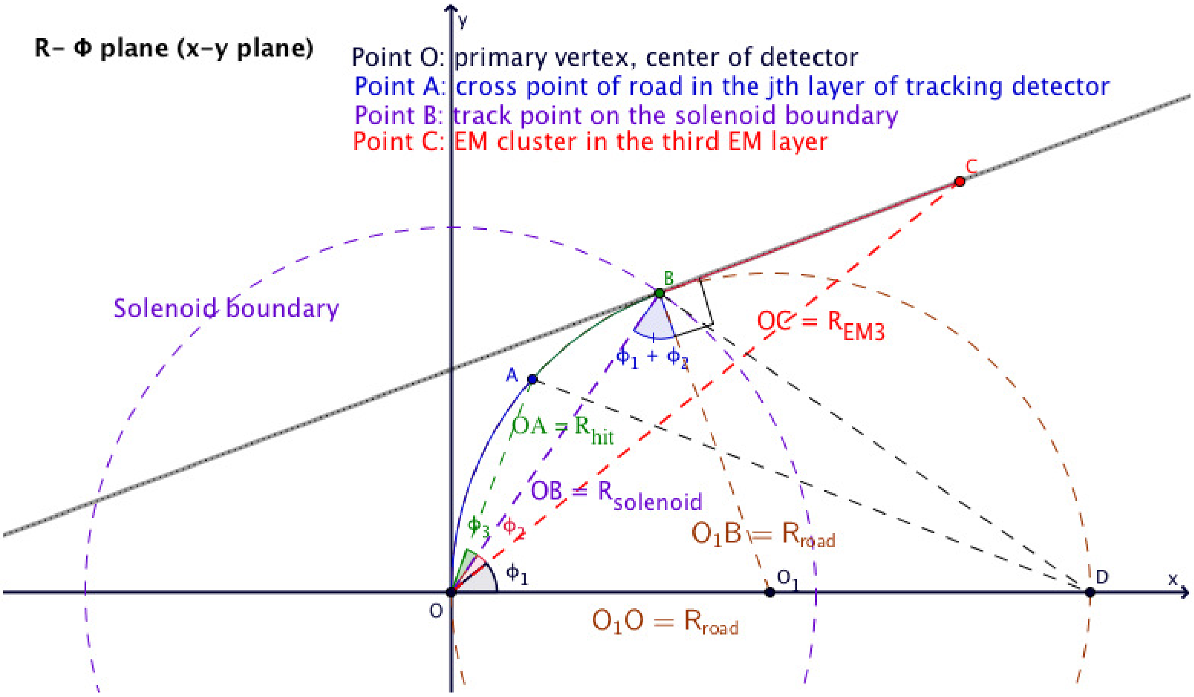

Figure 4.3: An example of a left road defined for an EM cluster in the CC.

$\angle OBC$ equals to $\pi/2 + \phi_1 + \phi_2$. ϕ_1, ϕ_2 and ϕ_3 can be calculated by solving triangles $\triangle DOA, \triangle DOB$ and $\triangle COB$. The main source of uncertainty for the estimation of ϕ_A comes from ϕ_1, i.e. the position of the EM cluster.

- Step 2. Find the hit in the SMT and CFT axial layers which is closest to the road in ϕ, and that in the CFT stereo layers in z (distance in z is used due to the fact that the CFT stereo layers are not parallel to the beam pipe). The closest hit is associated to the road if its distance to the road is within the road width in its layer/disk. Consequently, each detector layer has one associated hit at most.

- Step 3. For both of the two roads of an considered CC EM cluster, count the number of associated hits from Step 2 in different groups of layers (disks) (N_{hits}^{smtB}, N_{hits}^{cftA}, and N_{hits}^{cftS}).

- Step 4. Choose the road with bigger N_{hits}^{total}; take N_{hits}^{smtB}, N_{hits}^{cftA}, and N_{hits}^{cftS} as input variables to train the ANN, and obtain the HoR discriminant.

EC EM objects:

- Step 1-3. Same as those for CC EM objects, but additionally count N_{hits}^{smtD};

- Step 4. Estimate N_{max}^{i}, and thus get R^i (i = $smtB$, $smtD$, $cftA$, and $cftS$).

- Step 5. Choose the road with bigger N_{hits}^{total}; use R^i ($i = smtB$, $smtD$, $cftA$, and $cftS$) of the chosen road as input variables to train the ANN, and obtain the HoR discriminant.

The

4.3 The HoR discriminant in the CC

As described in Section 4.2, the development of the HoR discriminant consists of two main steps: (i) estimation of the road width for each layer/disk (denoted as D_i for the ith layer); and (ii) tuning the ANN discriminant, HoR$_{CC}$. The estimation of D_i is presented in Section 4.3.1 followed by the tuning of the ANN discriminant in Section 4.3.2. In order to validate the HoR$_{CC}$ discriminant, Section 4.3.3 documents its performance for events from different processes, and events with different tracking requirements. Section 4.3.4 gives examples of applying the HoR$_{CC}$ discriminant together with the most commonly used electron (photon) selection criteria in the D0 collaboration designed by the EM object ID (EMID) group.

4.3.1 Road widths in the CC

A proper choice of the road width (D_i) in an SMT or CFT layer/disk should allow only the hits made by an electron ending in the considered EM object, but allow few noisy hits. Thus, electrons with good quality of tracks are selected from genuine $Z/\gamma^* \rightarrow e^+e^-$ data with an integrated luminosity of 0.7 fb^{-1}. Details of the $Z/\gamma^* \rightarrow e^+e^-$ event selection can be found in Reference [17].

Figure. 4.4 shows the distribution of the distance between the hit cluster and the cross point of the road in each detector layer/disk, $\Delta\phi_i$ and Δz_i, where $\Delta\phi_i$ is for the ith SMT barrel and CFT axial layer in ϕ and Δz_i is for the ith CFT stereo layer in z. Distributions of EM road and CPS road are shown in black and red, respectively. The distributions indicate that the matched CPS cluster provides better resolution than the EM objects. Thus two sets of the road width D_i are estimated, with one for CPS road and the other for EM road. CPS road is used if the EM object has a matched CPS cluster, otherwise EM road is used. D_i is estimated from a Gaussian fit of the distribution of $\Delta\phi_i$ and Δz_i, as shown in Figure 4.5 - Figure 4.10. Please note that these distributions are not Gaussian distributions. Discussions about the structures of these distributions are provided later in this section. The Gaussian fit is just for getting an estimation of D_i.

Only the standard deviation (σ) from the fit result is used. 1.5σ, 2σ and 3σ were considered as possible choices for D_i and 2σ was chosen based on the performance of ANN discriminant. Other than the standard deviation from the Gaussian fit result, there are other alternatives for the road width estimation, e.g. the RMS of the distribution or the width of a symmetric band around 0 which includes 65% of all the entries. However, these alternatives introduce more dependence on the tails of the distribution which are made by random/noisy hits in the detector.

The distributions of $\Delta\phi_i$ for the CPS road in the SMT barrel layers have unique structures. The structures are caused by those EM objects whose roads pass through gaps between sensors or dead sensors. In either case, the closest hit in an adjacent sensor would be chosen.

- Figure 4.11(a) shows an end view of the SMT barrel sensors. Figure 4.11(b) shows the ϕ distribution of hits in the fourth layer of sensors in one SMT barrel. The ϕ gap in this layer is ~ 0.5. Hits found along roads passing through these gaps contribute to the shoulders of the $\Delta\phi_i$ distributions.
- There are some dead sensors in certain SMT layers. Figure 4.11(c) shows the ϕ distribution of hits found in the SMT barrel 6 layer 4 sensors. Three modules out of six were not functioning. Hits found for roads passing through these dead sensors contribute to the dips on both sides of the peak in $\Delta\phi_i$ distributions, e.g SMT layer 4 and SMT layer 6 in Figure. 4.4, also in Figure 4.5.

In Figure 4.6, the width of the $\Delta\phi_i$ distributions in outer CFT layers are smaller than those in inner layers. It agrees with the fact that more fibers are installed in the outer layers[3].

The structures of the $\Delta\phi_i$ distributions are less pronounced in the EM road distributions, Figure 4.8 - Figure 4.10. It is simply because the calorimeter provides a poorer position resolution than the preshower detector and the positions of the road in each layer are smeared by the position resolution of preshower detector or calorimeter.

---

[3] The number of fibers range from 2560 to 7040 in one CFT layer. More details can be found in Reference [10]

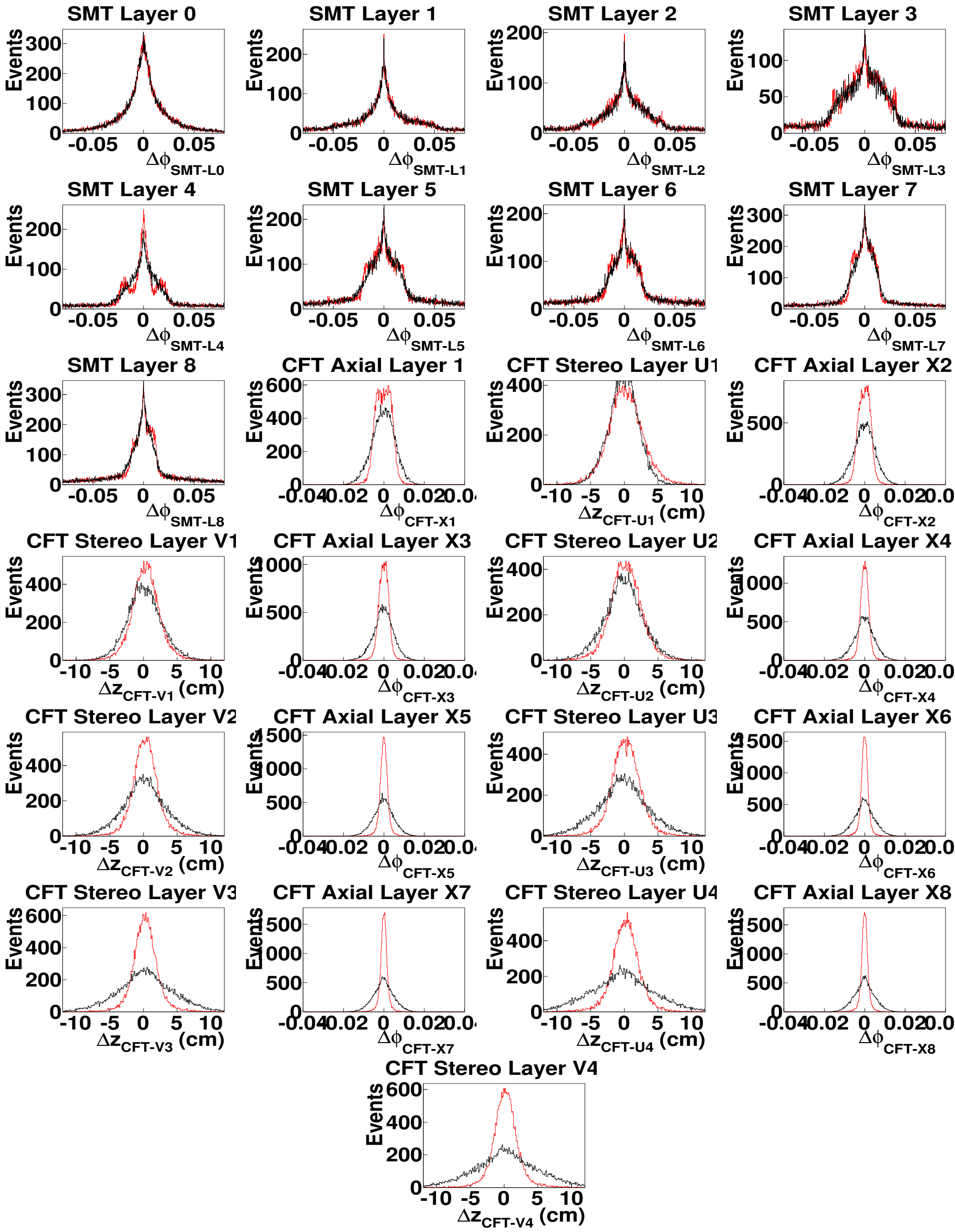

Figure 4.4: $\Delta\phi_i$ (in the ith SMT barrel and CFT axial layers) and Δz_i (in the ith CFT stereo layers) for the CPS road (red) and the EM road (black). SMT barrel layers are labeled from 0 to 8, where layer 0 denotes the innermost SMT barrel layer 0, layer 1 and 2 denote the two sublayers of the 1st SMT barrel layer, and so forth for 3-4, 5-6 and 7-8. CFT axial layers are labeled from “X1” to “X8”. “V1” (“(U1) to “V4” (“U4”) label the four CFT layers with a stereo angle in ϕ of $+3°$ $(-3°)$.

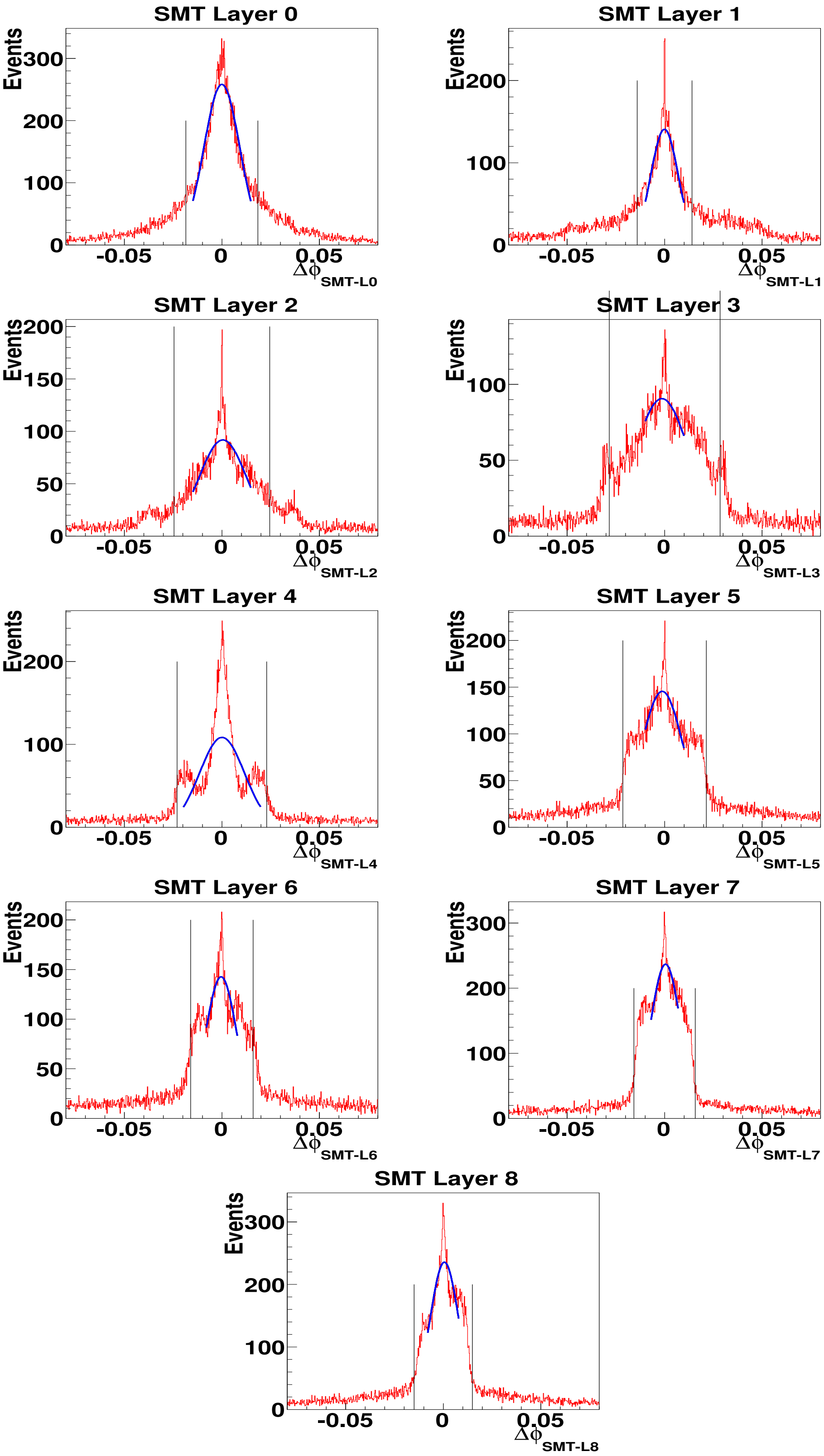

Figure 4.5: $\Delta\phi_i$ in the ith SMT barrel layers for the CPS road. Blue curves are the fitted Gaussian distributions. Vertical lines indicate the estimated D_i ($\pm 2\sigma$).

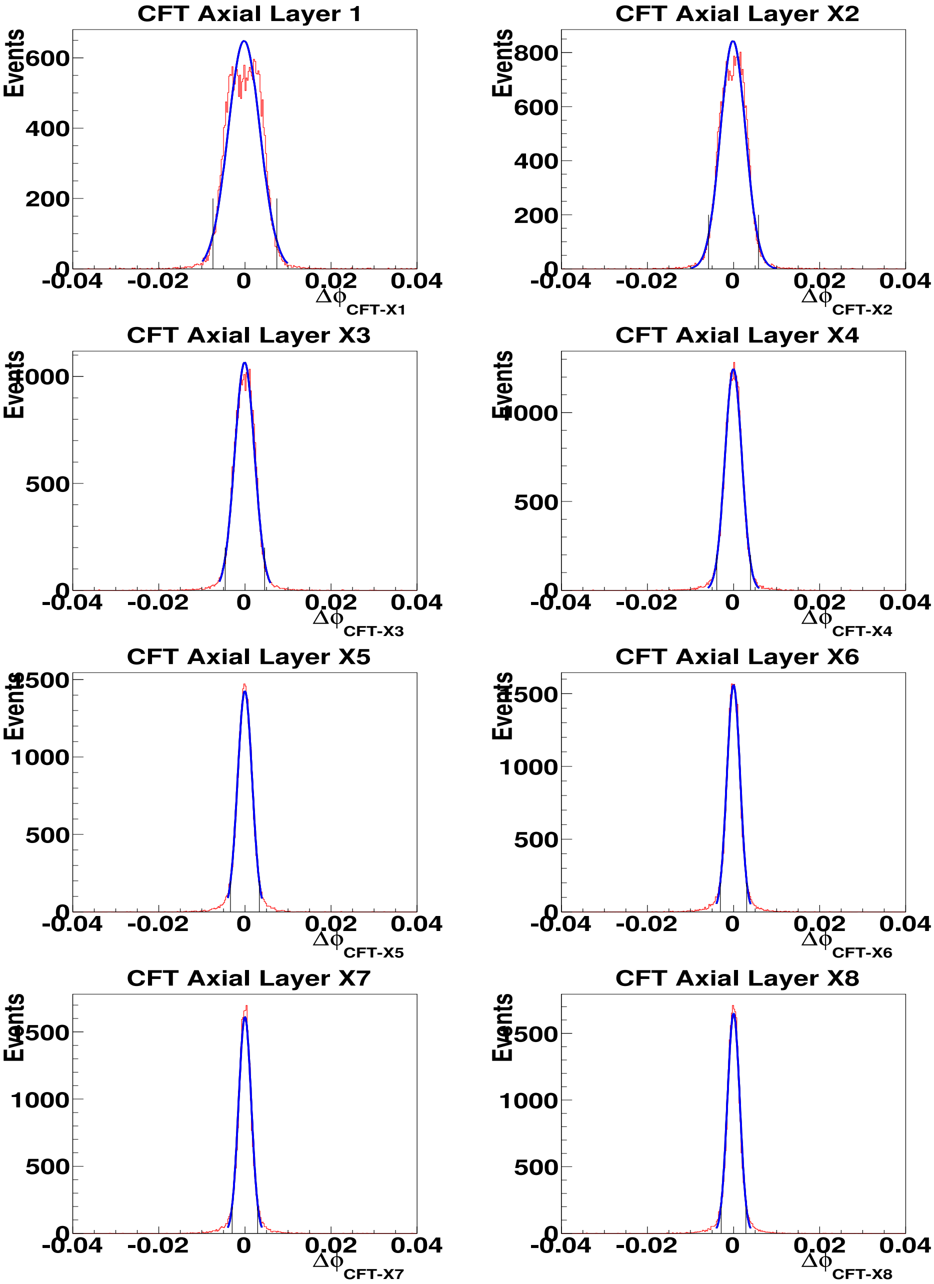

Figure 4.6: $\Delta\phi_i$ in the ith CFT axial layers for the CPS road. Blue curves are the fitted Gaussian distributions. Vertical lines indicate the estimated D_i ($\pm 2\sigma$).

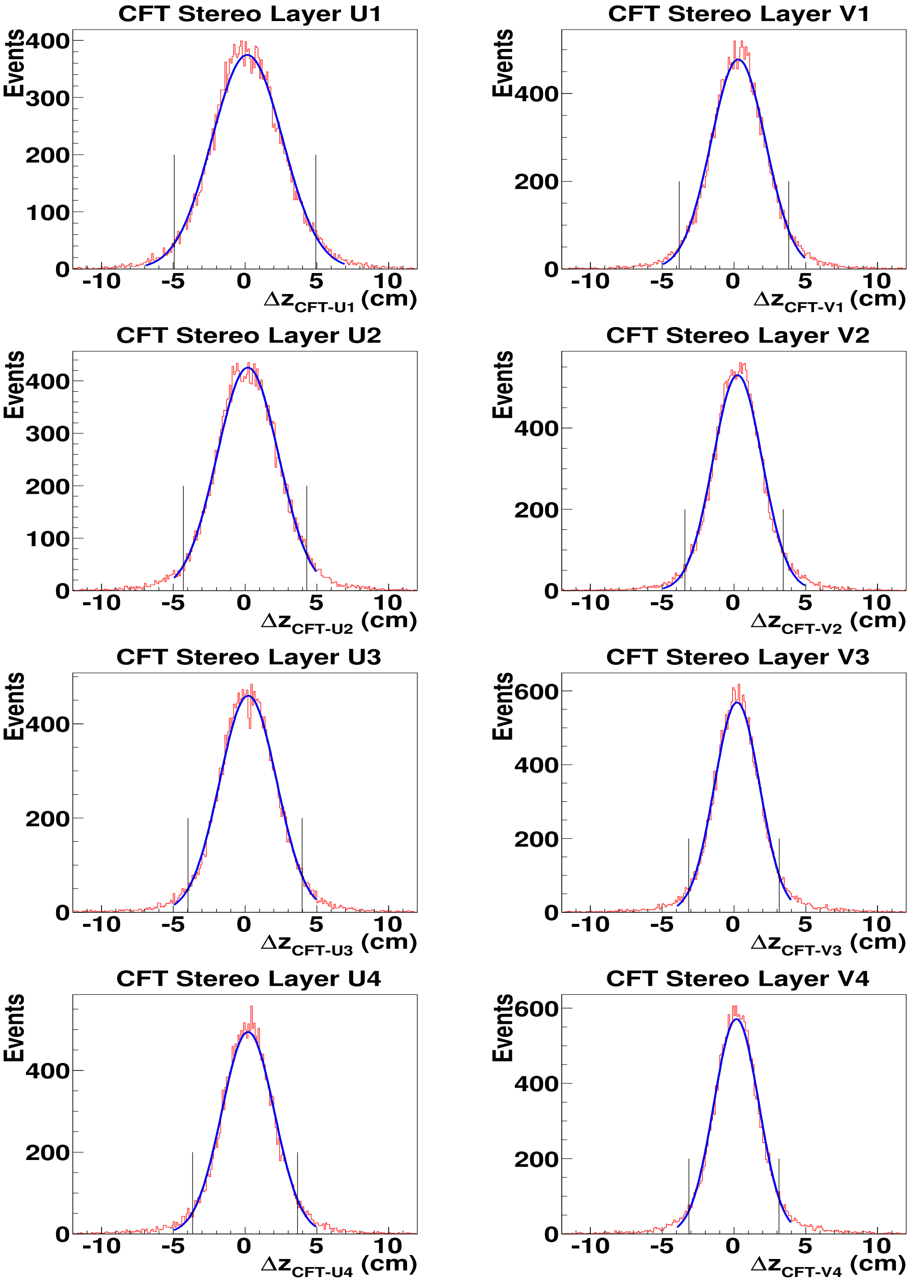

Figure 4.7: Δz_i in the ith CFT stereo layers for the CPS road. Blue curves are the fitted Gaussian distributions. Vertical lines indicate the estimated D_i ($\pm 2\sigma$).

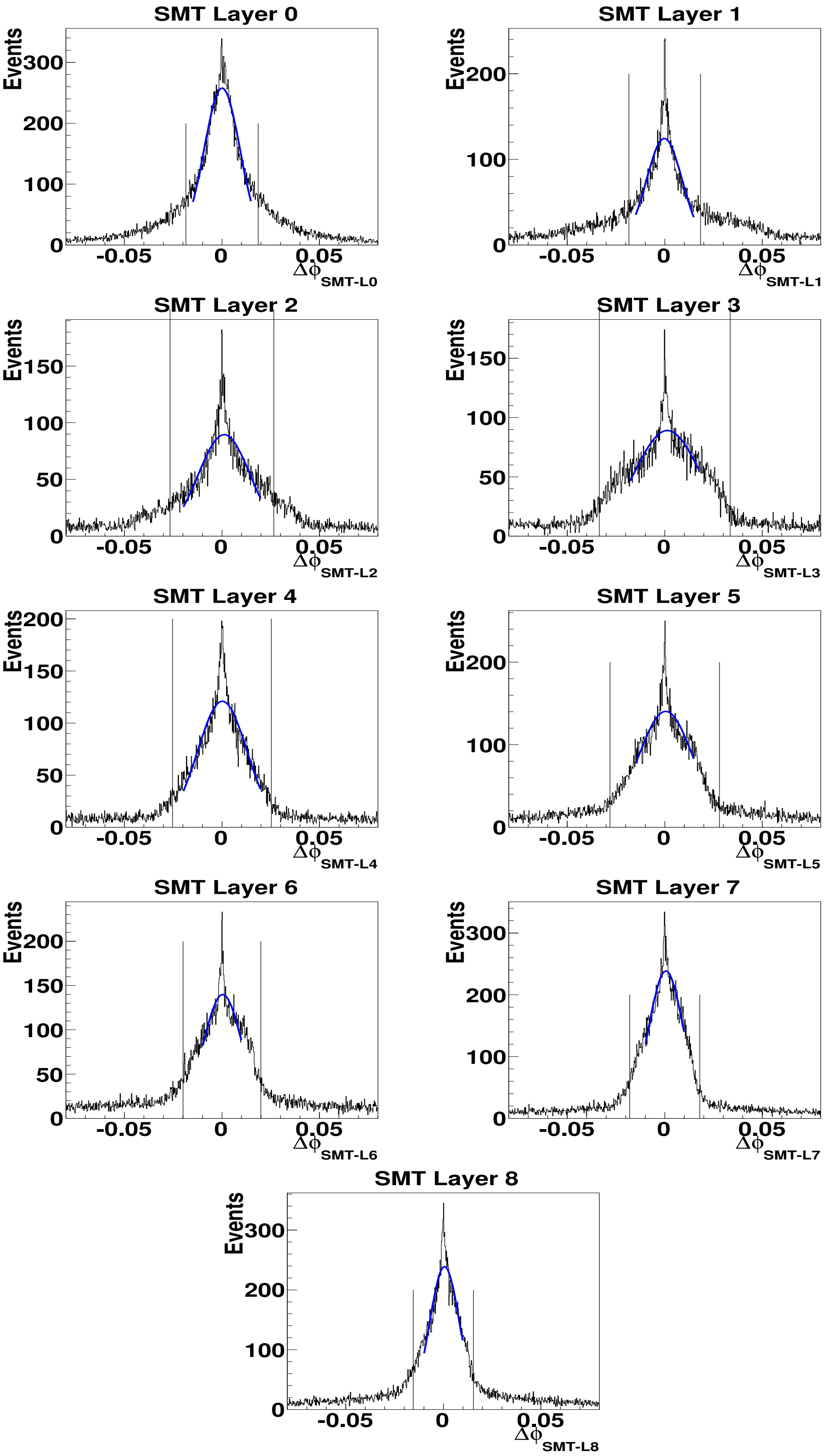

Figure 4.8: $\Delta\phi_i$ in the ith SMT barrel layers for the EM road. Blue curves are the fitted Gaussian distributions. Vertical lines indicate the estimated D_i ($\pm 2\sigma$).

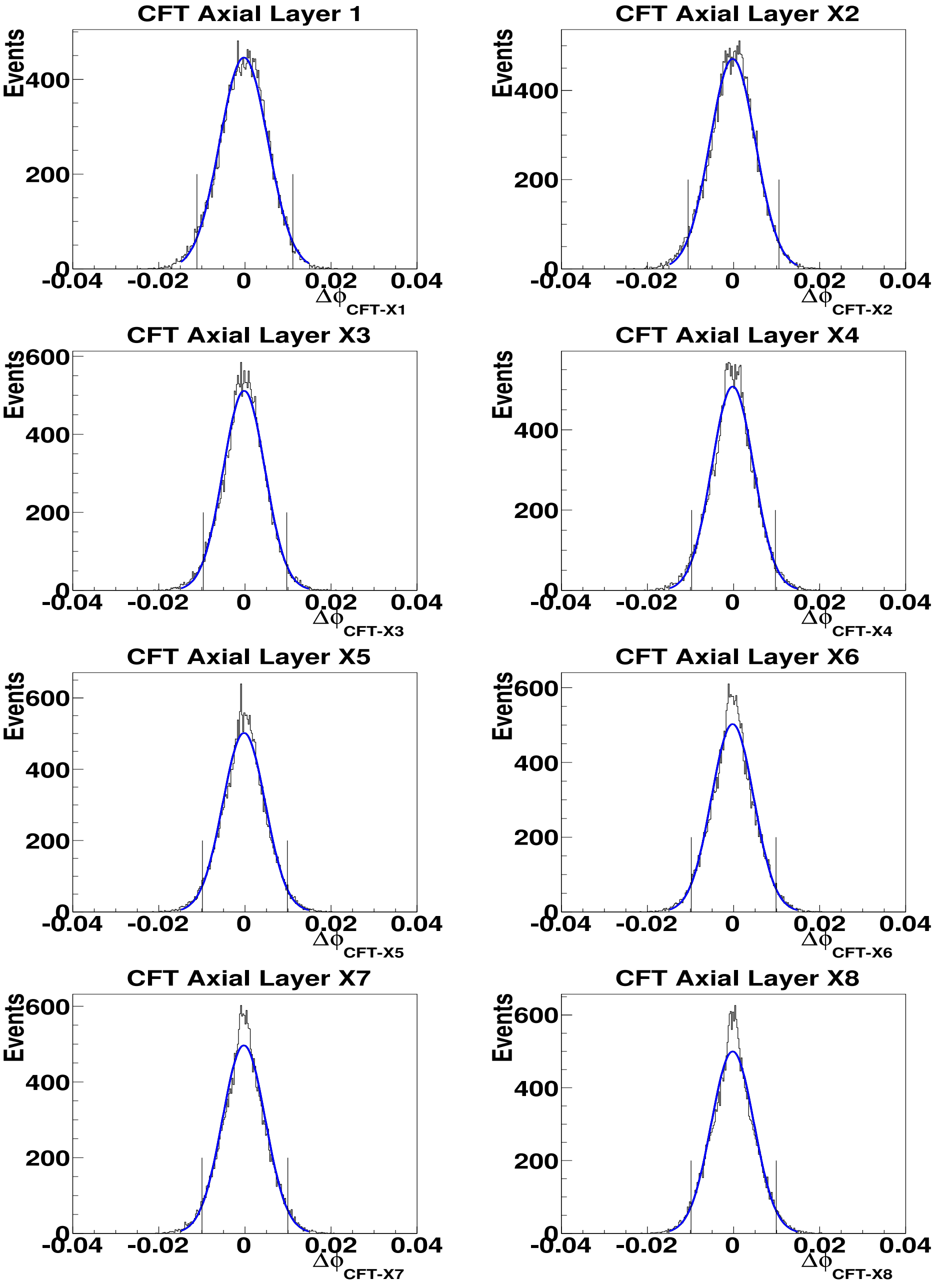

Figure 4.9: $\Delta\phi_i$ in the ith CFT axial layers for the EM road. Blue curves are the fitted Gaussian distributions. Vertical lines indicate the estimated D_i ($\pm 2\sigma$).

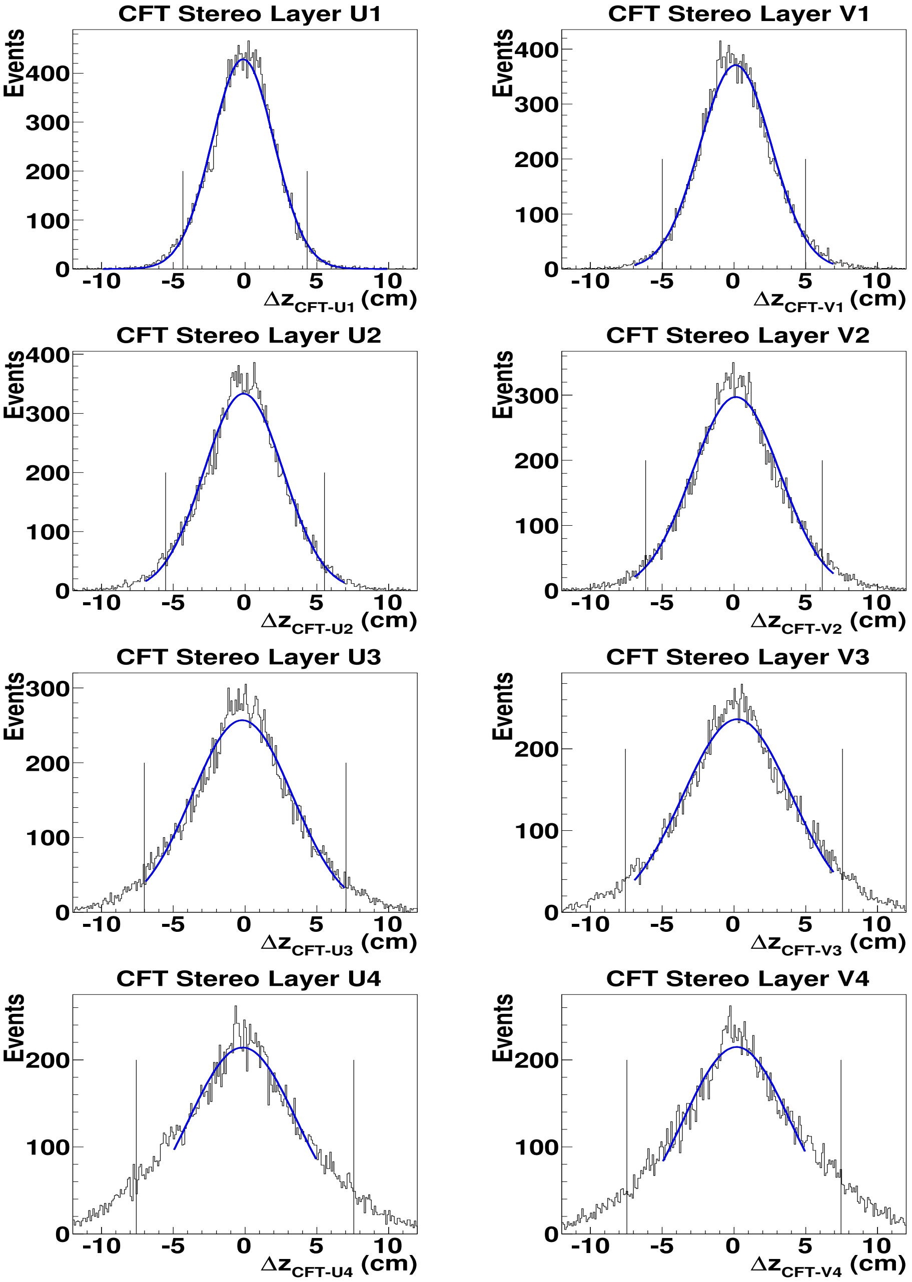

Figure 4.10: Δz_i in the ith CFT stereo layers for the EM road. Blue curves are the fitted Gaussian distributions. Vertical lines indicate the estimated D_i ($\pm 2\sigma$).

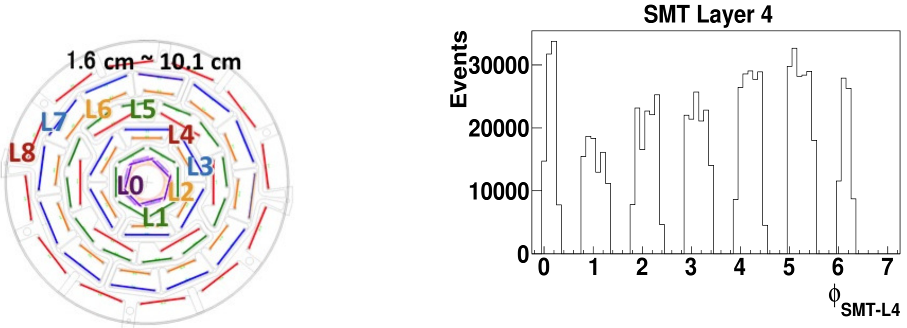

(a) End view of SMT barrel sensors.

(b) ϕ distribution of hits in the 4th layer of sensors in one SMT barrel.

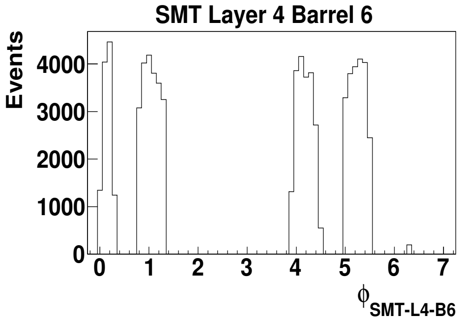

(c) ϕ distribution of hits in the SMT barrel 6 layer 4 sensors.

Figure 4.11: Distributions to help understanding the structures of $\Delta\phi_i$ distributions.

4.3.2 Input variables to the ANN for CC EM objects

The HoR$_{CC}$ discriminant is tuned by using the ANN. Signals for the ANN are electron candidates and backgrounds are photon candidates. Electron and photon candidates are EM objects from different samples but selected with the same selection criteria. The selection criteria only include calorimeter based cuts; there are no requirements in the tracking system. Electron candidates are selected from $Z/\gamma^* \to e^+e^-$ data samples with an integrated luminosity of 1.2 fb $^{-1}$; photon candidates are from QCD di-γ MC samples. Technically, the "tag-and-probe method" is used when selecting electron candidates (it is not used when selecting photon candidates). Probes, which are EM objects selected by calorimeter based cuts only, are taken as electron candidates. Photon candidates are EM objects directly selected from the QCD di-γ MC events with the same selection criteria. Data is not used here due to the difficulty of getting pure photon signals. Instead, MC samples with full detector simulation are used. Possible effect of this approach is the tuned ANN discriminant would give a lower selection efficiency on photons in data since random/noisy hits are impossible to be fully simulated, consequently making MC photons slightly more 'signal-like'. This effect can be corrected by the application of scale factors between data and MC for object selection efficiency, which is the case for most analyses.

Details of the selection criteria for signals and backgrounds can be found in Reference [17].

As cross checks, electron/photon candidates from $Z/\gamma^* \to e^+e^-$ MC and QCD multijet MC samples are selected using the same selection criteria and compared with signals and backgrounds in every step.

As described in Section 4.2, the input variables to the ANN for tuning HoR$_{CC}$ are N_{hits}^{smtB}, N_{hits}^{cftA}, and N_{hits}^{cftS} from the road with bigger N_{hits}^{total}. Additionally, a boolean variable, useCPS, is included in the input variables. It indicates the road type (CPS road or EM road).

$\chi_{hits}^{2(i)}$ are defined for each group of layers (disks), where i denotes the type of the group ($i = smtB$, $smtD$, $cftA$, and $cftS$). It is defined by

$$\chi_{hits}^{2(i)} = \frac{1}{N_{hits}^{i}} \cdot \sum_{j} \left(\frac{\delta_j}{D_j} \right)^2 ,$$

where δ_j is $\Delta\phi_j$ for SMT and CFT stereo layers and Δz_j for CFT axial layers, and j denotes the jth layer/disk of the group i. In case of the two roads of an considered EM object have the same N_{hits}^{total}, the road with a smaller $\chi_{hits}^{2(total)}$ is chosen, where $\chi^{2(total)}_{hits} = \chi^{2(smtB)}_{hits} + \chi^{2(cftA)}_{hits}$. Distributions of these input variables can be found in Fig. 4.12. Distributions of the $\chi^{2(smtB)}_{hits}$, $\chi^{2(cftA)}_{hits}$, $\chi^{2(cftS)}_{hits}$and N^{total}_{hits} can be found in Figure 4.13. Distributions of Zee MC events are slightly more "signal-like" than those for Zee data events. This is due to the limited simulation of detector inefficiency, e.g. lack of implementation of real-time minor detector failures.

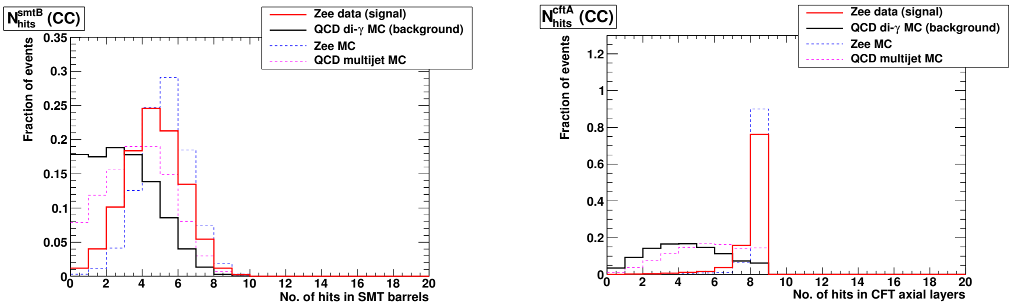

(a) N^{smtB}_{hits} (b) N^{cftA}_{hits}

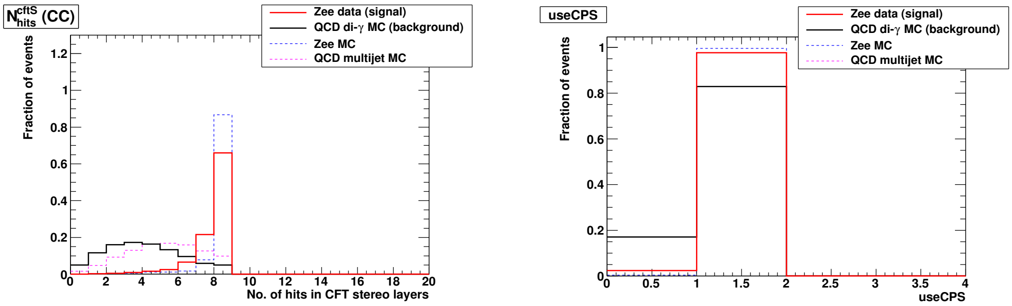

(c) N^{cftS}_{hits} (d) useCPS

Figure 4.12: Input variables to the ANN for tuning HoR_{CC}.

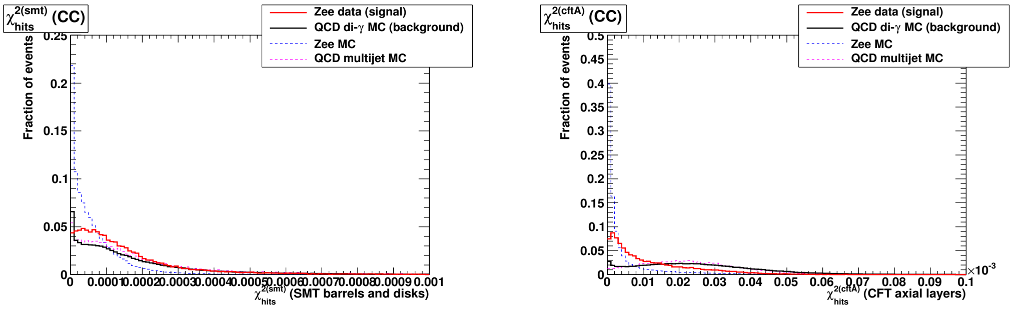

(a) $\chi^{2(smt)}_{hits}$ (b) $\chi^{2(cftA)}_{hits}$

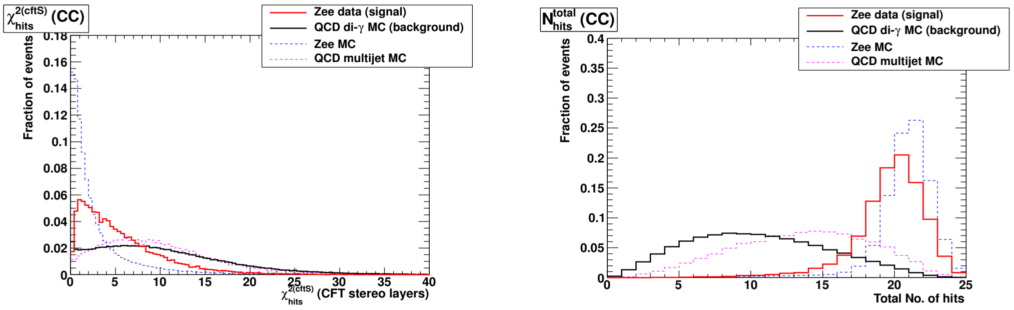

(c) $\chi^{2(cftS)}_{hits}$ (d) N^{total}_{hits}

Figure 4.13: Distributions of $\chi^{2(smt)}_{hits}$, $\chi^{2(cftA)}_{hits}$, $\chi^{2(cftS)}_{hits}$ and N^{total}_{hits} for EM objects in the CC.

4.3.3 Performance of the HoR discriminant in the CC

The HoR_{CC} discriminant can be used in two ways: (i) $\mathrm{HoR}_{CC} > x_i$, where x_i is the cut value, or (ii) $\mathrm{HoR}_{CC} < x_i$. The first type of cut is for selecting electron candidates; the second is for selecting photon candidates. To study the performance of HoR_{CC}, distributions of efficiencies for both types of cuts are shown together with the distribution of HoR_{CC}, as in Figure 4.14.

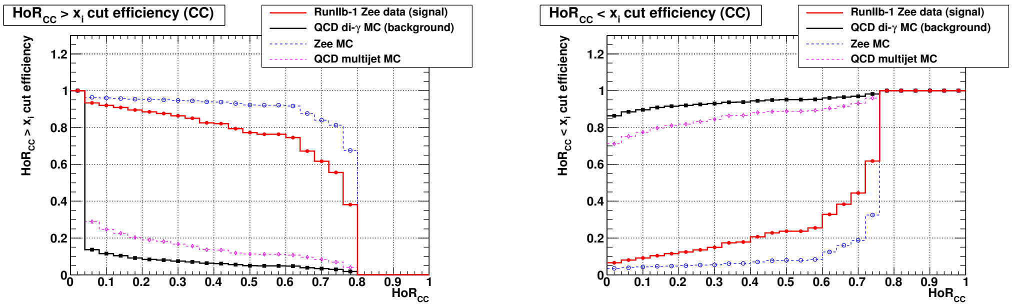

(a) Efficiencies of $\mathrm{HoR}_{CC} > x_i$ for electron identification

(b) Efficiencies of $\mathrm{HoR}_{CC} < x_i$ for photon identification

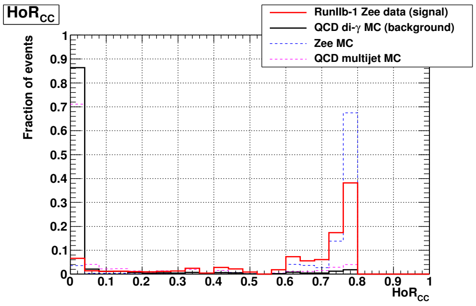

(c) HoR_{CC}

Figure 4.14: Efficiencies of HoR_{CC} cuts and distributions of HoR_{CC}.

Figure 4.15 shows dependence of the $\mathrm{HoR}_{CC} > 0.2$ cut efficiency for EM objects with $P_{trk} < 0.0$. The dependence on EM object transverse energy (E_T), η and ϕ in the detector coordinate system (η_{det}, and ϕ_{det}) has been studied. No obvious dependence is found for these variables. HoR_{CC} cut efficiencies for $Z/\gamma^* \to e^+e^-$ data events in different instantaneous luminosity range are compared in Figure 4.16. HoR_{CC} cut efficiency goes up as instantaneous luminosity increases. This is as expected, since more hits are present in the tracking system in high instantaneous luminosity environment.

As the HoR method is supplementary to the track-matching algorithm, the HoR discriminants are better to be used together with the track-matching requirements ($P_{trk} > 0.0$ or $P_{trk} < 0.0$). Thus two recommended ways to use the HoR discriminants are:

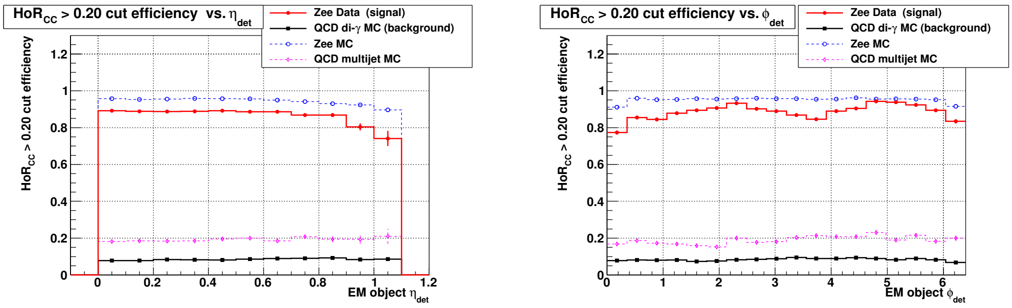

(a) Eff. vs. η_{det} (b) Eff. vs. ϕ_{det}

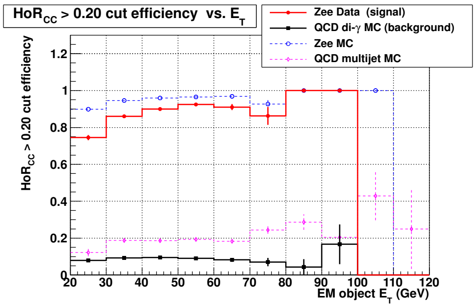

(c) Eff. vs. E_T

Figure 4.15: HoR$_{CC}$ > 0.2 cut efficiencies as functions of E_T, η_{det} and ϕ_{det}.

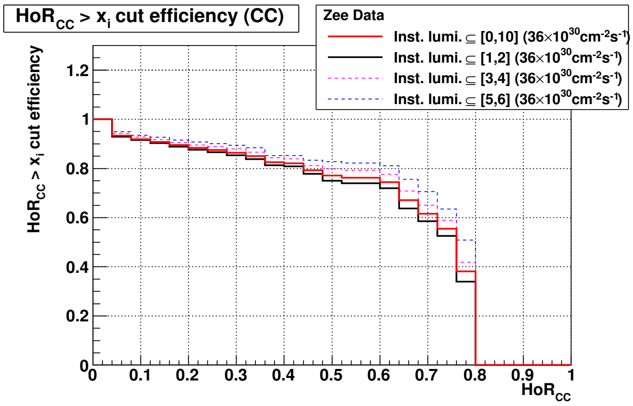

Figure 4.16: HoR$_{CC}$ $> x_i$ cut efficiencies for $Z/\gamma^* \to e^+e^-$ data events in different instantaneous luminosity range.

- HoR$_{CC}$ $> x_i$ or $P_{trk} \geq 0.0$ for selecting electron candidates;
- HoR$_{CC}$ $< x_i$ and $P_{trk} < 0.0$ for selecting photon candidates.

To evaluate the actual gain of using the HoR discriminant, the HoR$_{CC}$ cut efficiencies are also shown separately for EM objects with $P_{trk} \geq 0.0$ (Figure 4.17) and $P_{trk} < 0.0$ (Figure 4.18).

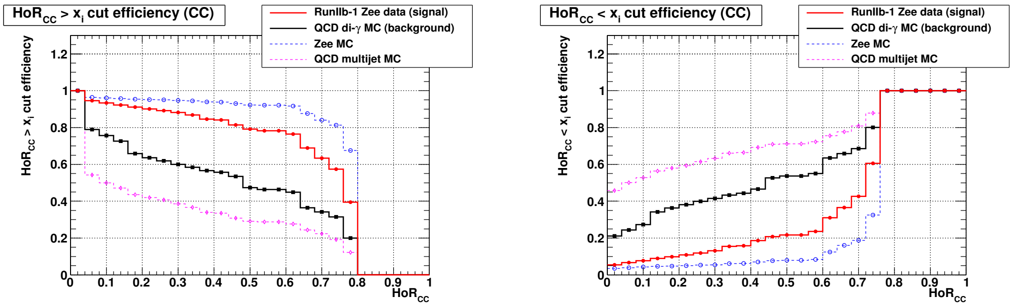

(a) Efficiencies of HoR$_{CC}$ $> x_i$ for electron identification
(b) Efficiencies of HoR$_{CC}$ $< x_i$ for photon identification

Figure 4.17: Efficiencies of HoR$_{CC}$ cuts for CC EM objects with $P_{trk} > 0.0$.

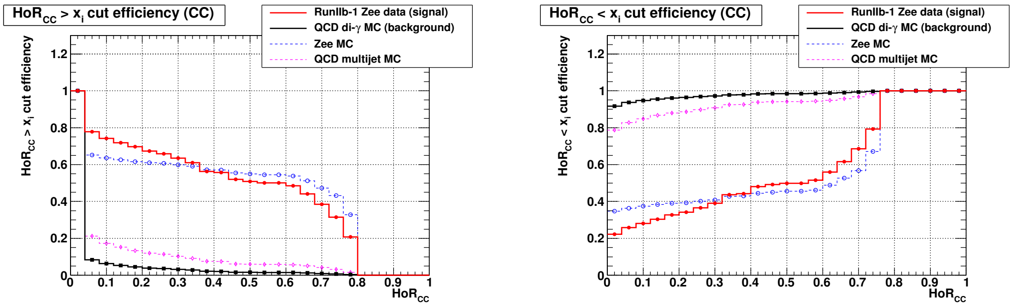

(a) Efficiencies of HoR$_{CC}$ $> x_i$ for electron identification
(b) Efficiencies of HoR$_{CC}$ $< x_i$ for photon identification

Figure 4.18: Efficiencies of HoR$_{CC}$ cuts for CC EM objects with $P_{trk} < 0.0$.

Figure 4.19 and Figure 4.20 compare the cut efficiencies of the current HoR$_{CC}$ with previous HoR$_{CC}$ (developed during RunIIa). Figure 4.19 shows the HoR$_{CC}$ $> x_i$ cut efficiencies for selecting electron candidates; and Figure 4.19 shows the HoR$_{CC}$ $< x_i$ cut efficiencies for selecting photon candidates. Figure 4.19(b) and Figure 4.19(b) indicate the current HoR$_{CC}$ has slightly better performance (higher signal to background ratios) for both electron and photon identification. The improvements are contributed by (i) more accurate road widths (road widths were not updated after RunIIa for the previous HoR$_{CC}$); (ii) using additional detector layers (SMT layer 0 was not yet installed during RunIIa); (iii) using ANN to tune the discriminant instead of a simple likelihood function.

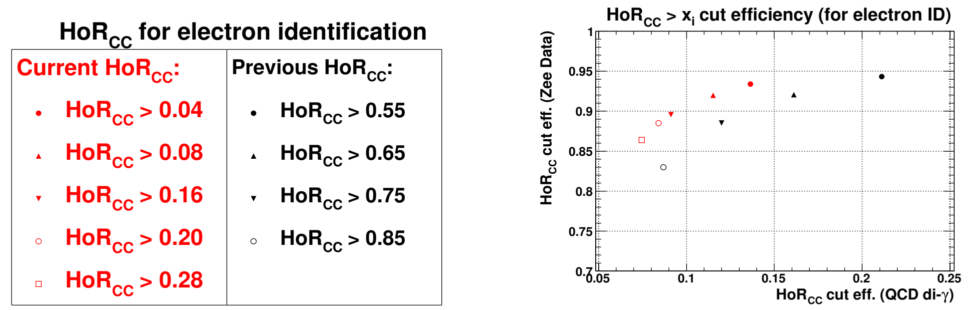

(a) Legend

(b) Zee data (signal) vs. QCD di-γ (background)

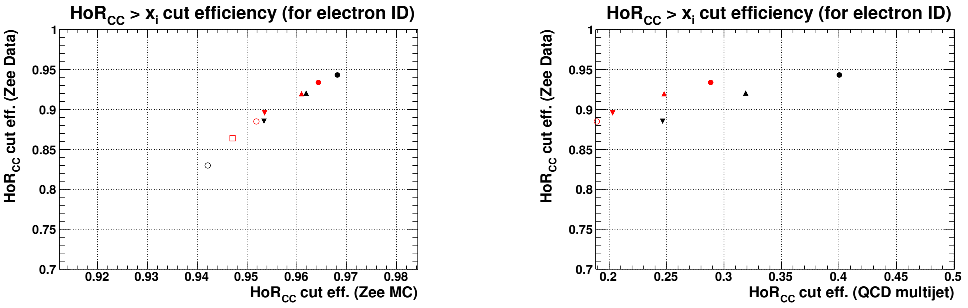

(c) Zee data (signal) vs. Zee MC

(d) Zee data (signal) vs. QCD multijet

Figure 4.19: Comparisons of the current HoR$_{CC}$ cut efficiencies with the previous HoR$_{CC}$ for electron identification (EM objects selected from Zee data events are signal electron candidates and those from QCD di-γ events are background electron candidates).

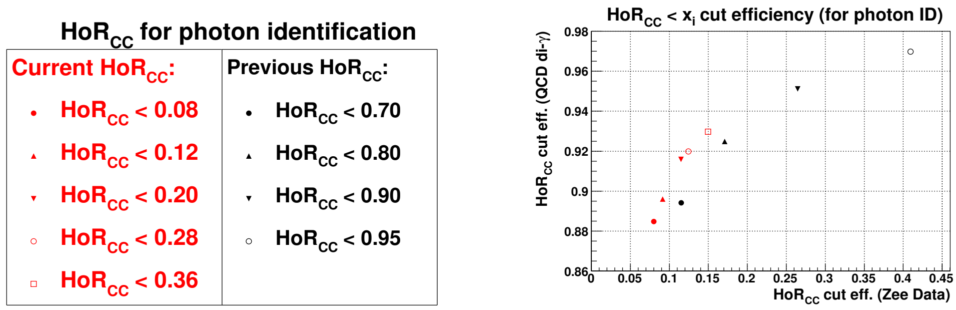

(a) Legend

(b) QCD di-γ (signal) vs. Zee data (background)

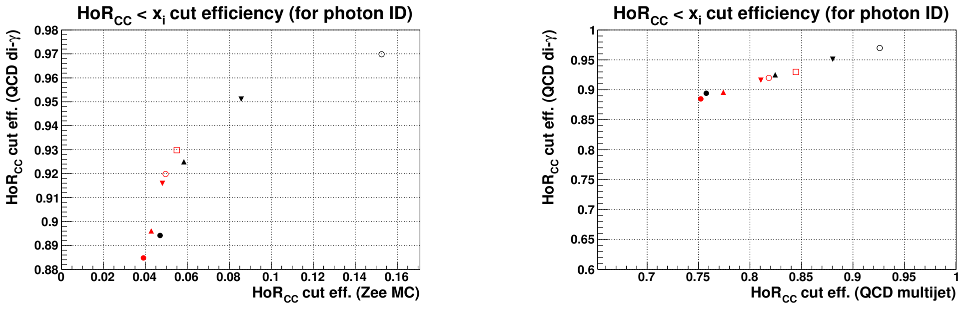

(c) QCD di-γ (signal) vs. Zee MC

(d) QCD di-γ (signal) vs. QCD multijet

Figure 4.20: Comparisons of the current HoR$_{CC}$ cut efficiencies with the previous HoR$_{CC}$ for photon identification (EM objects selected from QCD di-γ events are signal photon candidates and those from Zee data events are background photon candidates).

4.3.4 Application of the HoR discriminant in the CC

Application of the HoR discriminant for electron identification in the CC

This section gives an example of using the HoR_{CC} discriminant in the electron identification. The cut on HoR_{CC} discriminant is used together with the electron selection criteria "CC Point0" [18]. The "CC Point0" criteria is provided by the D0 EMID group and widely used by many analyses to select electrons in the CC[4].

Table 4.1 shows the cut efficiency of P_{trk} for "CC Point0" electron candidates. The HoR_{CC} cut efficiencies for electrons candidates passing these P_{trk} cuts are further listed separately in Table 4.2. These efficiencies are also plotted in Figure 4.21.

Cut type	$P_{trk} < 0.0$	$P_{trk} \geq 0.0$
Zee data	0.073	0.927
Zee MC	0.029	0.971
QCD di-γ	0.925	0.075
QCD multijet	0.687	0.313

Table 4.1: P_{trk} cut efficiencies of "CC Point0" electrons.

Electron type	$P_{trk} < 0.0$				$P_{trk} \geq 0.0$			
Cut type	$\mathrm{HoR}_{CC} >$				$\mathrm{HoR}_{CC} >$			
	0.04	0.08	0.12	0.16	0.04	0.08	0.12	0.16
Zee data	0.730	0.697	0.676	0.655	0.935	0.923	0.910	0.897
Zee MC	0.632	0.614	0.602	0.592	0.959	0.955	0.950	0.946
QCD di-γ	0.085	0.064	0.055	0.046	0.791	0.758	0.728	0.663
QCD multijet	0.264	0.220	0.197	0.174	0.507	0.461	0.432	0.400

Table 4.2: HoR_{CC} cut efficiencies of "CC Point0" electrons for electrons passing different P_{trk} requirements.

Based on the efficiencies listed in Table 4.1 and Table 4.2, the combined efficiencies (passing both cuts on HoR_{CC} and P_{trk}, or passing either cuts on HoR_{CC} or P_{trk}) can be directly calculated, as shown in Table 4.3 and Table 4.4.

Compared to only using cut on P_{trk}, requiring electron candidates to pass either cuts on HoR_{CC} or P_{trk} enlarges the signal efficiency, but still maintains control of the background efficiency; requiring electron candidates to pass both cuts on HoR_{CC} and P_{trk} reduces the background efficiency, but retains a relatively high signal efficiency simultaneously. By utilizing the HoR_{CC} discriminant,

---

[4] Other names of electron and photon selection criteria mentioned later in this chapter, such as "CC Core1", "EC Point0" and "EC Core1", are also designed by the D0 EMID group and widely used by many analyses for electron/photon selection.

Cut type	$P_{trk} \geq 0.0$ **or** HoR$_{CC} >$				$P_{trk} \geq 0.0$
	0.04	0.08	0.12	0.16	
Zee data	0.980	0.978	0.977	0.975	0.927
Zee MC	0.989	0.989	0.989	0.988	0.971
QCD di-γ	0.154	0.135	0.126	0.118	0.075
QCD multijet	0.495	0.464	0.448	0.432	0.313

Table 4.3: Efficiencies of "CC Point0" electrons passing the cuts on either HoR$_{CC}$ **or** P_{trk} (The last column lists the efficiencies of $P_{trk} \geq 0.0$ as a reference.)

Cut type	$P_{trk} \geq 0.0$	$P_{trk} \geq 0.0$ **and** HoR$_{CC} >$			
		0.04	0.08	0.12	0.16
Zee data	0.927	0.867	0.856	0.844	0.832
Zee MC	0.971	0.931	0.927	0.922	0.918
QCD di-γ	0.075	0.060	0.057	0.055	0.050
QCD multijet	0.313	0.159	0.144	0.135	0.125

Table 4.4: Efficiencies of "CC Point0" electrons passing the cuts on both HoR$_{CC}$ **and** P_{trk} (The second column lists the efficiencies of $P_{trk} \geq 0.0$ as a reference.)

physics analyzers have more options of the cuts yielding different signal to background fractions. Thus, statistical and systematic uncertainties can be better balanced by selecting the proper cuts.

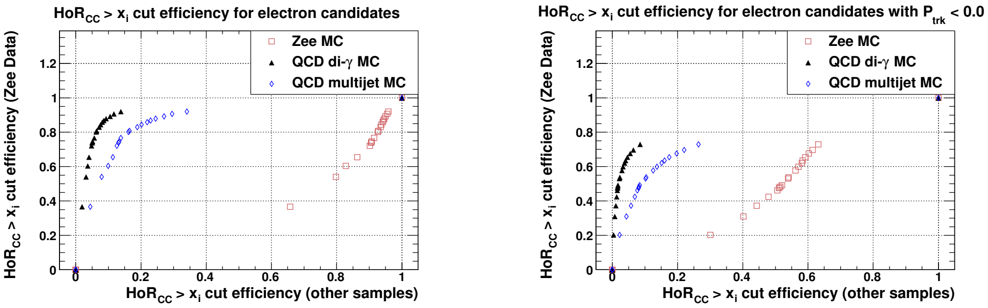

(a) No P_{trk} cut

(b) $P_{trk} < 0.0$

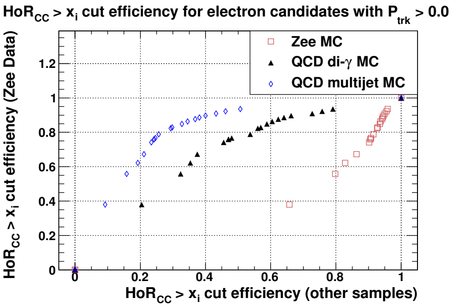

(c) $P_{trk} \geq 0.0$

Figure 4.21: HoR$_{CC}$ cut efficiencies of "CC Point0" electrons with different P_{trk} requirements.

Application of the HoR discriminant for photon identification in the CC

Similarly, to give an example of using the HoR_{CC} discriminant with the photon identification, the photon selection criteria "CC Core1" [19] are used together with the cut on HoR_{CC}.

Table 4.5 shows the cut efficiency of P_{trk} for "CC Core1" photon candidates.

Cut type	$P_{trk} < 0.0$	$P_{trk} \geq 0.0$
Zee data	0.075	0.925
Zee MC	0.028	0.972
QCD di-γ	0.929	0.071
QCD multijet	0.727	0.273

Table 4.5: P_{trk} cut efficiencies of "CC Core1" photons.

Table 4.6 lists the cut efficiency of using different HoR_{CC} for EM objects with $P_{trk} < 0.0$ and $P_{trk} \geq 0.0$. These cut efficiencies are also plotted in Figure 4.22.

Photon type	$P_{trk} < 0.0$				$P_{trk} \geq 0.0$			
Cut type	$\text{HoR}_{CC} <$				$\text{HoR}_{CC} <$			
	0.76	0.64	0.32	0.12	0.76	0.64	0.32	0.12
Zee data	0.797	0.574	0.413	0.309	0.608	0.314	0.136	0.081
Zee MC	0.688	0.513	0.434	0.402	0.329	0.128	0.059	0.047
QCD di-γ	0.997	0.988	0.973	0.948	0.795	0.631	0.415	0.278
QCD multijet	0.981	0.942	0.895	0.831	0.893	0.778	0.664	0.565

Table 4.6: HoR_{CC} cut efficiencies of "CC Core1" photons with different P_{trk} requirements.

Table 4.7 and Table 4.8, which can be calculated from the efficiencies listed in Table 4.5 and Table 4.6, show the efficiencies of the combined cut.

Cut type	$P_{trk} < 0.0$ **or** $\text{HoR}_{CC} <$				$P_{trk} < 0.0$
	0.76	0.64	0.32	0.12	
Zee data	0.812	0.606	0.457	0.361	0.075
Zee MC	0.697	0.527	0.450	0.419	0.028
QCD di-γ	1.000	0.999	0.998	0.996	0.929
QCD multijet	0.995	0.984	0.971	0.954	0.727

Table 4.7: Efficiencies of "CC Core1" photons passing the cuts on either HoR_{CC} **or** P_{trk} (The last column lists the efficiencies of $P_{trk} < 0.0$ as a reference.)

Cut type	$P_{trk} < 0.0$	$P_{trk} < 0.0$ **and** HoR$_{CC}$ <			
		0.76	0.64	0.32	0.12
Zee data	0.075	0.046	0.024	0.010	0.006
Zee MC	0.028	0.009	0.004	0.002	0.004
QCD di-γ	0.929	0.739	0.586	0.386	0.258
QCD multijet	0.727	0.649	0.566	0.483	0.411

Table 4.8: Efficiencies of "CC Core1" photons passing the cuts on both HoR$_{CC}$ **and** P_{trk} (The second column lists the efficiencies of $P_{trk} < 0.0$ as a reference.)

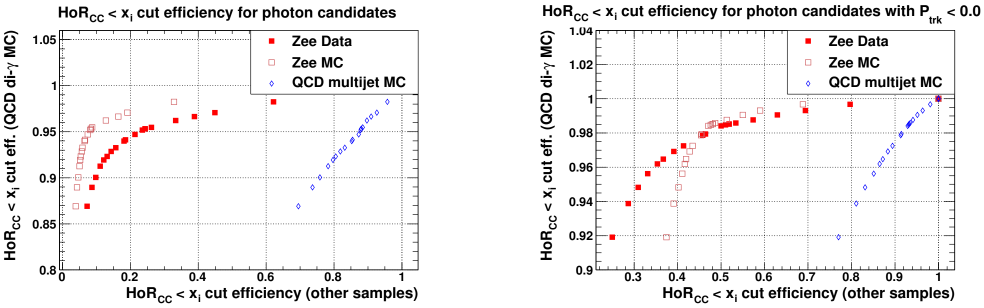

(a) No P_{trk} cut

(b) $P_{trk} < 0.0$

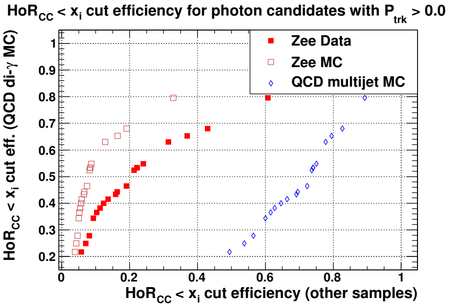

(c) $P_{trk} \geq 0.0$

Figure 4.22: HoR$_{CC}$ cut efficiencies of "CC Core1" photons with different P_{trk} requirements.

4.4 The HoR discriminant in the EC

Same as the HoR method used for EM objects in the CC, the development of the HoR discriminant for EM objects in the EC consists of two main steps: i) estimation of the road width, D_i; and ii) tuning the ANN discriminant. Section 4.4.1 describes the estimation of D_i. The tuning of the HoR discriminant is described in Section 4.4.2. Section 4.4.3 documents the HoR performance for events from different processes, and events with different tracking requirements. Section 4.4.4 gives examples of applying the discriminant together with the electron (photon) selection criteria designed by the D0 EMID group.

4.4.1 Road widths in the EC

The road widths in the SMT barrel and CFT layers are kept the same for EC EM objects. Since hits in the SMT F-disks and H-disks are utilized for EC EM objects, we need to estimate the road width for those SMT disks. The procedure is the same as that in the CC, except that electrons in the EC are used.

The road widths (D_i) for each SMT F-disk and H-disk are shown in Figure 4.23, Figure 4.24 and Figure 4.25.

---

[4] The outer H-disks, H-Disk 1 and H-Disk 4, were not working properly. They are not used in the data taking.

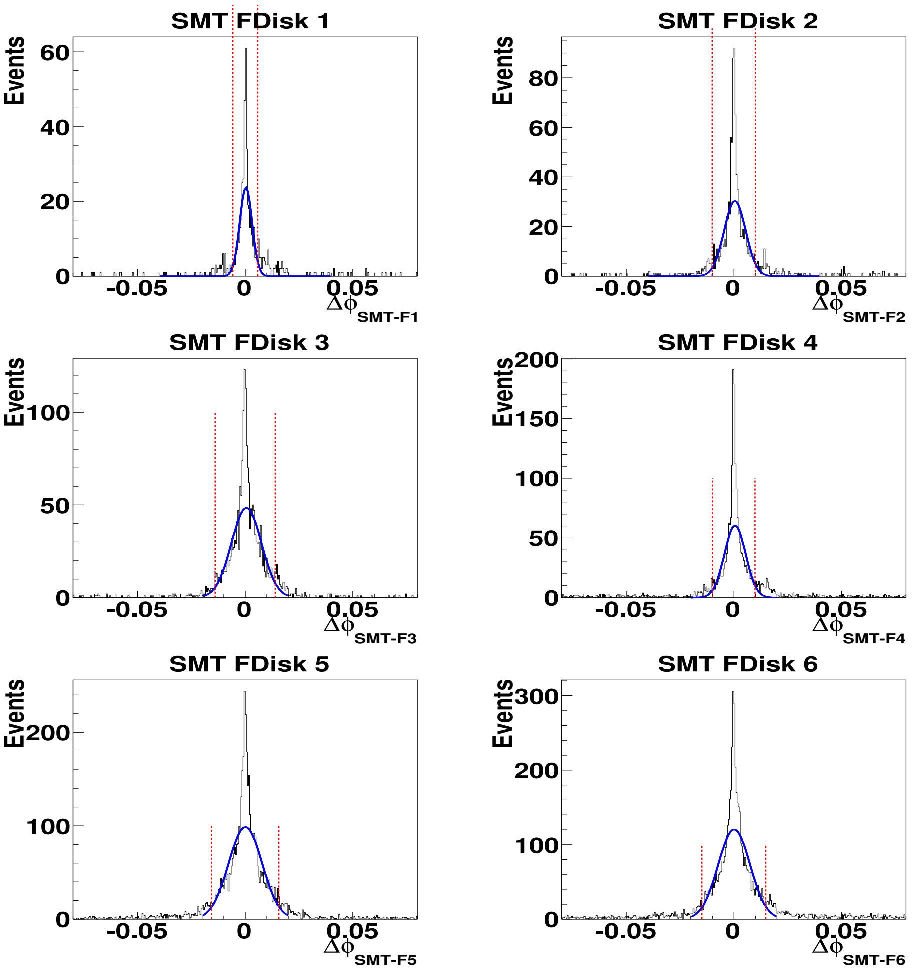

Figure 4.23: $\Delta\phi_i$ in the ith SMT disks (F-Disk 1 to F-Disk 6) for the EM road. Blue curves are the fitted Gaussian distributions. Vertical lines indicate the estimated D_i ($\pm 2\sigma$).

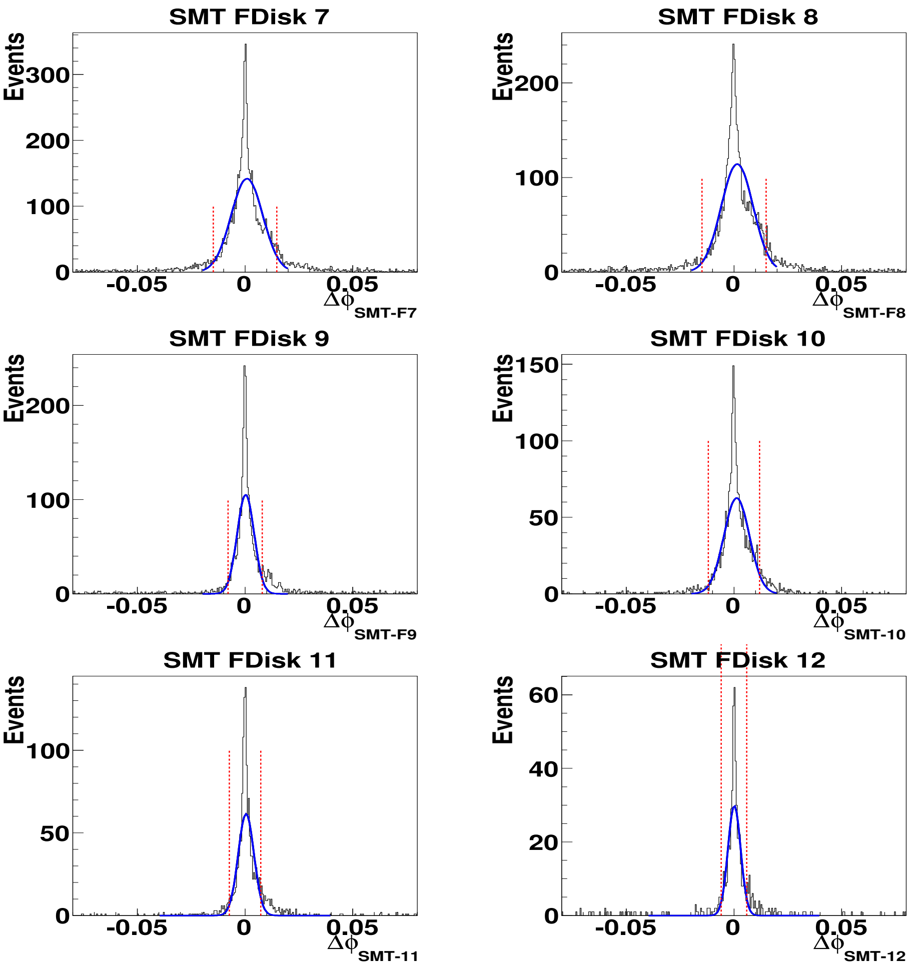

Figure 4.24: $\Delta\phi_i$ in the ith SMT disks (F-Disk 7 to F-Disk 12) for the EM road. Blue curves are the fitted Gaussian distributions. Vertical lines indicate the estimated D_i ($\pm 2\sigma$).

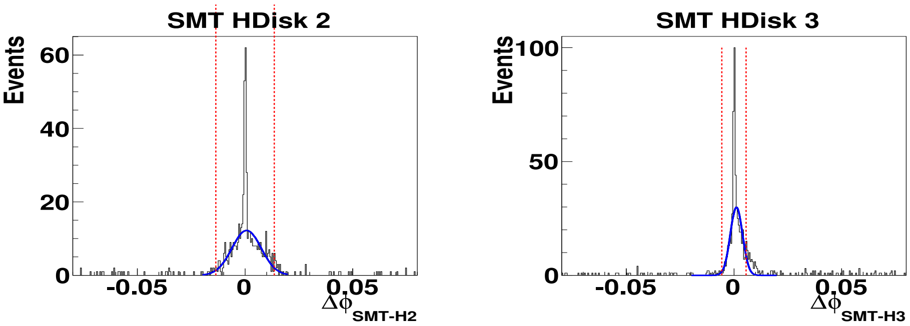

Figure 4.25: $\Delta\phi_i$ in the ith SMT disks (H-Disk 2 and H-Disk 3) for the EM road. Blue curves are the fitted Gaussian distributions. Vertical lines indicate the estimated D_i ($\pm 2\sigma$).

4.4.2 Input variables to the ANN for EC EM objects

Similar to the tuning of HoR$_{CC}$, electron and photon candidates are used as signals and backgrounds to the ANN, respectively. Details of the selection criteria for signals and backgrounds can be found in Reference [17].

Additionally, electron and photon candidates from $Z/\gamma^* \rightarrow e^+e^-$ MC and QCD multijet MC samples are selected using the same selection criteria and compared with signals and backgrounds in every step.

As described in Section 4.2, the input variables to the ANN for tuning HoR for EC EM objects are R^{smtB}, R^{smtD}, R^{cftA} and R^{cftS}.

Due to the poor CFT coverage in the forward region, there are quite many EC EM objects for which the roads do not pass through any CFT layers. In order to improve the training of the ANN, we separate the EC EM objects into two groups. One is for those EC EM objects for which the roads pass through at least one CFT layer ($N^{cft}_{max} \geq 1$), and the other is for those EC EM objects for which the roads do not pass through any CFT layers but only SMT layers or disks ($N^{cft}_{max} = 0$).

For the former group, R^{smtB}, R^{smtD}, R^{cftA} and R^{cftS} are used as input variables (denote the HoR discriminant as HoR$^{NN4}_{EC}$); for the latter group, only R^{smtB} and R^{smtD} are used (denote the HoR discriminant as HoR$^{NN2}_{EC}$). Approximately, 80% of EC EM objects have $N^{cft}_{max} \geq 1$ and are subjected to HoR$^{NN4}_{EC}$; and others have $N^{cft}_{max} = 0$ and are subjected to HoR$^{NN2}_{EC}$.

Distributions of these input variables can be found in Figure 4.26. Also shown in Figure 4.26 are distributions of N^i_{hits} and N^i_{max} ($i = smtB$, $smtD$, $cftA$, and $cftS$). Distributions of $\chi^{2(smt)}_{hits}$, $\chi^{2(cftA)}_{hits}$, N^{smt}_{hits} ($N^{smt}_{hits} = N^{smtB}_{hits} + N^{smtD}_{hits}$), and N^{total}_{hits} can be found in Figure 4.27; just as that in the CC, these variables are used to decide which road to chosen from the two roads of an EM object.

4.4.3 Performance of the HoR discriminant in the EC

The HoR$^{NN4}_{EC}$ and HoR$^{NN2}_{EC}$ discriminants can be used in both electron and photon identification. Electron (photon) candidates can be selected by requiring HoR$^{NN4}_{EC}$ (if $N^{cft}_{max} \geq 1$) or HoR$^{NN2}_{EC}$ (if $N^{cft}_{max} = 0$) to be greater (smaller) than a certain cut value; To study the performance of HoR$^{NN4}_{EC}$ (HoR$^{NN2}_{EC}$), cut efficiencies of selecting electron and photon candidates are shown in Figure 4.28 (Figure 4.29).

The dependences on E_T, η_{det} ϕ_{det} and instantaneous luminosity have also been studied for both HoR$^{NN4}_{EC}$ and HoR$^{NN2}_{EC}$. Figure 4.30 shows HoR$^{NN4}_{EC} >$ 0.2 cut efficiencies as functions of E_T, η_{det} and ϕ_{det}. Figure 4.31 shows similar

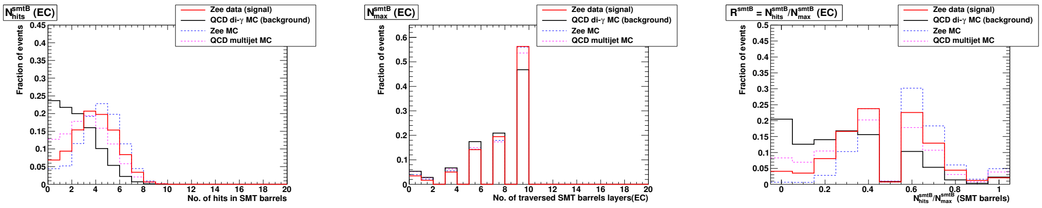

(a) N^{smtB}_{hits} (b) N^{smtB}_{max} (c) R^{smtB}

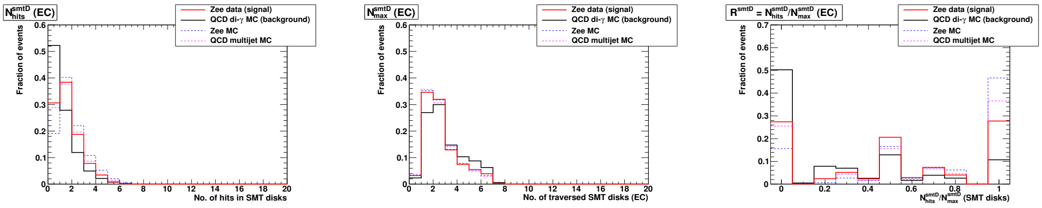

(d) N^{smtD}_{hits} (e) N^{smtD}_{max} (f) R^{smtD}

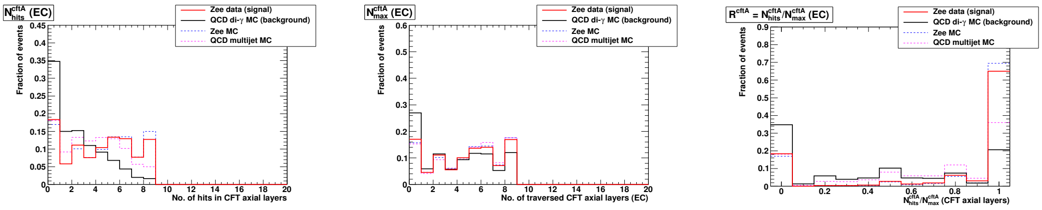

(g) N^{cftA}_{hits} (h) N^{cftA}_{max} (i) R^{cftA}

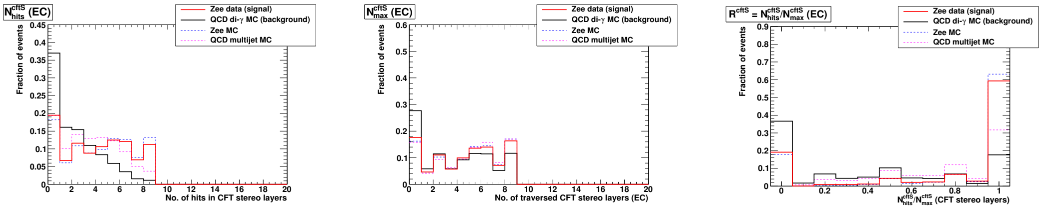

(j) N^{cftS}_{hits} (k) N^{cftS}_{max} (l) R^{cftS}

Figure 4.26: Distributions of N^i_{hits}, N^i_{max}, and R^i for EC EM objects (i = $smtB$, $smtD$, $cftA$, and $cftS$).

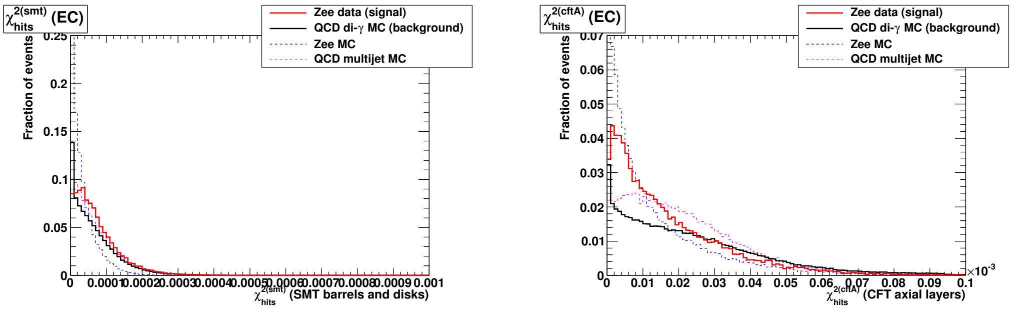

(a) $\chi^{2(smt)}_{hits}$ (b) $\chi^{2(cftA)}_{hits}$

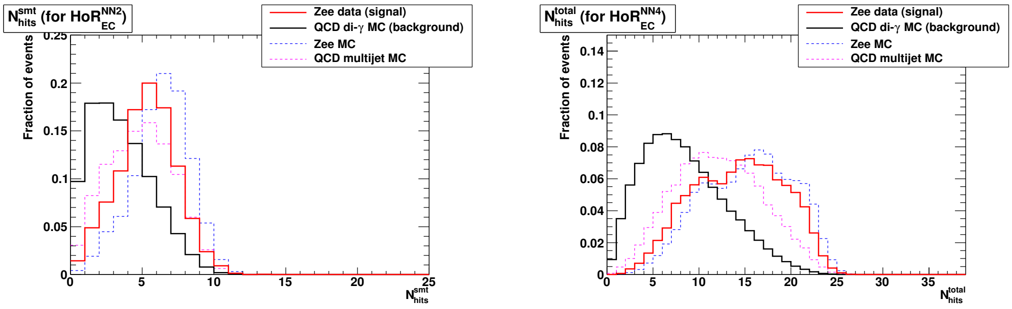

(c) N^{smt}_{hits} (d) N^{total}_{hits}

Figure 4.27: Distributions of $\chi^{2(smt)}_{hits}$, $\chi^{2(cftA)}_{hits}$, N^{smt}_{hits} and N^{total}_{hits} for EC EM objects.

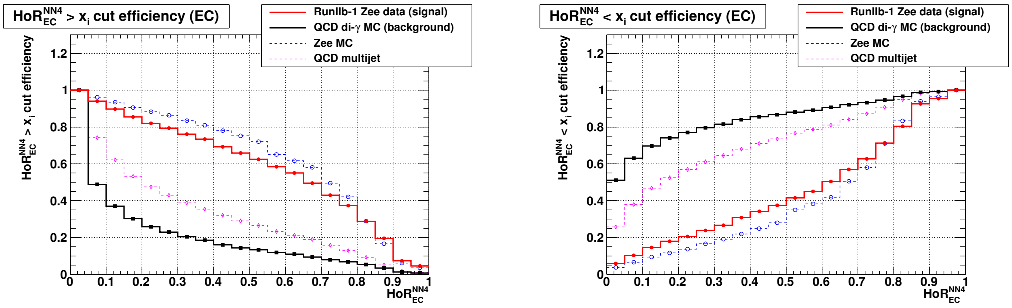

(a) Efficiencies of HoR$^{NN4}_{EC}$ $> x_i$ for electron identification (b) Efficiencies of HoR$^{NN4}_{EC}$ $< x_i$ for photon identification

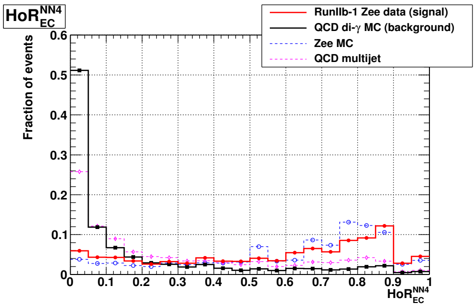

(c) HoR$^{NN4}_{EC}$

Figure 4.28: Efficiencies of HoR$^{NN4}_{EC}$ cut and distribution of HoR$^{NN4}_{EC}$.

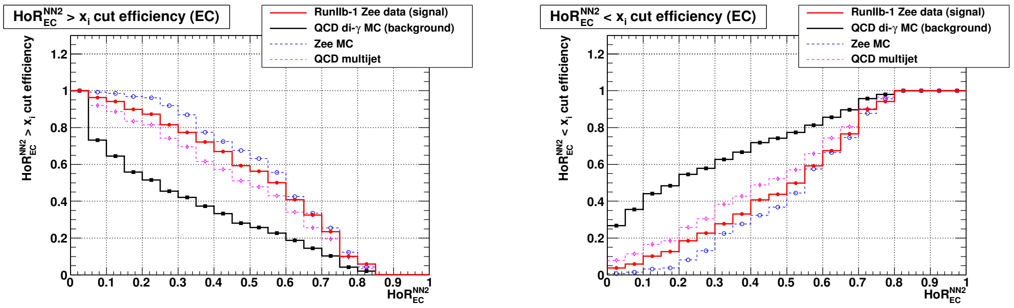

(a) Efficiencies of HoR$_{EC}^{NN2} > x_i$ for electron identification

(b) Efficiencies of HoR$_{EC}^{NN2} < x_i$ for photon identification

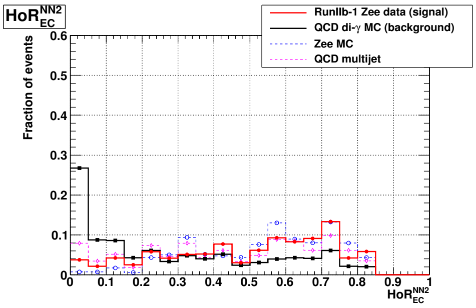

(c) HoR$_{EC}^{NN2}$

Figure 4.29: Efficiencies of HoR$_{EC}^{NN2}$ cut and distribution of HoR$_{EC}^{NN2}$.

distributions for HoR$_{EC}^{NN2} > 0.2$ cut.

Similar to Figure 4.17 and Figure 4.18, Figure 4.32 and Figure 4.33 show the HoR$_{EC}^{NN4}$ (HoR$_{EC}^{NN2}$) cut efficiencies for EC EM objects with $P_{trk} \geq 0.0$ and $P_{trk} < 0.0$, respectively.

Obviously, HoR$_{EC}^{NN4}$ and HoR$_{EC}^{NN2}$ would have a strong correlation with P_{trk}. EM objects with a good matched track are more likely to be electron candidates, and thus have a high HoR$_{EC}^{NN4}$ or HoR$_{EC}^{NN2}$ value. Figure 4.32(a) and Figure 4.32(b) show the separation in HoR$_{EC}^{NN4}$ between electron and photon candidates for EM objects with $P_{trk} \geq 0.0$. The separation in HoR$_{EC}^{NN4}$ is small in this case. The separation in HoR$_{EC}^{NN2}$ is negligible, as shown in Figure 4.32(c) and Figure 4.32(d). It suggests that using HoR$_{EC}^{NN4}$ (HoR$_{EC}^{NN2}$) on EM objects with $P_{trk} \geq 0.0$ would not bring much gain to electron and photon identification.

HoR$_{EC}^{NN4}$ and HoR$_{EC}^{NN2}$ performs much better on EM objects with $P_{trk} < 0.0$, as shown in Figure 4.33. Thus, more electron candidates can be genuinely selected by requiring on EM objects to pass either cut on HoR$_{EC}^{NN4}$ (HoR$_{EC}^{NN2}$) or P_{trk} (e.g. "HoR$_{EC}^{NN4} > 0.2$ or $P_{trk} > 0.0$"); and more backgrounds to photon candidates can be suppressed by using cuts as "HoR$_{EC} < x_i$ and $P_{trk} < 0.0$", where x_i is the cut value, and HoR$_{EC}$ is either HoR$_{EC}^{NN4}$ or HoR$_{EC}^{NN2}$ depending on N_{max}^{cft}.

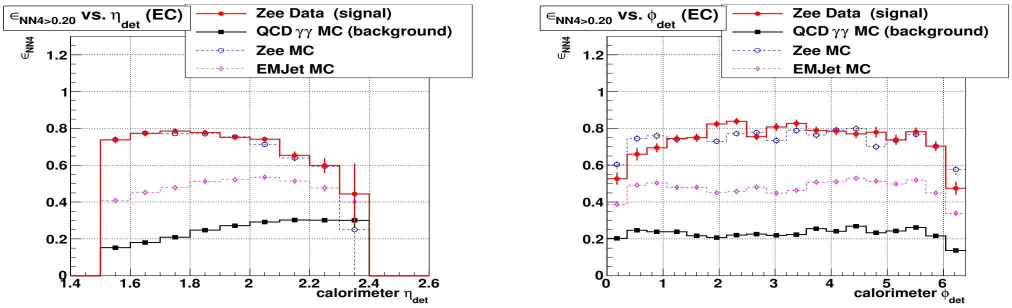

(a) Eff. vs. η_{det} (b) Eff. vs. ϕ_{det}

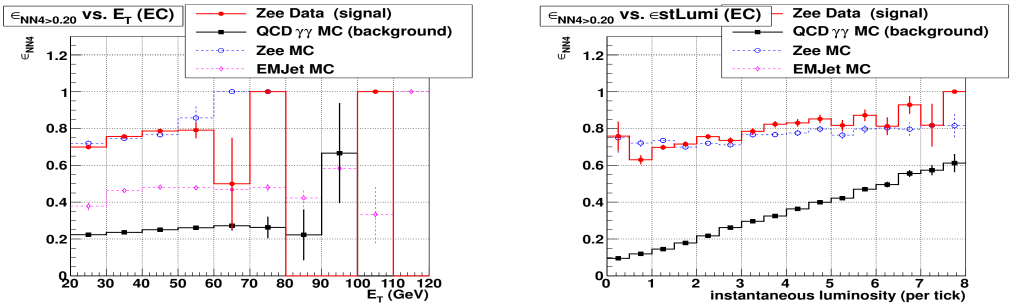

(c) Eff. vs. E_T (d) Eff. vs. instanteneous luminosity

Figure 4.30: $\text{HoR}_{EC}^{NN4} > 0.2$ cut efficiences as functions of E_T, η_{det}, ϕ_{det} and instantaneous luminosity.

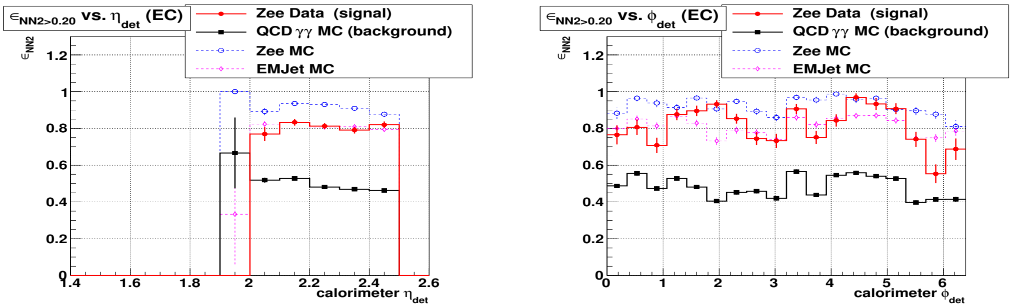

(a) Eff. vs. η_{det} (b) Eff. vs. ϕ_{det}

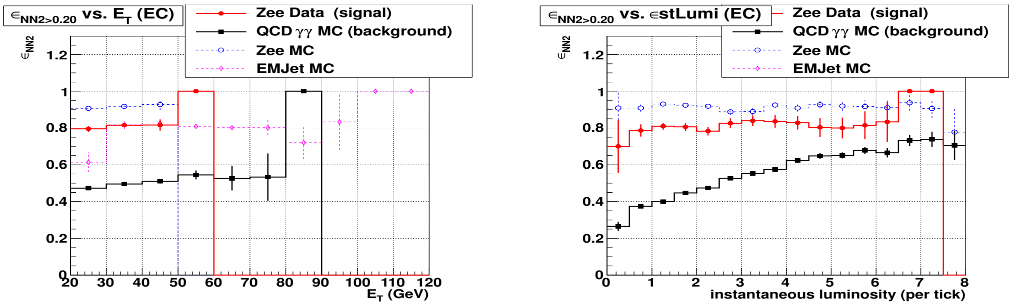

(c) Eff. vs. E_T (d) Eff. vs. instanteneous luminosity

Figure 4.31: $\text{HoR}_{EC}^{NN2} > 0.2$ cut efficiences as functions of E_T, η_{det}, ϕ_{det} and instantaneous luminosity.

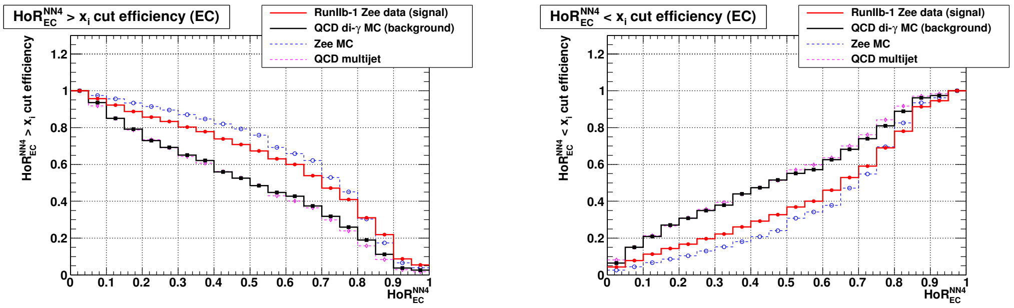

(a) Efficiencies of $\text{HoR}_{EC}^{NN4} > x_i$ for electron identification

(b) Efficiencies of $\text{HoR}_{EC}^{NN4} < x_i$ for photon identification

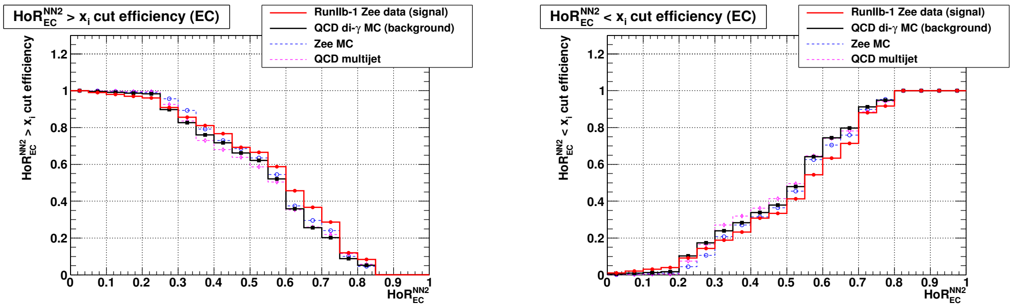

(c) Efficiencies of $\text{HoR}_{EC}^{NN2} > x_i$ for electron identification

(d) Efficiencies of $\text{HoR}_{EC}^{NN2} < x_i$ for photon identification

Figure 4.32: Efficiencies of HoR_{EC}^{NN4} and HoR_{EC}^{NN2} cuts for EC EM objects with $P_{trk} > 0.0$.

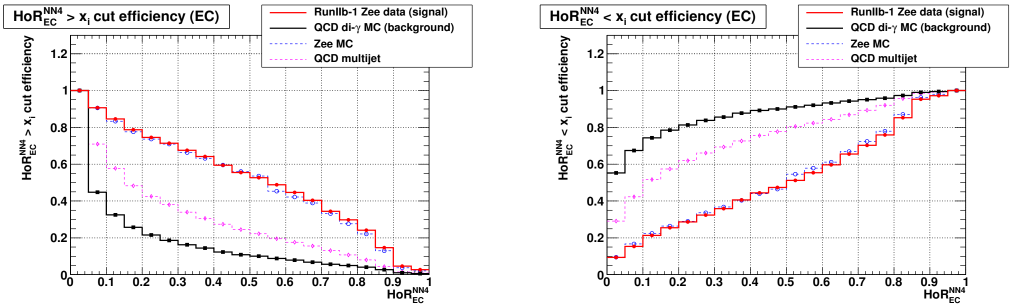

(a) Efficiencies of HoR$_{EC}^{NN4} > x_i$ for electron identification

(b) Efficiencies of HoR$_{EC}^{NN4} < x_i$ for photon identification

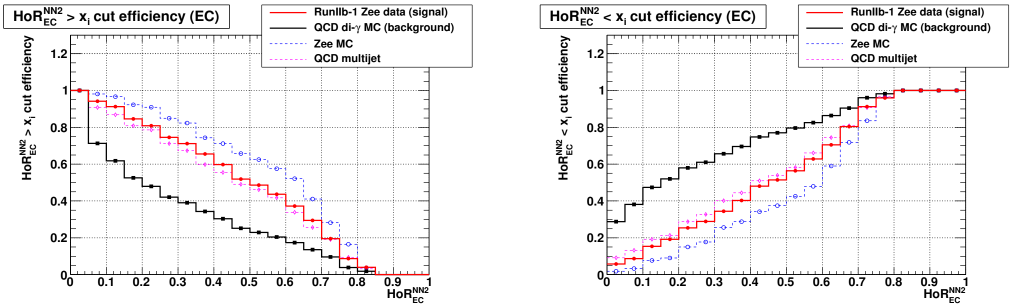

(c) Efficiencies of HoR$_{EC}^{NN2} > x_i$ for electron identification

(d) Efficiencies of HoR$_{EC}^{NN2} < x_i$ for photon identification

Figure 4.33: Efficiencies of HoR$_{EC}^{NN4}$ cuts for EC EM objects with $P_{trk} < 0.0$.

4.4.4 Application of the HoR discriminant in the EC

Application of the HoR discriminant for electron identification in the EC

An example of using the HoR discriminant with the electron identification is given in this section. The selection criteria "EC Point0" [18] designed by the D0 EMID group are used together with cuts on HoR_{EC} (HoR_{EC}^{NN4} or HoR_{EC}^{NN2}) for selecting electron candidates.

Table 4.9 shows the fractions of "EC Point0" electrons with $N_{max}^{cft} = 0$ and $N_{max}^{cft} \geq 1$. Electron candidates with $N_{max}^{cft} \geq 1$ ($N_{max}^{cft} = 0$) are subjected to HoR_{EC}^{NN4} (HoR_{EC}^{NN2}).

	$N_{max}^{cft} = 0$ (HoR_{EC}^{NN2})	$N_{max}^{cft} \geq 1$ (HoR_{EC}^{NN4})
Zee data	0.179	0.821
Zee MC	0.164	0.837
QCD di-γ	0.275	0.725
QCD multijet	0.192	0.808

Table 4.9: Fractions of "EC Point0" electrons with $N_{max}^{cft} = 0$ and $N_{max}^{cft} \geq 1$.

Table 4.10 and table 4.11 show the cut efficiencies of P_{trk} for "EC Point0" electrons which are subjected to HoR_{EC}^{NN4} and HoR_{EC}^{NN2}, respectively.

Cut Type	$P_{trk} \geq 0.0$	$P_{trk} < 0.0$
Zee data	0.662	0.339
Zee MC	0.819	0.1818
QCD di-γ	0.081	0.920
QCD multijet	0.152	0.848

Table 4.10: Cut efficiency of P_{trk} for "EC Point0" electrons which are subjected to HoR_{EC}^{NN4} ($N_{max}^{cft} \geq 1$).

Cut Type	$P_{trk} \geq 0.0$	$P_{trk} < 0.0$
Zee data	0.425	0.575
Zee MC	0.652	0.348
QCD di-γ	0.070	0.930
QCD multijet	0.135	0.865

Table 4.11: Cut efficiency of P_{trk} for "EC Point0" electrons which are subjected to HoR_{EC}^{NN2} ($N_{max}^{cft} = 0$).

Table 4.12 (Table 4.13) lists the efficiencies of different HoR_{EC}^{NN4} (HoR_{EC}^{NN2}) cuts for EM objects with $P_{trk} < 0.0$; these efficiencies are also shown in Figure 4.34 (Figure 4.35).

As described in Section 4.4.3, both HoR_{EC}^{NN4} and HoR_{EC}^{NN2} are recommended to be use together with P_{trk}, e.g. "$\mathrm{HoR}_{EC}^{NN4} > 0.2$ or $P_{trk} > 0.0$", for electron

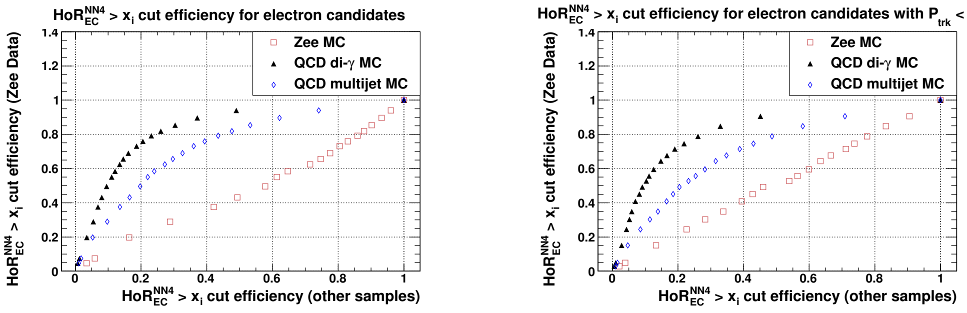

(a) No P_{trk} cut (b) $P_{trk} < 0.0$

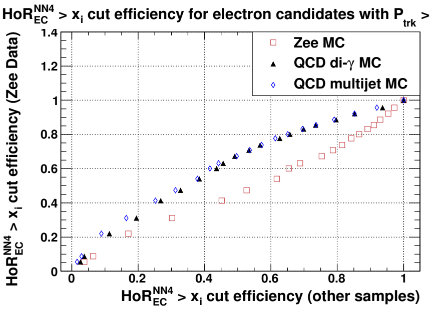

(c) $P_{trk} \geq 0.0$

Figure 4.34: HoR$_{EC}^{NN4}$ cut efficiencies of “EC Point0” electrons with different P_{trk} requirements.

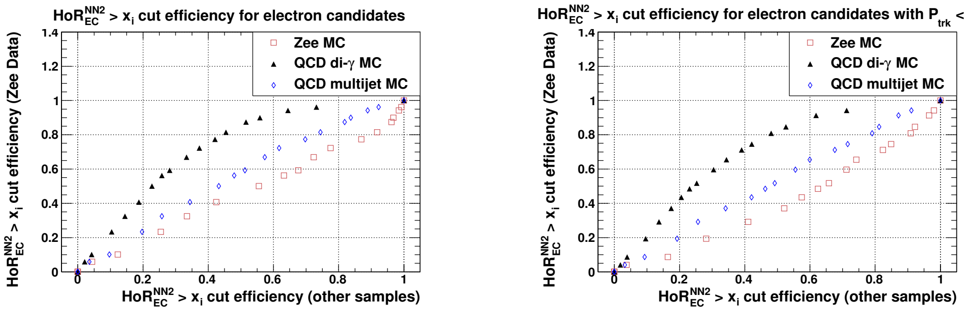

(a) No P_{trk} cut (b) $P_{trk} < 0.0$

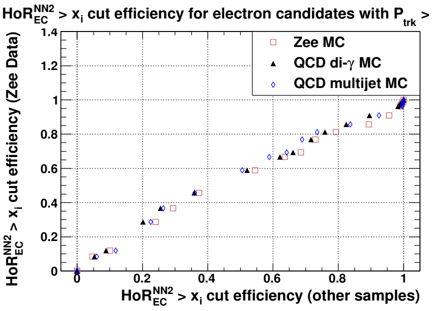

(c) $P_{trk} \geq 0.0$

Figure 4.35: HoR$_{EC}^{NN2}$ cut efficiencies of “EC Point0” electrons with different P_{trk} requirements.

Cut type	$\text{HoR}_{EC}^{NN4} > 0.05$	$\text{HoR}_{EC}^{NN4} > 0.15$	$\text{HoR}_{EC}^{NN4} > 0.4$	$\text{HoR}_{EC}^{NN4} > 0.65$
Zee data	0.906	0.788	0.596	0.409
Zee MC	0.905	0.776	0.599	0.395
QCD di-γ	0.451	0.261	0.126	0.070
QCD multijet	0.709	0.486	0.282	0.165

Table 4.12: HoR_{EC}^{NN4} cut efficiencies for “EC Point0” electrons with $P_{trk} < 0.0$.

Cut type	$\text{HoR}_{EC}^{NN2} > 0.05$	$\text{HoR}_{EC}^{NN2} > 0.15$	$\text{HoR}_{EC}^{NN2} > 0.4$	$\text{HoR}_{EC}^{NN2} > 0.65$
Zee data	0.942	0.847	0.596	0.292
Zee MC	0.980	0.922	0.712	0.410
QCD di-γ	0.712	0.526	0.304	0.137
QCD multijet	0.911	0.812	0.555	0.257

Table 4.13: HoR_{EC}^{NN2} cut efficiencies for “EC Point0” electrons with $P_{trk} < 0.0$.

identification. The efficiencies of the combined cuts are shown in Table 4.14. These efficiencies can be calculated out from Table 4.9 - Table 4.13.

From Table 4.14, one can find that the P_{trk} cut efficiency for “EC Point0” electrons is merely 61.88%. With the help of HoR_{EC}, the signal (electron candidates selected from Zee data events) selection efficiency can reach up to 96.78% with a relatively low background (electron candidates selected from QCD di-γ MC events) efficiency.

As is the case for the HoR_{CC} discriminant, HoR_{EC} provides analyzers more options. Analyses that are limited by the number of forward electrons, such as the measurement of Z/γ^* boson rapidity shape, can benefit from the HoR discriminants.

Cut type	$P_{trk} < 0.0$ **or** $\text{HoR}_{EC} >$				$P_{trk} < 0.0$
	0.05	0.15	0.4	0.65	
Zee data	0.968	0.925	0.846	0.763	0.619
Zee MC	0.985	0.962	0.923	0.875	0.792
QCD di-γ	0.561	0.386	0.240	0.160	0.078
QCD multijet	0.786	0.617	0.434	0.305	0.149

Table 4.14: Efficiencies of “EC Point0” electrons passing the cuts on either HoR_{EC} **or** P_{trk}, where HoR_{EC} is HoR_{EC}^{NN4} if $N_{max}^{cft} \geq 1$ or HoR_{EC}^{NN2} if $N_{max}^{cft} = 0$. The last column lists the efficiencies of $P_{trk} < 0.0$ as a reference.

Application of the HoR discriminant for photon identification in the EC

Similar studies have been done for EC photon identification. “EC Core1” photon selection criteria designed by the D0 EMID group are used together with the HoR discriminant.

Table 4.15 shows the fractions of “EC Core1” photons with $N^{cft}_{max} = 0$ and $N^{cft}_{max} \geq 1$. Photon candidates with $N^{cft}_{max} \geq 1$ ($N^{cft}_{max} = 0$) are subjected to HoR^{NN4}_{EC} (HoR^{NN2}_{EC}).

	$N^{cft}_{max} = 0$ (HoR^{NN2}_{EC})	$N^{cft}_{max} \geq 1$ (HoR^{NN4}_{EC})
Zee data	0.172	0.828
Zee MC	0.157	0.844
QCD di-γ	0.268	0.732
QCD multijet	0.207	0.793

Table 4.15: Fractions of “EC Core1” photons with $N^{cft}_{max} = 0$ and $N^{cft}_{max} \geq 1$.

Table 4.16 and table 4.17 show the cut efficiencies of P_{trk} for “EC Core1” photons which are subjected to HoR^{NN4}_{EC} and HoR^{NN2}_{EC}, respectively.

Cut Type	$P_{trk} \geq 0.0$	$P_{trk} < 0.0$
Zee data	0.670	0.330
Zee MC	0.824	0.177
QCD di-γ	0.083	0.918
QCD multijet	0.162	0.838

Table 4.16: Cut efficiency of P_{trk} for “EC Core1” photons which are subjected to HoR^{NN4}_{EC} ($N^{cft}_{max} \geq 1$).

Cut Type	$P_{trk} \geq 0.0$	$P_{trk} < 0.0$
Zee data	0.423	0.578
Zee MC	0.651	0.349
QCD di-γ	0.070	0.930
QCD multijet	0.133	0.867

Table 4.17: Cut efficiency of P_{trk} for “EC Core1” photons which are subjected to HoR^{NN2}_{EC} ($N^{cft}_{max} = 0$).

Table 4.18 (Table 4.19) lists the HoR^{NN4}_{EC} (HoR^{NN2}_{EC}) cut efficiencies for EC EM objects with $P_{trk} < 0.0$; these efficiencies are also presented in Figure 4.36 (Figure 4.37).

The efficiencies of the combined cut (HoR and track quality) are shown in Table 4.20, which can be calculated from the efficiencies listed in Table 4.15 - Table 4.19. Using $P_{trk} < 0.0$ cut only gives 37.22% background (photon candidates selected from Zee data events) efficiency. When further requiring on the HoR

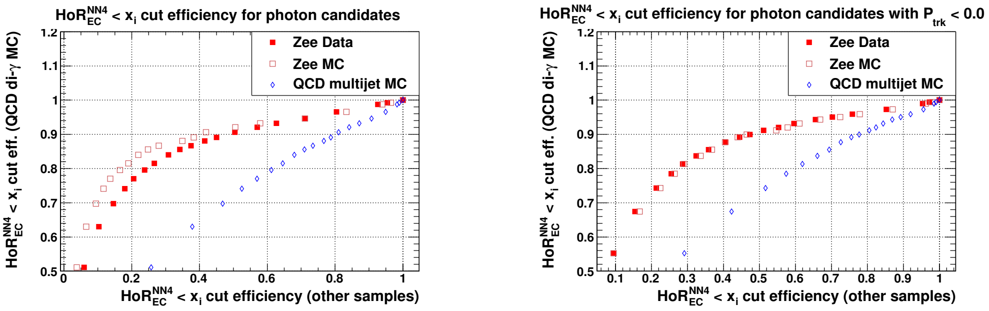

(a) No P_{trk} cut (b) $P_{trk} < 0.0$

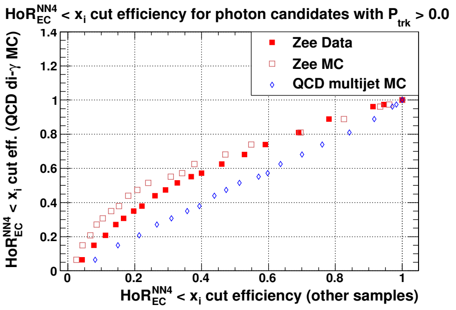

(c) $P_{trk} \geq 0.0$

Figure 4.36: HoR$^{NN4}_{EC}$ cut efficiencies of "EC Core1" electrons with different P_{trk} requirements.

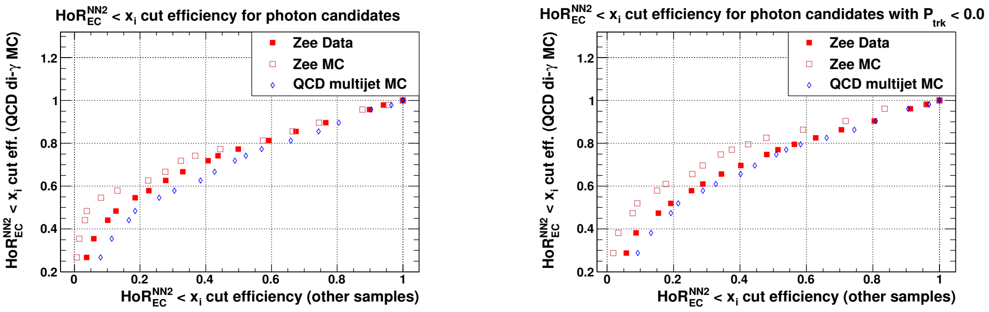

(a) No P_{trk} cut (b) $P_{trk} < 0.0$

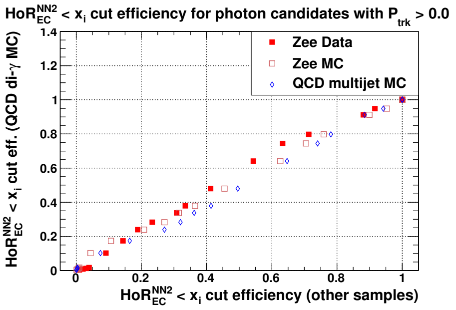

(c) $P_{trk} \geq 0.0$

Figure 4.37: HoR$^{NN2}_{EC}$ cut efficiencies of "EC Core1" electrons with different P_{trk} requirements.

Cut type	$\mathrm{HoR}_{EC}^{NN4} < 0.85$	$\mathrm{HoR}_{EC}^{NN4} < 0.75$	$\mathrm{HoR}_{EC}^{NN4} < 0.55$	$\mathrm{HoR}_{EC}^{NN4} < 0.25$
Zee data	0.853	0.703	0.512	0.287
Zee MC	0.870	0.724	0.546	0.290
QCD di-γ	0.973	0.950	0.911	0.813
QCD multijet	0.956	0.893	0.805	0.620

Table 4.18: HoR_{EC}^{NN4} cut efficiencies for “EC Core1” photons with $P_{trk} < 0.0$.

Cut type	$\mathrm{HoR}_{EC}^{NN2} < 0.75$	$\mathrm{HoR}_{EC}^{NN2} < 0.70$	$\mathrm{HoR}_{EC}^{NN2} < 0.65$	$\mathrm{HoR}_{EC}^{NN2} < 0.55$
Zee data	0.913	0.804	0.705	0.563
Zee MC	0.835	0.718	0.589	0.425
QCD di-γ	0.961	0.904	0.864	0.796
QCD multijet	0.906	0.809	0.744	0.582

Table 4.19: HoR_{EC}^{NN2} cut efficiencies for “EC Core1” photons with $P_{trk} < 0.0$.

discriminants, the background efficiency can be reduced to 13.42%. Analyzers now have more options for photon identification.

Cut type	$P_{trk} < 0.0$	$P_{trk} < 0.0$ **and** HoR_{EC} cut			
		$\mathrm{HoR}_{EC}^{NN4} < 0.85$ $\mathrm{HoR}_{EC}^{NN2} < 0.75$	$\mathrm{HoR}_{EC}^{NN4} < 0.75$ $\mathrm{HoR}_{EC}^{NN2} < 0.70$	$\mathrm{HoR}_{EC}^{NN4} < 0.55$ $\mathrm{HoR}_{EC}^{NN2} < 0.65$	$\mathrm{HoR}_{EC}^{NN4} < 0.25$ $\mathrm{HoR}_{EC}^{NN2} < 0.55$
Zee data	0.372	0.323	0.272	0.210	0.134
Zee MC	0.204	0.175	0.147	0.114	0.067
QCD di-γ	0.921	0.893	0.864	0.828	0.745
QCD multijet	0.844	0.798	0.738	0.668	0.516

Table 4.20: Efficiencies of “EC Core1” photons passing the cuts on either HoR_{EC} **and** P_{trk}, where HoR_{EC} is HoR_{EC}^{NN4} if $N_{max}^{cft} \geq 1$ or HoR_{EC}^{NN2} if $N_{max}^{cft} = 0$. The second column lists the efficiencies of $P_{trk} < 0.0$ as a reference.

4.5 Conclusion

In this chapter, by using the data collected during the D0 RunIIb period, (i) we optimized the HoR$_{CC}$ discriminant by using SMT layer 0 in addition to other SMT and CFT layers; (ii) we developed the HoR$_{EC}^{NN4}$ and HoR$_{EC}^{NN2}$ discriminants for EC EM objects with the consideration of the tracking system's geometry; and (iii) we used the ANN to tune the HoR discriminants.

The performance of the HoR discriminants has been studied in several ways: (i) checking the separation between electrons and photons for EM objects with different track qualities and for EM objects from different samples ($Z/\gamma^* \to e^+e^-$ data/MC, QCD di-γ MC and QCD multijet MC samples); (ii) checking the dependences of the HoR cut efficiencies on $\eta_{det}, \phi_{det}, E_T$ and instantaneous luminosity. These studies suggest that the HoR discriminants provide good separation between electrons and photons; there are no obvious dependences on η_{det}, ϕ_{det} and E_T but there is a dependence on instantaneous luminosity (especially for HoR$_{EC}^{NN2}$). However, the dependence on instantaneous luminosity is reasonable and irreducible, simply due to the fact that many more hits present in higher instantaneous luminosity environment.

A comparison between the current HoR$_{CC}$ and the previous HoR$_{CC}$ discriminant has been made. The comparison shows the current HoR$_{CC}$ has better performances on both electron and photon identifications. The improvements are contributed by (i) using more accurate road widths (road widths are not updated after RunIIa in the previous HoR$_{CC}$); (ii) having one more detector layer, SMT layer 0; (iii) using the ANN to tune the HoR$_{CC}$ discriminant instead of using a simple likelihood function. Although the improvements of HoR$_{CC}$ are small, the development of the current HoR$_{CC}$ is an essential cross check of the method in the CC prior to the development the HoR$_{EC}$ discriminants in the EC.

Examples of using the HoR discriminants in electron and photon identifications are given. With the help of the HoR discriminants, analyzers have more options of electron and photon identification in their analysis.

Additional cross checks are provided in Appendix C, including:

- a cross check of the HoR performance using data taking in a different period, as in Appendix C.1,
- a study of the performance of HoR$_{EC}^{NN4}$ and HoR$_{EC}^{NN2}$ on random noise, as in Appendix C.2.

The HoR discriminants are used in the Z boson rapidity shape measurement presented in this thesis. The number of forward electrons is crucial to this measurement. Forward electrons which fail cluster-track matching algorithm are selected by using the HoR discriminants. An overall tracking efficiency of $\sim 90\%$ for forward electron candidates is achieved. Thanks to this, the statistical uncertainties in high boson rapidity regions, where the results are most interesting, are largely reduced.

Chapter 5

Measurement of the shape of the boson rapidity distribution

5.1 Introduction

5.1.1 Motivation of the measurement

Precise theoretical calculations using perturbative quantum chromodynamics (QCD) serve a critical role for understanding experimental results at hadron colliders. The precision of these calculations is currently limited by the uncertainties in the parton distribution functions (PDF). Thus the precise understanding of the PDFs is crucial for many electroweak measurements, such as the measurement of W mass, the measurement of forward-backward charge asymmetry in Z boson decays, etc. Also, it will be particularly important for analysis of data at the large Hadron Collider (LHC), since small deviations from the standard model can be revealed during the future 14 TeV run. However, the PDFs at present cannot be calculated directly. Instead, they are obtained from analysis of data from a broad range of processes.

The measurement of PDFs at high momentum transfer (Q^2) has traditionally been performed using high-momentum jet spectra. An alternative way for studying the PDFs is using dilepton production from Z/γ^* bosons. At the Tevatron, Z/γ^* bosons are produced through the annihilation of a quark and an antiquark. Kinematic distributions for the process can be precisely reconstructed. The leptonic signature allows for precise measurement of the energies and trajectories, and the backgrounds to dilepton final states are small. Especially, among all of the kinematic distributions, the distribution of Z/γ^* boson rapidity provides a wealth of information.

At leading order (LO), if we denote the momentum fractions which are carried by the partons, i.e. the incident quarks, in the proton and antiproton as x_1 and x_2, respectively, the rapidity of the boson can be defined as $y = \frac{1}{2}\ln\frac{E+p_L}{E-p_L}$, where E is the energy of the boson and p_L is the momentum component parallel to the beam axis [20]. Thus, the rapidity of the boson, in turn, can be represented by

$$x_{1,2} = \frac{M_{Z/\gamma^*}}{\sqrt{s}}e^{\pm y}, \tag{5.1}$$

where M_{Z/γ^*} is the mass of the boson, and $\sqrt{s}$ is the center-of-mass energy. This relation is also shown in Figure 5.1.

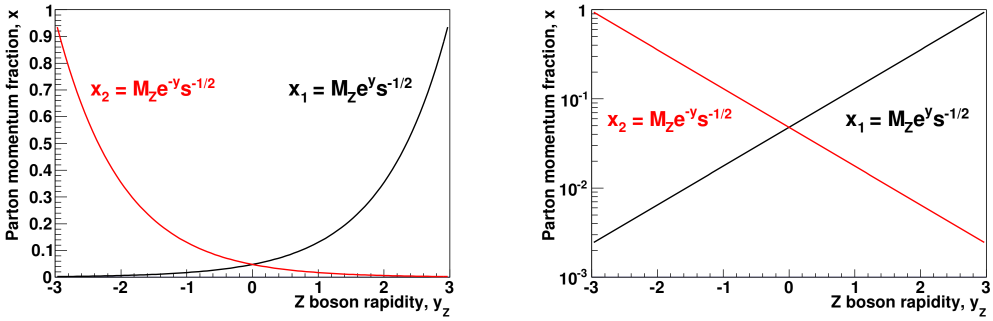

(a) Linear scale

(b) Log scale

Figure 5.1: The relation between the parton momentum fraction and the rapidity of the Z boson at the LO [20].

As indicated by Equation 5.1, the boson rapidity is directly related to the momentum fractions x as well as the M_{Z/γ^*}. Figure 5.1 clearly shows for small boson rapidities, the incident quarks will have x values that are roughly equal in size. For high boson rapidities, one of the incident quarks may have x close to 1 and the other may have the x as low as ~ 0.005. Thus, the forward region probes quarks with low x as well as quarks with very large x.

Due to a smaller cross section and lower acceptance, the PDFs have not yet been well tested in the forward region. The PDFs are mainly determined by the jet cross section data and by inclusive lepton scattering data in this regime. The jet cross section data have very different experimental and theoretical systematic uncertainties to the data of dilepton decays of Z/γ^* bosons. The inclusive lepton scattering data have much lower Q^2. Thus the measurements with the dilepton decays of Z/γ^* bosons will have very different experimental and theoretical systematic uncertainties.

In the following sections, a measurement of the normalized differential cross section

$$\frac{1}{\sigma}(\frac{d\sigma(Z/\gamma^* \to e^+e^-}{dy})_i = \frac{(\epsilon \times A)_{avg}}{N^{obs}_{total} - N^{bg}_{total}} \frac{N^{obs}_i - N^{bg}_i}{\Delta_i(\epsilon \times A)_i}, \tag{5.2}$$

where index i indicates the rapidity bin, is presented. In the first term on the right-hand side, ϵ_{avg} and A_{avg} represent the average efficiency and acceptance for kinematic and geometric cuts. N^{obs}_{total} and N^{bk}_{total} is the total number of candidate bosons and that of background events, respectively. ϵ_i, A_i, N^{obs}_i and N^{bg}_i in the second term are the same as those in the first term, but determined in each rapidity bin i. Δ_i is the width of the ith rapidity bin.

Measuring the normalized differential cross sections reduces many of the systematic uncertainties. Particularly the systematic uncertainty of luminosity, which is $\sim 6\%$ at the Tevatron, can be largely reduced or even eliminated.

Similar measurements were performed at the Tevatron by both the D0 and CDF collaboration, with 0.4 fb^{-1} [21] and 2.1 fb^{-1} [22] of data, respectively. Different from the D0 collaboration, the CDF collaboration measured the absolute differential cross section. Both of the results were limited by the statistical uncertainty of data at the time of publication. Now with the advantage of the full dataset from D0 detector during the whole RunII of the Tevatron, which has an integrated luminosity up to 9.86 fb^{-1}, the statistical uncertainty is no longer a limiting factor for this measurement.

A previous measurement of the rapidity distribution is also available for dimuon pairs in the Z-bosons mass region [23]. The kinematic limit of $|y|$ for Z boson produced at $\sqrt{s} = 1.96$ TeV is 3.0. This result of dimuon channel was limited to low boson rapidity region where $|y| < 1$, mainly due to the coverage of the muon detector in η. With the good coverage of EM calorimeter in the D0 detector, our measured rapidity range extends to $|y| \sim 2.9$.

5.1.2 Challenge of the measurement

In the process of dilepton production, the kinematic variables of the two electrons and Z/γ^* boson rapidity satisfies the relation

$$y = \frac{1}{2}\ln(\frac{E^{e_1} + p^{e_1}_z + E^{e_2} + p^{e_2}_z}{E^{e_1} - p^{e_1}_z + E^{e_2} - p^{e_2}_z}), \tag{5.3}$$

where $e_{1(2)}$ denotes the first (second) electron with no discernment of the charge, E represents the electron energy and p_z is the z component of the momentum. As revealed by this equation, the precision of the Z/γ^* boson rapidity shape relies highly on the precision of the energy measured for electrons, as well as their direction relative to the beam, which can be represented by the polar angle θ. In practice, we use the pseudorapidity η instead of the polar angle θ to reflect the direction of electrons relative to the beam. The variable η is defined as

$$\eta = -\ln(\tan(\theta/2)). \tag{5.4}$$

The η of the electrons are highly correlated with the boson rapidity. This correlation is shown in Figure 5.2.

The challenge for this analysis is to measure the rapidity distribution in the high rapidity region. Since electrons tend to have high η in the high boson rapidity region, precisely reconstructing events with those electrons is critical to this measurement.

In practice, those electrons are mainly detected by the forward EM calorimeters (Endcap EM calorimeters, EC) of the D0 detector. The EC calorimeter coverage in η is relatively high, however the tracking detector has a much smaller coverage in this case. Thus, the electrons in the EC would either have a much lower tracking efficiency ($\sim 60\%$) than those in the Central calorimeter (CC) ($\sim 90\%$), if requiring the electron to have a matched track reconstructed in the tracking detector; or the electrons would suffer from a large background contamination if not applying any tracking requirements. In the first case, due to the already low cross section in the high boson rapidity region, a large statistical uncertainty would appear in the final results. In the latter case, a bigger contribution of systematic uncertainties from background estimation as well as electron reconstruction need to be introduced in the final results. Neither of these two cases are ideal for this measurement.

By taking the advantage of the HoR discriminants described in Chapter 4, we manage to balance the above two cases in a good manner. The non-track-matched electrons in the EC are used. A cut on the HoR variable is applied to those electrons. As illustrated in Chapter 4, selecting the non-track-matched electrons in the EC with this variable can give a high signal efficiency while maintaining a relatively low background efficiency at the same time. In the final result for the forward region, this HoR variable helped us to reduce the statistical uncertainties but keep the systematic uncertainty from background estimation under control.

As indicated by Equation 5.3, the other kinematic variable, which is directly related with the boson rapidity, is the electron p_T. Since the cross section drops rapidly as the boson rapidity increases, the ability to select low p_T electrons is important for obtaining a reasonable acceptance. In practice, we use a p_T cut of 25 GeV for the CC electrons, while a p_T cut of 20 GeV is used for the EC electrons.

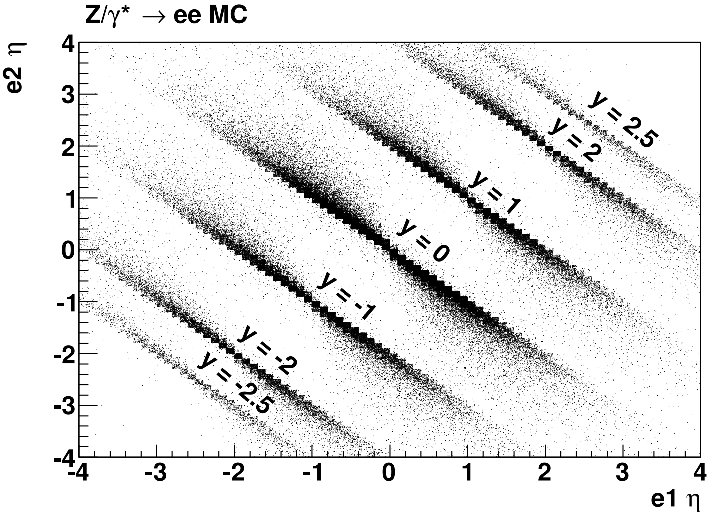

Figure 5.2: Scatter plot of the η of electron 1 vs. that of electron 2 from Z/γ^* Monte Carlo provided by PYTHIA [24]. No cuts other than the boson rapidity and mass applied. Each band shows the distribution at the indicated boson rapidity.

5.2 Measurement Strategy

5.2.1 Measurement method

This measurement focuses on the shape of the boson rapidity. The measurement is done in the following steps:

- Apply event selection cuts and obtain events with two good electrons;
- Estimate QCD and other SM background and subtract these backgrounds from data to obtain the reconstructed boson rapidity shape of e^+e^- pairs, which is just the observed shape of Z/γ^* bosons.
- Estimate the efficiency and acceptance ($\epsilon \times A$) for the event selection used in the data events;
- Use this $\epsilon \times A$ to correct the observed shape of the boson rapidity.

Details of the event selection criteria are described in Section 5.2.2.

The QCD background is directly estimated from data. Details of this estimation will be described in Section 5.5.2.

The SM backgrounds contributions are relatively small. Those backgrounds are estimated from the fully simulated MC samples and normalized using the corresponding cross section together with the integrated luminosity. Details about these MC samples and the cross sections for each background channel can be found in Section 5.2.4.

The $\epsilon \times A$ is measured in the fully simulated MC samples. For these MC samples, two levels of information are available, which we denote as the generator level and the reconstructed level information. The generator level information refers to the theoretical prediction used in the event generator. The reconstructed level information is obtained after passing the same events through the detector simulation. The reconstructed level information is comparable to the actual data collected by the detector. Technically, the $\epsilon \times A$ is obtained by taking the ratio of the kinematic distributions in reconstructed level to those in generator level. However, due to the imperfect, simulation of the detector, the reconstructed MC events do not represent the data in every aspect. To address this issue, we applied various corrections to the MC samples. Details can be found in Section 5.3.

With the $\epsilon \times A$ measured from the corrected MC samples, we use Equation 5.2 to obtain the shape of the Z/γ^* boson rapidity.

5.2.2 Event selection

The objective of the event selection is to select a relatively background free sample of Z/γ^* events but maintain as high an $\epsilon \times A$ as possible.

In general, the event selection requires two good EM objects to be present in the EM calorimeters, together with additional requirements on the associated tracks if these are present or the HoR variable if not.

Details of the event selections are as given in the following.

- The instantaneous luminosity measured by the luminosity detector is not zero at the time of the occurrence of the event, $L_{inst} > 0$ cm^{-2}s^{-1}.
- Good data quality is required. The data quality cut ensures the Tevatron and the D0 detector are in good condition when the event occurred. Runs, luminosity block numbers and events marked as bad are removed from the event selection. Different from many other analyses of the D0 data, we do not check the condition of the muon system. This is simply because the muon system, which sits outside of EM calorimeters, will not affect our signal. Also the possible background to the signal which has muons involved in the final states is negligible in our case.

- The event should fire a proper trigger. More information on these trigger requirements is given in Section 5.2.3. Obviously this cut and those defined above are only applicable to data events.

- The z-coordinate of the reconstructed primary vertex, $|z_{pvtx}|$, need to be within $[-40, 40]$ cm. This ensures the event occurs in the region which is well covered by the detector.

- Two reconstructed electrons passing the electron selection criteria need to be found in the event. The electron selection criteria are listed below. Although both the track-matched and non-track-matched electrons in the EC are used in this measurement, we only consider events with at least one track-matched electrons. I.e. the events with two non-track-matched electrons are not used.

- The invariant mass of the two electrons, M_{ee}, should be within $[66, 116]$ GeV. This is a window with an equivalent size of ~ 25 GeV below and above the Z boson mass.

The electron selection (EMID) criteria are listed below. The following cuts are chosen to select a genuine electron in the CC:

- $|\eta_{det}| < 1.1$, where the η_{det} is the η of the electron in the detector coordinate system and 1.1 is the coverage of the central EM calorimeter;

- $E_T > 25$ GeV, where E_T is the transverse energy measured in the EM calorimeter;

- $I_{cal} < 0.15$;

- $F_{EM} > 0.9$;

- $\chi^{2(7)}_{EM} < 12$;

- a spatially matched track which satisfies the following requirements:
  - $r_{dca} < 0.02$ cm, where r_{dca} is distance of closest approach to the beam spot;
  - track $p_T > 10.0$ GeV;
  - $\chi^2_{trk}/n.d.f < 9.95$, where the $\chi^2_{trk}/n.d.f$ represents the goodness of fit when reconstructing the track using hit clusters in the tracking detector;

  - $N_{SMT} \geq 2$, where N_{SMT} is the number of SMT hit clusters associated with the track;
  - $N_{CFT} \geq 9$, where N_{CFT} is the number of CFT hit clusters associated with the track.

Note that we only use track-matched electrons in CC.

The following requirements are used for selecting EC electrons:

- $1.5 < |\eta_{det}| < 3.2$, i.e. in the EC;
- $E_T > 20$ GeV;
- $I_{cal} < 0.1$;
- $F_{EM} > 0.9$;
- $\chi^{2(8)}_{EM} < 10$;
- the EM objects passing the cuts above should also pass any of the following tracking requirements:
  - the EM object has a spatially matched track in the tracking detector;
  - or $0.1 < \text{HoR}^{NN4}_{EC} < 1.0$ for electron candidates pass through both SMT and CFT layers;
  - or $0.1 < \text{HoR}^{NN2}_{EC} < 1.0$ for electron candidates which only pass through SMT layers.

Note that we select both track-matched and non-track-matched electrons. For the non-track-matched electrons, a cut on the HoR variable is applied.

Depending on the EM calorimeters in which the electrons are detected, we categorize events into three topologies:

- CC-CC, which has two track-matched electrons in the CC;
- CC-EC, which has one track-matched electron in the CC, and one electron in the EC;
- EC-EC, which has two electrons in the EC of which at least one has a matched track.

5.2.3 Data sample and trigger

The data used in this measurement were collected between April 2002 and February 2006 (Run IIa) and between June 2006 and September 2011 (Run IIb). This represents the complete Run II dataset, which has an integrated luminosity of 9.86 fb^{-1} .

Technically, the data are split into three subsets representing three different run periods, and each of the three subsets of data is analyzed independently. The division of the data set is mainly due to the change of running conditions of the D0 detector and/or that of the Tevatron during different run periods. Such changes of running conditions include the increase in instantaneous luminosity, the new installation of detector components (e.g the SMT layer 0 sensors) and different calibrations of the EM calorimeters, etc. These changes should be properly taken care of in the detector simulation for MC samples. In this measurement, different MC simulations corresponding to each subset of the data are used. We denoted the three subsets of data as Run2a, Run2b−12, and Run2b−34.

Table 5.1 shows the integrated luminosity for each subset.

Integrated Luminosity	
Run period	Integrated luminosity (pb^{-1})
Run2a	1104.40
Run2b-12	4313.84
Run2b-34	4440.3
Total	9858.54

Table 5.1: Integrated luminosity for each subset of data.

Due to the fact that the $Z \to ee$ process has two high p_T electrons in the final state, the di-EM OR triggers are used in this analysis. As can be seen from the name, the di-EM triggers are based on the EM objects found by the EM calorimeters; and these triggers would be fired by the presence of two EM objects. The “tag-and-probe method” is used to estimate the trigger efficiencies in data. The details of the di-EM triggers as well as the “tag-and-probe method” of studying the trigger efficiencies can be found in the reference [25].

Primarily, the di-EM trigger efficiency is dependent on the E_T of EM objects. Thus the E_T of the two EM objects are used as dependent variables for the measured efficiency. The efficiencies are measured separately for CC-CC, CC-EC and EC-EC events. Figure 5.3, Figure 5.4 and Figure 5.5 show the trigger efficiencies for events in each category. The measured efficiency is found to be $99.8 \pm 0.1\%$ in total for selecting dielectron events with electrons with $p_T >$

25 GeV.

The trigger efficiencies as functions of the rapidity, the transverse momentum and the mass of the reconstructed bosons are also shown respectively in Figure 5.6, Figure 5.7 and Figure 5.8.

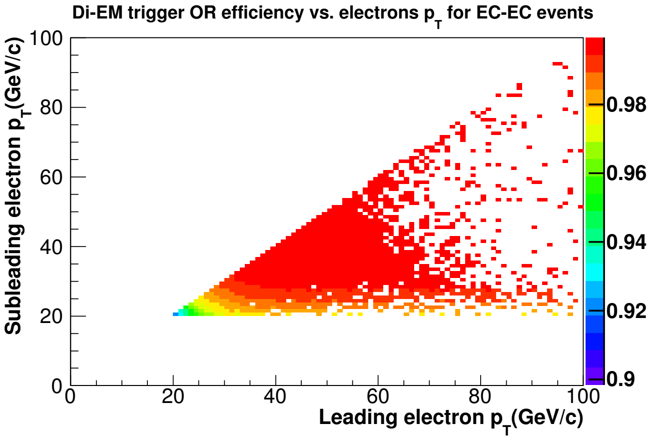

Figure 5.3: The trigger efficiencies as a function of the two electrons p_T for CC-CC events.

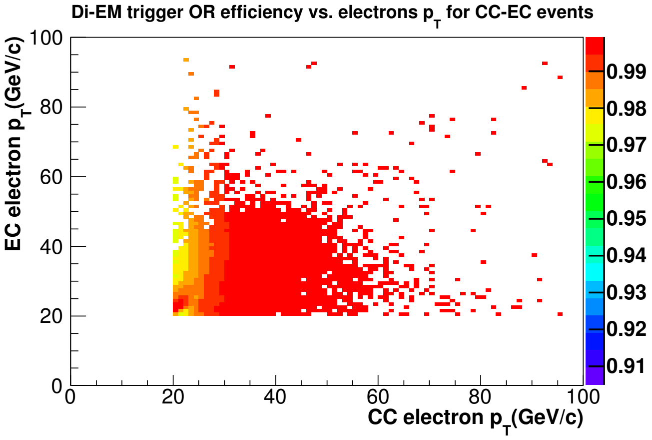

Figure 5.4: The trigger efficiencies as a function of the two electrons p_T for CC-EC events.

5.2.4 Monte Carlo samples for signal and backgrounds

Similar to the data samples, the MC samples used in this analysis consist of three subsets. Each subset corresponds to one subset of data samples.

The MC samples for signal were generated for the dielectron mass within [60, 130] GeV. The samples were generated with the PYTHIA [24] MC event generator. The set of PDFs used is CTEQ6L1 [26].

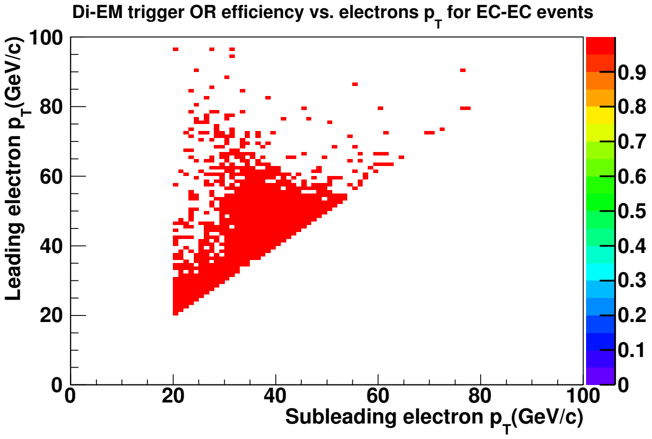

Figure 5.5: The trigger efficiencies as a function of the two electrons p_T for EC-EC events.

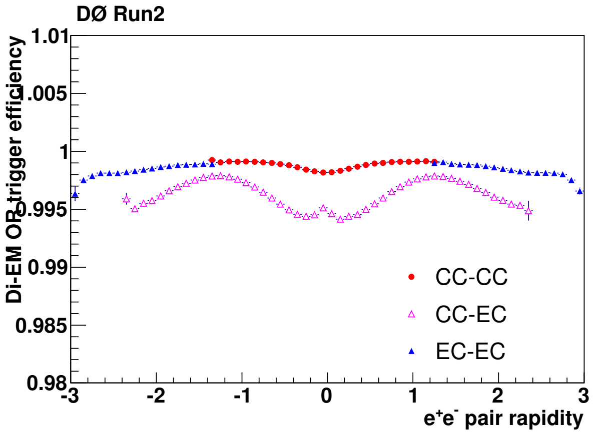

Figure 5.6: The trigger efficiencies as a function of the reconstructed boson rapidity.

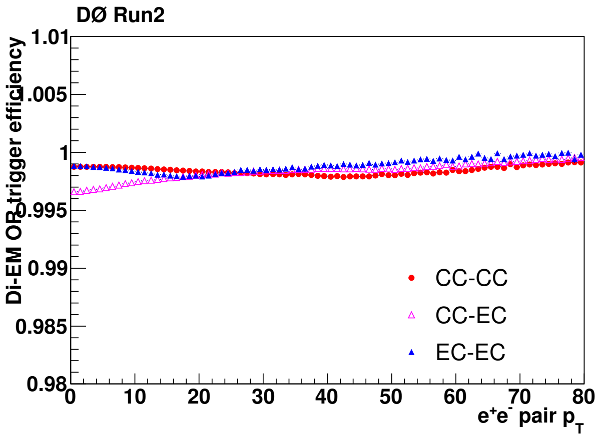

Figure 5.7: The trigger efficiencies as a function of the reconstructed boson p_T.

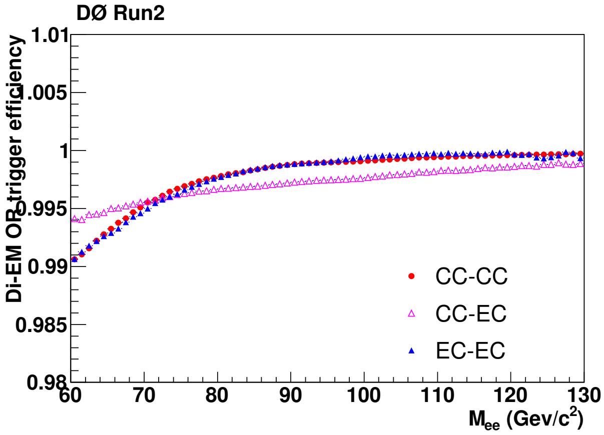

Figure 5.8: The trigger efficiencies as a function of the reconstructed boson mass, i.e. the invariant mass of the two electrons.

The MC samples of backgrounds, such as $Z/\gamma^* \to \tau^+\tau^-$, diboson and $t\bar{t}$ background were generated by PYTHIA with the CTEQ6L1 PDF set as well.

The MC samples for $W + jets$ background, in order to improve the simulation of the hadronization and parton shower. were firstly generated by the the ALPGEN [27] event generator and processed later by PYTHIA.

Table 5.2 shows the cross sections times branching fractions and initial numbers of events of these Monte Carlo samples. We directly normalize the $Z/\gamma^* \to e^+e^-$ signal MC samples to the background subtracted data, thus the cross section for the signal samples is not presented in the table.

All of the MC samples were processed through a GEANT-3 [28] based simulation of the D0 detector and the same reconstruction software as used for the data.

MC Samples				
Event Type	$\sigma \cdot$ BR [pb]	Number of Events		
		Run2a	Run2b-1	Run2b-3
Signal				
$Z/\gamma^* \to e^+e^-(m_Z \in [60, 130]\text{GeV})$	–	5.1M	7.4M	18.0M
Backgrounds				
$Z/\gamma^* \to \tau^+\tau^-(m_Z \in [15, 60]\text{GeV})$	525.6 [29]	3.0M	5.5M	5.7M
$Z/\gamma^* \to \tau^+\tau^-(m_Z \in [60, 130]\text{GeV})$	254.0 [29]	14.6M	9.2M	9.5M
$Z/\gamma^* \to \tau^+\tau^-(m_Z \in [130, 250]\text{GeV})$	1.91 [29]	0.5M	4.5M	3.8M
$Z/\gamma^* \to \tau^+\tau^-(m_Z \in [250, 500]\text{GeV})$	0.16 [29]	0.2M	2.6M	2.9M
WW	12.1 [30]	3.4M	5.5M	2.9M
WZ	3.7 [30]	1.6M	3.5M	1.7M
ZZ	1.4 [30]	1.6M	3.6M	2.5M
$t\bar{t}$	6.1 [31]	1.0M	2.2M	1.8M
$W + jets$	– [32]	130.1M	210.5M	232.4M

Table 5.2: The cross sections times branching fractions, and the initial number of events of the MC samples.

5.3 Corrections to MC samples

Since $\epsilon \times A$ will be obtained by taking the ratio of the reconstructed boson rapidity distribution to the theoretical prediction at the generator level any inaccuracy in aspects of detector simulation in the MC samples would reduce the precision of this measurement.

In this section, we address the following issues with the PYTHIA MC samples.

- The primary vertex z and the instantaneous luminosity profiles used in MC are found to be slightly different to data when looking at the full dataset. Simple reweightings of the distributions are applied to the MC events.
- The shape of the p_T distribution for Z/γ^*bosons at generator level is not accurately simulated in PYTHIA, which is a leading-order (LO) generator. A more accurate theoretical prediction is desired.
- The efficiencies of event selection, in particular, the efficiencies of single electron selection, are overestimated in the MC samples. Scale factors need to be applied to MC events to make the event selection efficiency agree with data.

The corrections are developed by addressing these issues step-by-step. At last, by applying all the corrections together, we managed to get a decent simulation of data in many aspects, especially in those distributions which are crucial in this measurement. Detailed data and MC comparison are provided in Section 5.6.

5.3.1 Z boson p_T and rapidity reweighting to ResBos

The ResBos event generator is a NLO generator which utilizes resummation mechanism on soft gluon emission at Next-to-Next-Leading-Log (NNLL) order and LEO electroweak corrections [33]. Many results, such as the ϕ^*_η measurement at D0 [34], indicates that ResBos provides a more accurate theoretical prediction of the Z/γ^* boson p_T and rapidity distributions than Pythia, which only provides LO predictions. Thus, in order to improve the simulation in the Pythia full MC sample, a reweighting factor, which is a function of the boson p_T and rapidity, has been applied to the Pythia MC events. The procedure is as follows.

- Firstly, we make the 2D plot of boson p_T and y by using the generator level information of events in both of the Pythia and ResBos samples;
- Secondly, after normalizing these two 2D plots to unity, we make the ratio $R_{ij} = n_{ij}^{ResBos}/n_{ij}^{PYTHIA}$, where i, j denote the ith p_T bin and the jth rapidity bin, and n_{ij} is the bin content of the 2D plot after normalizing to unity.
- Lastly, depending on the p_T and rapidity for the Z/γ^* bosons, the corresponding R_{ij} is applied as an event weight to the Pythia MC events. This correction, as an event weight, is not only used during making generator level distributions but also used during making reconstructed level distributions.

The predictions of the Z/γ^* boson p_T and rapidity are shown in Figure 5.9 and Figure 5.10, respectively.

The 2D reweighting factor is shown in Figure 5.11.

5.3.2 Corrections for the event selection efficiency

To address the difference of the event selection efficiency between data and MC, correction factors, which are scale factors of the data/MC efficiencies, have been estimated and applied to MC events. These corrections relate only to the detector simulations. Thus they are applicable only to the reconstructed level distributions.

These corrections (or scale factors) are explained as follows.

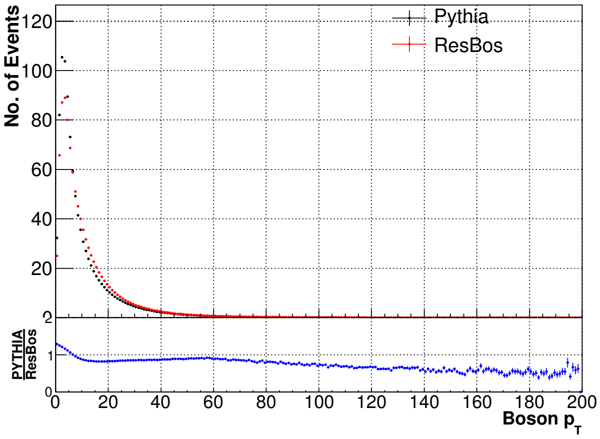

Figure 5.9: The predictions of Z/γ^*boson p_T in PYTHIA and RESBOS.

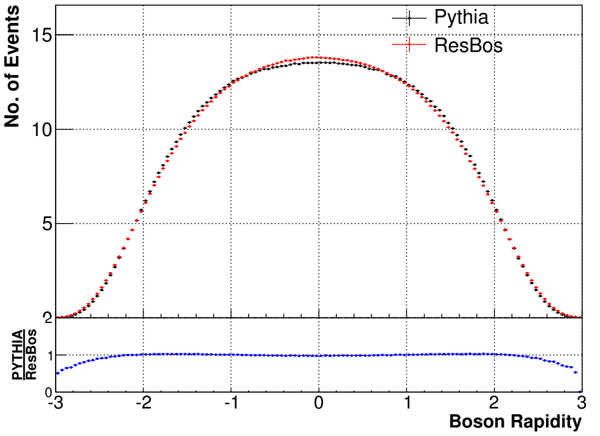

Figure 5.10: The predictions of Z/γ^*boson rapidity in PYTHIA and RESBOS.

- The trigger efficiency in data ($\epsilon_{trigger}$) is applied as an event weight to the MC events. The trigger efficiency, depending on the p_T of the two electrons, which have been shown in Figure 5.3, Figure 5.4 and Figure 5.5 is applied to different type of MC events accordingly. This correction is overall a quite small correction.

- Scale factors for the single electron selection efficiencies are estimated and applied to the MC events. The cuts used in both the CC and EC electron selection are split into three groups: the preselection, the calorimeter based identification (Cal-ID) and the tracking requirements. The efficiencies for each group of cuts are measured in both data and MC samples using the "tag-and-probe method". They are measured separately for CC and EC electrons. Scale factors of the efficiencies in data and MC are taken as

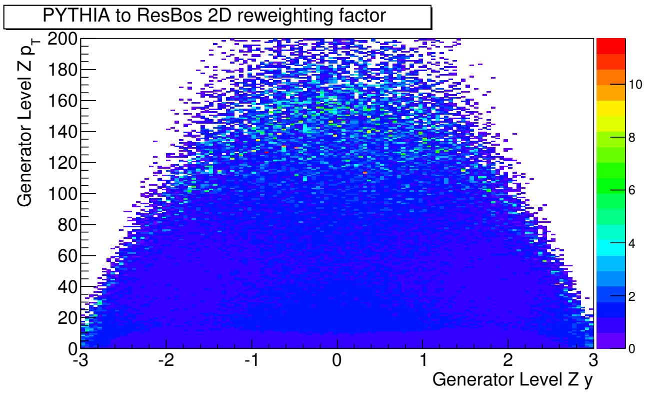

Figure 5.11: 2D reweighting factor used to improve the Z/γ^* boson p_T simulation in Pythia MC samples. (A few (~ 8) bins have reweighting factors greater than 5. Events with Z/γ^* boson p_T and y in those bins are not reweighted by these factors, i.e setting the reweighting factors in those bins to be 1.)

correction factors to MC sample. The cut efficiencies in MC are then scaled to the same efficiencies in data. These scale factors are as functions of various parameters, such as the electron η_{det}, p_T, η_{phy}, z_{pvtx}, etc. They are chosen by taking the most significant dependencies. More details of the "tag-and-probe method" are described below.

Electron candidates passing a set of requirements that are tighter than those employed in the standard event selection are defined as tag electrons. The same tag electrons are used when measuring the efficiency for each groups of cuts. The probe electron is then selected by requiring $80 < M_{ee} < 100$ GeV. Probe electrons form a minimally biased electron sample with high purity and are optimal for studying the selection efficiencies.

These tag electrons are chosen with the requirements below:

- $|\eta_{det}| < 1.1$ and in the fiducial region of CC;
- $E_T > 30$ GeV;
- $F_{EM} > 0.95$;
- $I_{cal} < 0.10$;
- $\chi^{2(7)}_{EM} < 12$;
- $L^8_{EM} > 0.9$, where L^8_{EM} is a likelihood based variable that combines tracking and shower shape information;
- a spatially matched track which satisfies the following requirements:

  - $|d_{vtxz}| < 3$ cm, where d_{vtxz} is the distance between the track z and the primary vertex z.
  - track $p_T > 25$ GeV;
  - $E_{cal}/p_{trk} < 1.2$, where E_{cal} is the energy measured in the calorimeter and p_{trk} is the momentum of the matched track;
  - $r_{dca} < 0.02$ cm, $\chi^2_{trk}/n.d.f < 5.0$, $N_{SMT} \geq 2$, $N_{CFT} \geq 9$.

Details of the selection of probe electrons and the measured efficiencies, as well as the chosen scale factors for future application on MC samples are described below for each group of cuts separately.

Electron preselection efficiency

To obtain the probe electron, a test track opposite to the tag electron is selected with:

- track $p_T > 15$ GeV, $|d_{vtxz}| < 3$ cm,
- $r_{dca} < 0.02$ cm, $\chi^2_{trk}/n.d.f < 5.0$, $N_{SMT} \geq 2$, $N_{CFT} \geq 9$;
- opposite charged compared to the tag electron;
- the extrapolation of the track would fall with the acceptance of either the CC or EC;
- $|\Delta\phi(testtrack, tagtrack)| > 2$, where $\Delta\phi(testtrack, tagtrack)$ is the difference in ϕ between the tag electron and the test track;
- $80 < M(tag, test\ track) < 100$ GeV, where $M(tag, test\ track)$ is the invariant mass of the tag electron and the test track.

The probe electrons are taken as denominator of the preselection efficiency.

The probe electrons (test tracks) are then matched with an EM object in $\Delta R < 0.14$ to obtain candidate preselected electrons. The candidates that satisfy the following requirements are taken as the numerator of preselection efficiency:

- $F_{EM} > 0.8$
- $I_{cal} < 0.2$

The measured efficiencies for CC and EC electrons in Run2b-34 are shown in Figure 5.12 (CC) and Figure 5.13 (EC). The results for Run2a and Run-12 are found to be very similar. They are included in Appendix A.1.1.

The corresponding data/MC scale factors are shown in Figure 5.14 as functions of L_{inst}, z_{pvtx}, electron η_{det}, η_{phy} and p_T. No significant dependencies are found for these variables. The biggest dependence is found to be on the electron η_{det}.

We choose the scale factor of electron η_{det} to correct MC events.

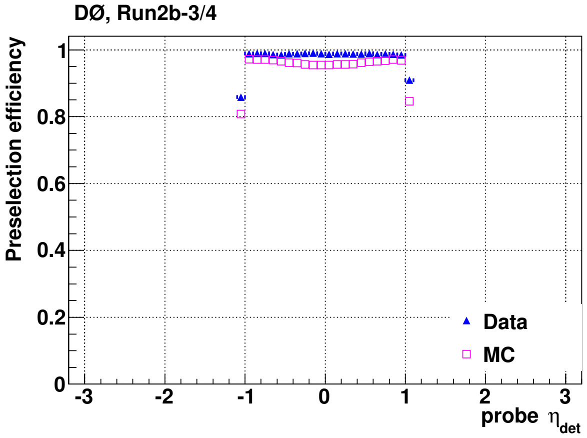

Figure 5.12: Electron preselection efficiency in the CC for data and MC events.

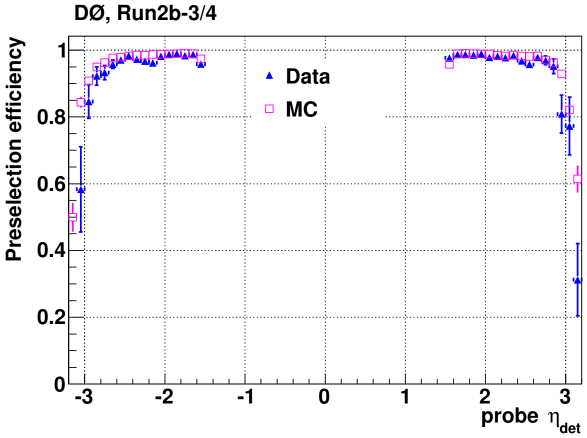

Figure 5.13: Electron preselection efficiency in the EC for data and MC events.

The Cal-ID efficiency

The Cal-ID contains the same group of cuts as in the standard event selection for electrons, except that no requirements are made on the tracking quality.

When measuring the Cal-ID efficiency for CC electrons, the same tag electrons and test tracks are used as measuring the preselection efficiency. The probe electrons, which are found by matching EM objects with the test track in a cone of $\Delta R < 0.14$, need to pass the preselection cuts.

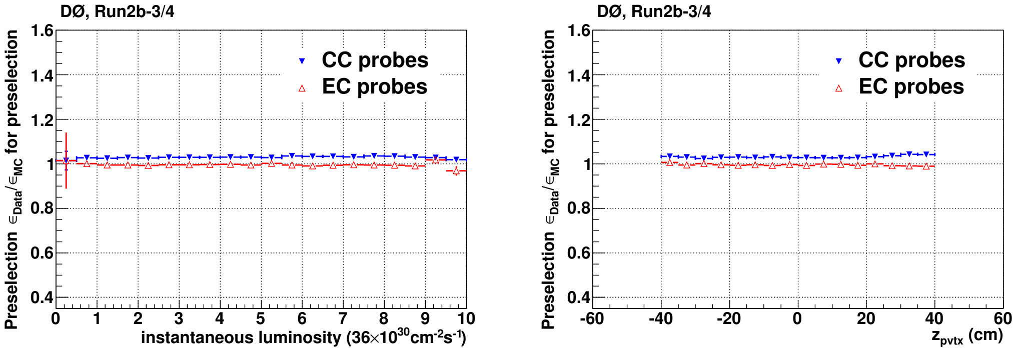

(a) s.f vs. L_{inst} (b) s.f vs. z_{pvtx}

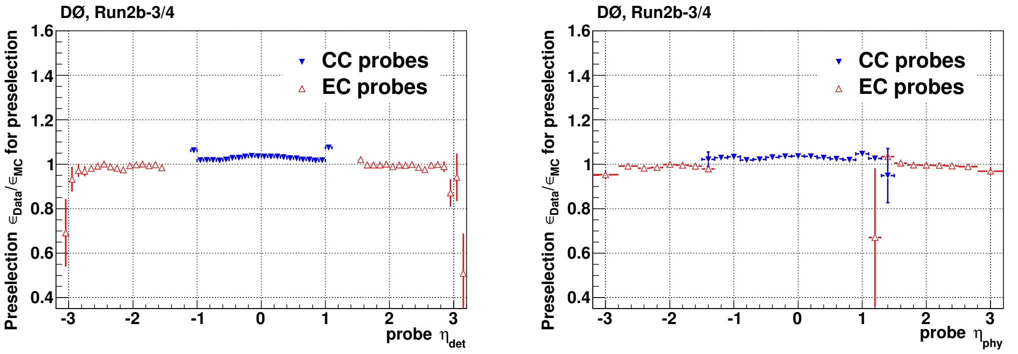

(c) s.f vs. η_{det} of probe electron (d) s.f vs. η_{phy} of probe electron

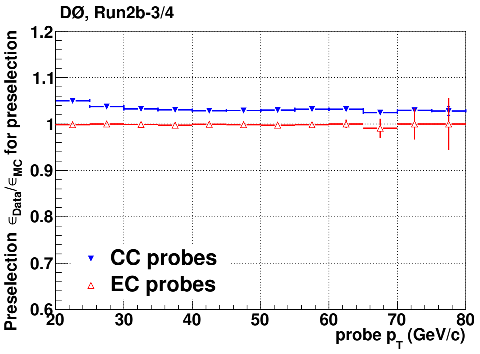

(e) s.f vs. p_T of probe electron

Figure 5.14: Scale factors (s.f.) for electron preselection efficiency between data and MC. The scale factor of η_{det} is chosen as the correction to be applied to MC events.

Since the EC electrons with no matched tracks are also used in our event selection, selecting test tracks prior to probe electrons would lead to a biased sample of EC probe electrons. Different from the procedure used for CC electrons, we select the probe electrons directly from EM objects found in the EC. Those EM objects also need to pass the preselection cut and the cut on the invariant mass of the tag-probe pair, which is $80 < M_{ee} < 100$ GeV.

The Cal-ID efficiencies are calculated by using the probe electrons as denominator, and those pass Cal-ID cuts as numerator. The measured efficiencies vs. η_{det} for CC and EC electrons in Run2b-34 can be found in Figure 5.15 (CC) and Figure 5.16 (EC). Similar results for other subsets of data and MC are included in Appendix A.1.2.

The efficiencies vs. electron p_T are shown in Figure 5.17 (CC) and Figure 5.18 (EC).

The corresponding data/MC scale factors are presented in Figure 5.19 as functions of L_{inst}, z_{pvtx}, electron η_{det}, η_{phy} and p_T.

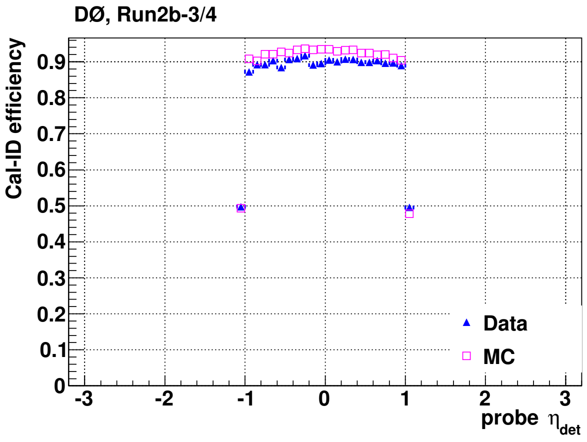

Figure 5.15: Electron Cal-ID efficiency vs. electron η_{det} in the CC for data and MC events.

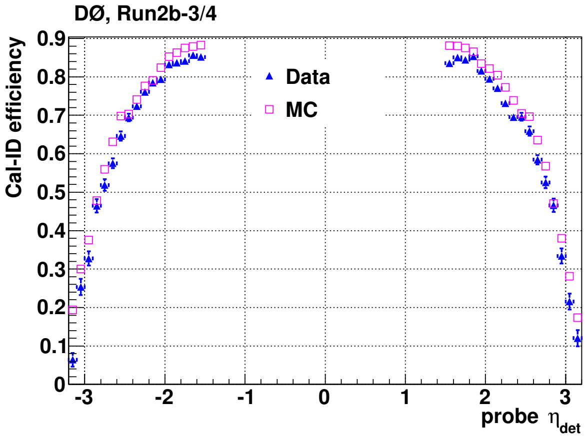

Figure 5.16: Electron Cal-ID efficiency vs. electron η_{det} in the EC for data and MC events.

Dependencies are found on both of the electron η_{det} and p_T. Instead of using a two-dimensional scale factor depending on both of the variables (which may have large statistical uncertainty if using a small bin size or may not solve the dependence accurately enough if using a relatively big bin size), we use a scale

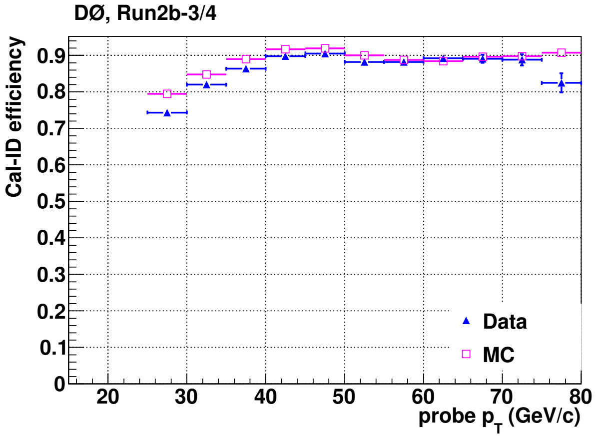

Figure 5.17: Electron Cal-ID efficiency vs. electron p_T in the CC for data and MC events.

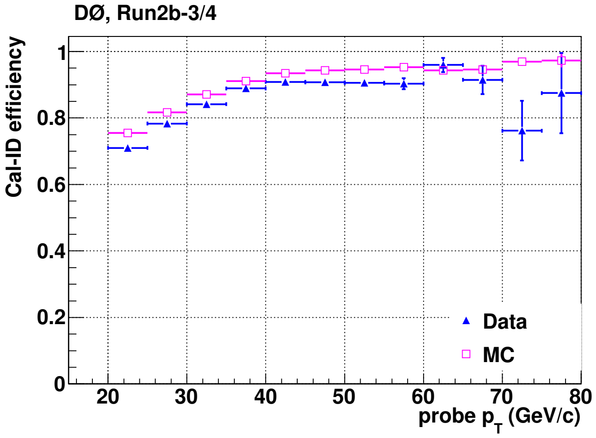

Figure 5.18: Electron Cal-ID efficiency vs. electron p_T in the EC for data and MC events.

factor only dependent on electron η_{det}. This scale factor is treated as a first order correction. It only corrects the dependence of electron η_{det}. The dependence of electron p_T is not addressed. Thus a second order correction, which is a scale factor dependent on electron η_{phy} and p_T, is chosen. Adding the electron η_{phy} as an additional dependent variable is simply due to its high correlation with both the z_{pvtx} and electron η_{det}.

Since the dependencies are less significant on p_T and η_{phy}, especially after applying the first order correction, a choice of bigger bin size would still be able to take care of the dependence, and be free from lack of statistics in certain bins.

The same tag-probe pairs, with the application of the first order correction, are used to estimate the second order correction. The actual values of the second order corrections are shown in Figure 5.20 (CC) and Figure 5.21 (EC).

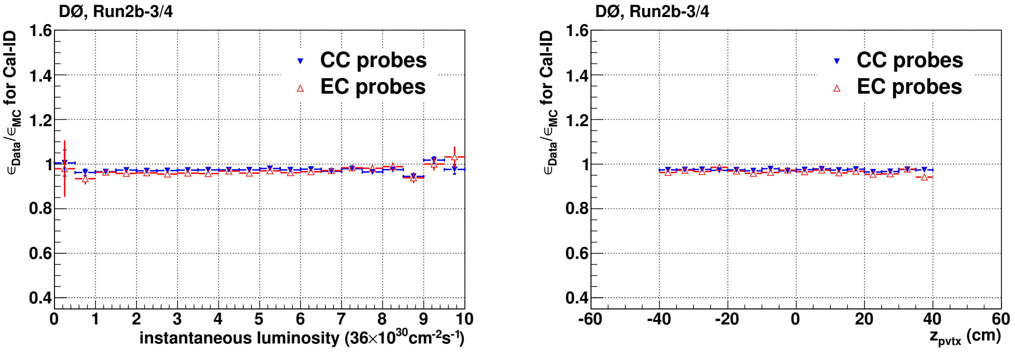

(a) s.f vs. L_{inst} (b) s.f vs. z_{pvtx}

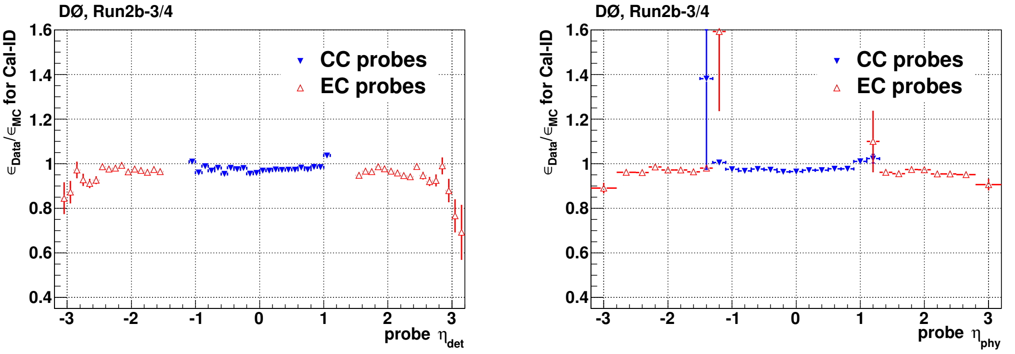

(c) s.f vs. η_{det} of probe electron (d) s.f vs. η_{phy} of probe electron

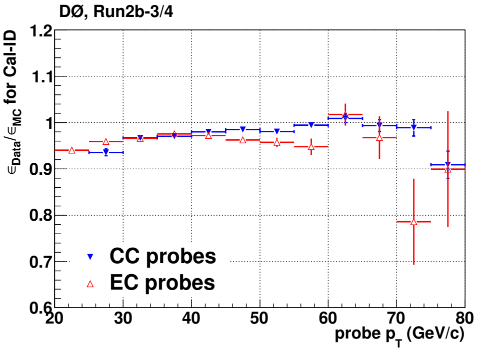

(e) s.f vs. p_T of probe electron

Figure 5.19: Scale factors (s.f.) for electron Cal-ID efficiency between data and MC. The scale factor of η_{det} is chosen as the first order correction to be applied to MC events.

The tracking efficiency

The tracking efficiency of electrons consists of three types. Each corresponds to the tracking requirements used in the event selection. They are as follows:

- Type I: the efficiency of tracking cuts used in the event selection for electrons in the CC;
- Type II: similar to Type I, but for electrons in the EC;

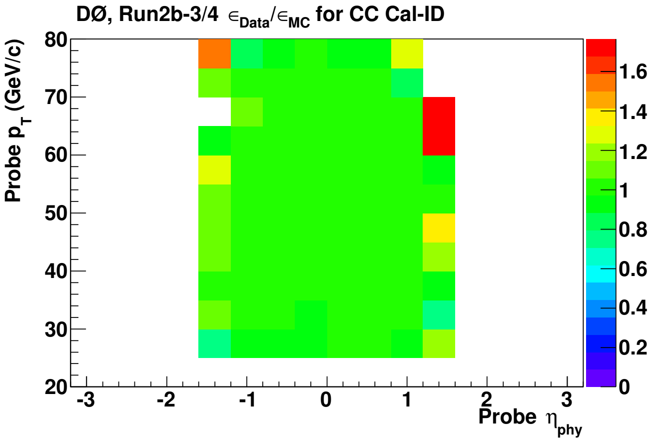

Figure 5.20: Second order correction to be applied to MC events for correcting electron Cal-ID efficiency dependence of electron p_T and electron η_{phy} in the CC. Correction factors are set to 1.0 for the empty bins and bins with the initial correction factor not within [0.1, 2.0].

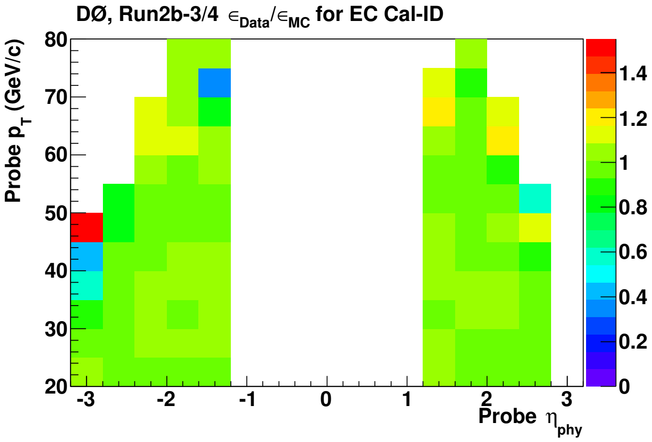

Figure 5.21: Second order correction to be applied to MC events for correcting electron Cal-ID efficiency dependence of electron p_T and electron η_{phy} in the EC. Correction factors are set to 1.0 for the empty bins and bins with the initial correction factor not within [0.1, 2.0].

- Type: III: the cut efficiency of the HoR variable for non-track-matched EM objects in EC.

The last two efficiencies are complementary to each other, and thus are measured together.

The Cal-ID cuts are used to select probe electrons for measuring the tracking efficiency. Additionally, a cut on the difference in ϕ_{det} between the tag and probe electron is employed as $\Delta\phi(tag, probe) > 2$.

The probe electrons are taken as the denominator and those satisfying the tracking requirements are taken as the numerator of the efficiency. The measured efficiencies of Type I, II and III in Run2b-34 can be found in Figure 5.22, Figure 5.23 and Figure 5.24 respectively. Results for Run2a and Run2b-12 are included in Appendix A.1.3.

The corresponding scale factors are given in Figure 5.25 (Type I and Type II), and Figure 5.26 (Type III). The scale factors are found to be dependent on the L_{inst}, z_{pvtx} and η_{det}. The scale factor of η_{det} is chosen as a first order correction to be applied to MC events.

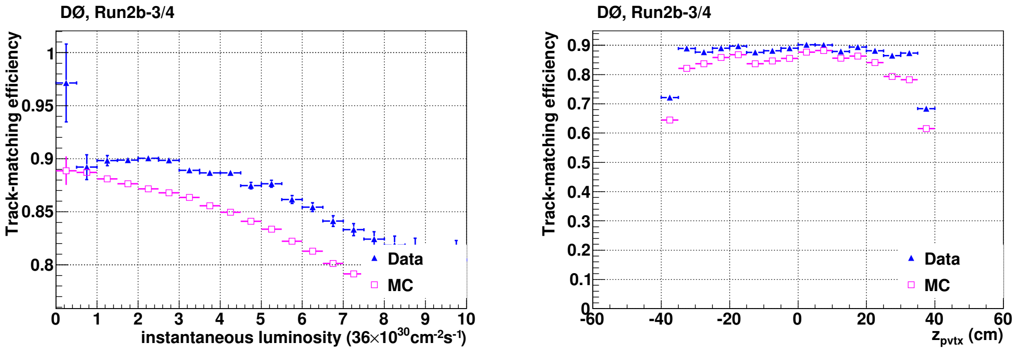

(a) ϵ_{CCtrk} vs. L_{inst} (b) ϵ_{CCtrk} vs. z_{pvtx}

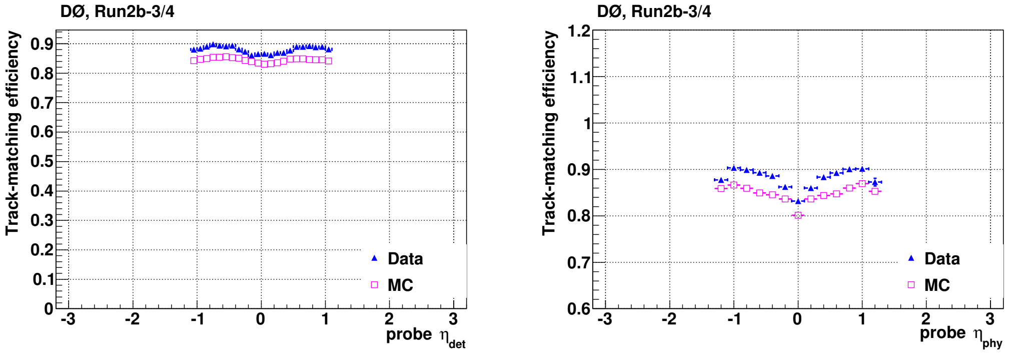

(c) ϵ_{CCtrk} vs. η_{det} of probe electron (d) ϵ_{CCtrk} vs. η_{phy} of probe electron

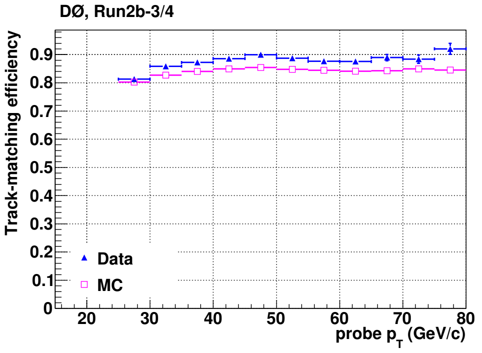

(e) ϵ_{CCtrk} vs. p_T of probe electron

Figure 5.22: Type I tracking efficiencies (ϵ_{CCtrk}) for electron in the CC for data and MC events.

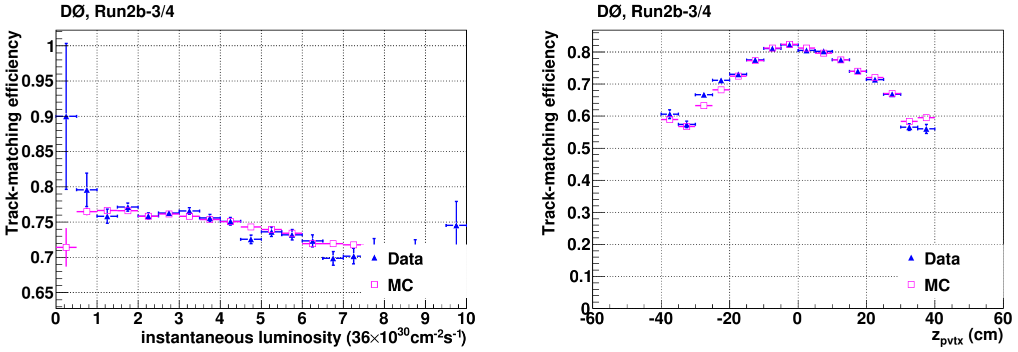

(a) ϵ_{ECtrk} vs. L_{inst} (b) ϵ_{ECtrk} vs. z_{pvtx}

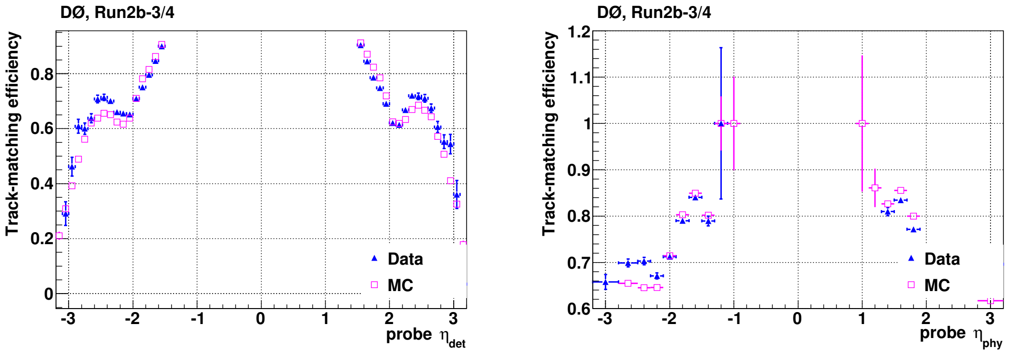

(c) ϵ_{ECtrk} vs. η_{det} of probe electron (d) ϵ_{ECtrk} vs. η_{phy} of probe electron

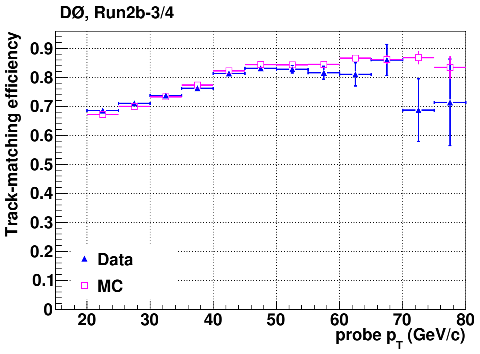

(e) ϵ_{ECtrk} vs. p_T of probe electron

Figure 5.23: Type II tracking efficiencies (ϵ_{ECtrk}) for electron in the EC for data and MC events.

A second order correction, which is dependent on electron η_{phy} and z_{pvtx}, is developed by following the same the procedure used in the study of Cal-ID efficiency. They are shown in Figure 5.27.

Additionally, a correction correction dependent on the L_{inst} is also developed using the same procedure, as shown in Figure 5.28.

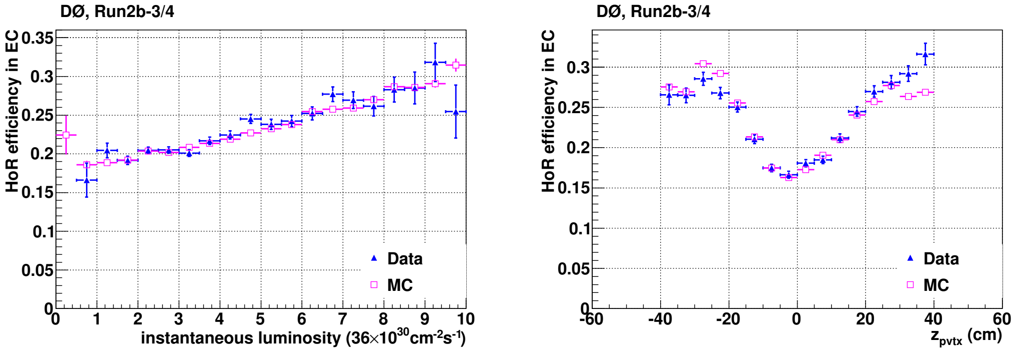

(a) ϵ_{EC_HoR} vs. L_{inst} (b) ϵ_{EC_HoR} vs. z_{pvtx}

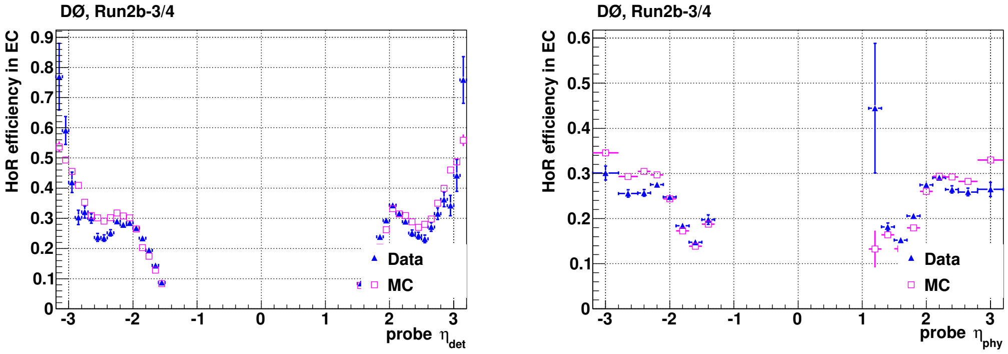

(c) ϵ_{EC_HoR} vs. η_{det} of probe electron (d) ϵ_{EC_HoR} vs. η_{phy} of probe electron

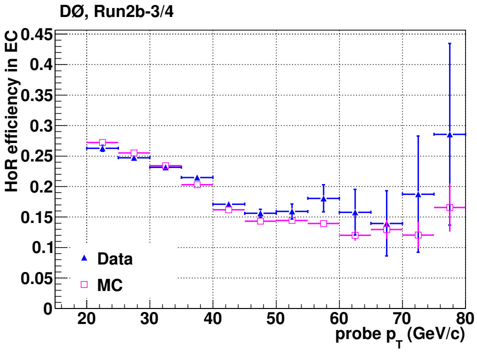

(e) ϵ_{EC_HoR} vs. p_T of probe electron

Figure 5.24: Type III tracking efficiencies (ϵ_{EC_HoR}) for electron in the EC for data and MC events.

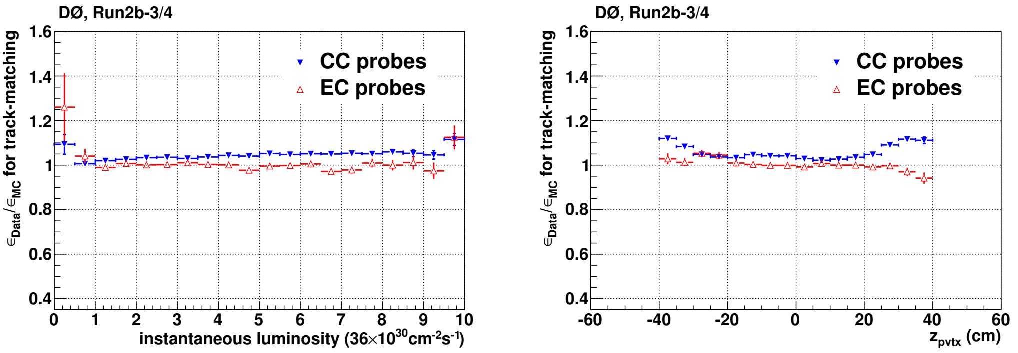

(a) s.f vs. L_{inst} (b) s.f vs. z_{pvtx}

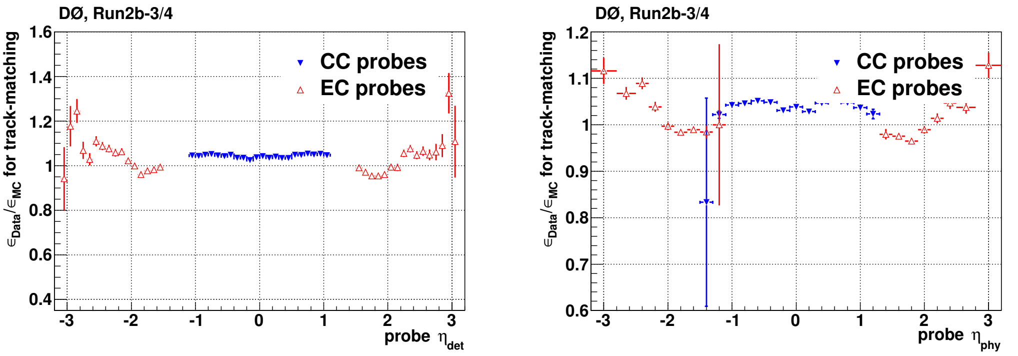

(c) s.f vs. η_{det} of probe electron (d) s.f vs. η_{phy} of probe electron

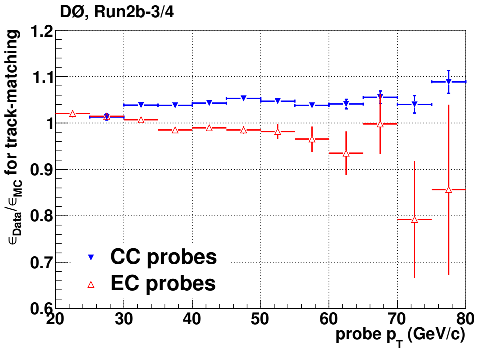

(e) s.f vs. p_T of probe electron

Figure 5.25: Scale factors (s.f.) for the tracking efficiencies of electron in the CC (Type I) and in the EC (Type II) between data and MC. The scale factor of η_{det} is chosen as the first order correction to be applied to MC events.

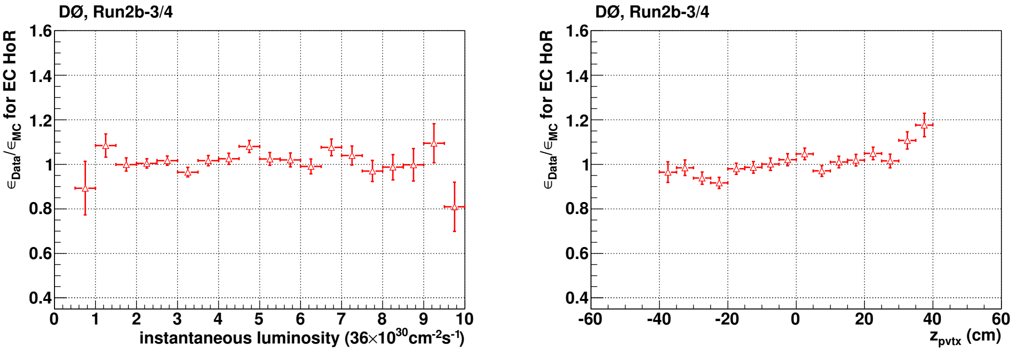

(a) s.f vs. L_{inst} (b) s.f vs. z_{pvtx}

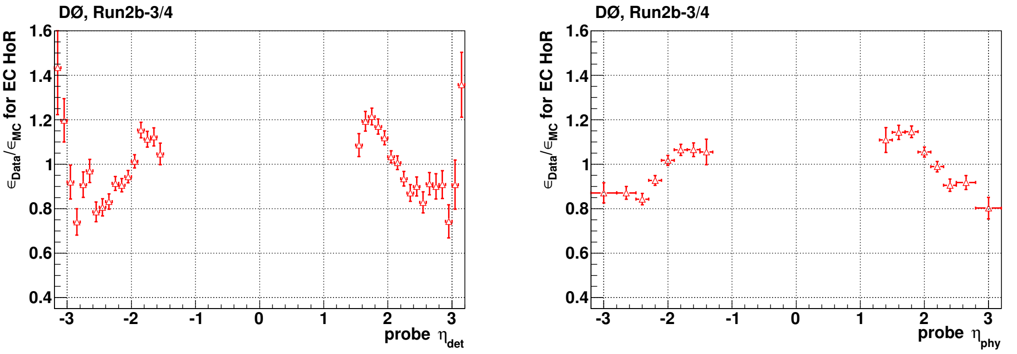

(c) s.f vs. η_{det} of probe electron (d) s.f vs. η_{phy} of probe electron

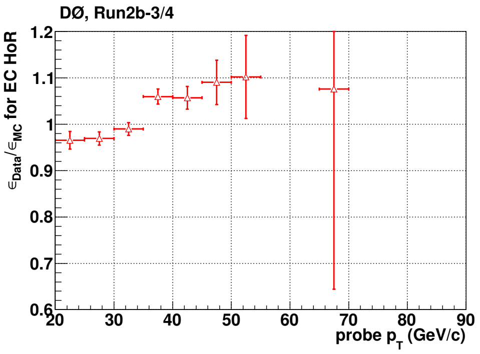

(e) s.f vs. p_T of probe electron

Figure 5.26: Scale factors (s.f.) for the cut on the HoR variable for non-track-matched electrons in the EC (Type III) between data and MC. The scale factor of η_{det} is chosen as the first order correction to be applied to MC events.

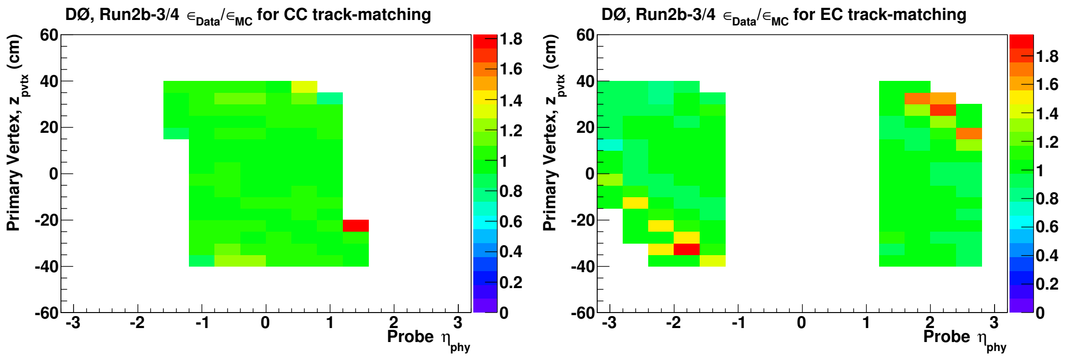

(a) 2D s.f (2nd order) for Type I

(b) 2D s.f (2nd order) for Type II

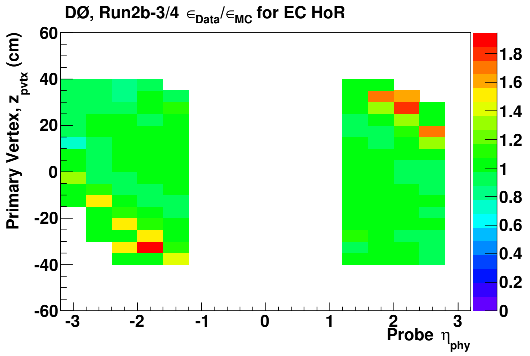

(c) 2D s.f (2nd order) for Type III

Figure 5.27: Second order scale factors (s.f.) as functions of z_{pvtx} and electron η_{phy} for each type of tracking efficiency. Correction factors are set to 1.0 for the empty bins and bins with the initial correction factor not within [0.1, 2.0].

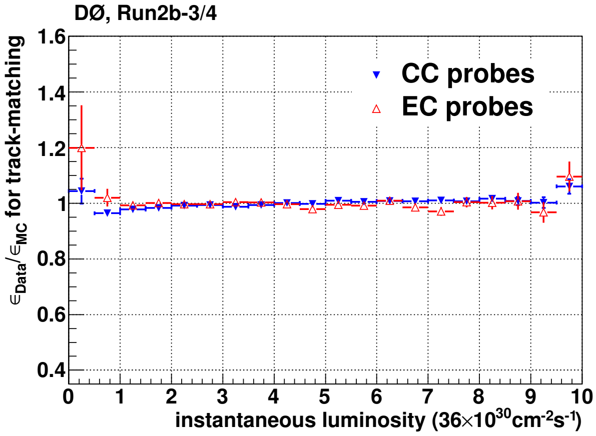

(a) 1D s.f (2nd order) for Type I and Type II

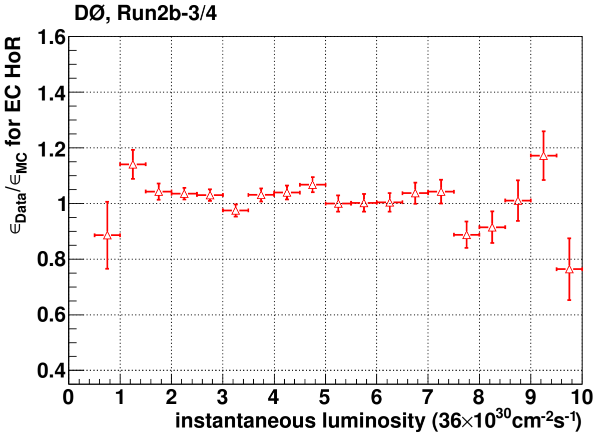

(b) 1D s.f (2nd order) for Type III

Figure 5.28: Second order scale factors (s.f.) as functions of L_{inst} for each type of tracking efficiency.

5.4 Estimation of efficiency and acceptance, $\epsilon \times A$

As explained in Section 5.1.1 and Section 5.2.1, the $\epsilon \times A$ obtained from the fully simulated MC samples will be used to correct the shape of the Z/γ^* boson rapidity.

After applying all the MC corrections described in Section 5.3, we now calculate the $\epsilon \times A$ as a function of Z/γ^* boson rapidity. The calculation is done by dividing the reconstructed boson rapidity distributions by that in generator level.

The generator level boson rapidity is the prediction provided by the ResBos event generator, as shown previously in Figure 5.10. The reconstructed level boson rapidity distribution is shown in Figure 5.29.

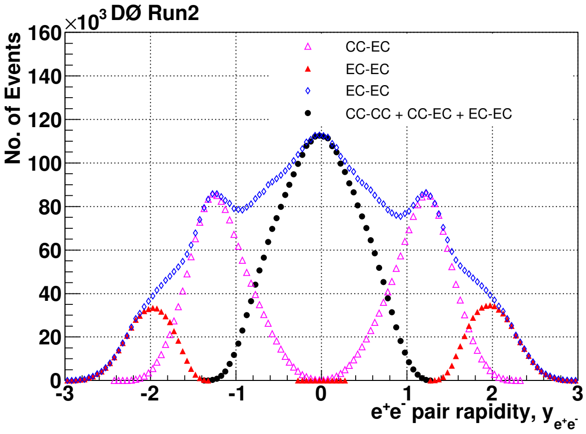

Figure 5.29: Reconstructed level boson rapidity.

Figure 5.30 shows the $\epsilon \times A$ for each subset of data with no discernment for the event type. Figure 5.31 shows the $\epsilon \times A$ for each type of events. In the central region with boson rapidity $|y| < 1$, all three subsets of data give similar $\epsilon \times A$. The case changed in the region of $|y| > 1$. This change is caused by the change of tracking efficiency of EC electrons.

The $\epsilon \times A$ is above 20% for the region with boson rapidity $|y| < 2.2$. It drops rapidity beyond this region. Only EC-EC events contribute to the $\epsilon \times A$ when $|y| > 2.2$.

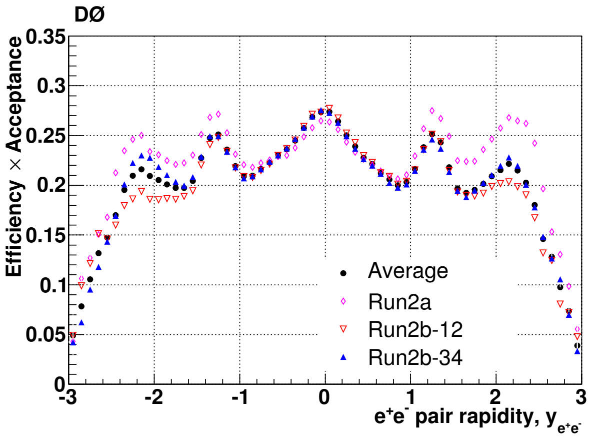

Figure 5.30: $\epsilon \times A$ obtained from MC samples for each subset of data.

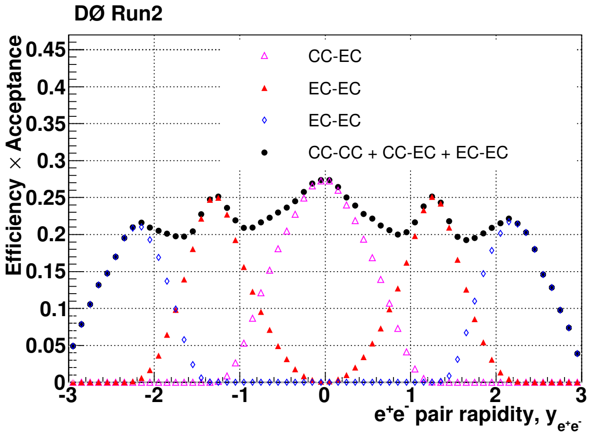

Figure 5.31: $\epsilon \times A$ obtained from MC samples for each type of events.

5.5 Backgrounds

Since our signal process $p\bar{p} \to Z/\gamma^* + X \to ee + X$ is mainly characterized by two electrons in the final state, any other processes with two electrons or other particles which could be misidentified as electrons in the final state could pass the event selection defined in Section 5.2.2, and thus make a contribution to the set of background events.

The possible background processes considered in this measurement are:

- QCD mulitjet events, in which jets are misidentified as electrons;
- $W + jets$, where one electron is produced from the decay of the W boson and another electron is formed by a misidentified jet/γ;
- $Z/\gamma^* \to \tau^+\tau^- \to e^+e^-\nu_\tau\nu_e\bar{\nu}_\tau\bar{\nu}_e$;
- $W^+W^- \to e^+e^-\nu_e\bar{\nu}_e$;

- $W^{\pm}Z$, where $Z \to e^+e^-$;
- ZZ, where $Z \to e^+e^-$;
- $t\bar{t} \to Wb + W\bar{b} \to e\nu b + e\nu\bar{b}$.

The event selection managed to keep the total background level around 3%. All the backgrounds except QCD multijet background, which could be fairly well modeled by the electroweak theory, are denoted as electroweak backgrounds and discussed in Section 5.5.1. The QCD multijet background is discussed in Section 5.5.2.

5.5.1 Electroweak backgrounds

All of the electroweak backgrounds are estimated from MC samples. These samples are listed in Section 5.2.4, together with the cross section used for normalization. All of the MC corrections described in Section 5.3, except the PYTHIA to RESBOS reweighting, which is only applicable to the signal MC samples, are applied when estimating the electroweak backgrounds. The same event selection criteria are applied.

W+*jets* events are found to be the biggest background source among all of the electroweak backgrounds. The estimated number of events from each background process are listed in Table 5.3. The total electroweak background fraction is found to be $\sim 0.3\%$.

5.5.2 QCD multijet background

QCD multijet events have a huge production rate at the Tevatron. They are found to be the dominant background source in this measurement.

QCD multijet events may pass the event selection when two of the jets are mis-identified as electrons. The rate for a jet to be mis-identified as an electron in the CC is fairly small due to the tight tracking requirements. It is relatively higher in the EC, where the tracking requirement for electrons is loosened.

Different from the estimation of the electroweak backgrounds, estimation of the QCD multijet background is done by using data events. We utilize one of the unique signatures of the signal process, the invariant mass spectrum of the two electrons in the final state, to estimate the overall QCD multijet background fraction.

In practice, this is done step-by-step as follows.

- Select a multijet enriched sample by reversing the shower shaper requirement ($\chi^{2(7)}_{EM}$ or $\chi^{2(8)}_{EM}$) on the two electron candidates;
- Obtain the invariant mass distribution from the $Z/\gamma^* \to e^+e^-$ signal MC events, with all the MC corrections applied;
- Obtain the invariant mass distribution from data events, with the electroweak backgrounds subtracted, only the QCD multijet background is believed to remain in the data events after the subtraction;
- Utilize the three invariant mass distributions altogether to get a best fit of the normalization factor for the multijet enriched sample. The invariant mass range used in this fit is $[60, 130]$ GeV, which is the full range of the dielectron mass used when generating the signal MC. Studies of using slightly different mass ranges, e.g. $[62, 128]$ GeV and $[65, 125]$ GeV, have been made. The studies show negligible differences between different mass ranges.

The estimation of QCD multijet background is done separately for CC-CC, CC-EC, and EC-EC events, and it is done separately for each subset of data.

The invariant mass distributions for the full dataset are shown in Figure 5.32, for each type of events.

The estimated numbers of QCD events are listed in Table 5.3 for different subsets of data and for the complete data set.

Process	Subset			Combined
	Run2a	Run2b-12	Run2b-34	
$W + X$	141.96	224.38	282.23	648.56
$Z/\gamma^* \to \tau^+\tau^-$	59.86	172.64	180.32	412.82
WW	16.02	57.26	59.00	132.27
WZ	27.92	108.42	111.41	247.75
ZZ	21.04	80.91	82.47	184.43
$t\bar{t}$	7.82	25.14	26.08	59.04
Total EWK backgrounds	274.62	668.75	741.51	**1684.87**
QCD background	966.60	4423.73	4873.78	**10264.12**
Total backgrounds	1241.22	5092.48	5615.29	**11948.99**
Data	65798	258520	265852	**590170**

Table 5.3: Observed number of events in data and estimated number of events for each background.

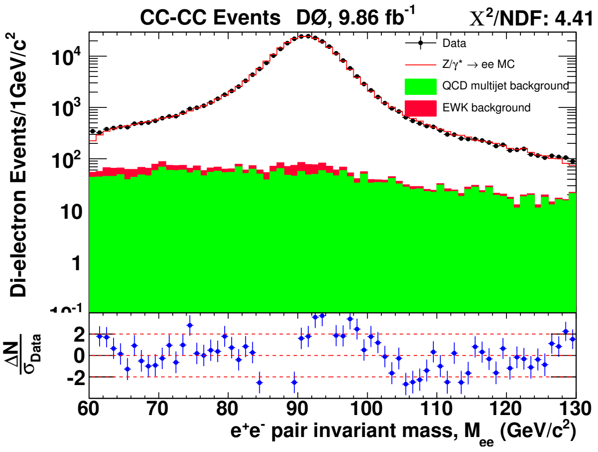

(a) CC-CC

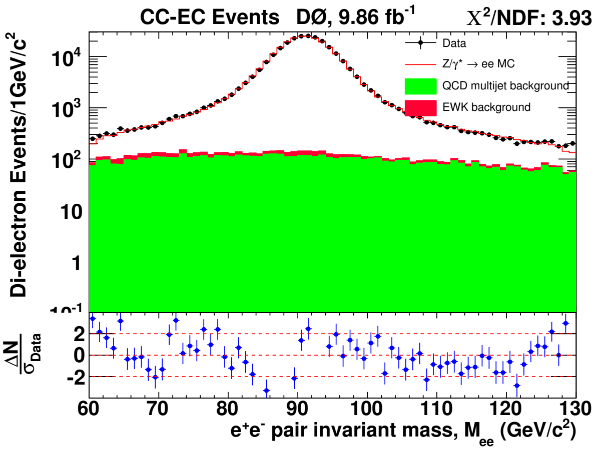

(b) CC-EC

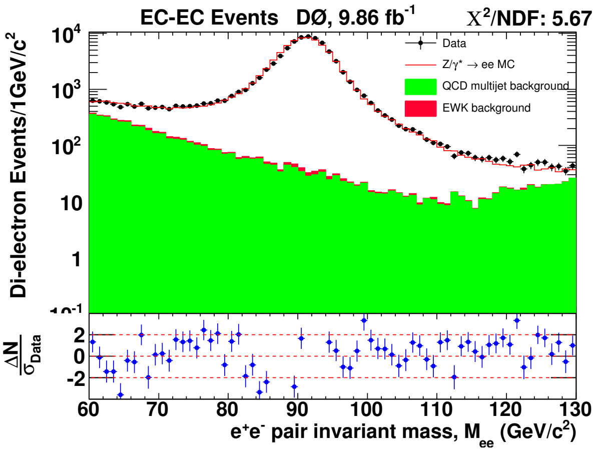

(c) EC-EC

Figure 5.32: Distributions of the invariant mass of the two electron candidates for each type of events.

5.6 Data and MC comparison

Data and MC distributions are compared to cross check the MC corrections and the background estimation.

The standard event selection cuts are applied, except for the invariant mass distributions, which do not have the mass cuts applied.

Figure 5.33 is the legend for all the plots shown in this section.

Distributions have been made for the following variables.

- z_{pvtx}, shown in Figure 5.34;
- η_{det}, shown in Figure 5.35;
- η_{phy}, shown in Figure 5.36;
- $\Delta\phi_{det}$ between the two electrons , shown in Figure 5.37;
- electron p_T, shown in Figure 5.38;
- $\cos\theta^*$, where θ^* is the polar angle of the electrons in the Collines-Soper frame [35], shown in Figure 5.39
- M_{ee}, shown in Figure 5.40;
- reconstructed boson p_T, shown in Figure 5.41;
- reconstructed boson rapidity, shown in Figure 5.42;

Comparisons are made for CC-CC, CC-EC and EC-EC events separately, as well as for the entire data set together. The uncertainties shown in these plots are statistical. Comparisons for individual data taking periods are provided in Appendix A.2.

To examine the agreement between data and MC, a χ^2 test considering only the statistical errors, is performed for each distribution.

The level of agreement between data and MC is modest. Residual discrepancies are assigned as systematic uncertainties on $\epsilon \times A$.

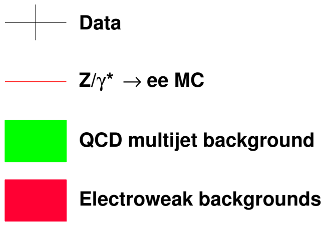

Figure 5.33: Legend for the plots within this section.

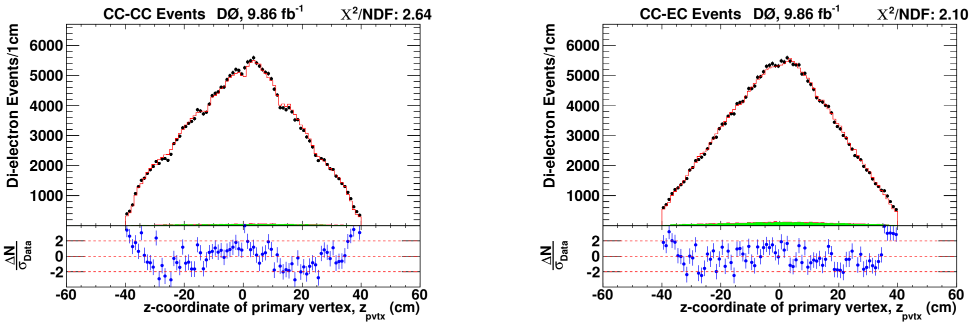

(a) CC-CC

(b) CC-EC

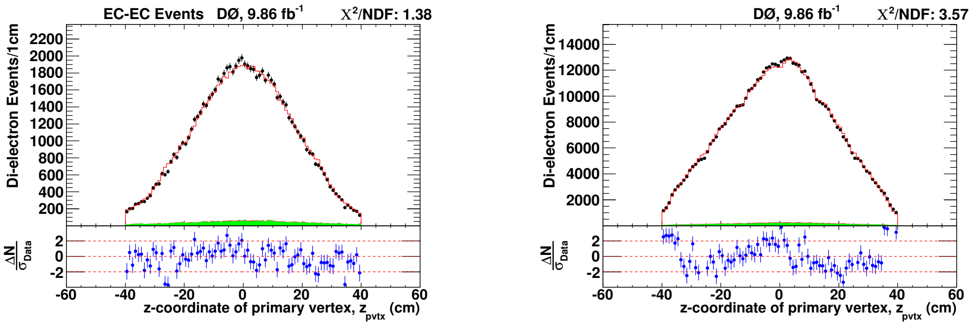

(c) EC-EC

(d) All events

Figure 5.34: Distributions of the z-coordinate of the primary vertex.

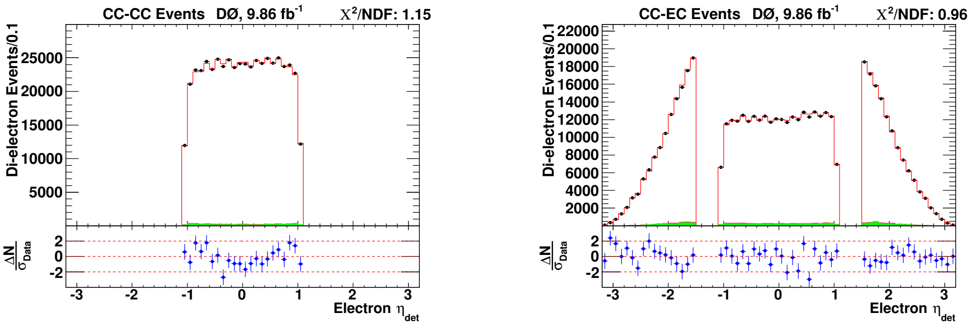

(a) CC-CC (b) CC-EC

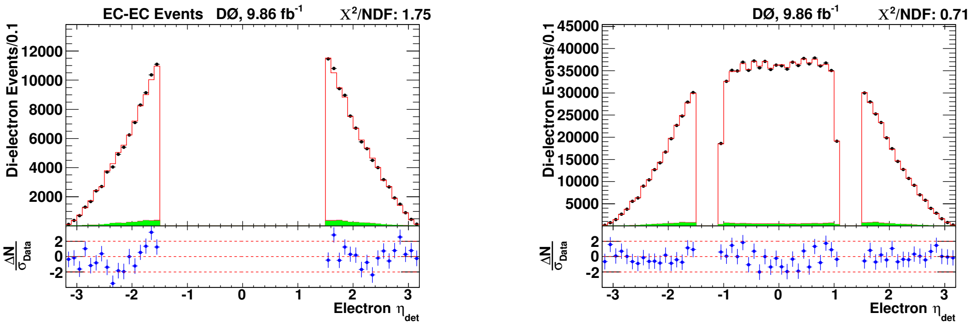

(c) EC-EC (d) All events

Figure 5.35: Distributions of the electron η_{det}.

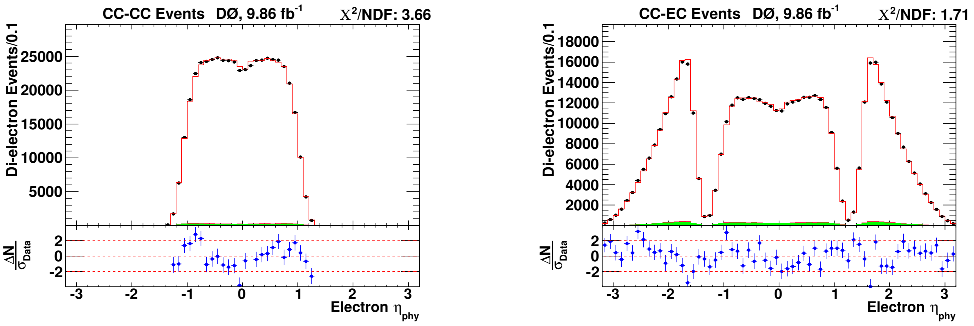

(a) CC-CC (b) CC-EC

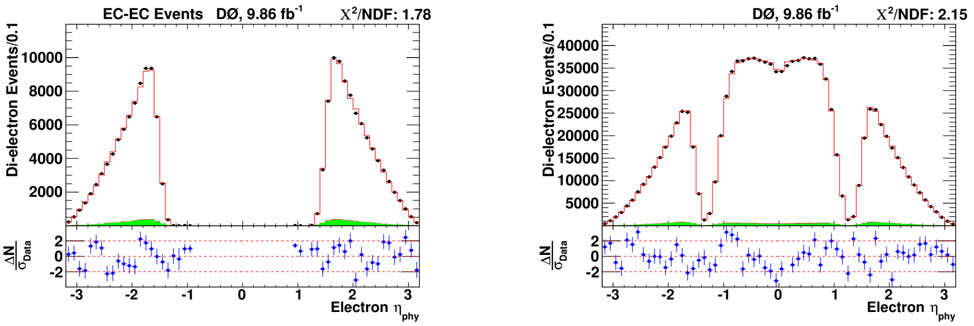

(c) EC-EC (d) All events

Figure 5.36: Distributions of the electron η_{phy}.

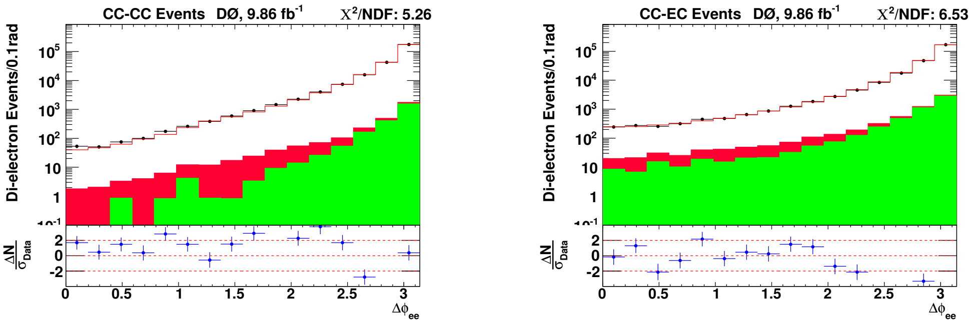

(a) CC-CC (b) CC-EC

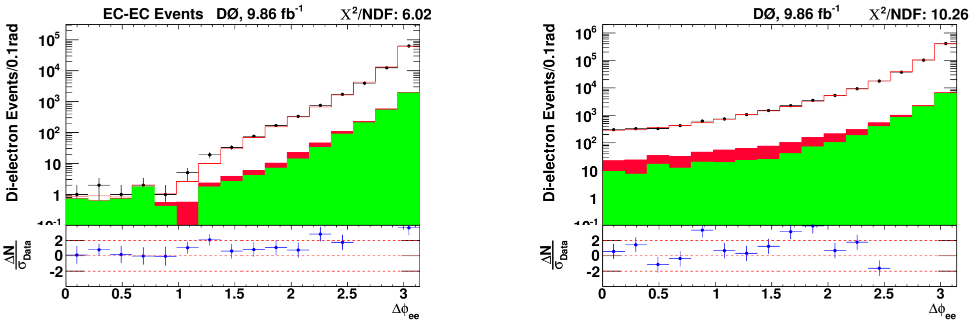

(c) EC-EC (d) All events

Figure 5.37: Distributions of $\Delta\phi_{det}$ between the two electrons.

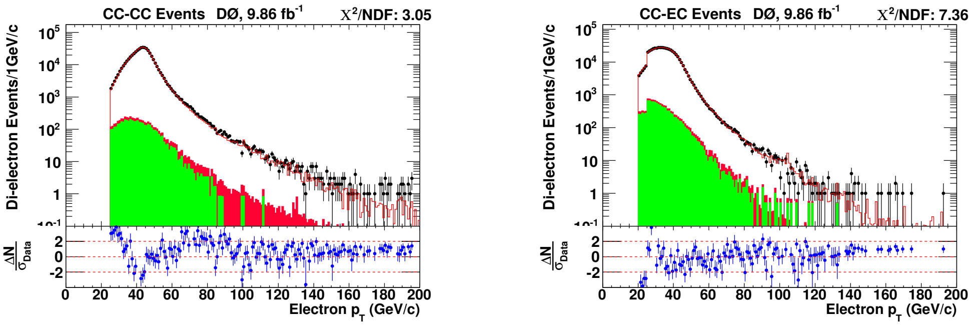

(a) CC-CC (b) CC-EC

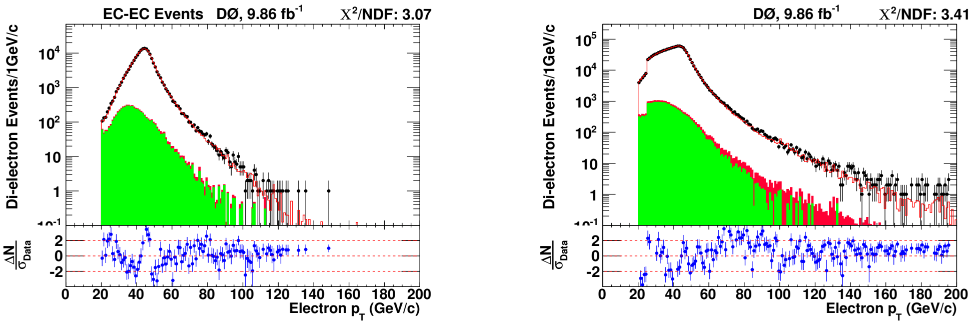

(c) EC-EC (d) All events

Figure 5.38: Distributions of the electron p_T.

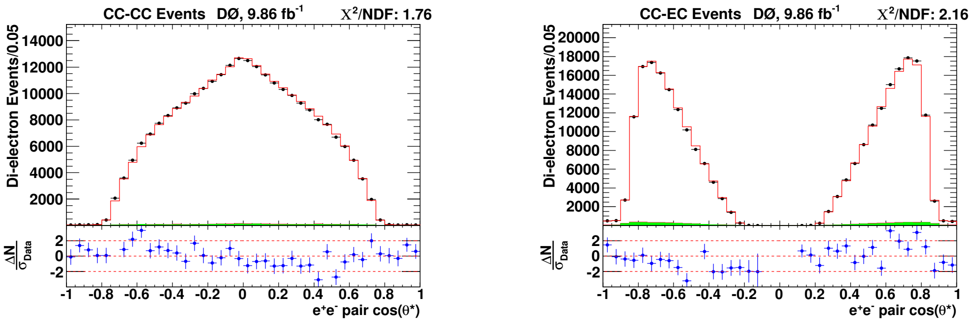

(a) CC-CC (b) CC-EC

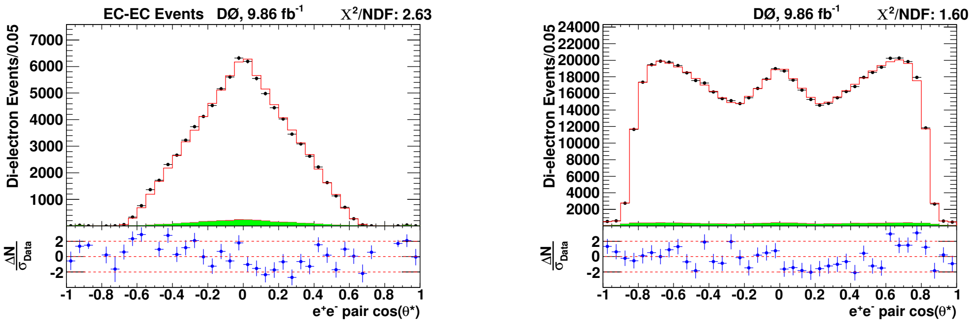

(c) EC-EC (d) All events

Figure 5.39: Distributions of $\cos\theta^*$.

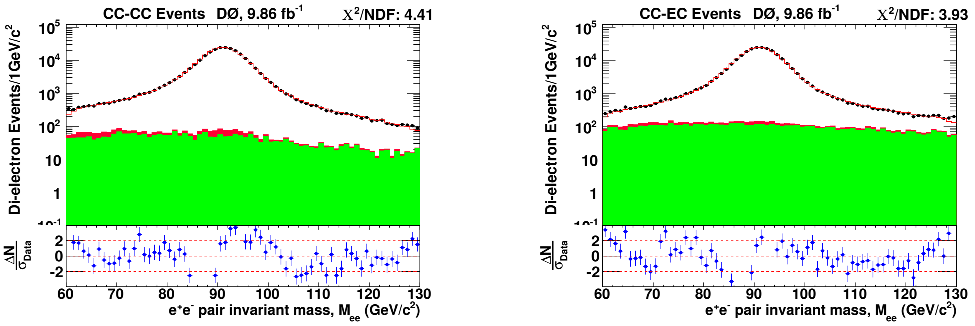

(a) CC-CC (b) CC-EC

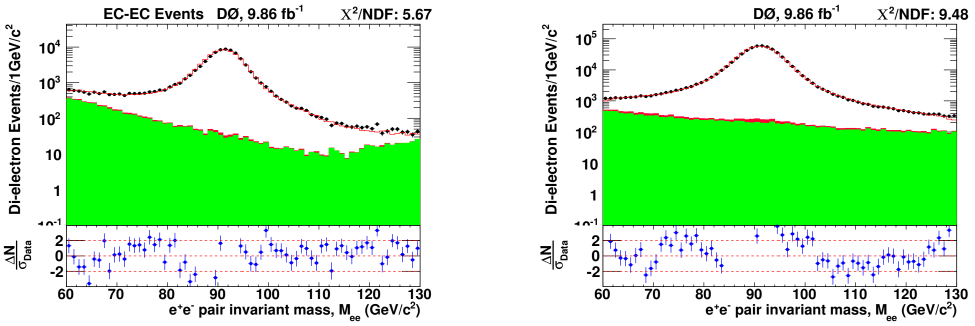

(c) EC-EC (d) All events

Figure 5.40: Distributions of the invariant mass of e^+e^- pairs.

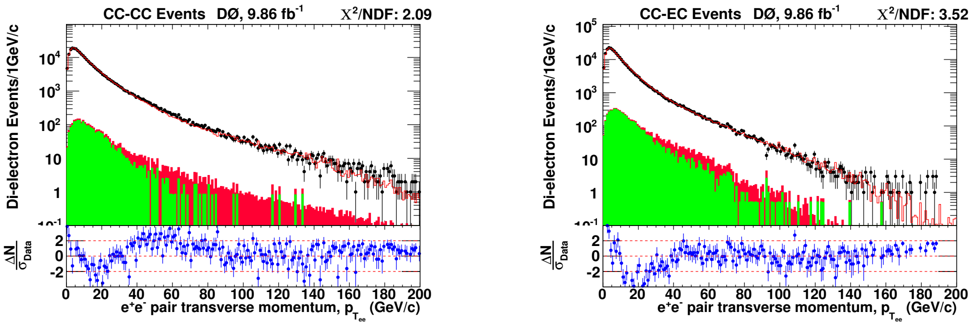

(a) CC-CC

(b) CC-EC

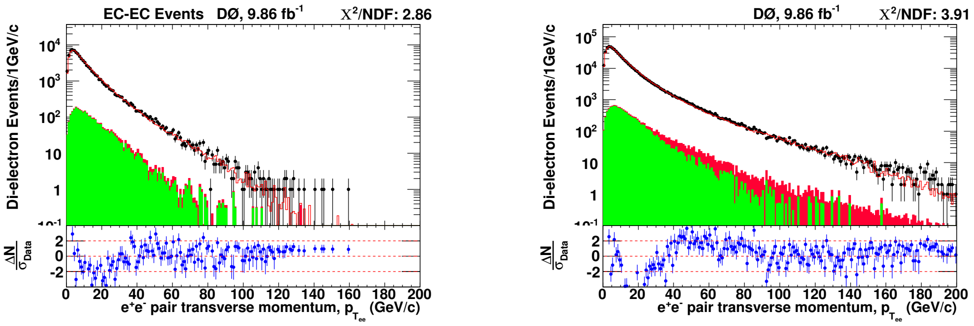

(c) EC-EC

(d) All events

Figure 5.41: Distributions of the reconstructed boson p_T.

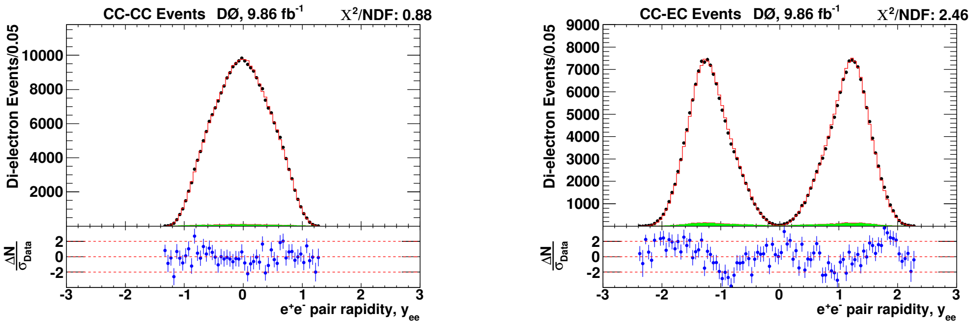

(a) CC-CC

(b) CC-EC

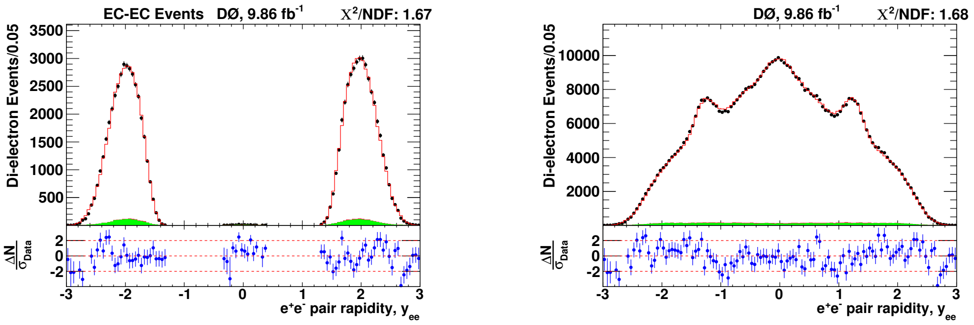

(c) EC-EC

(d) All events

Figure 5.42: Distributions of the reconstructed boson rapidity.

5.7 Bin-by-bin unfolding

The reconstructed boson rapidity shape, as shown in Figure 5.42, is smeared by detector resolution and affected by the detector acceptance, and thus does not represent the actual Z/γ^* boson rapidity shape. Unfolding is needed to eliminate these detector effects.

As discussed in Section 5.2.1, we use the $\epsilon \times A$ estimated from the fully simulated MC samples to unfold the data. Technically, by following Equation 5.2, the $(\epsilon \times A)_i$ is applied in reciprocal for each bin of the reconstructed boson rapidity distribution observed in data (with all backgrounds subtracted).

Due to the finite resolution of the detector, a certain fraction of events in a given rapidity bin originates from a nearby bin. This is the so-called event migration. The approach of bin-by-bin unfolding chosen in this analysis is suitable only if the event migration was small. Fortunately, in this measurement, the event migration is small enough for this bin-by-bin unfolding approach to be valid.

The event migration estimated from MC events is shown in Figure 5.43. For most bins, approximately 8% of the events are shifted to each adjacent bin.

The net effect of the event migration (net migration), is relatively small (less than 0.5% for most bins). The net migration is the ratio of the generator level Z rapidity distribution to the reconstructed boson distribution for the MC events which pass the event selection. It is shown in Figure 5.44.

The event migration can also be reflected by the bin purity of MC events, which, by definition, is the fraction of events in a certain boson rapidity bin at generator level, and which are in the same bin at the reconstructed level. It is shown in Figure 5.45.

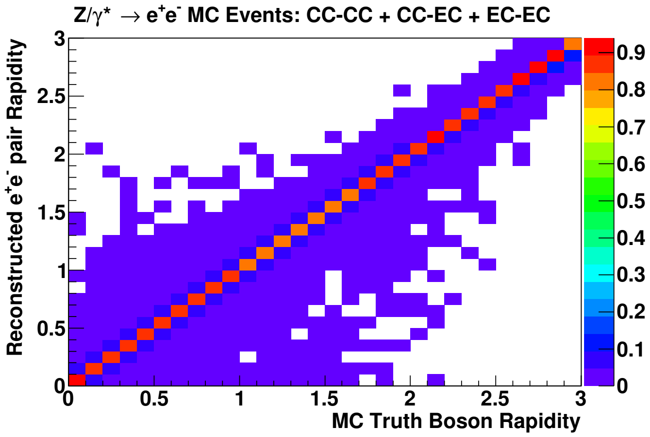

Figure 5.43: Event migration simulated in MC events.

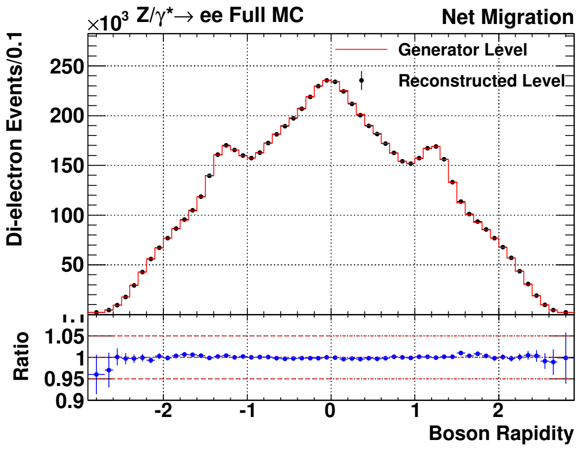

Figure 5.44: Comparison of boson rapidity shape between generator level and reconstructed level. The net migration is shown as the ratio of reconstructed boson rapidity distribution to generator level distribution for the same MC events which pass event selection.

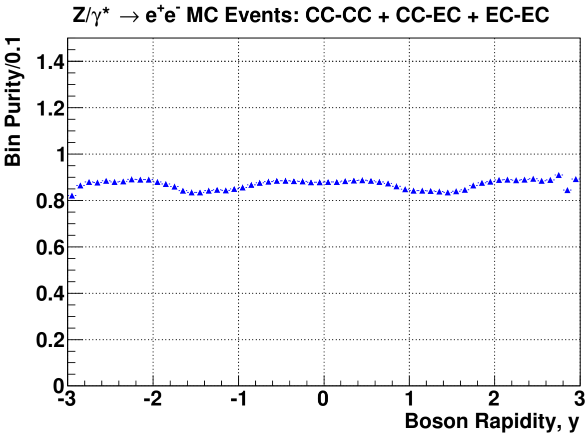

Figure 5.45: Bin purity simulated in MC events.

5.8 Systematic uncertainties

A number of systematic uncertainties are considered in this measurement. They include systematic uncertainties that arise from the estimation of $\epsilon \times A$ and that from the background estimation.

The systematic uncertainties that contribute to $\epsilon \times A$ can be classified into two groups, one for those arise from the theory prediction used in MC samples, which affects both the generator level and reconstructed level distribution; and the other for those arise from the detector simulation, which affects the reconstructed level distribution only.

The systematic uncertainties that contribute to $\epsilon \times A$ are as follows.

1. Systematic uncertainties affecting both generator level and reconstructed

level distributions are:

  (a) PDFs used in MC samples;
  (b) QED final state radiation (FSR) correction;
  (c) modeling of Z/γ^* boson rapidity shape.

2. Systematic uncertainties affecting reconstructed level distribution are:
   (a) trigger efficiency;
   (b) corrections for electron selection (EMID);
   (c) electron energy scale and resolution.

Detailed discussions for each source of systematic uncertainties are covered below.

5.8.1 PDFs

The PDF set used when generating signal MC samples is CTEQ6.1M. It is defined by twenty orthogonal parameters (eigenvectors), which are shifted separately to their positive and negative 1σ limits, providing a set of 40 PDFs for error determination.

We perform the measurement of $\epsilon \times A$ for MC samples using each of these 40 PDFs. The difference relative to the base PDF can be found in Figure 5.46.

We follow the procedure described in Reference [37] to calculate the overall uncertainty on the $\epsilon \times A$ caused by PDFs. It is determined by:

$$\Delta X = \frac{1}{2}\left(\sum_{i=1}^{20}[X(S_i^+) - X(S_i^-)]^2\right)^{1/2}, \tag{5.5}$$

where X is the $\epsilon \times A$ and $X(S_i^\pm)$ are the $\epsilon \times A$ based on the PDF sets $S_i^\pm$ from the eigenvector basis.

The determined systematic uncertainty, which is plotted as relative uncertainty against boson rapidity, can be found in Figure 5.47. The statistical and systematic uncertainties (all sources combined) of the measured boson rapidity are also shown for comparison purpose.

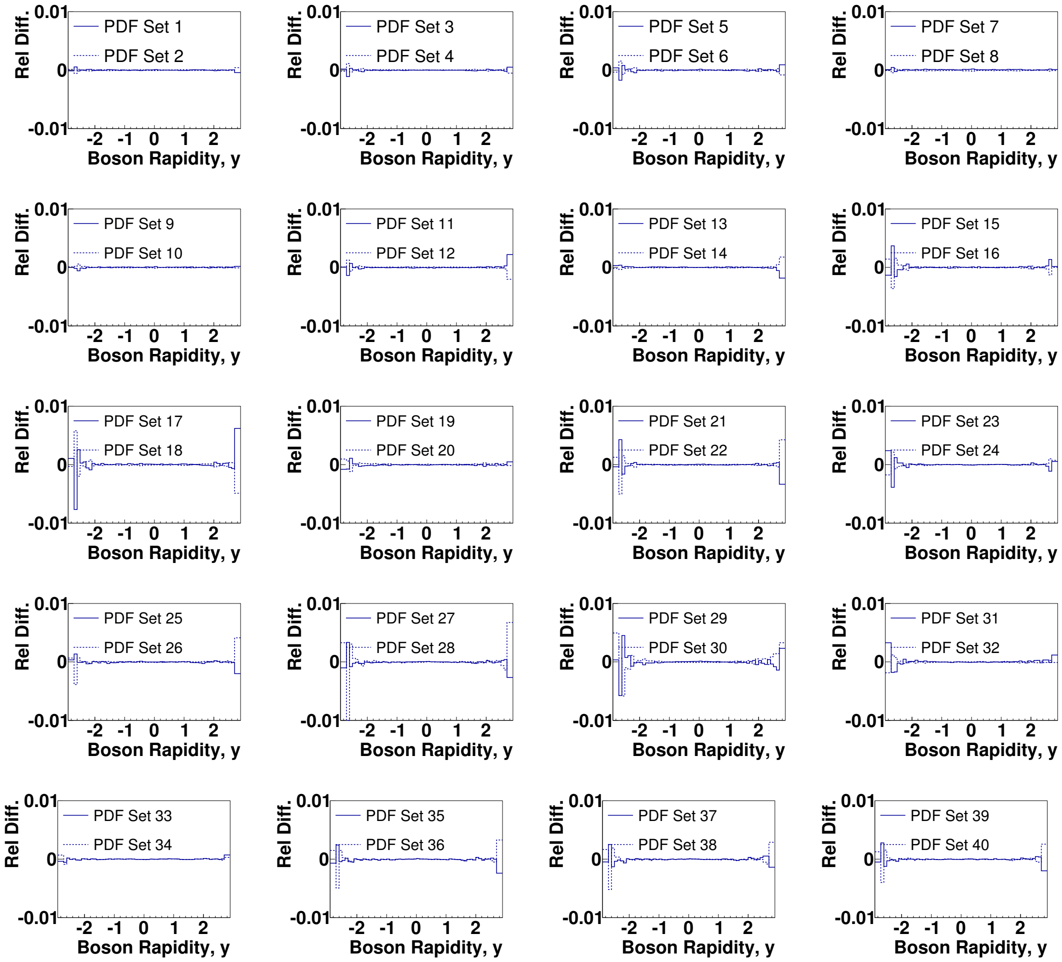

Figure 5.46: The relative difference on $\epsilon \times A$ compared to the base PDF for each error PDF in CTEQ6.1M.

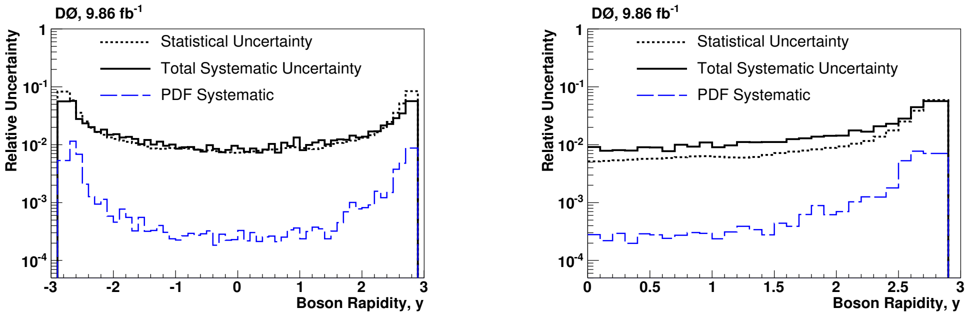

(a) $-2.9 < y < 2.9$ (b) $0 < |y| < 2.9$

Figure 5.47: Relative uncertainty due to the PDFs.

5.8.2 QED FSR

A systematic uncertainty is assigned to take care of the the QED FSR modeling in the MC event generator. It is determined by scaling the number of FSR events, which are events with emitted photons in the final state, by ±20%. The relative changes resulting in the $\epsilon \times A$ as a function of boson rapidity, is taken as the systematic uncertainty. It is relatively a small uncertainty ($\sim 0.2\%$) in this measurement, as shown in Figure 5.48.

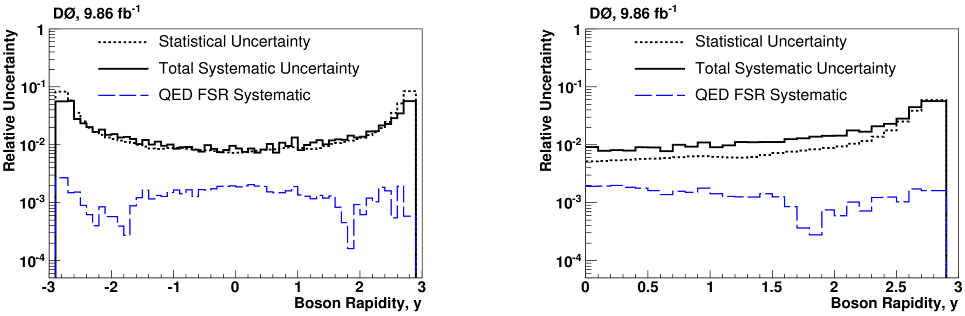

(a) $-2.9 < y < 2.9$ (b) $0 < |y| < 2.9$

Figure 5.48: Relative uncertainty caused by the FSR modeling in MC event generator.

5.8.3 Modeling of Z/γ^* boson rapidity shape

In the reconstructed boson rapidity distributions for CC-EC events, which can be found in Figure 5.42b, the difference between data and MC is found to have a structure dependent on the reconstructed boson rapidity. One possible cause is the underlying modeling of Z/γ^* boson rapidity used in MC event generator.

We reweight both of the generator level and reconstructed level boson rapidity shape by the factor shown in Figure 5.49, which effectively is equivalent to changing the modeling of boson rapidity used in the event generator. This reweighting factor can be obtained by taking the ratio of the generator level distribution from another NLO event generator, such as MC@NLO [36], or simply the unfolded data distribution. to the generator level distribution from ResBos. The structure seen in Figure 5.42b is no longer present after this reweighting has taken place. Instead, a much improved agreement between data and MC is observed. The change of the $\epsilon \times A$ caused by this reweighting factor is then taken as an estimation of this systematic uncertainty. It is shown in Figure 5.50.

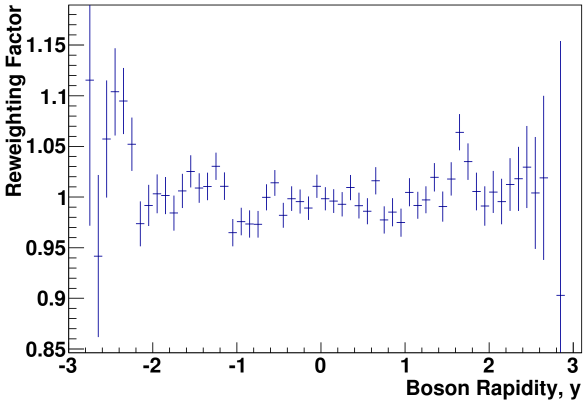

Figure 5.49: Rweighting factor to change the boson rapidity modeling in the event generator, which helps to eliminates data/MC discrepancy in Figure 5.42b.

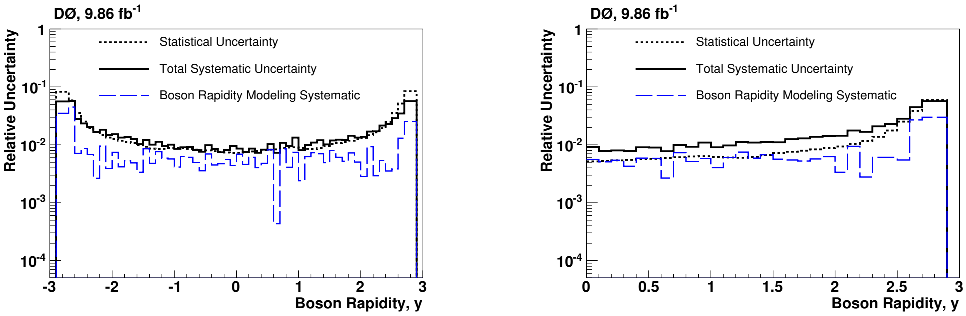

(a) $-2.9 < y < 2.9$ (b) $0 < |y| < 2.9$

Figure 5.50: Relative uncertainty from the modeling of boson rapidity in MC.

5.8.4 Trigger efficiency corrections

We determine the systematic uncertainty from the trigger efficiency correction by varying the measured trigger efficiency ($\epsilon_{trigger}$) by ±1 standard deviation when using it in reciprocal as an event weight ($1/\epsilon_{trigger}$) to MC events.

The systematic uncertainty, shown in Figure 5.51, is determined by the resulting change in $\epsilon \times A$ as a function of boson rapidity.

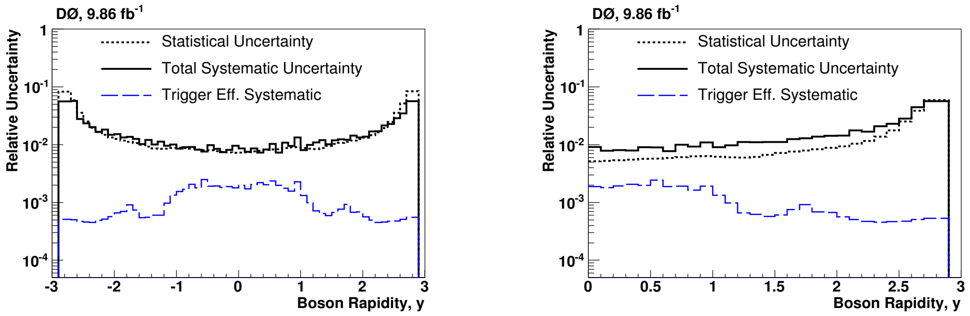

(a) $-2.9 < y < 2.9$

(b) $0 < |y| < 2.9$

Figure 5.51: Relative uncertainty due to the trigger efficiency correction.

5.8.5 Electron selection efficiency corrections

The systematic uncertainty contributed by the corrections of electron selection efficiency consists of two components. One is denoted as the statistical component; the other is denoted as the method component. These two components are treated as non-correlated systematic uncertainties, and thus are added in quadrature when calculating the total systematic uncertainty.

These two components are explained as follows.

- Since the electron efficiency corrections are essentially the scale factors of efficiencies, all of the uncertainties on the measured data/MC efficiencies, would contributed to the systematic uncertainty of the corrections. The method described in [38] is used to determine the uncertainty of the measured efficiency arising from the limited size of the data sample. The resulting systematic uncertainty on the scale factor, which contributes to the uncertainty of $\epsilon \times A$, is denoted as the statistical component.

- The method component of the systematic uncertainty refers to the uncertainty caused by the "tag-and-probe method".

  The background contamination in the tag-probe pairs surely will lead to a biased result of the electron efficiencies. To estimate this contribution, selection cuts are tightened on the tag electron. It reduces the background at the expense of statistical precision. The change of efficiencies measured in data and MC with the "tighter" tag electron is propagated to the $\epsilon \times A$ as a function of boson rapidity. Technically, this is done by following the same procedure described in Section 5.3 and Section 5.4, and re-evaluating the $\epsilon \times A$ with this choice of tag electron. The difference resulting in $\epsilon \times A$ as a function of boson rapidity is taken as an estimation of the systematic uncertainty from this source.

As we know, the "tag-and-probe method" in the efficiency measurement may produce a biased result if the efficiency for the probe electron passing the selection criteria is correlated with that of the tag electron. This correlation in efficiency is mainly caused by the kinematic correlations between the tag and probe electrons. In our case, the systematic uncertainty contributed by this effect is neglected due to these two reasons: 1) the efficiency does not affect the $\epsilon \times A$ directly, since it is estimated from the fully simulated MC samples, only the data/MC scale factors of efficiencies matter in our case; 2) the scale factors we use have included the dependence on the kinematic variables of the probe electron (p_T and η).

The systematic uncertainties for the electron selection efficiency corrections are evaluated separately for the corrections of the preselection efficiency, the Cal-ID efficiency and the tracking efficiency. Each of these is treated as non-correlated systematic uncertainty, and is added in quadrature when calculating the total systematic uncertainty.

Figure 5.52 shows the relative uncertainty for the statistical component, and Figure 5.53 shows that for the method component. The combination of these two components is shown in Figure 5.54.

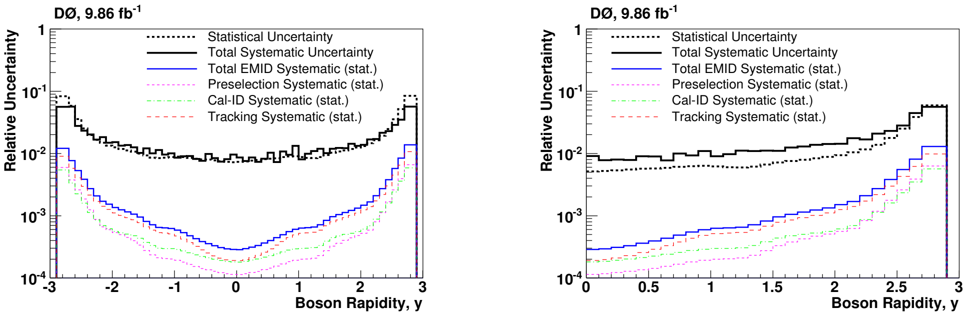

(a) $-2.9 < y < 2.9$ (b) $0 < |y| < 2.9$

Figure 5.52: Relative uncertainty (plotted against boson rapidity) contributed by the electron selection (denoted as EMID in the plots) efficiency corrections (statistical component).

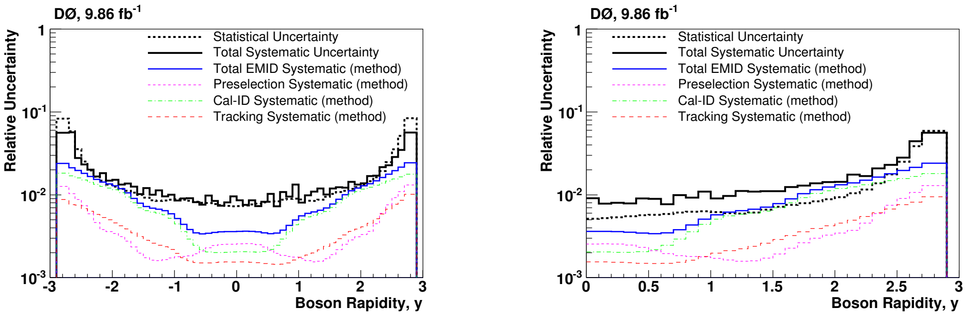

(a) $-2.9 < y < 2.9$ (b) $0 < |y| < 2.9$

Figure 5.53: Relative uncertainty (plotted against boson rapidity) contributed by the EMID efficiency corrections (method component).

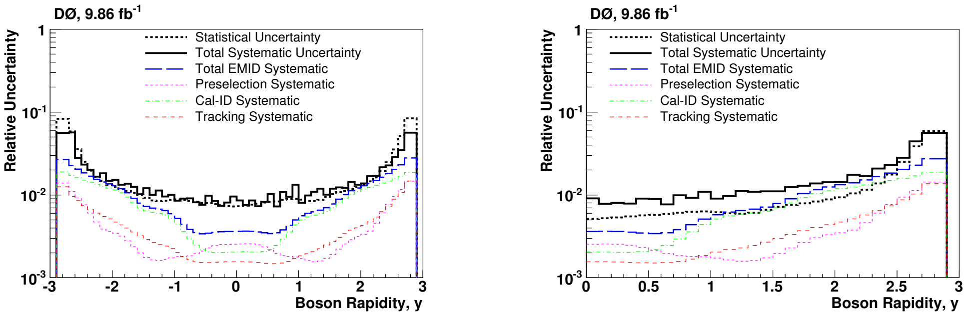

(a) $-2.9 < y < 2.9$ (b) $0 < |y| < 2.9$

Figure 5.54: Relative uncertainty contributed by the EMID efficiency corrections (statistical and method components combined).

5.8.6 Electron energy scale and resolution

The energy scale for electrons in MC is corrected to match the observed Z boson pole position. The statistical uncertainties of the calibration parameters applied to MC in this correction are considered as a source of systematic uncertainty to the $\epsilon \times A$. This is estimated by varying each of the parameters by ± 1 standard deviation. The relative changes resulting in $\epsilon \times A$ are taken as the systematic uncertainty. Figure 5.55 shows the corresponding relative uncertainty as a function of boson rapidity.

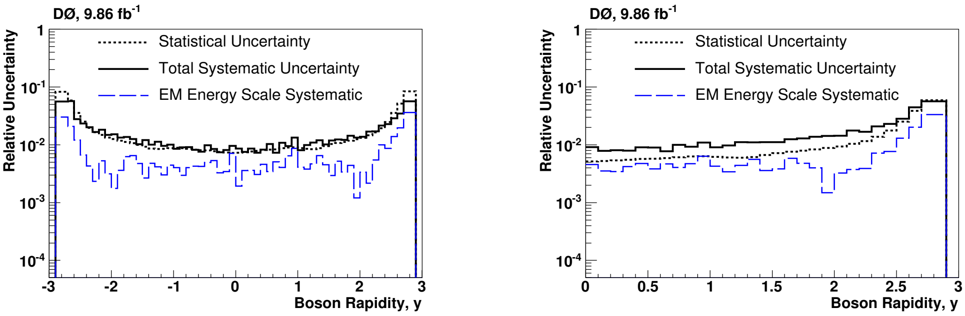

(a) $-2.9 < y < 2.9$ (b) $0 < |y| < 2.9$

Figure 5.55: Relative uncertainty from electron energy scale.

The electron energy resolution is corrected mainly to match the observed Z boson pole width. A procedure similar to that described above is followed. Figure 5.56 shows the determined relative uncertainty.

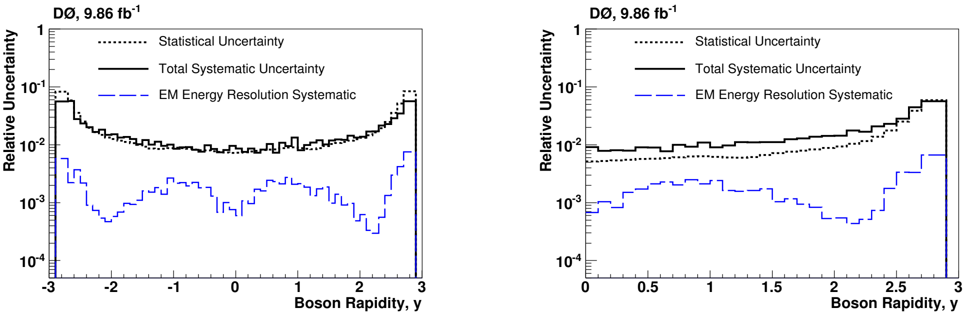

(a) $-2.9 < y < 2.9$ (b) $0 < |y| < 2.9$

Figure 5.56: Relative uncertainty from electron energy smear.

5.8.7 Other sources of systematic uncertainties on $\epsilon \times A$

Additional sources of systematic uncertainties on $\epsilon \times A$ are introduced to take care of residual discrepancies found between data and MC. These uncertainties are obtained by brutally introducing a reweighting factor to the reconstructed level events, which eliminates the discrepancies; the propagated change of $\epsilon \times A$ as a function of boson rapidity is then taken as the systematic uncertainty. This is likely to be an overestimation of the systematic uncertainty.

The residual discrepancies found in the distribution of M_{ee} and reconstructed boson p_T are considered. Part of these discrepancies may have been taken care of by introducing other systematic uncertainties, e.g. those from electron efficiency corrections, electron energy scale and resolution. Thus the determined systematic uncertainties are likely to be overestimated. However they provide a relatively small contribution to the overall systematic uncertainty. Therefor further detailed study is not necessary at this point. These systematic uncertainties can be found in Figure 5.57 (for boson p_T) and Figure 5.58 (for M_{ee}).

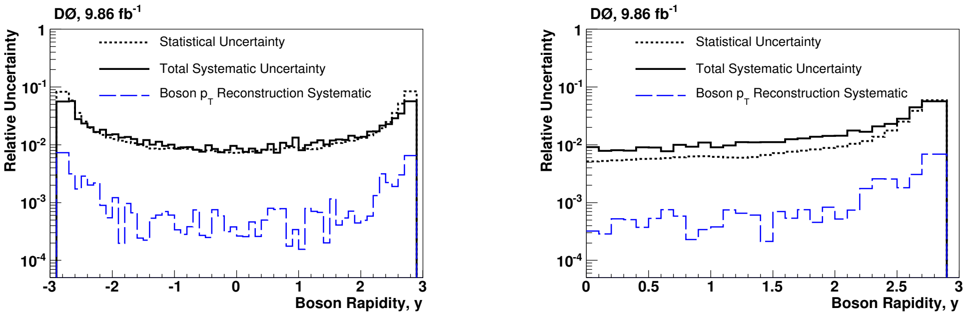

(a) $-2.9 < y < 2.9$ (b) $0 < |y| < 2.9$

Figure 5.57: Systematic uncertainty (shown as relative uncertainty against boson rapidity) assigned for the discrepancies in the reconstructed boson p_T between data and MC.

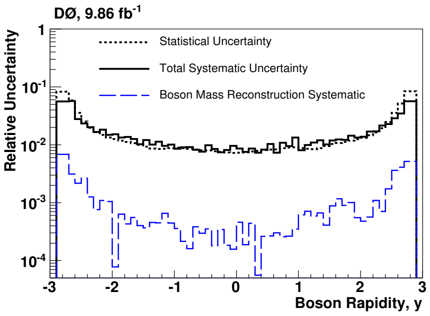

(a) $-2.9 < y < 2.9$ (b) $0 < |y| < 2.9$

Figure 5.58: Systematic uncertainty (shown as relative uncertainty against boson rapidity) assigned for the discrepancies in the reconstructed boson mass M_{ee} between data and MC.

5.8.8 Background systematic

Lastly, the systematic uncertainty from the background estimation is studied. The uncertainty due to the QCD multijet background are determined by varying the the reversed electron shower shape requirements when selecting the background enriched sample from data.

For the other backgrounds, which are estimated from MC samples, the systematic uncertainty of luminosity (6.1%) and that of the cross section used for normalization are considered. Since the level of these backgrounds are quite small, the systematic uncertainties from these backgrounds are found to be rather small. The uncertainty from background estimation is shown in Figure 5.59.

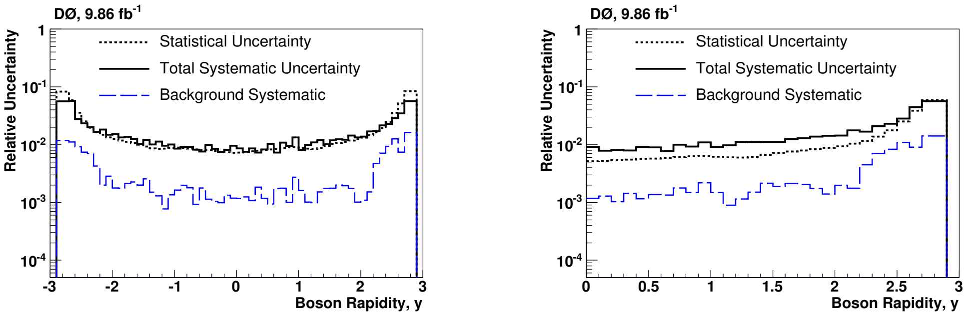

(a) $-2.9 < y < 2.9$ (b) $0 < |y| < 2.9$

Figure 5.59: Relative uncertainty contributed by the background estimation.

5.8.9 Summary of the systematic uncertainties

Each source of systematic uncertainties discussed previously is considered to be uncorrelated with each other, but each has a bin-to-bin correlation in boson rapidity. They are added in quadrature to give the total systematic uncertainties for each bin of boson rapidity . The total systematic uncertainty is found to be at the same level as the statistical uncertainty, as shown in Figure 5.60.

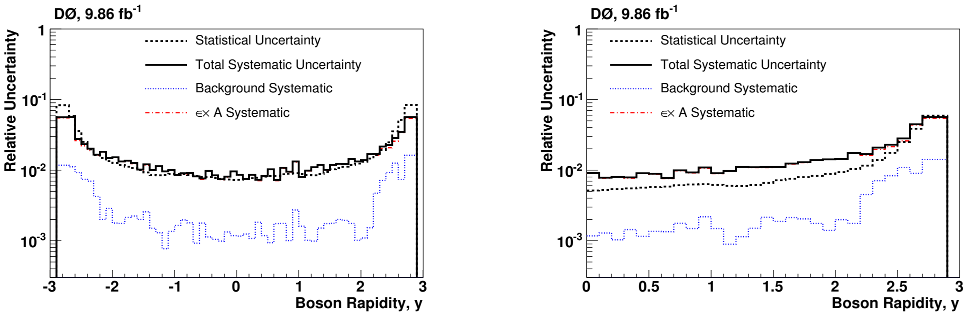

(a) $-2.9 < y < 2.9$ (b) $0 < |y| < 2.9$

Figure 5.60: Relative uncertainties plotted against boson rapidity.

Different sources of systematic uncertainties are compared together in Figure 5.61 and Figure 5.62.

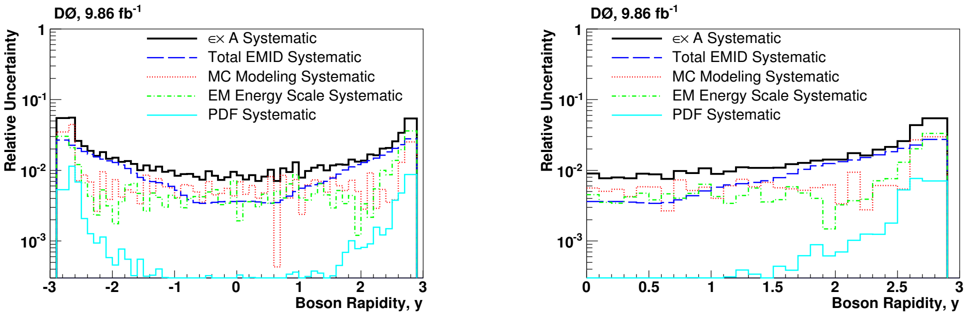

(a) $-2.9 < y < 2.9$ (b) $0 < |y| < 2.9$

Figure 5.61: Relative uncertainties plotted against boson rapidity for EMID efficiency corrections, boson rapidity modeling, electron energy scale and PDFs systematic. Total systematic uncertainty of $\epsilon \times A$ is shown for comparison purpose.

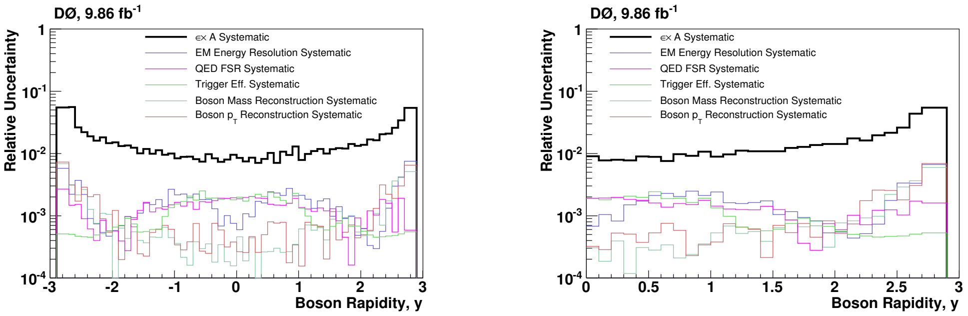

(a) $-2.9 < y < 2.9$

(b) $0 < |y| < 2.9$

Figure 5.62: Relative uncertainties plotted against boson rapidity for other sources of systematic uncertainties, which are not shown in Figure 5.61. Total systematic uncertainty of $\epsilon \times A$ is shown for comparison purpose.

The main contributions to the systematic uncertainties in this measurement are found to be from the EMID corrections, electron energy scale and the underlying boson rapidity modeling in the MC event generator.

In Figure 5.63, comparisons of the relative uncertainties (systematic and statistical uncertainties combined) are made between the current result with the previously published CDF and D0 results. The relative uncertainties due to CT10 NLO PDFs used for a NLO calculation is also shown for comparison purpose. It is calculated by following the same procedure describe in Section 5.8.1. The uncertainties in the high boson rapidity region are much improved, for which, when compared with previous CDF (D0) result, the relative uncertainty in the last bin of boson rapidity drops down from $\sim 30\%$ ($\sim 42\%$) to $\sim 10\%$. Figure 5.64 compares current result with the previously published CDF 2.1 fb^{-1} result.

The measured $\epsilon \times A$ in bins of $|y|$ are shown in Table 5.4 together with the estimated systematic uncertainties. Results in bins of y can be found in Appendix B.1.

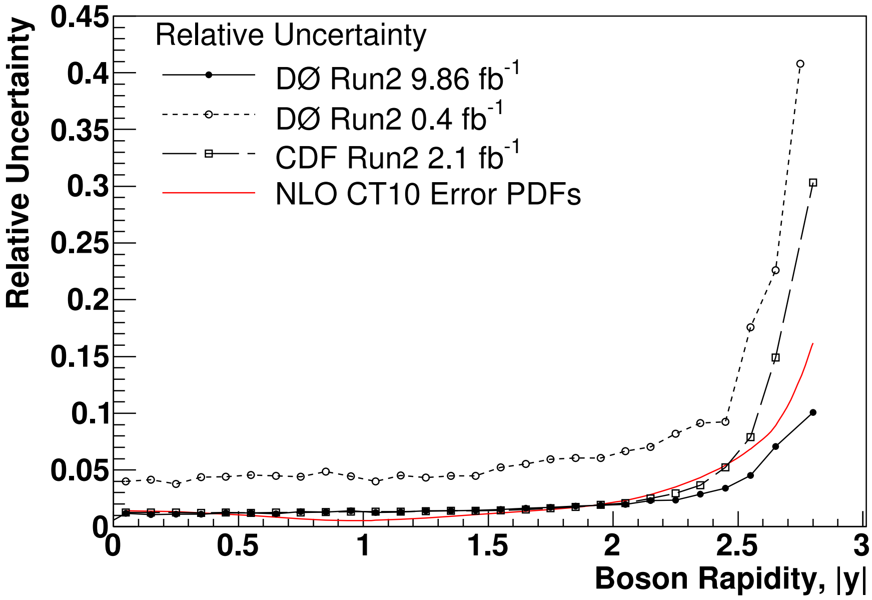

Figure 5.63: Relative uncertainties from this measurement and from the previous CDF and D0 result. PDF uncertainty on the boson rapidity shape using the CT10 NLO uncertainty PDF sets is also shown for comparison purpose.

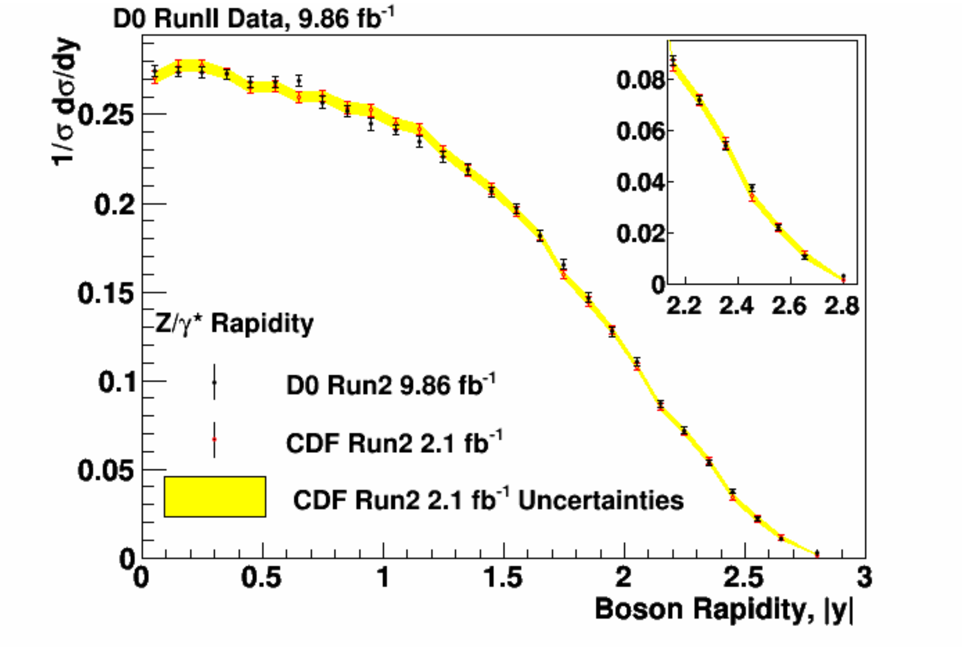

Figure 5.64: Comparison between the current measurement with the CDF 2.1 fb^{-1} measurement of $\frac{1}{\sigma} \times \frac{d\sigma}{dy}$ (statistical and systematic uncertainties combined) vs $|y|$.

$\lvert y\rvert$	$\epsilon\times$ A	δ(total)	$\delta(e^{-}s.f.)$		δ (E scale)	δ (PDF)	δ(y modeling)
			stat.	method			
0.05	0.2770	±0.0023	±0.0001	±0.0010	±0.0013	±0.0001	±0.0013
0.15	0.2673	±0.0021	±0.0001	±0.0010	±0.0009	±0.0001	±0.0014
0.25	0.2537	±0.0020	±0.0001	±0.0009	±0.0009	±0.0001	±0.0014
0.35	0.2427	±0.0020	±0.0001	±0.0009	±0.0010	±0.0000	±0.0012
0.45	0.2316	±0.0021	±0.0001	±0.0008	±0.0011	±0.0001	±0.0014
0.55	0.2252	±0.0017	±0.0001	±0.0008	±0.0009	±0.0001	±0.0009
0.65	0.2160	±0.0021	±0.0001	±0.0008	±0.0010	±0.0001	±0.0015
0.75	0.2100	±0.0017	±0.0001	±0.0008	±0.0009	±0.0001	±0.0010
0.85	0.2044	±0.0020	±0.0001	±0.0009	±0.0010	±0.0001	±0.0012
0.95	0.2074	±0.0022	±0.0001	±0.0011	±0.0013	±0.0001	±0.0011
1.05	0.2211	±0.0021	±0.0001	±0.0013	±0.0009	±0.0001	±0.0012
1.15	0.2432	±0.0021	±0.0002	±0.0015	±0.0008	±0.0001	±0.0010
1.25	0.2561	±0.0025	±0.0002	±0.0017	±0.0011	±0.0001	±0.0014
1.35	0.2483	±0.0027	±0.0002	±0.0017	±0.0014	±0.0001	±0.0014
1.45	0.2231	±0.0022	±0.0002	±0.0016	±0.0008	±0.0001	±0.0011
1.55	0.2020	±0.0022	±0.0002	±0.0016	±0.0008	±0.0001	±0.0012
1.65	0.1977	±0.0024	±0.0002	±0.0018	±0.0012	±0.0001	±0.0009
1.75	0.2014	±0.0026	±0.0002	±0.0021	±0.0010	±0.0001	±0.0010
1.85	0.2081	±0.0030	±0.0003	±0.0024	±0.0008	±0.0002	±0.0015
1.95	0.2166	±0.0029	±0.0003	±0.0027	±0.0003	±0.0001	±0.0008
2.05	0.2228	±0.0033	±0.0003	±0.0029	±0.0007	±0.0002	±0.0013
2.15	0.2299	±0.0035	±0.0004	±0.0032	±0.0008	±0.0002	±0.0010
2.25	0.2221	±0.0038	±0.0005	±0.0033	±0.0009	±0.0003	±0.0015
2.35	0.2087	±0.0040	±0.0006	±0.0034	±0.0015	±0.0003	±0.0011
2.45	0.1852	±0.0037	±0.0007	±0.0032	±0.0014	±0.0003	±0.0005
2.55	0.1497	±0.0040	±0.0008	±0.0030	±0.0020	±0.0008	±0.0012
2.65	0.1313	±0.0043	±0.0011	±0.0029	±0.0027	±0.0010	±0.0005
2.8	0.0939	±0.0044	±0.0013	±0.0023	±0.0032	±0.0007	±0.0004
2.90	-	-	-	-	-	-	

Table 5.4: Values of $\epsilon \times A$ together with contributions to the systematic uncertainty for $\epsilon \times A$ in bins of $|y|$.

5.9 Results

Since the direction of the magnetic filed used at D0 is reversed periodically, the events contribute to the $y < 0$ region are fully compatible with those to the $y > 0$ region. Therefore, the negative and positive bins can be combined to improve the statistical uncertainty. Table 5.5 lists the the values for the normalized cross section, $\frac{1}{\sigma} \times \frac{d\sigma}{dy}$, for the center of each $|y|$ bin. Results for each y bin before combing the positive and negative bins can be found in Appendix B.2.

$\|y\|$	$\frac{1}{\sigma} \times \frac{d\sigma}{dy} \pm stat. \pm syst.$	Candidate events	Background events	$\epsilon \times A$
0.05	$0.2746 \pm 0.0014 \pm 0.0023$	38,917	453.2 ± 45.1	0.2769 ± 0.0023
0.15	$0.2741 \pm 0.0014 \pm 0.0022$	37,865	459.2 ± 48.2	0.2698 ± 0.0021
0.25	$0.2737 \pm 0.0015 \pm 0.0022$	36,074	513.9 ± 36.7	0.2575 ± 0.0020
0.35	$0.2727 \pm 0.0015 \pm 0.0022$	34,284	491.4 ± 48.6	0.2456 ± 0.0020
0.45	$0.2685 \pm 0.0015 \pm 0.0025$	32,410	521.2 ± 36.8	0.2358 ± 0.0021
0.55	$0.2685 \pm 0.0015 \pm 0.0020$	31,543	521.2 ± 42.3	0.2295 ± 0.0017
0.65	$0.2688 \pm 0.0016 \pm 0.0026$	30,449	515.6 ± 40.2	0.2213 ± 0.0021
0.75	$0.2570 \pm 0.0016 \pm 0.0021$	28,333	556.7 ± 49.3	0.2154 ± 0.0017
0.85	$0.2518 \pm 0.0016 \pm 0.0024$	26,940	541.7 ± 39.3	0.2090 ± 0.0020
0.95	$0.2446 \pm 0.0015 \pm 0.0026$	26,353	529.2 ± 56.3	0.2105 ± 0.0022
1.05	$0.2414 \pm 0.0015 \pm 0.0023$	27,486	575.5 ± 39.9	0.2225 ± 0.0021
1.15	$0.2348 \pm 0.0014 \pm 0.0020$	29,088	606.5 ± 25.4	0.2421 ± 0.0021
1.25	$0.2258 \pm 0.0013 \pm 0.0022$	29,620	564.3 ± 33.2	0.2562 ± 0.0025
1.35	$0.2189 \pm 0.0013 \pm 0.0024$	28,072	575.3 ± 41.5	0.2505 ± 0.0027
1.45	$0.2063 \pm 0.0014 \pm 0.0020$	24,060	531.9 ± 50.7	0.2278 ± 0.0022
1.55	$0.1969 \pm 0.0014 \pm 0.0021$	20,727	505.9 ± 38.1	0.2057 ± 0.0022
1.65	$0.1819 \pm 0.0014 \pm 0.0022$	18,639	502.5 ± 38.5	0.2002 ± 0.0024
1.75	$0.1656 \pm 0.0013 \pm 0.0021$	17,149	505.2 ± 33.9	0.2024 ± 0.0026
1.85	$0.1466 \pm 0.0012 \pm 0.0021$	15,619	519.5 ± 26.5	0.2081 ± 0.0030
1.95	$0.1275 \pm 0.0011 \pm 0.0017$	14,012	499.5 ± 18.9	0.2147 ± 0.0029
2.05	$0.1107 \pm 0.0010 \pm 0.0017$	12,458	430.5 ± 23.8	0.2199 ± 0.0033
2.15	$0.0871 \pm 0.0009 \pm 0.0014$	10,134	375.9 ± 17.2	0.2273 ± 0.0035
2.25	$0.0719 \pm 0.0008 \pm 0.0013$	8,066	255.1 ± 35.0	0.2193 ± 0.0038
2.35	$0.0540 \pm 0.0007 \pm 0.0011$	5,662	164.0 ± 38.8	0.2050 ± 0.0040
2.45	$0.0375 \pm 0.0007 \pm 0.0008$	3,461	99.3 ± 28.1	0.1801 ± 0.0037
2.55	$0.0221 \pm 0.0006 \pm 0.0006$	1,706	46.9 ± 18.1	0.1509 ± 0.0040
2.65	$0.0106 \pm 0.0004 \pm 0.0004$	723	20.6 ± 6.3	0.1337 ± 0.0043
2.8	$0.0031 \pm 0.0002 \pm 0.0001$	311	7.7 ± 4.3	0.0969 ± 0.0044
2.90	-	-	-	-

Table 5.5: Summary of the measurement of $\frac{1}{\sigma}\frac{d\sigma}{dy}$ per rapidity bin for $Z/\gamma^* \to e^+e^-$events with mass $66 < M_{ee} < 116$ GeV.

We compared the measured results with QCD predictions using different PDFs. Comparisons are shown in Figure 5.65. The PDF sets used for various QCD predictions, obtained from the NLO generator ResBos, are listed as follows.

1. CTEQ6.1M [26],

2. CTEQ6.6M [39],
3. CT10 NLO [40],
4. MSTW2008 NLO [41];

The ratio of the measured results to the QCD predictions are also provide in Figure 5.66. Statistical and systematic uncertainties are all considered. Though, the QCD predictions are found to agree well with the data, with $\chi^2/d.o.f$ in the range of $[25/28, 37/28]$ [1], discrepancies can be found in the region of $|y| > 2.5$. This is the region where larger uncertainties from the current QCD predictions are found. Thus the current result provides a valuable input for the future development of QCD predictions. By including this latest result, the QCD predictions are expected to be considerably improved especially in the $|y| > 2.5$ region.

---

[1] The correlations between each source of the systematic uncertainties in different y bins are included in the χ^2 comparison. The method used to calculate $\chi^2/d.o.f$, when considering both statistical and systematic uncertainties, can be found in Reference [42].

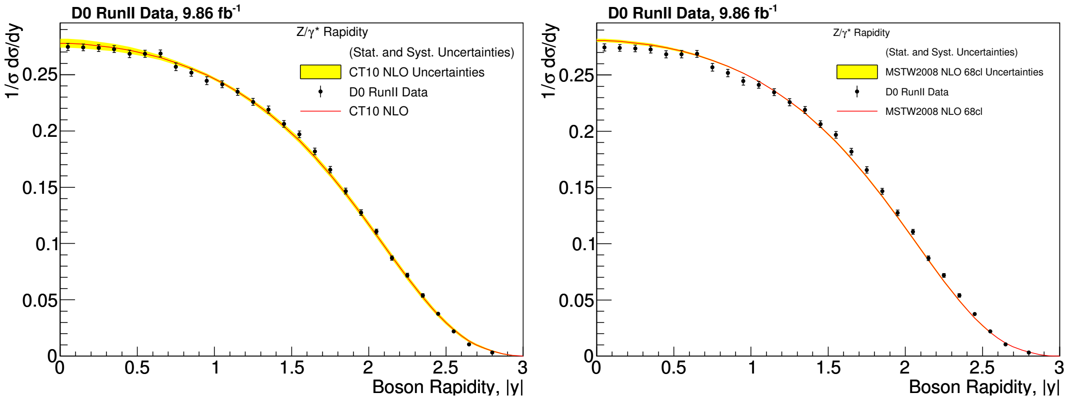

(a) CT10 NLO (b) MRST2008 NLO

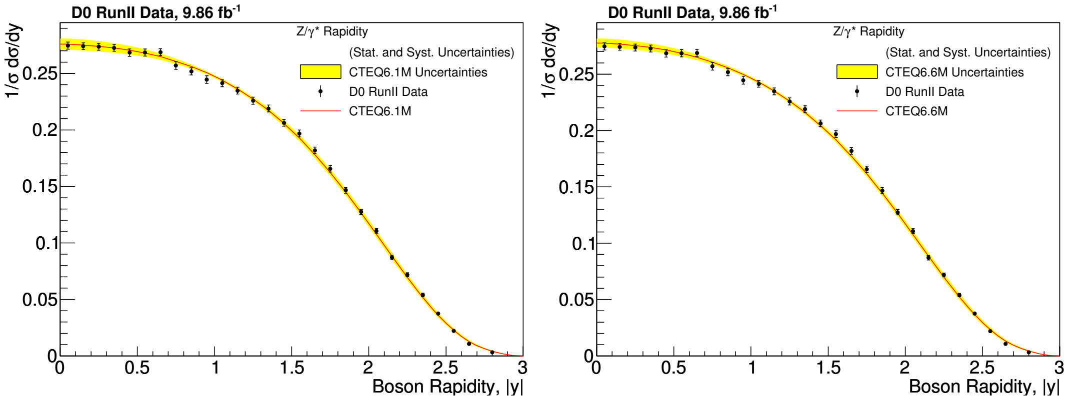

(c) CTEQ6.1M (d) CTEQ6.6M

Figure 5.65: Comparison between the current measurement of $\frac{1}{\sigma} \times \frac{d\sigma}{dy}$ (statistical and systematic uncertainties combined) vs $|y|$ with NLO QCD predictions provided by ResBos. The yellow bands corresponds to the PDF uncertainties in the theoretical predications.

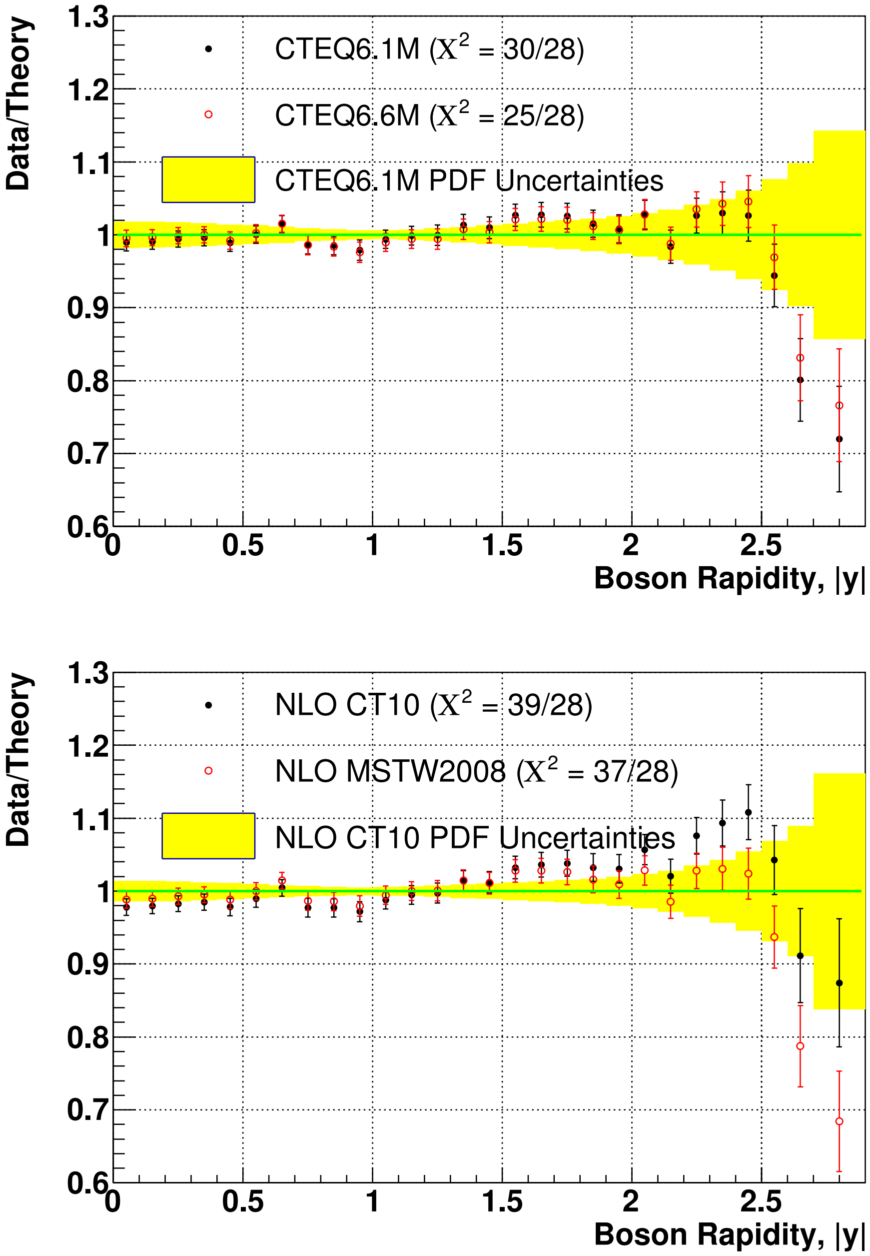

Figure 5.66: The ratio of the current measurement of $\frac{1}{\sigma} \times \frac{d\sigma}{dy}$ to the theoretical QCD predictions. The yellow bands corresponds to the PDF uncertainties in the theoretical predications.

Appendix A

Supplementary plots

A.1 MC corrections in Run2a and Run2b-12

A.1.1 Electron preselection efficiency

The electron preselection efficiencies and scale factor for Run2a and Run2b-12 subset (Figure A.1 - A.6) are shown in this section. These are the same sets of plots as in Section 5.3.2.

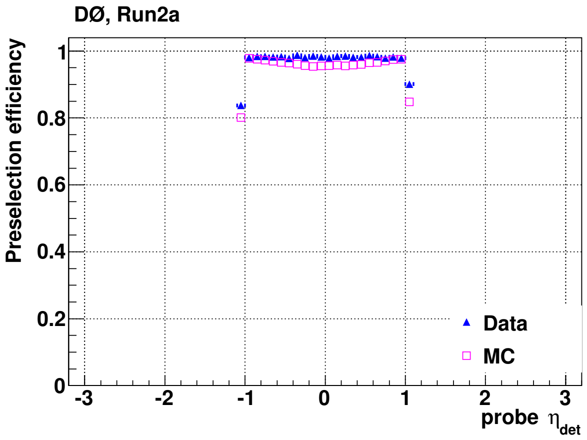

Figure A.1: Electron preselection efficiency in the CC for Run2a data and MC events.

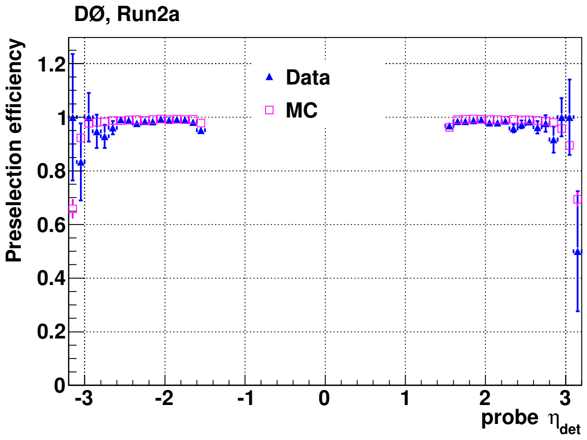

Figure A.2: Electron preselection efficiency in the EC for Run2a data and MC events.

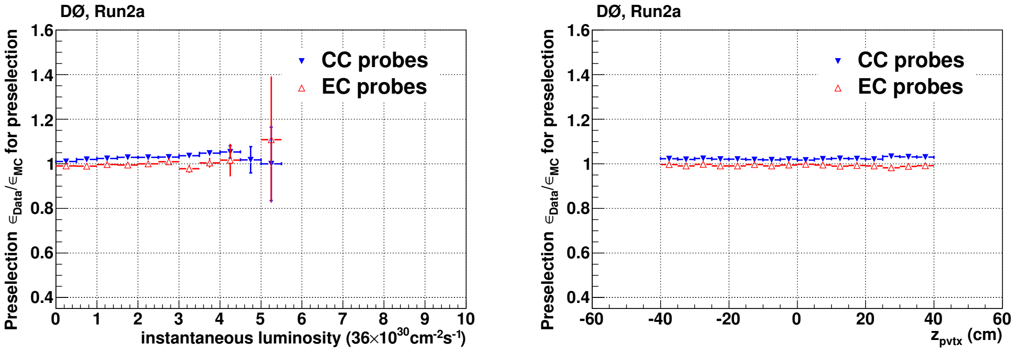

(a) s.f vs. L_{inst}

(b) s.f vs. z_{pvtx}

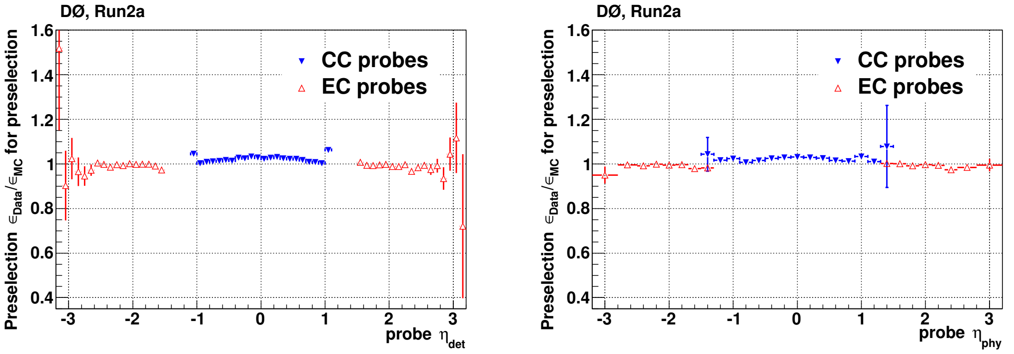

(c) s.f vs. η_{det} of probe electron

(d) s.f vs. η_{phy} of probe electron

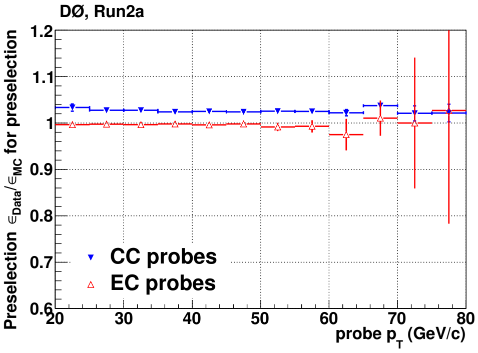

(e) s.f vs. p_T of probe electron

Figure A.3: Scale factors (s.f.) for electron preselection efficiency between Run2a data and MC.

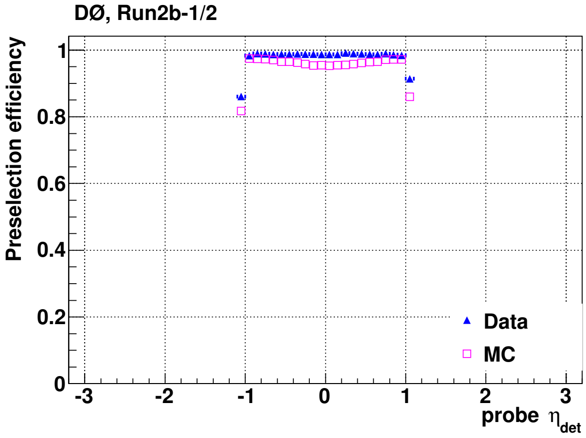

Figure A.4: Electron preselection efficiency in the CC for Run2b-12 data and MC events.

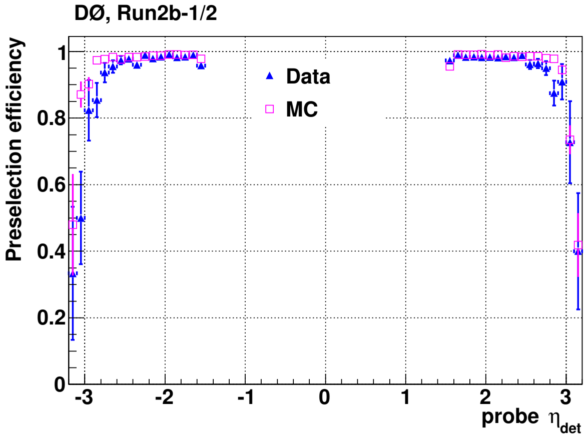

Figure A.5: Electron preselection efficiency in the EC for Run2b-12 data and MC events.

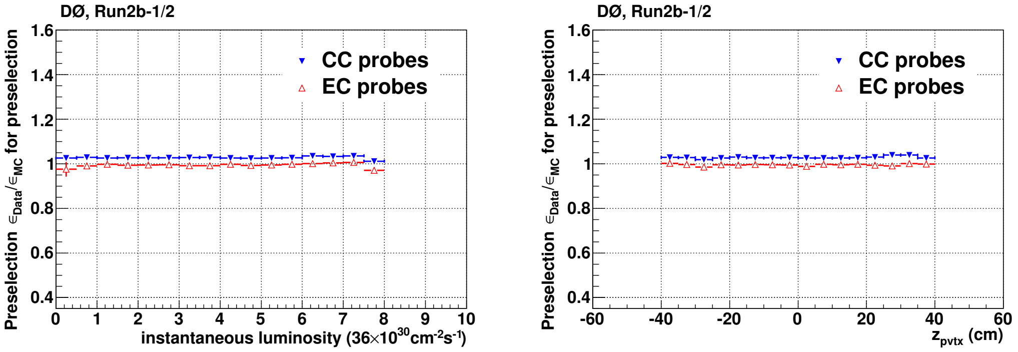

(a) s.f vs. L_{inst} (b) s.f vs. z_{pvtx}

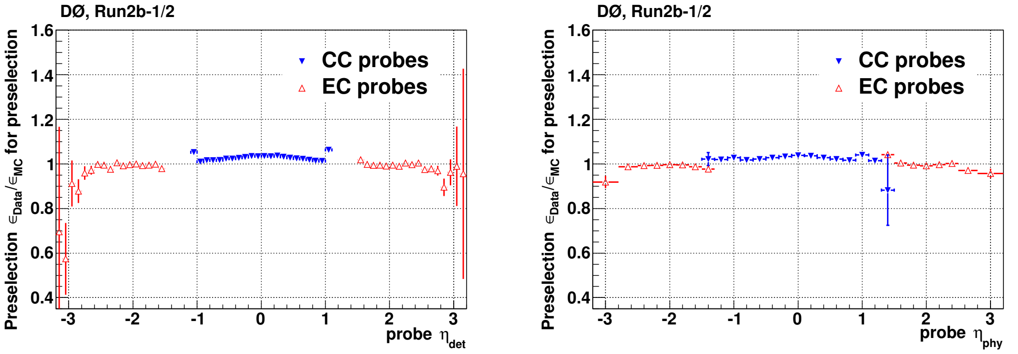

(c) s.f vs. η_{det} of probe electron (d) s.f vs. η_{phy} of probe electron

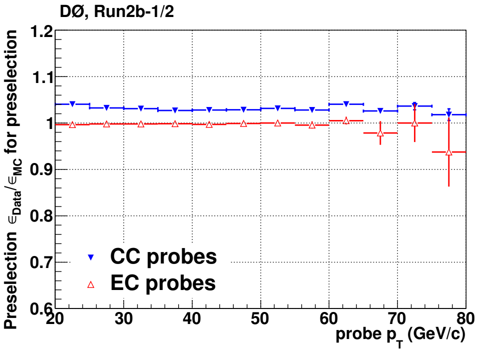

(e) s.f vs. p_T of probe electron

Figure A.6: Scale factors (s.f.) for electron preselection efficiency between Run2b-12 data and MC.

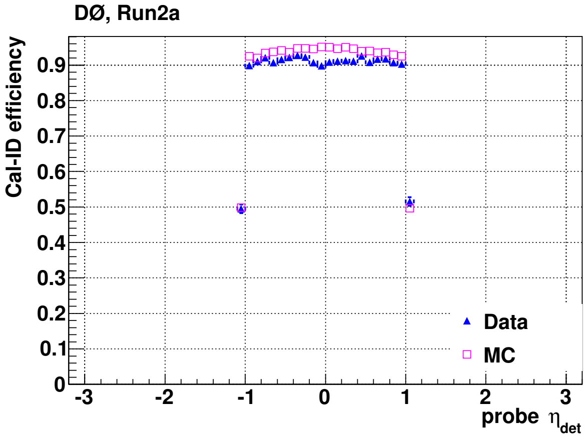

Figure A.7: Electron Cal-ID efficiency vs. electron η_{det} in the CC for Run2a data and MC events.

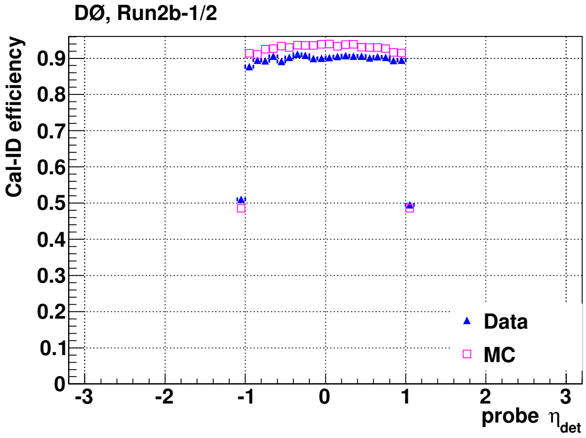

Figure A.8: Electron Cal-ID efficiency vs. electron η_{det} in the CC for Run2b-12 data and MC events.

A.1.2 The Cal-ID efficiency

The Cal-ID efficiency and scale factor for Run2a and Run2b-12 subset (Figure A.7 - A.20) are shown in this section. These are the same sets of plots as in Section 5.3.2.

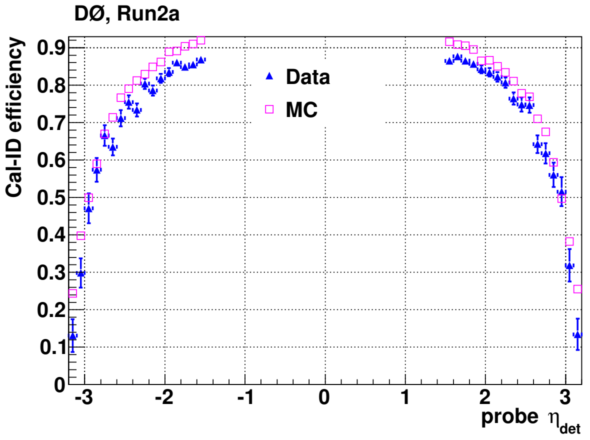

Figure A.9: Electron Cal-ID efficiency vs. electron η_{det} in the EC for Run2a data and MC events.

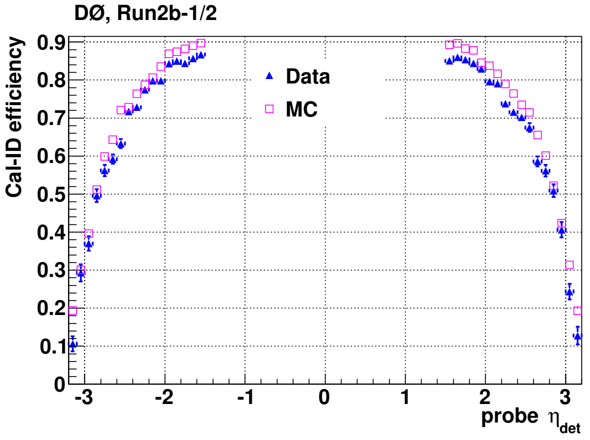

Figure A.10: Electron Cal-ID efficiency vs. electron η_{det} in the EC for Run2b-12 data and MC events.

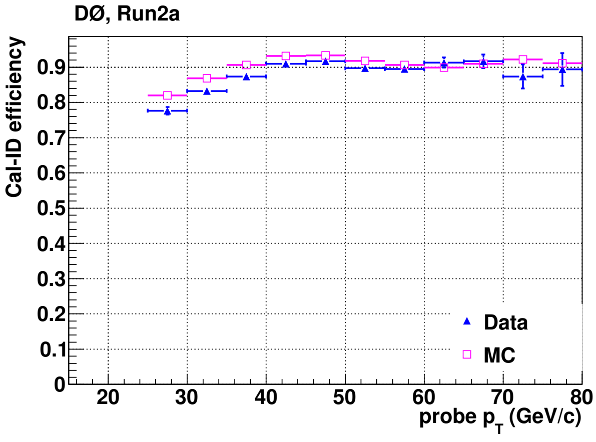

Figure A.11: Electron Cal-ID efficiency vs. electron p_T in the CC for Run2a data and MC events.

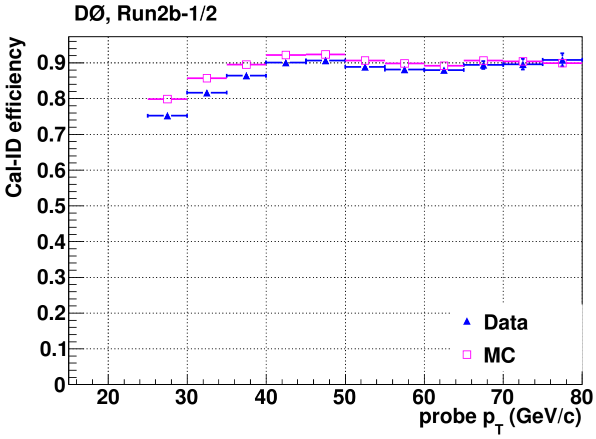

Figure A.12: Electron Cal-ID efficiency vs. electron p_T in the CC for Run2b-12 data and MC events.

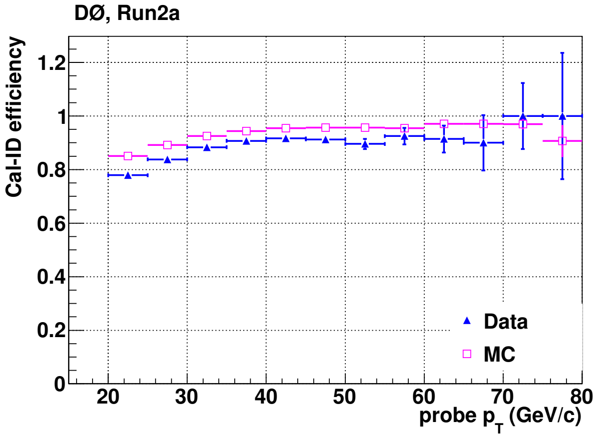

Figure A.13: Electron Cal-ID efficiency vs. electron p_T in the EC for Run2a data and MC events.

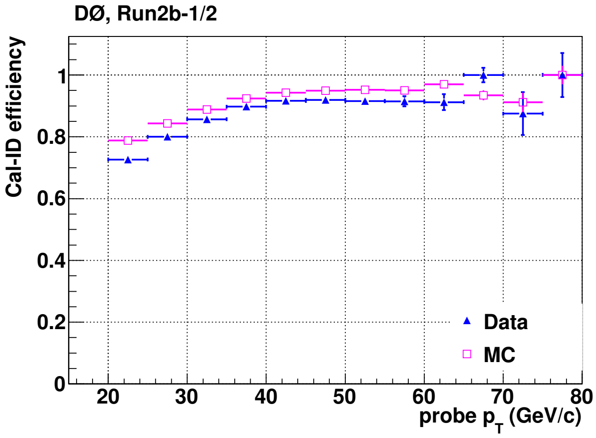

Figure A.14: Electron Cal-ID efficiency vs. electron p_T in the EC for Run2b-12 data and MC events.

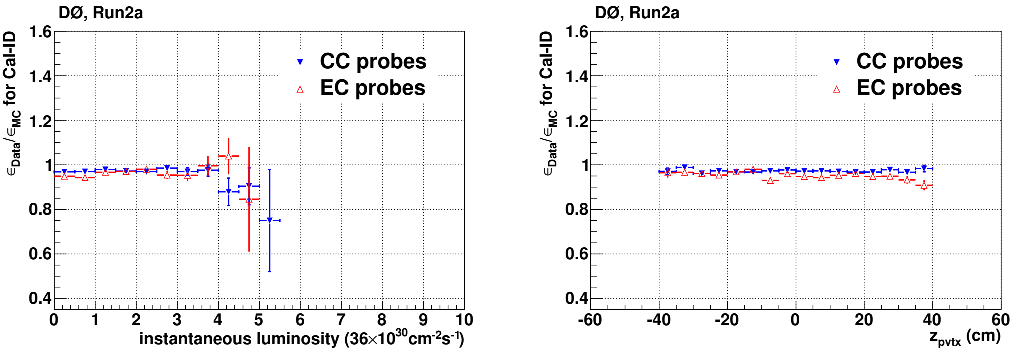

(a) s.f vs. L_{inst} (b) s.f vs. z_{pvtx}

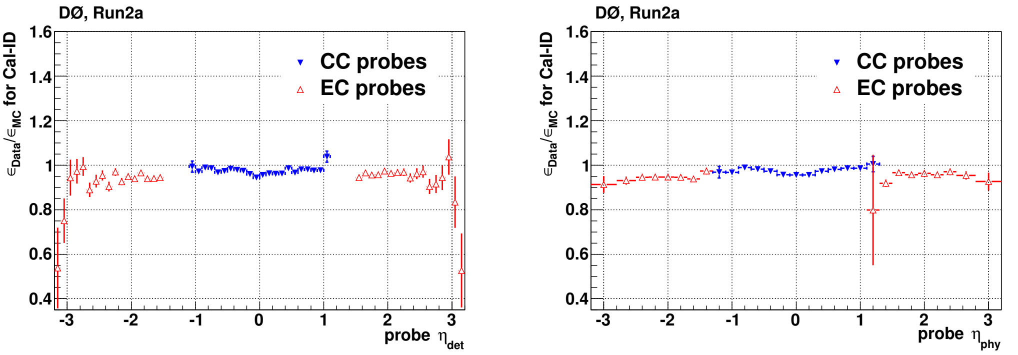

(c) s.f vs. η_{det} of probe electron (d) s.f vs. η_{phy} of probe electron

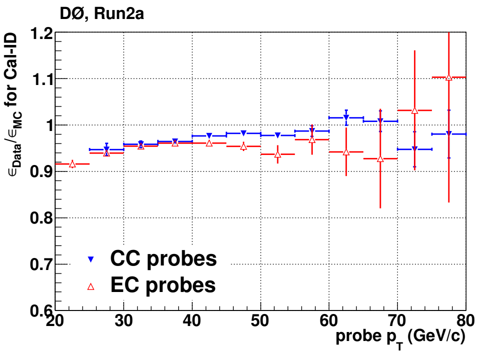

(e) s.f vs. p_T of probe electron

Figure A.15: First order scale factors (s.f.) for electron Cal-ID efficiency between Run2a data and MC.

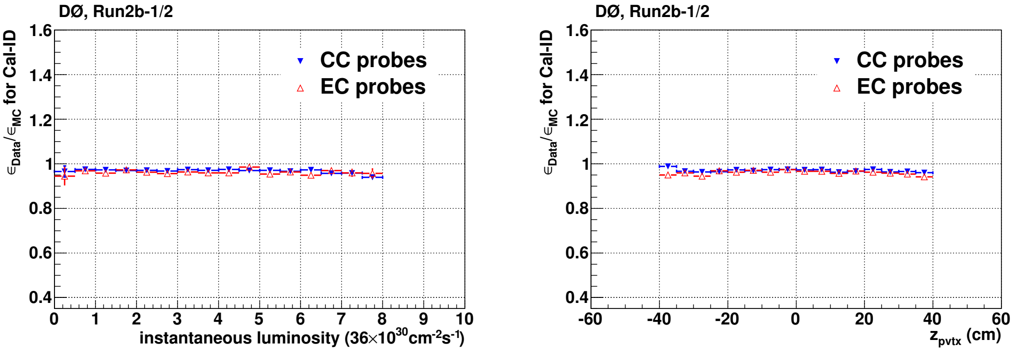

(a) s.f vs. L_{inst} (b) s.f vs. z_{pvtx}

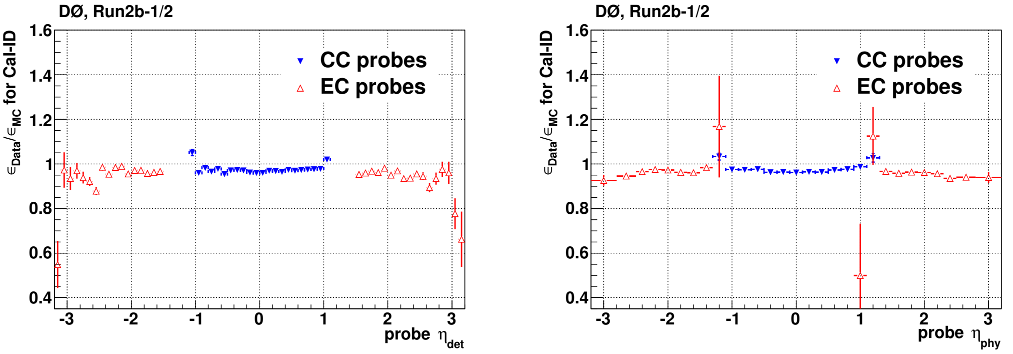

(c) s.f vs. η_{det} of probe electron (d) s.f vs. η_{phy} of probe electron

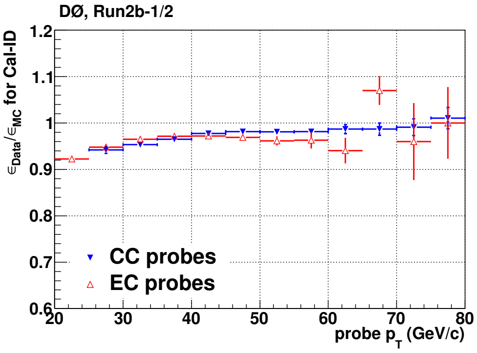

(e) s.f vs. p_T of probe electron

Figure A.16: First order scale factors (s.f.) for electron Cal-ID efficiency between Run2b-12 data and MC.

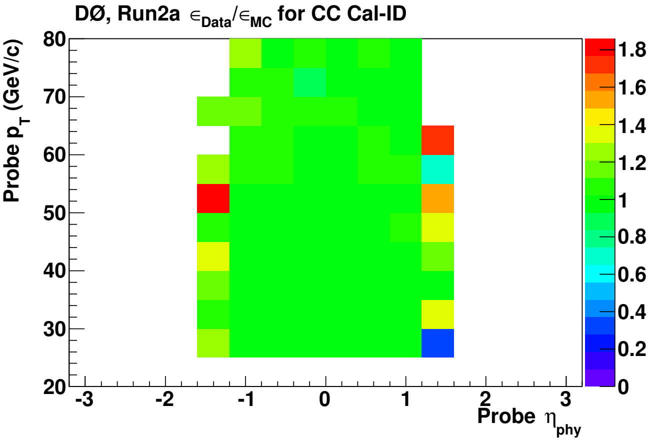

Figure A.17: Second order scale factors for electron Cal-ID efficiency vs. electron p_T and electron η_{phy} in the CC for Run2a data and MC events.

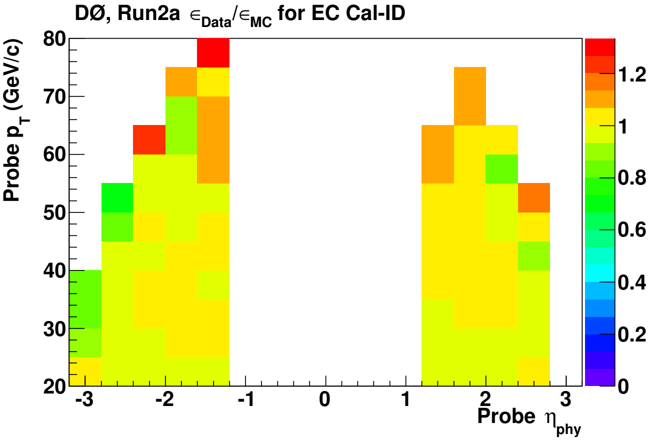

Figure A.18: Second order scale factors for electron Cal-ID efficiency vs. electron p_T and electron η_{phy} in the EC for Run2a data and MC events.

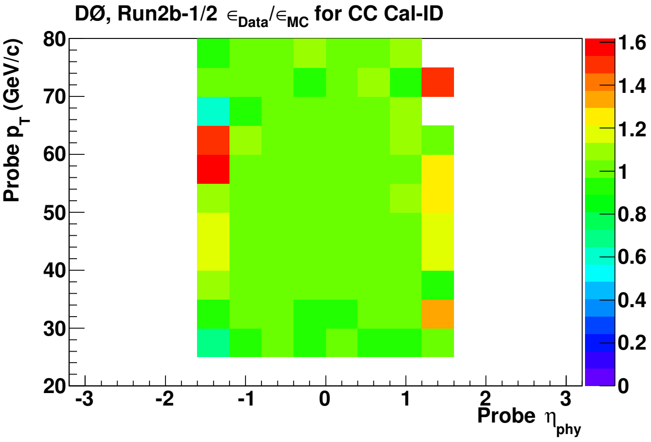

Figure A.19: Second order scale factors for electron Cal-ID efficiency vs. electron p_T and electron η_{phy} in the CC for Run2b-12 data and MC events.

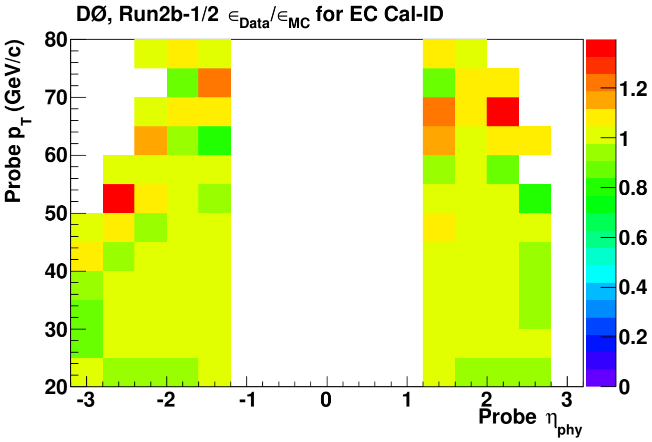

Figure A.20: Second order scale factors for electron Cal-ID efficiency vs. electron p_T and electron η_{phy} in the EC for Run2b-12 data and MC events.

A.1.3 The tracking efficiency

The tracking efficiency and scale factor for Run2a and Run2b-12 subset (Figure A.21 - A.32) are shown in this section. These are the same sets of plots as in Section 5.3.2.

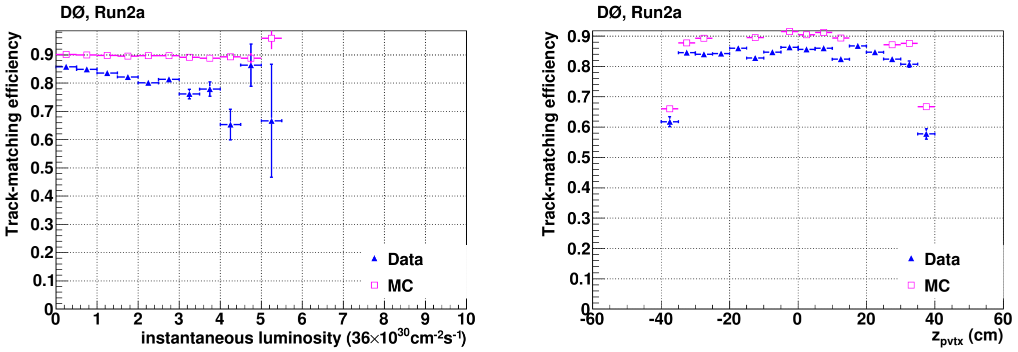

(a) ϵ_{CCtrk} vs. L_{inst} (b) ϵ_{CCtrk} vs. z_{pvtx}

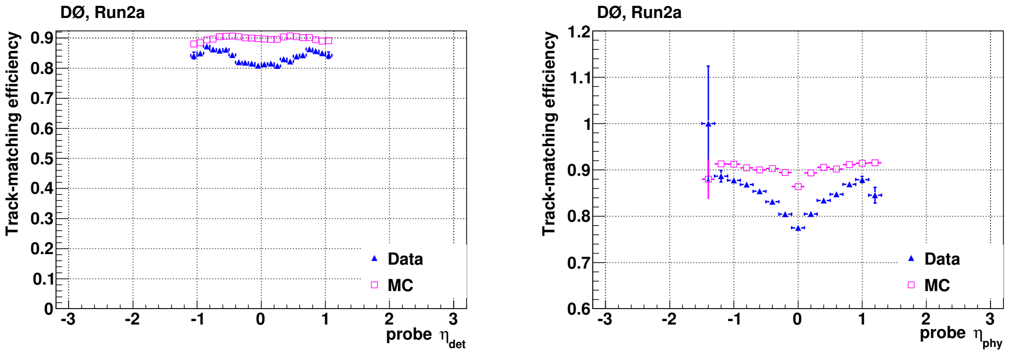

(c) ϵ_{CCtrk} vs. η_{det} of probe electron (d) ϵ_{CCtrk} vs. η_{phy} of probe electron

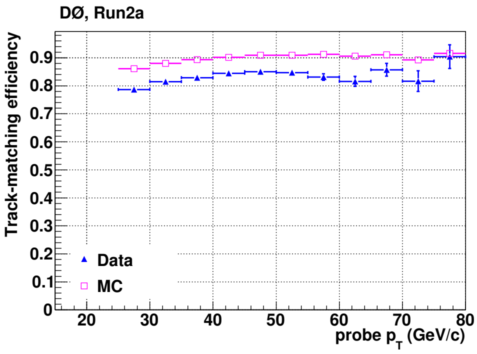

(e) ϵ_{CCtrk} vs. p_T of probe electron

Figure A.21: Type I tracking efficiencies (ϵ_{CCtrk}) for electron in the CC for Run2a data and MC events.

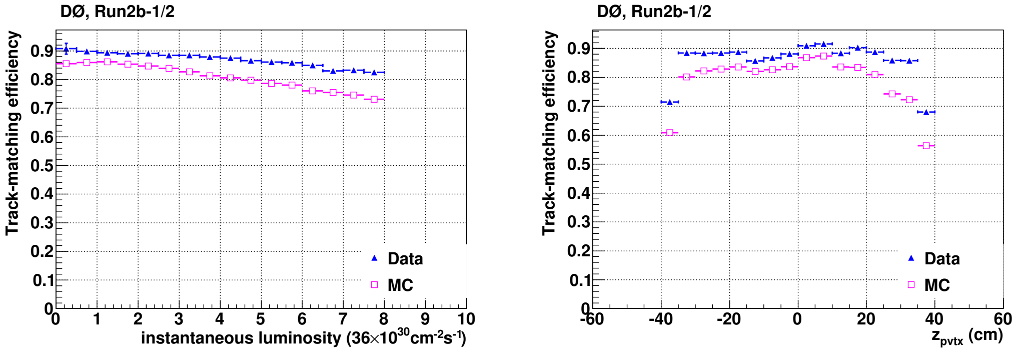

(a) ϵ_{CCtrk} vs. L_{inst} (b) ϵ_{CCtrk} vs. z_{pvtx}

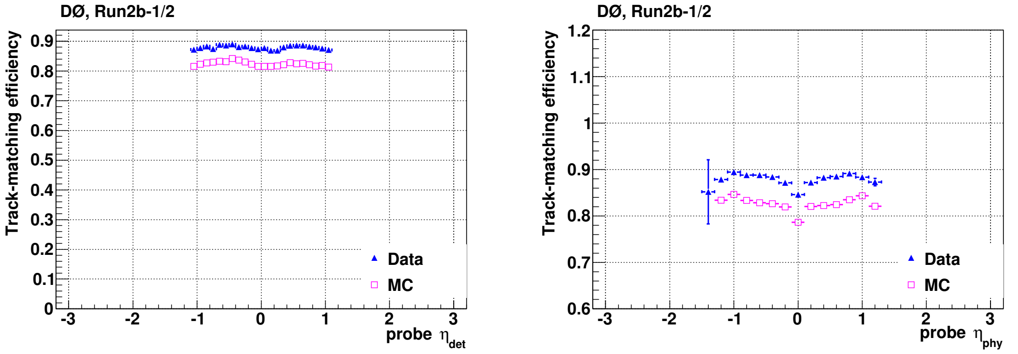

(c) ϵ_{CCtrk} vs. η_{det} of probe electron (d) ϵ_{CCtrk} vs. η_{phy} of probe electron

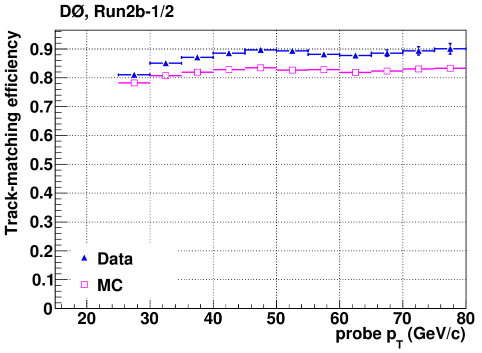

(e) ϵ_{CCtrk} vs. p_T of probe electron

Figure A.22: Type I tracking efficiencies (ϵ_{CCtrk}) for electron in the CC for Run2b-12 data and MC events.

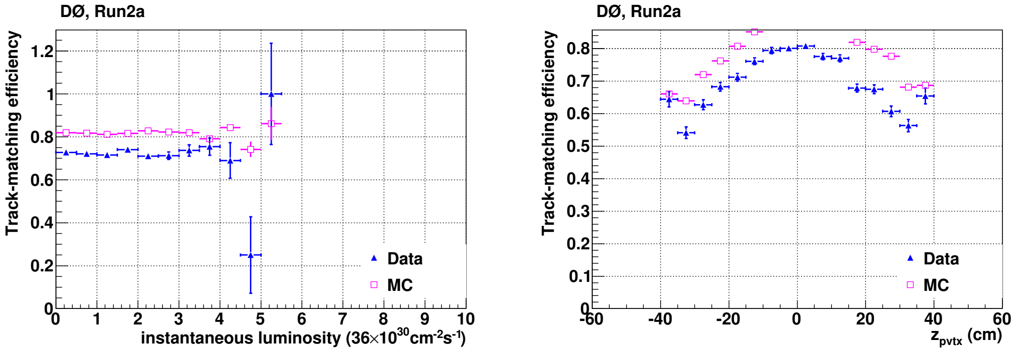

(a) ϵ_{ECtrk} vs. L_{inst}

(b) ϵ_{ECtrk} vs. z_{pvtx}

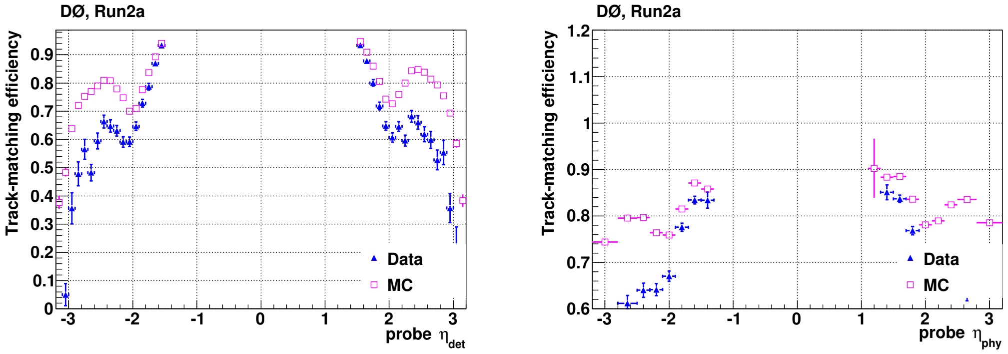

(c) ϵ_{ECtrk} vs. η_{det} of probe electron

(d) ϵ_{ECtrk} vs. η_{phy} of probe electron

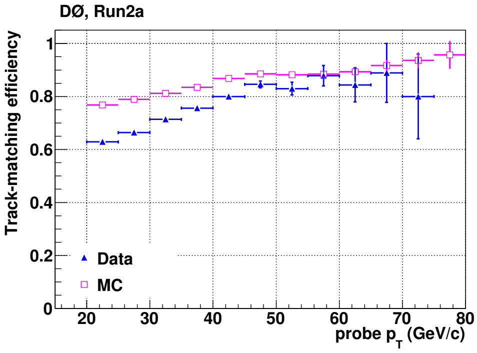

(e) ϵ_{ECtrk} vs. p_T of probe electron

Figure A.23: Type II tracking efficiencies (ϵ_{ECtrk}) for electron in the EC for Run2a data and MC events.

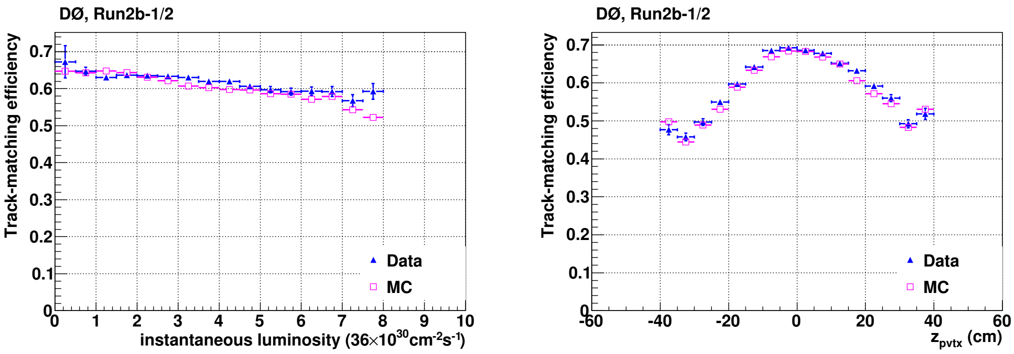

(a) ϵ_{ECtrk} vs. L_{inst}

(b) ϵ_{ECtrk} vs. z_{pvtx}

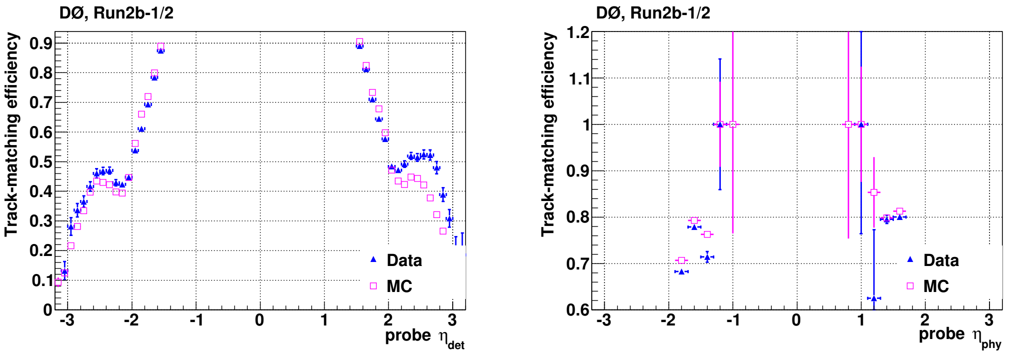

(c) ϵ_{ECtrk} vs. η_{det} of probe electron

(d) ϵ_{ECtrk} vs. η_{phy} of probe electron

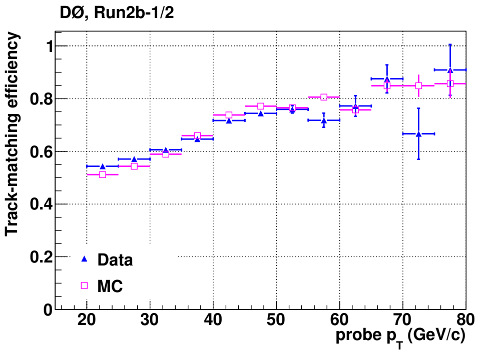

(e) ϵ_{ECtrk} vs. p_T of probe electron

Figure A.24: Type II tracking efficiencies (ϵ_{ECtrk}) for electron in the EC for Run2b-12 data and MC events.

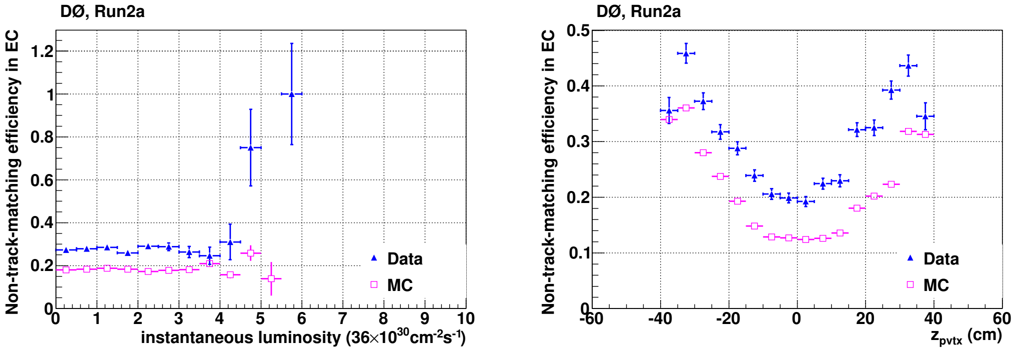

(a) ϵ_{EC_HoR} vs. L_{inst} (b) ϵ_{EC_HoR} vs. z_{pvtx}

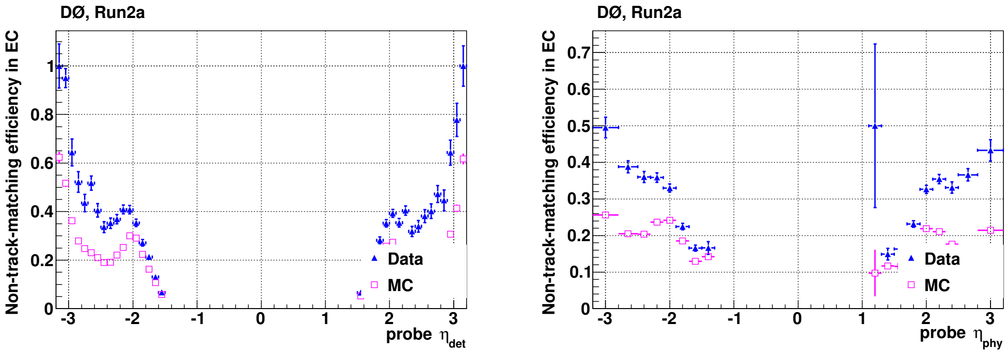

(c) ϵ_{EC_HoR} vs. η_{det} of probe electron (d) ϵ_{EC_HoR} vs. η_{phy} of probe electron

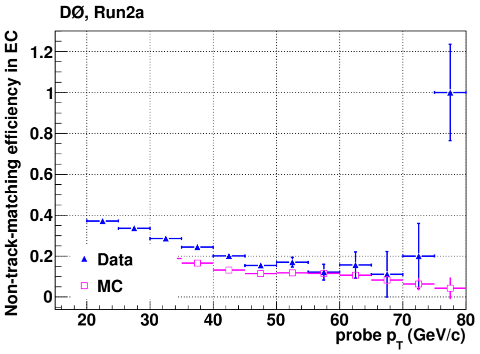

(e) ϵ_{EC_HoR} vs. p_T of probe electron

Figure A.25: Type III tracking efficiencies (ϵ_{EC_HoR}) for electron in the EC for Run2a data and MC events.

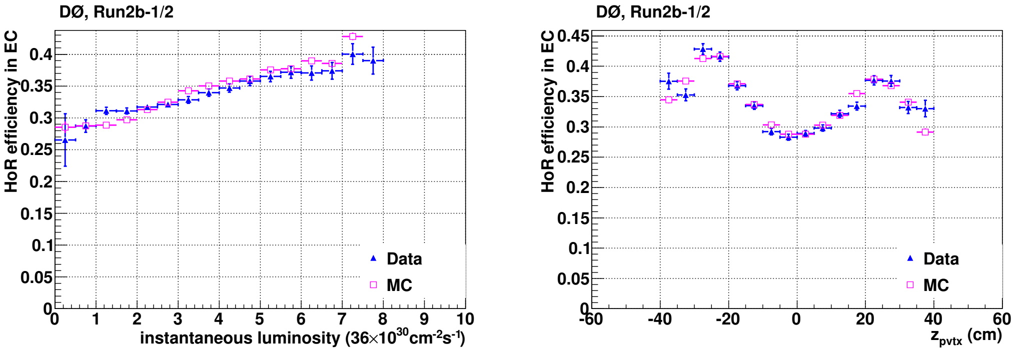

(a) ϵ_{EC_HoR} vs. L_{inst}

(b) ϵ_{EC_HoR} vs. z_{pvtx}

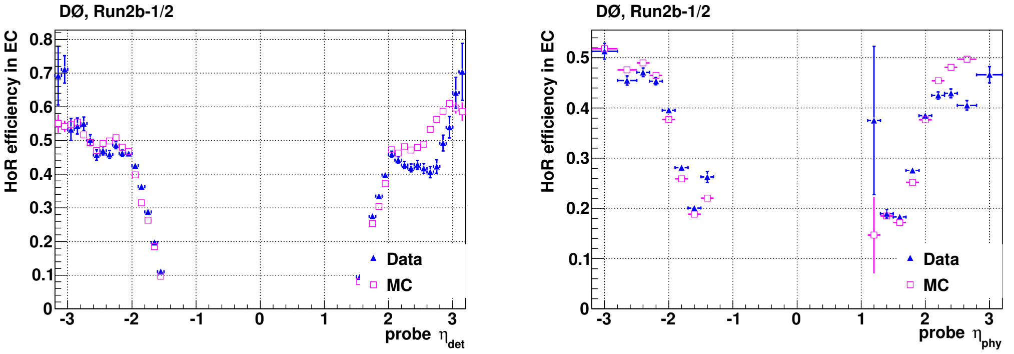

(c) ϵ_{EC_HoR} vs. η_{det} of probe electron

(d) ϵ_{EC_HoR} vs. η_{phy} of probe electron

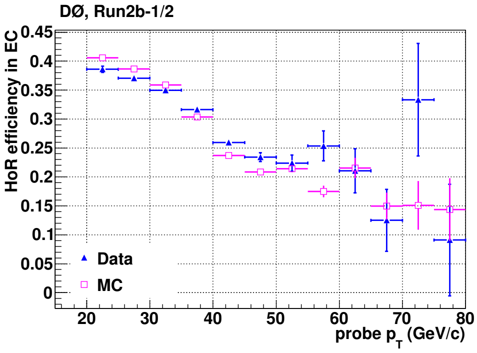

(e) ϵ_{EC_HoR} vs. p_T of probe electron

Figure A.26: Type III tracking efficiencies (ϵ_{EC_HoR}) for electron in the EC for Run2b-12 data and MC events.

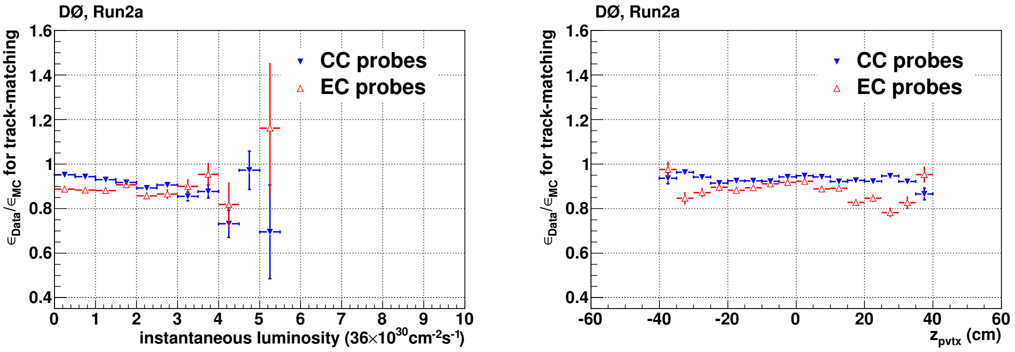

(a) s.f vs. L_{inst} (b) s.f vs. z_{pvtx}

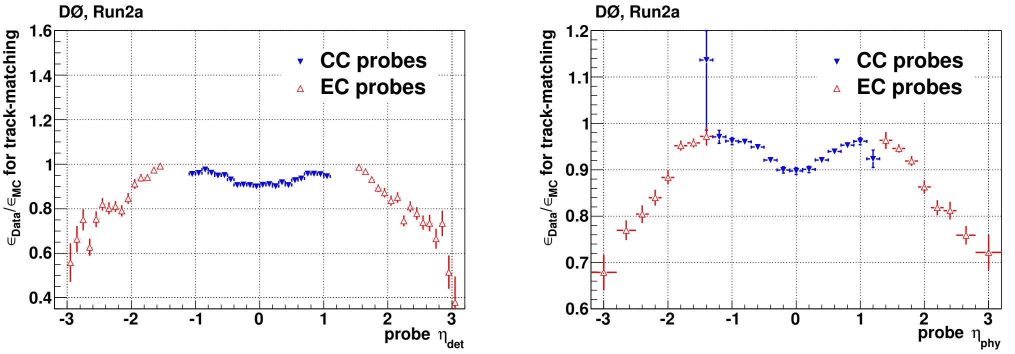

(c) s.f vs. η_{det} of probe electron (d) s.f vs. η_{phy} of probe electron

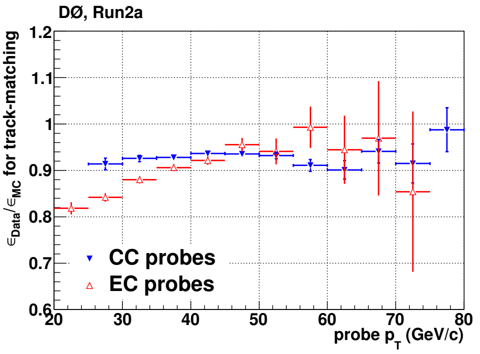

(e) s.f vs. p_T of probe electron

Figure A.27: First order scale factors (s.f.) for the tracking efficiencies of electron in the CC (Type I) and in the EC (Type II) between Run2a data and MC.

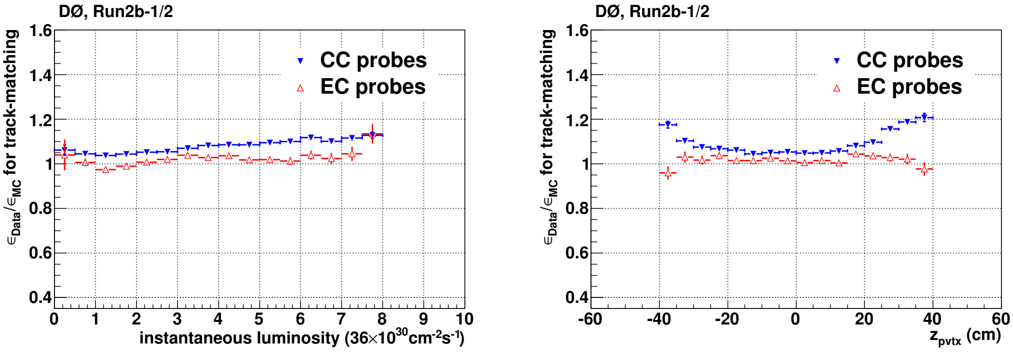

(a) s.f vs. L_{inst} (b) s.f vs. z_{pvtx}

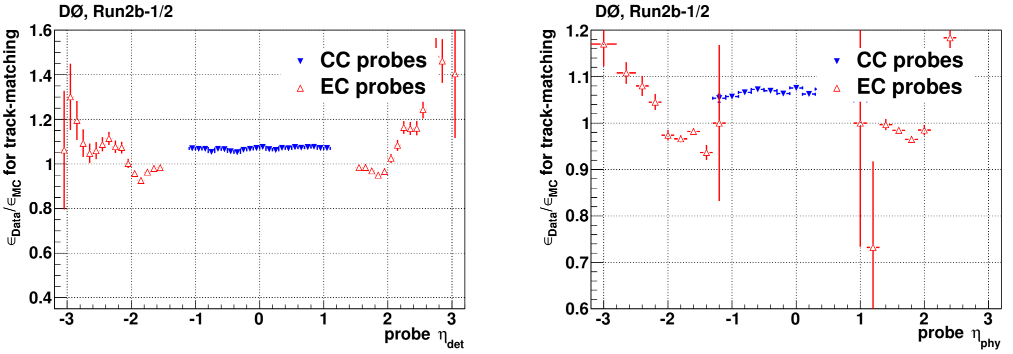

(c) s.f vs. η_{det} of probe electron (d) s.f vs. η_{phy} of probe electron

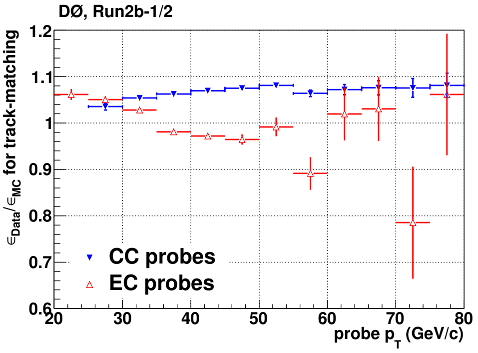

(e) s.f vs. p_T of probe electron

Figure A.28: First order scale factors (s.f.) for the tracking efficiencies of electron in the CC (Type I) and in the EC (Type II) between Run2b-12 data and MC.

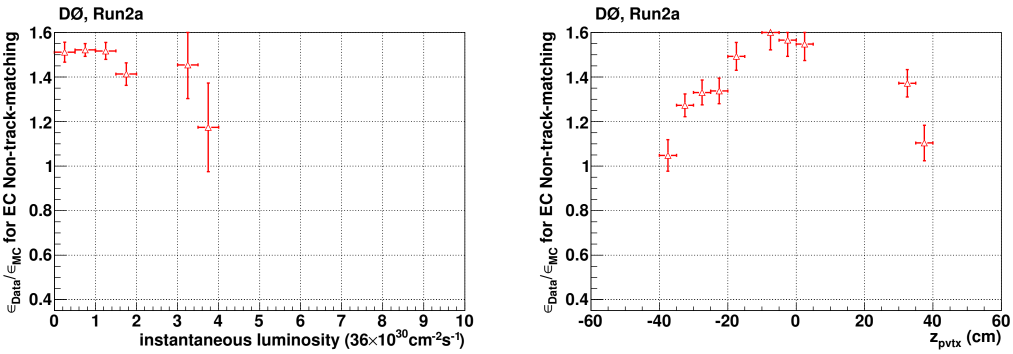

(a) s.f vs. L_{inst} (b) s.f vs. z_{pvtx}

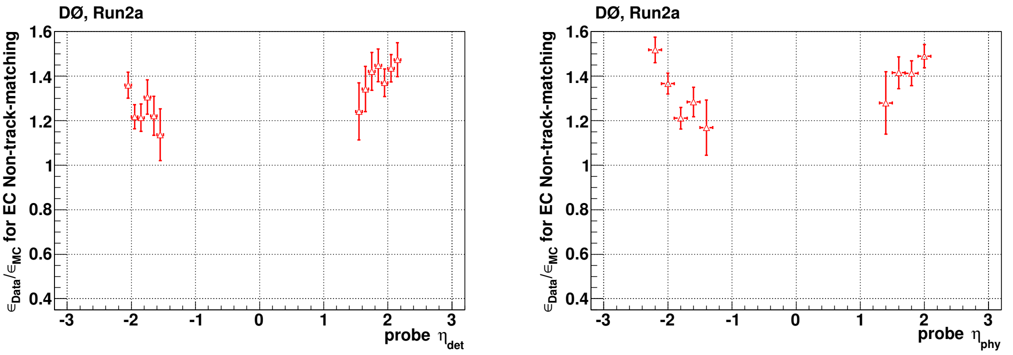

(c) s.f vs. η_{det} of probe electron (d) s.f vs. η_{phy} of probe electron

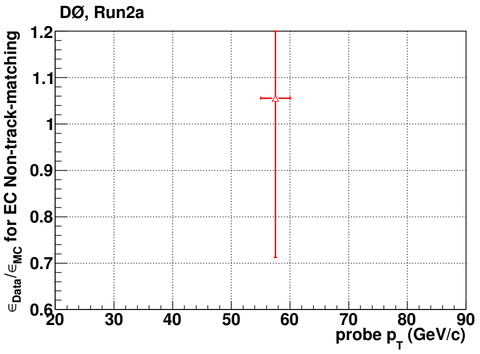

(e) s.f vs. p_T of probe electron

Figure A.29: First order scale factors (s.f.) for the cut on the HoR variable for non-track-matched electrons in the EC (Type III) between Run2a data and MC.

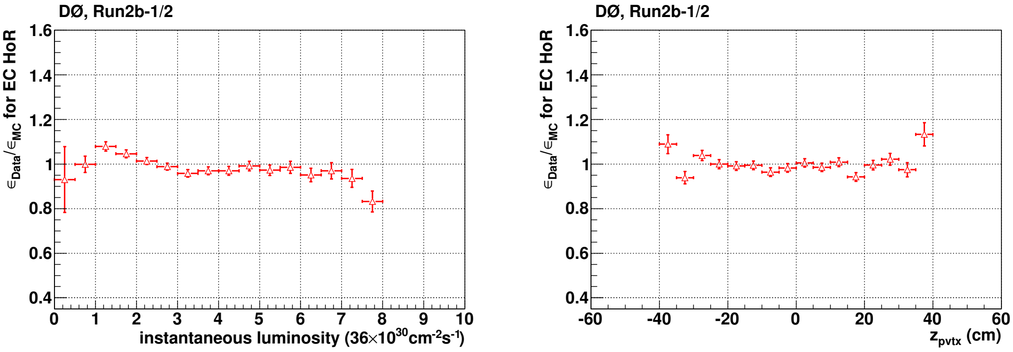

(a) s.f vs. L_{inst} (b) s.f vs. z_{pvtx}

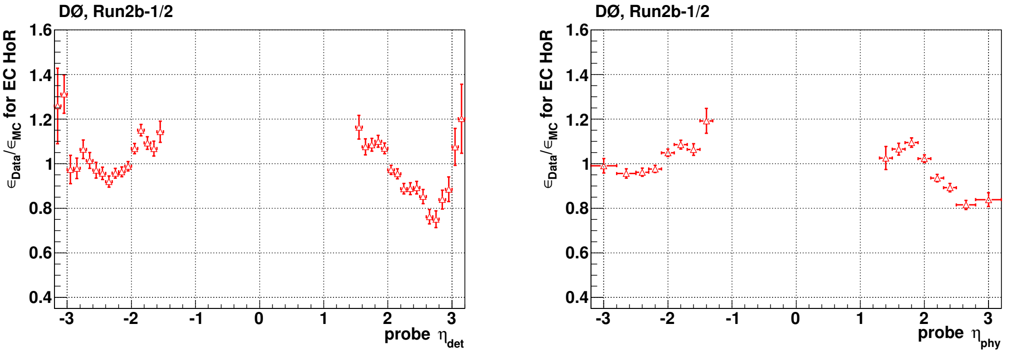

(c) s.f vs. η_{det} of probe electron (d) s.f vs. η_{phy} of probe electron

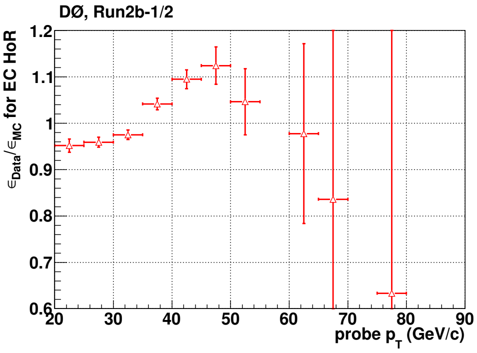

(e) s.f vs. p_T of probe electron

Figure A.30: First order scale factors (s.f.) for the cut on the HoR variable for non-track-matched electrons in the EC (Type III) between Run2b-12 data and MC.

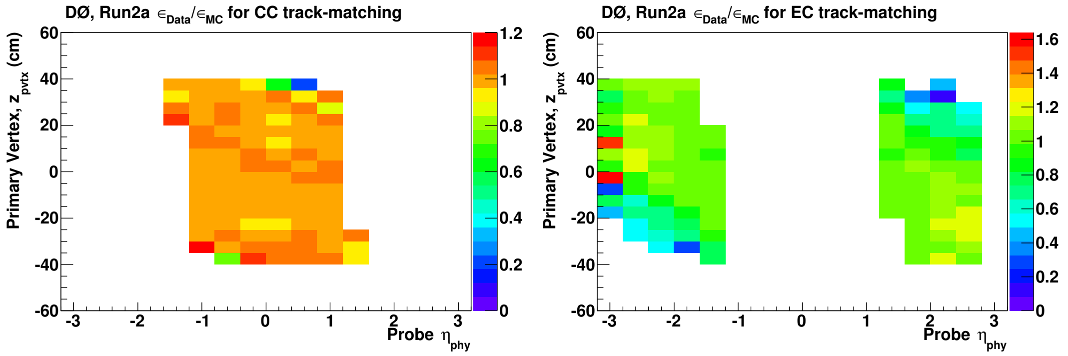

(a) 2D s.f (2nd order) for Type I (b) 2D s.f (2nd order) for Type II

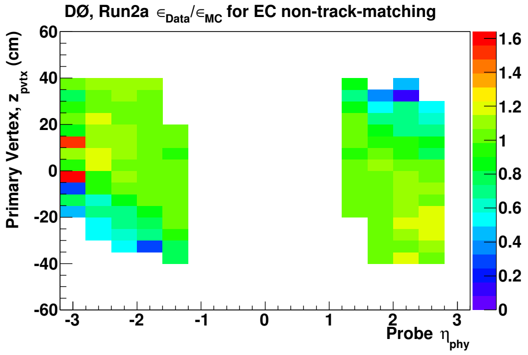

(c) 2D s.f (2nd order) for Type III

Figure A.31: Second order scale factors (s.f.) as functions of z_{pvtx} and electron η_{phy} for each type of tracking efficiency in Run2a data and MC.

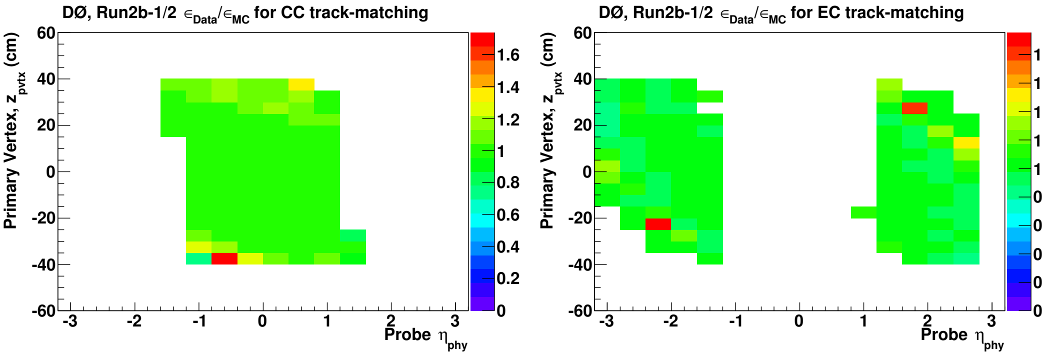

(a) 2D s.f (2nd order) for Type I (b) 2D s.f (2nd order) for Type II

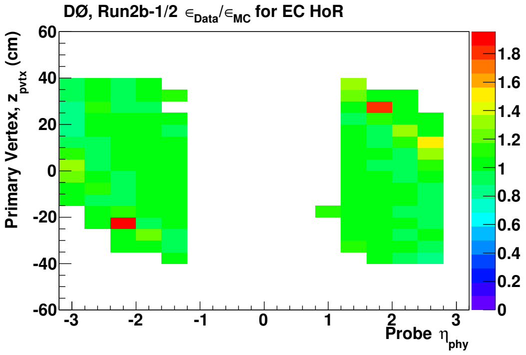

(c) 2D s.f (2nd order) for Type III

Figure A.32: Second order scale factors (s.f.) as functions of z_{pvtx} and electron η_{phy} for each type of tracking efficiency in Run2b-12 data and MC.

A.2 Data and MC comparison in each subset

Data and MC distributions are compared in each subset of data and MC in this section. The same legend as that for plots in Section 5.6 is used, and the same sets of distributions are made.

- z_{pvtx}, shown in Figure A.33 – A.35;
- η_{det}, shown in Figure A.36 – A.38;
- η_{phy}, shown in Figure A.39 – A.39;
- $\Delta\phi_{det}$ between the two electrons , shown in Figure A.42 – A.44;
- electron p_T, shown in Figure A.45 – A.47;
- $\cos(\theta^*)$, shown in Figure A.48 – A.50;
- M_{ee}, shown in in Figure A.51 – A.53;
- reconstructed boson p_T, shown in Figure A.54 – A.56;
- reconstructed boson rapidity, shown in Figure A.57 – A.59;

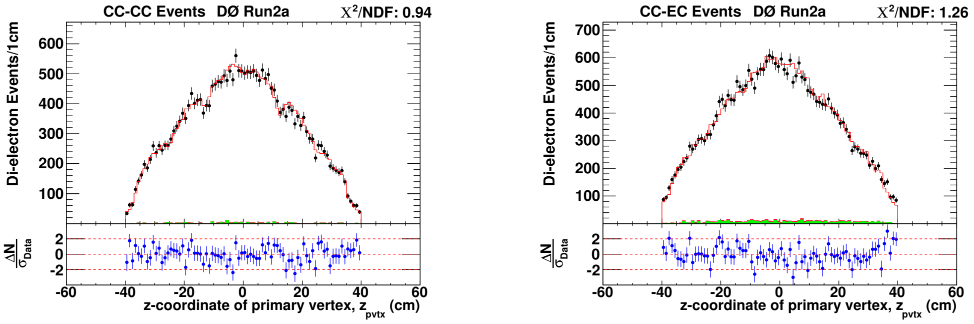

(a) CC-CC (b) CC-EC

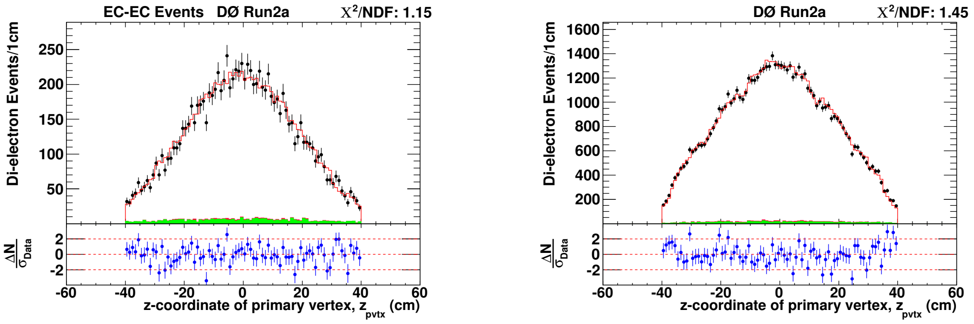

(c) EC-EC (d) All events

Figure A.33: Distributions of the zcoordinate of the primary vertex for Run2a data and MC.

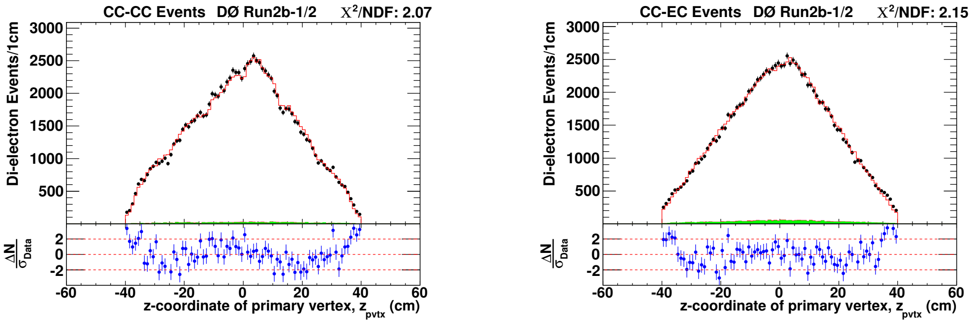

(a) CC-CC (b) CC-EC

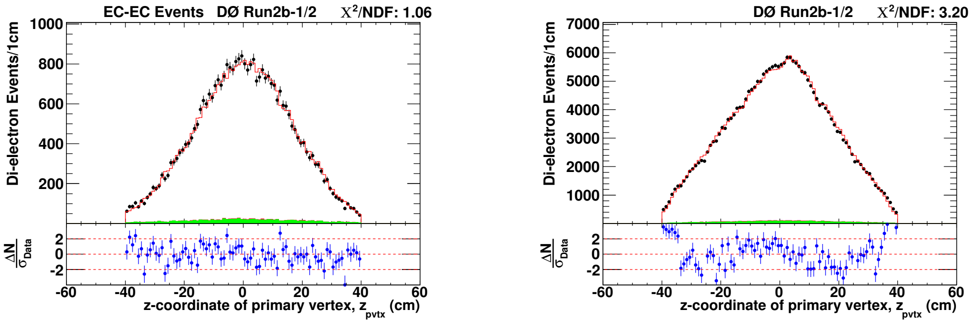

(c) EC-EC (d) All events

Figure A.34: Distributions of the zcoordinate of the primary vertex for Run2b-12 data and MC.

A.2 Data and MC comparison in each subset

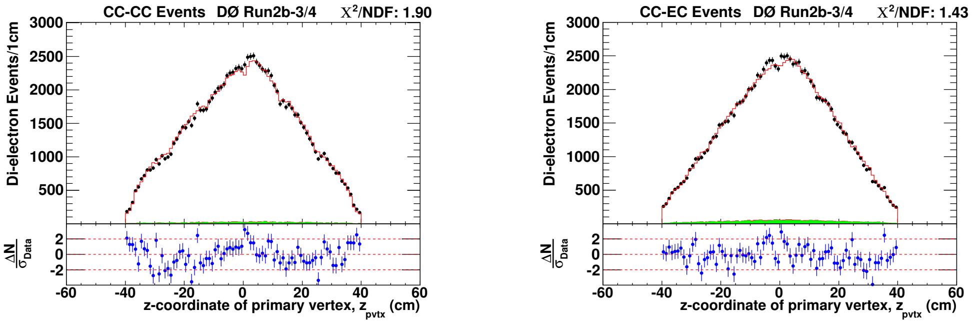

(a) CC-CC (b) CC-EC

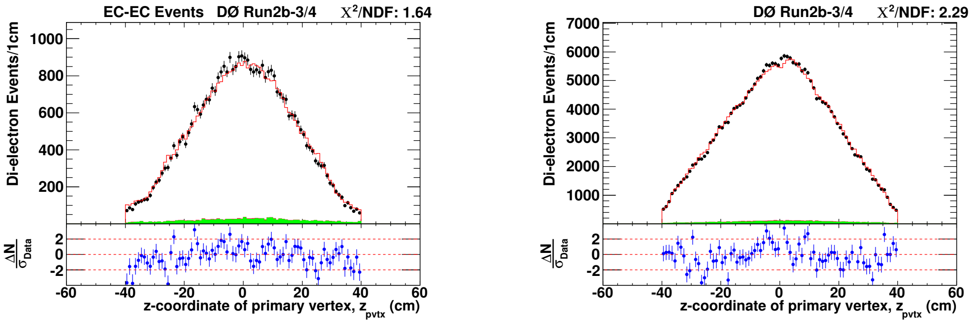

(c) EC-EC (d) All events

Figure A.35: Distributions of the zcoordinate of the primary vertex for Run2b-34 data and MC.

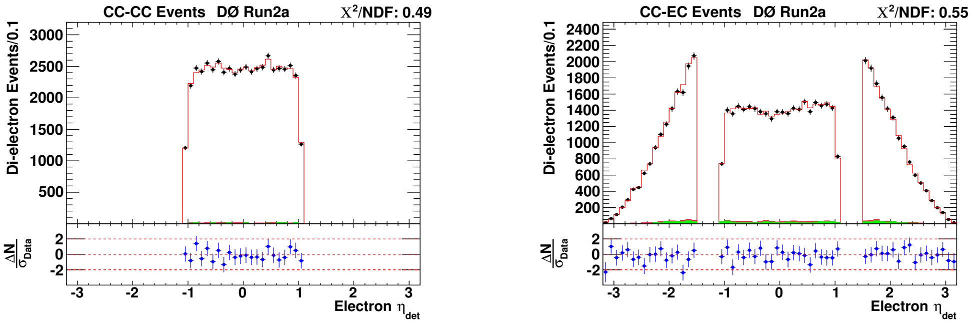

(a) CC-CC (b) CC-EC

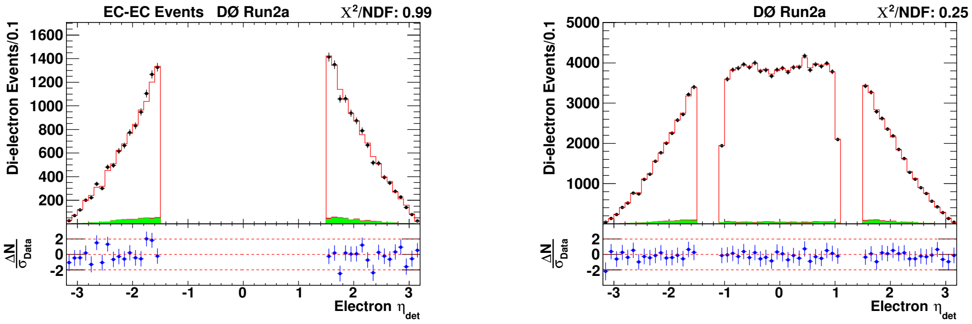

(c) EC-EC (d) All events

Figure A.36: Distributions of the electorn η_{det} for Run2a data and MC.

A.2 Data and MC comparison in each subset

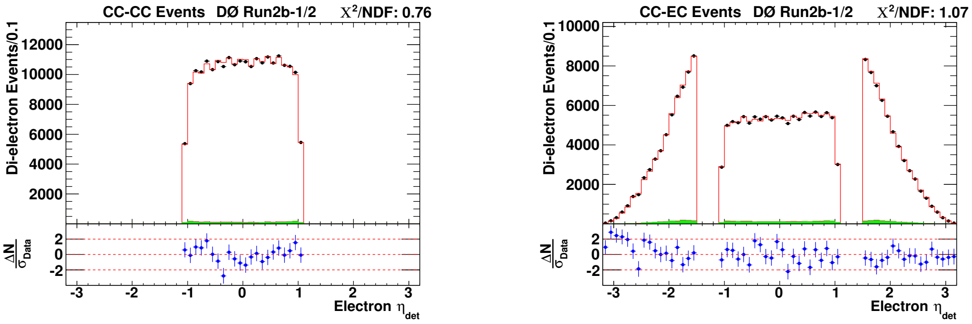

(a) CC-CC (b) CC-EC

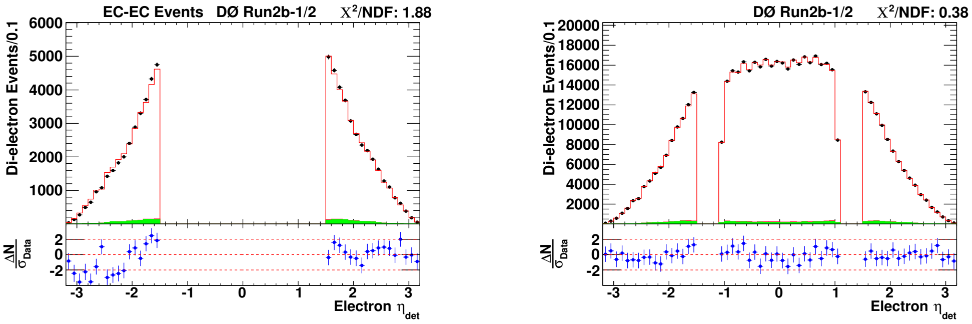

(c) EC-EC (d) All events

Figure A.37: Distributions of the electorn η_{det} for Run2b-12 data and MC.

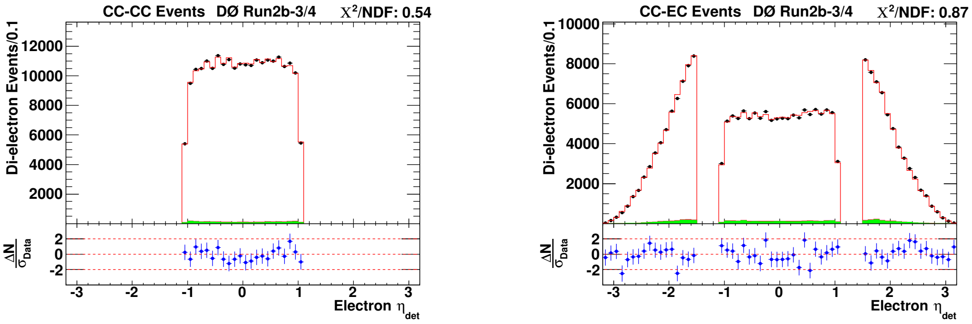

(a) CC-CC (b) CC-EC

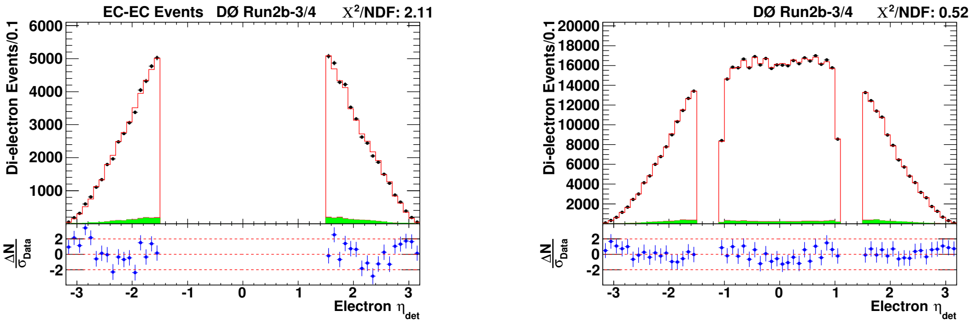

(c) EC-EC (d) All events

Figure A.38: Distributions of the electorn η_{det} for Run2b-34 data and MC.

A.2 Data and MC comparison in each subset

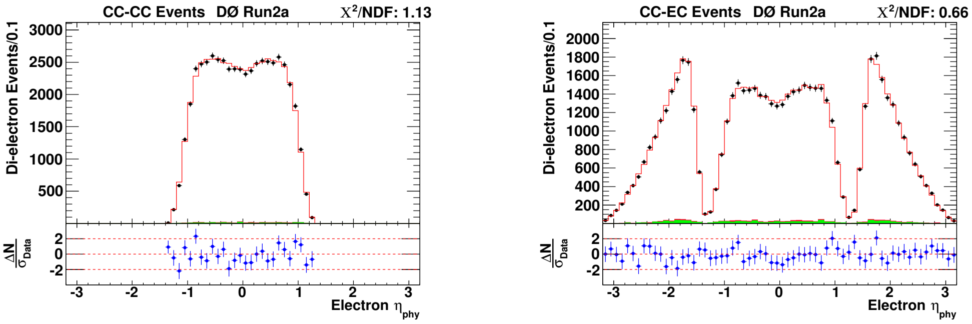

(a) CC-CC (b) CC-EC

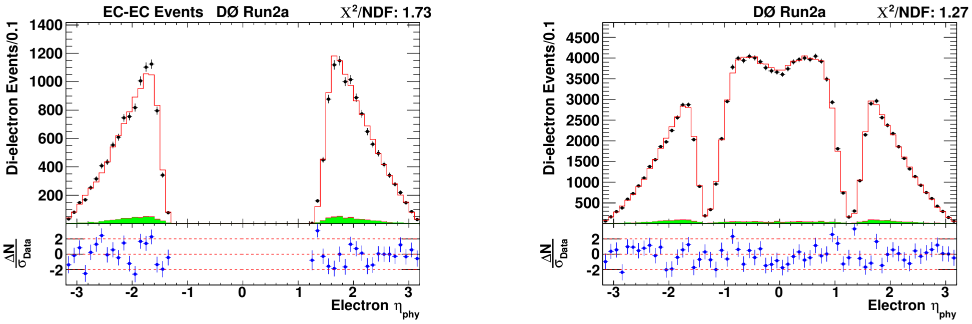

(c) EC-EC (d) All events

Figure A.39: Distributions of the electorn η_{phy} for Run2a data and MC.

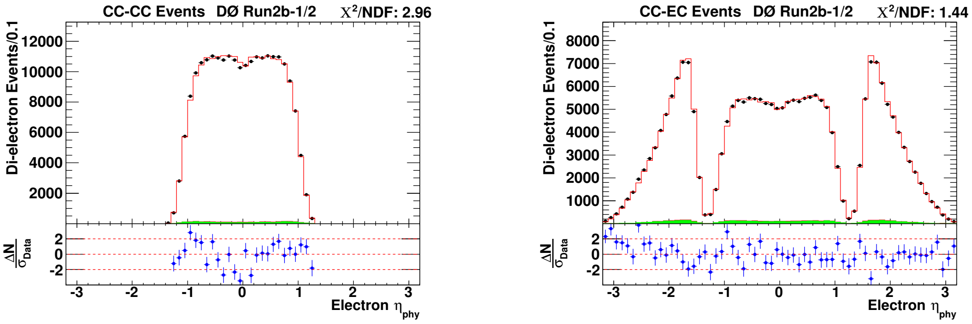

(a) CC-CC (b) CC-EC

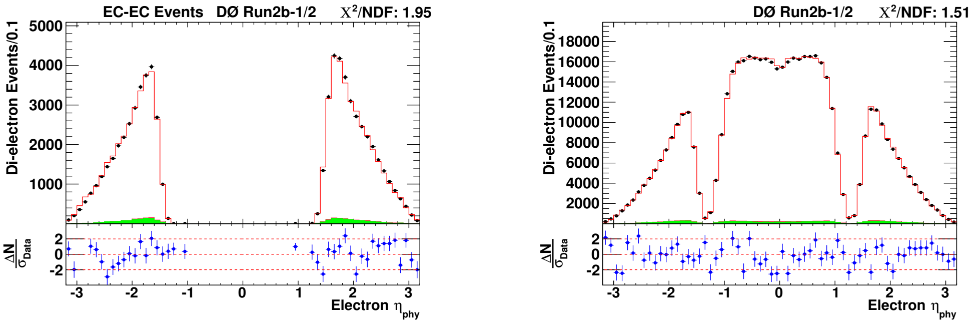

(c) EC-EC (d) All events

Figure A.40: Distributions of the electorn η_{phy} for Run2b-12 data and MC.

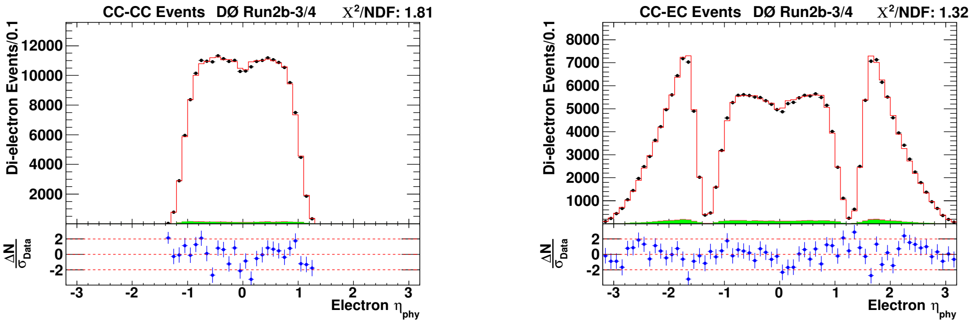

(a) CC-CC (b) CC-EC

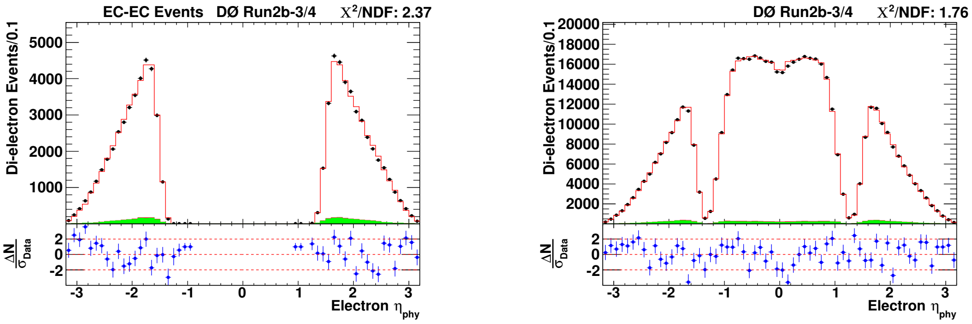

(c) EC-EC (d) All events

Figure A.41: Distributions of the electorn η_{phy} for Run2b-34 data and MC.

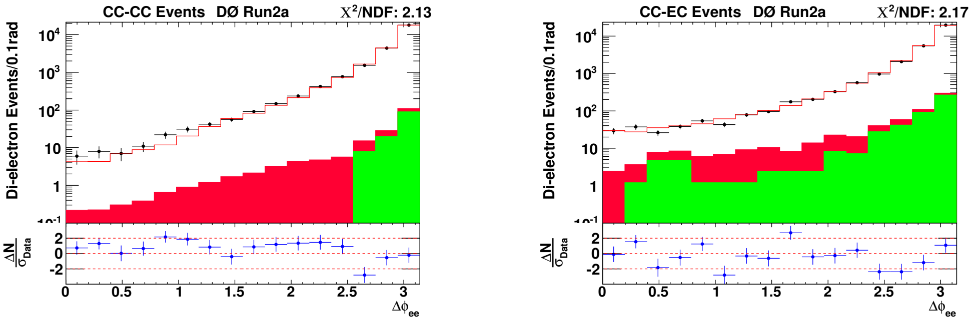

(a) CC-CC (b) CC-EC

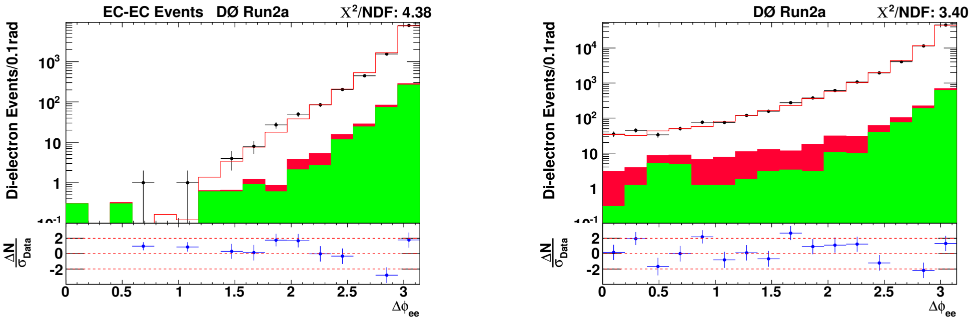

(c) EC-EC (d) All events

Figure A.42: Distributions of $\Delta\phi_{det}$ between the two electrons for Run2a data and MC.

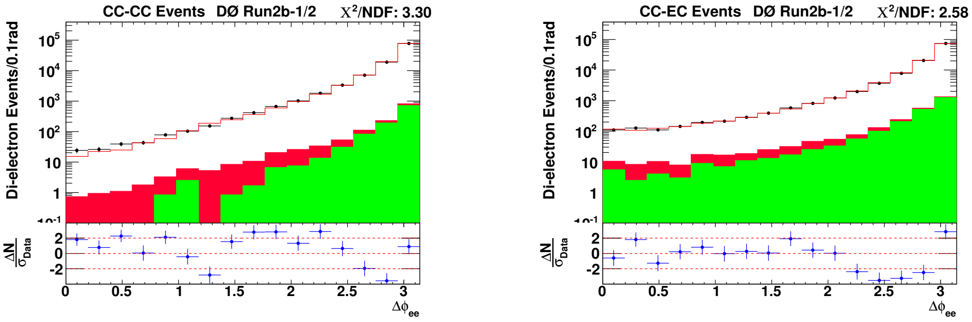

(a) CC-CC (b) CC-EC

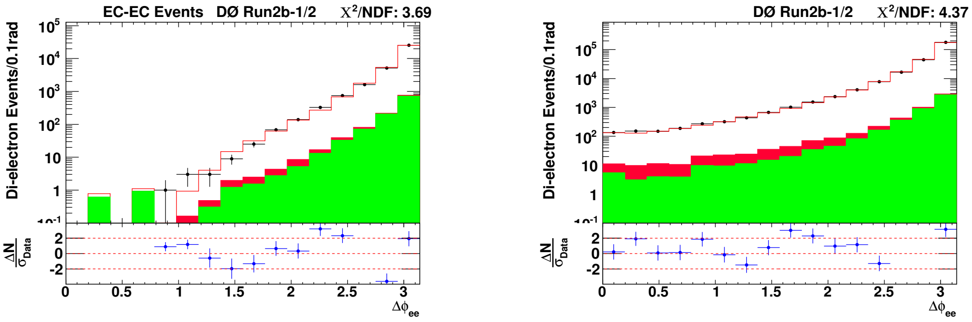

(c) EC-EC (d) All events

Figure A.43: Distributions of $\Delta\phi_{det}$ between the two electrons for Run2b-12 data and MC.

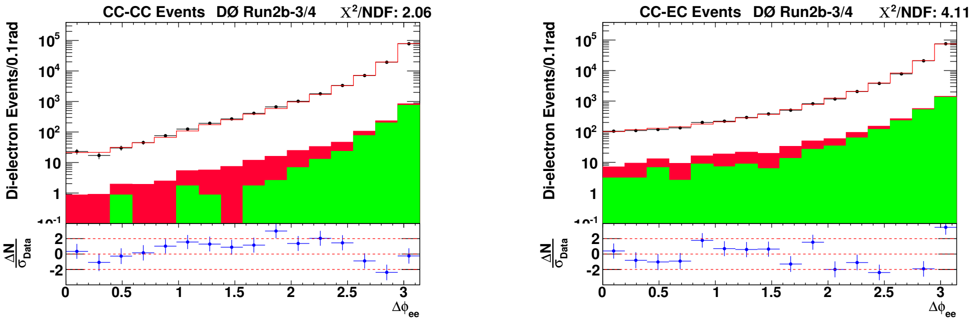

(a) CC-CC (b) CC-EC

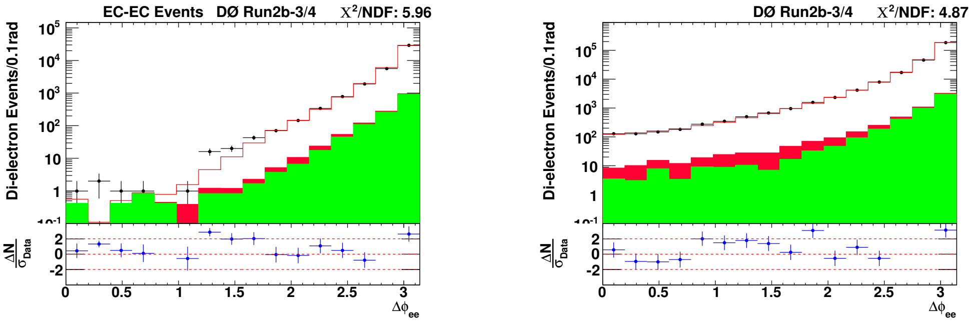

(c) EC-EC (d) All events

Figure A.44: Distributions of $\Delta\phi_{det}$ between the two electrons for Run2b-34 data and MC.

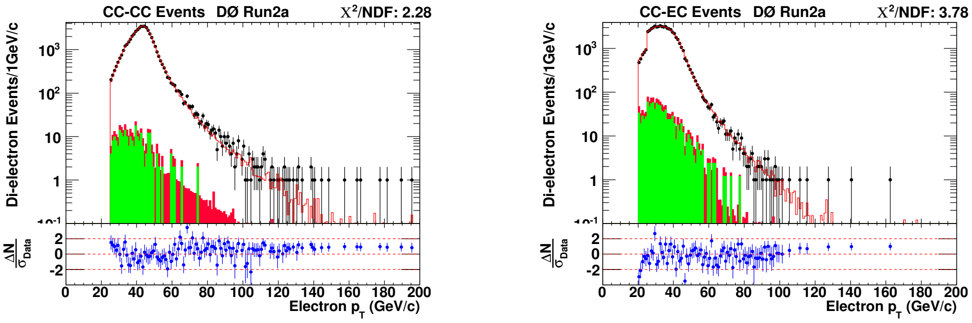

(a) CC-CC

(b) CC-EC

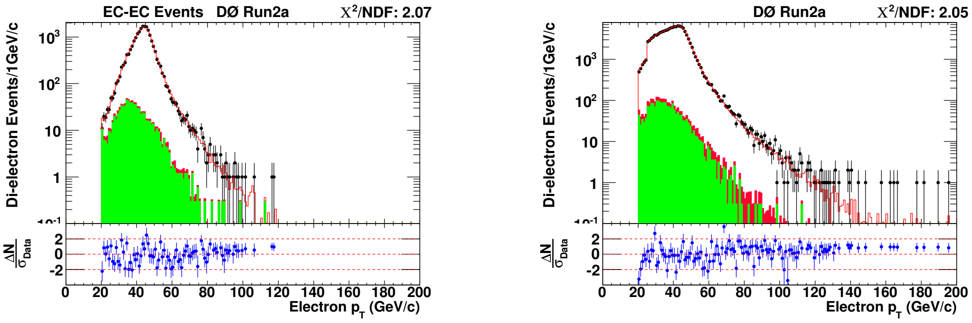

(c) EC-EC

(d) All events

Figure A.45: Distributions of the electorn p_T for Run2a data and MC.

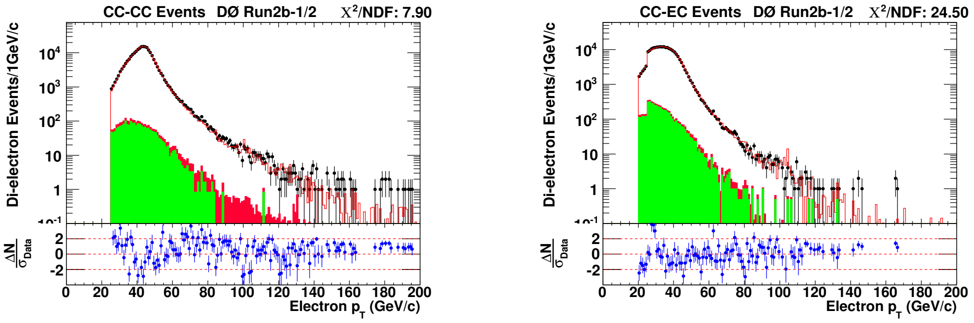

(a) CC-CC (b) CC-EC

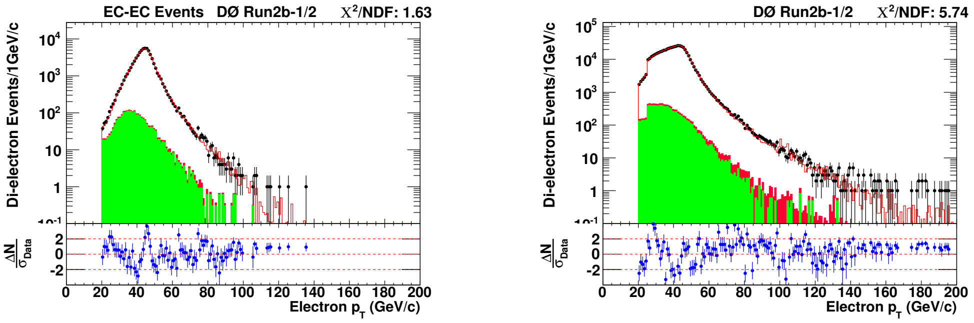

(c) EC-EC (d) All events

Figure A.46: Distributions of the electorn p_T for Run2b-12 data and MC.

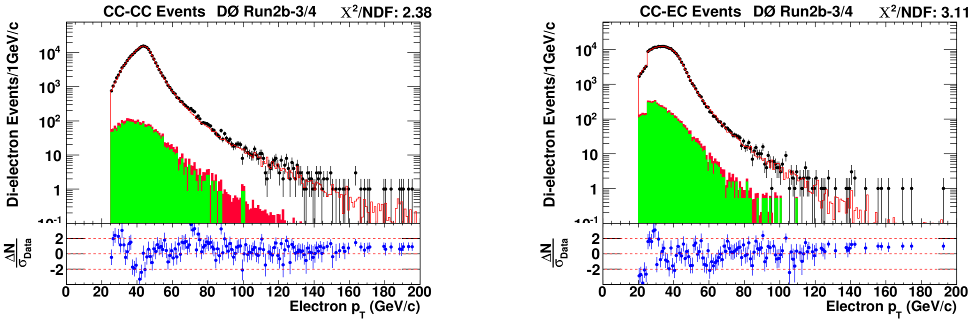

(a) CC-CC (b) CC-EC

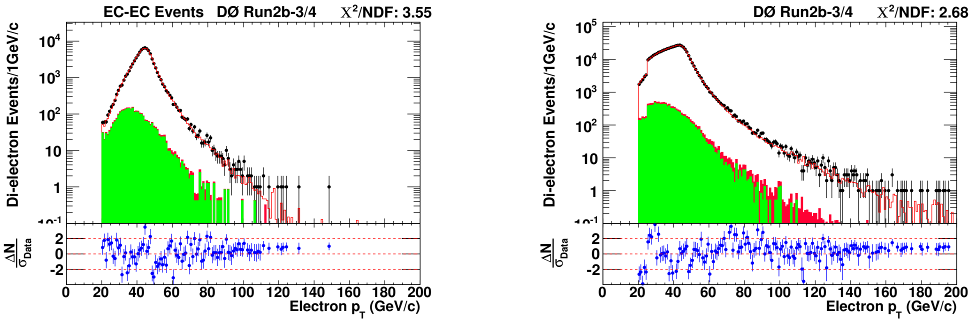

(c) EC-EC (d) All events

Figure A.47: Distributions of the electorn p_T for Run2b-34 data and MC.

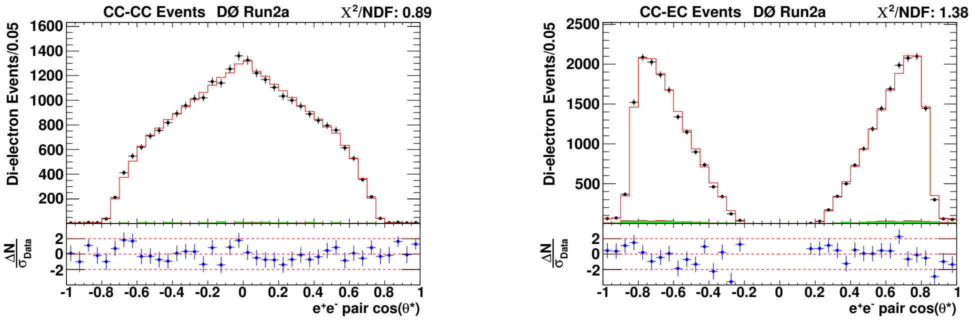

(a) CC-CC (b) CC-EC

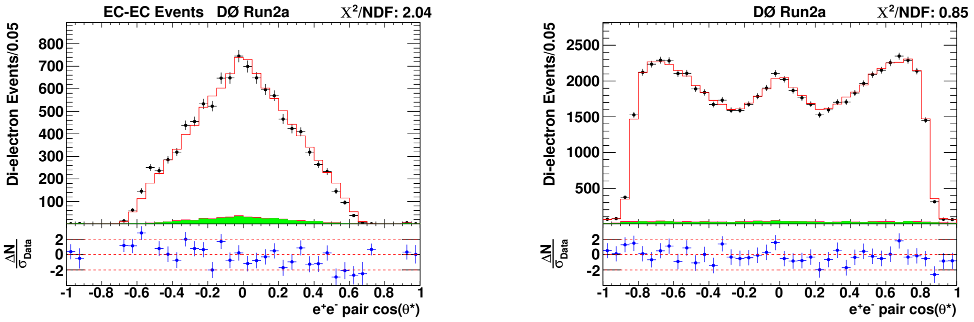

(c) EC-EC (d) All events

Figure A.48: Distributions of $\cos\theta^*$ for Run2a data and MC.

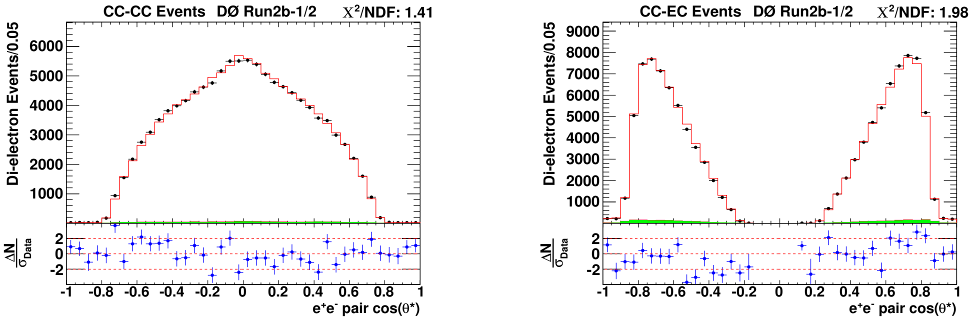

(a) CC-CC (b) CC-EC

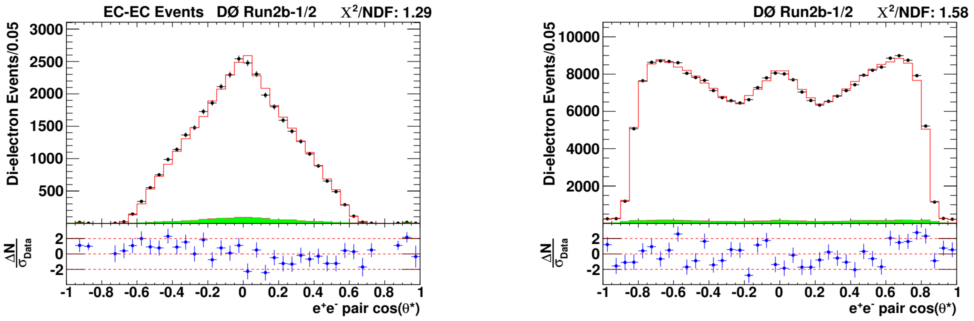

(c) EC-EC (d) All events

Figure A.49: Distributions of $\cos\theta^*$ for Run2b-12 data and MC.

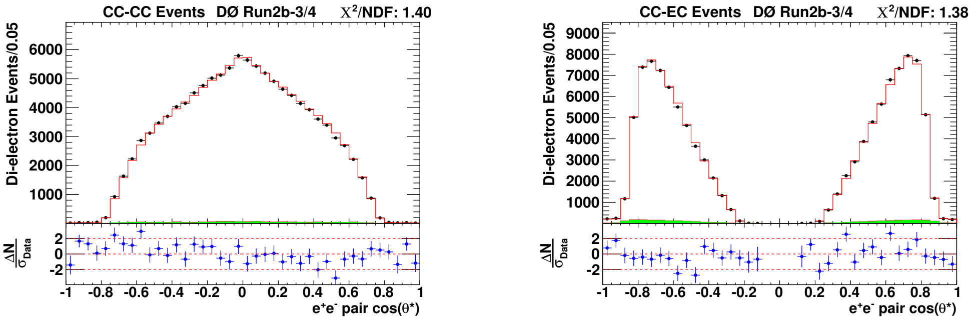

(a) CC-CC

(b) CC-EC

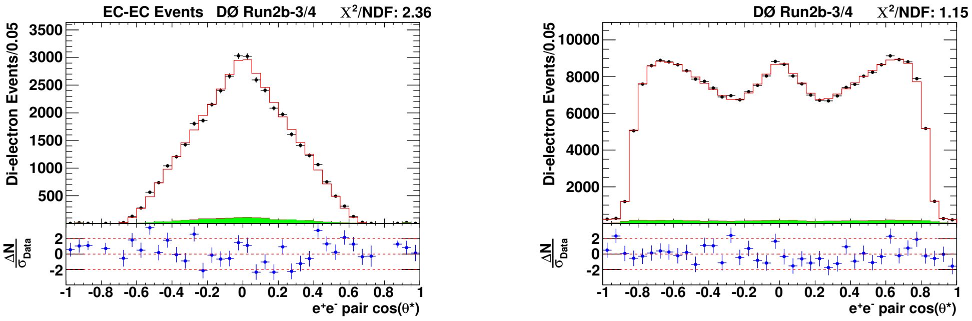

(c) EC-EC

(d) All events

Figure A.50: Distributions of $\cos\theta^*$ for Run2b-34 data and MC.

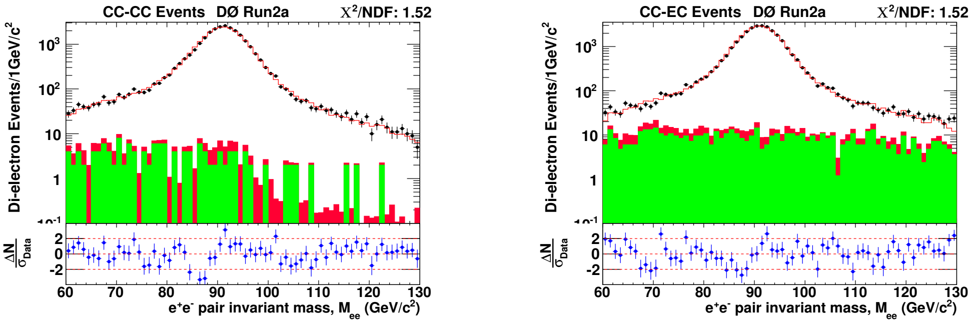

(a) CC-CC

(b) CC-EC

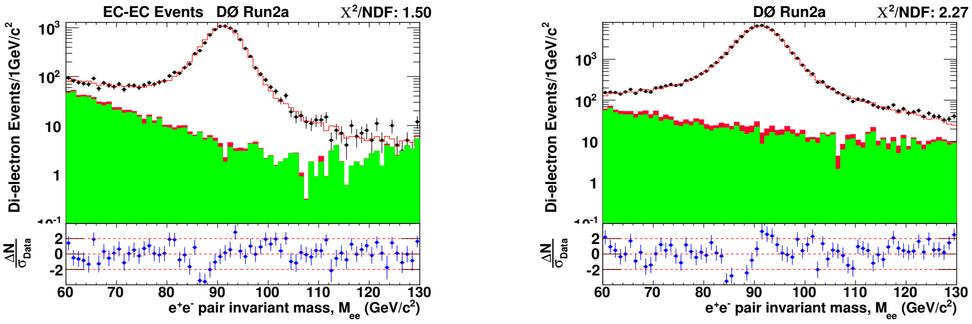

(c) EC-EC

(d) All events

Figure A.51: Distributions of the invariant mass of e^+e^- pairs for Run2a data and MC.

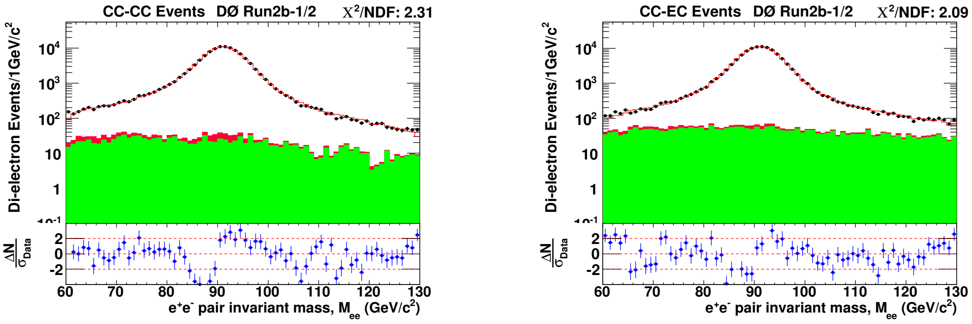

(a) CC-CC (b) CC-EC

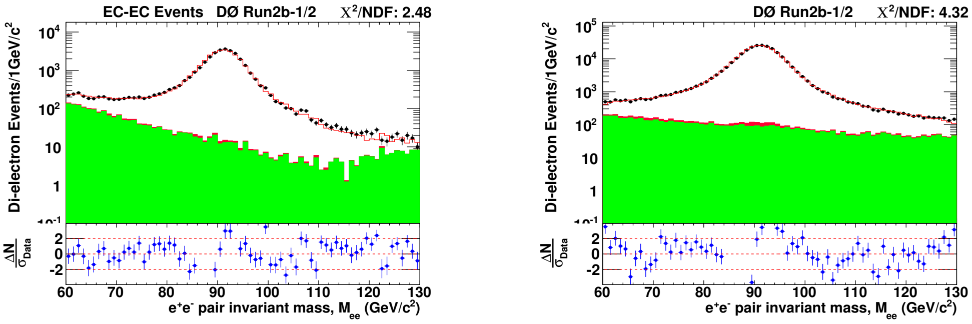

(c) EC-EC (d) All events

Figure A.52: Distributions of the invariant mass of e^+e^- pairs for Run2b-12 data and MC.

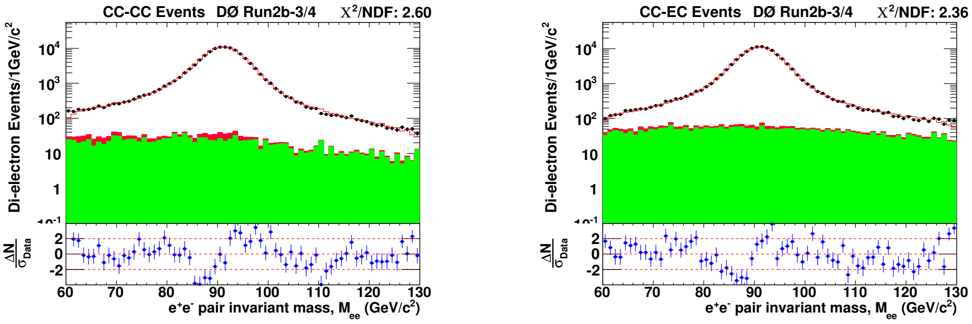

(a) CC-CC (b) CC-EC

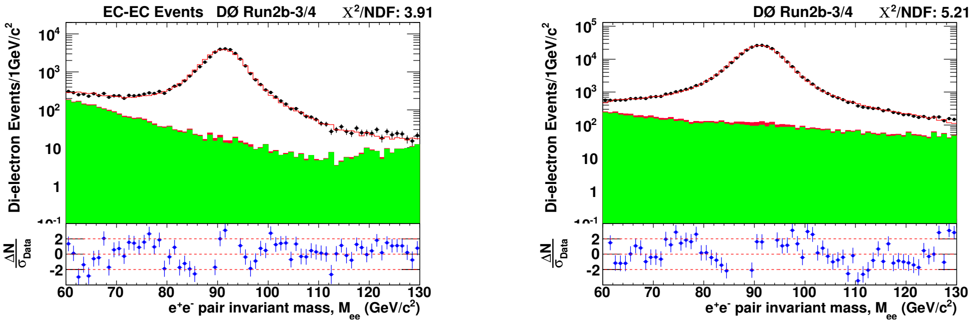

(c) EC-EC (d) All events

Figure A.53: Distributions of the invariant mass of e^+e^- pairs for Run2b-34 data and MC.

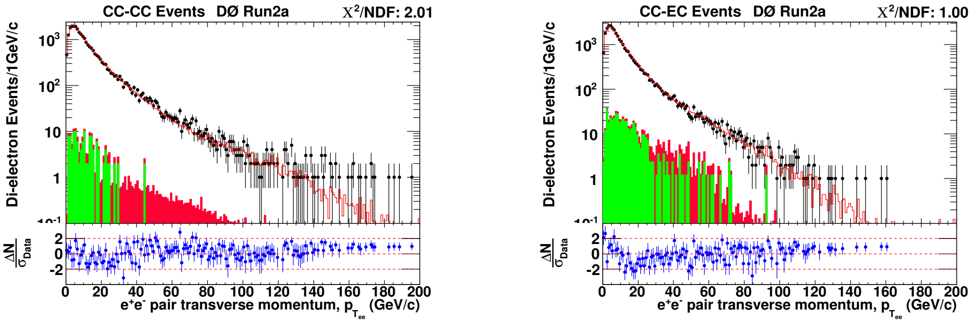

(a) CC-CC (b) CC-EC

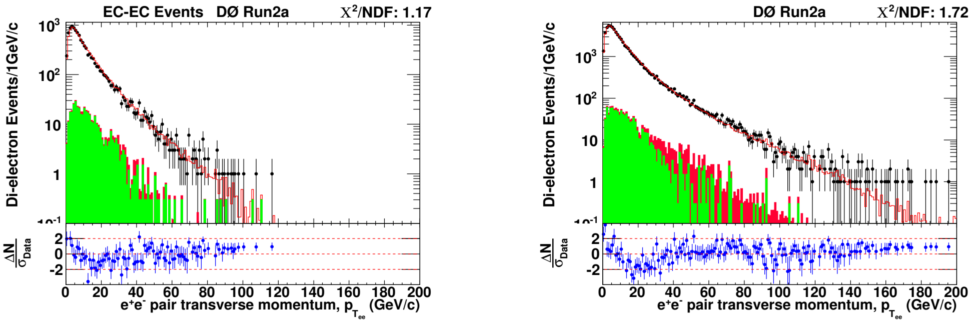

(c) EC-EC (d) All events

Figure A.54: Distributions of the reconstructed boson p_T for Run2a data and MC.

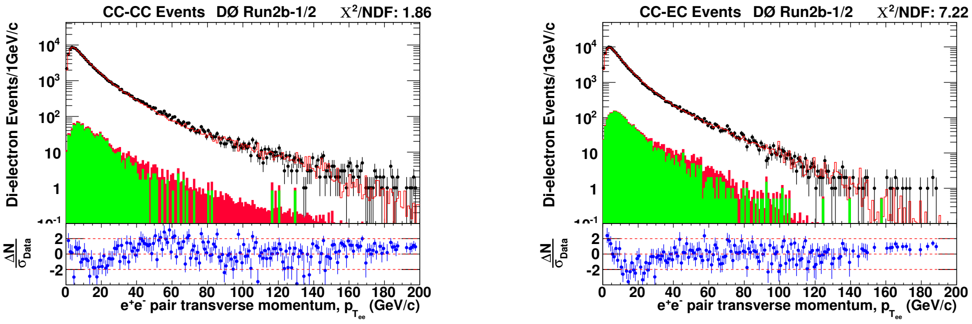

(a) CC-CC (b) CC-EC

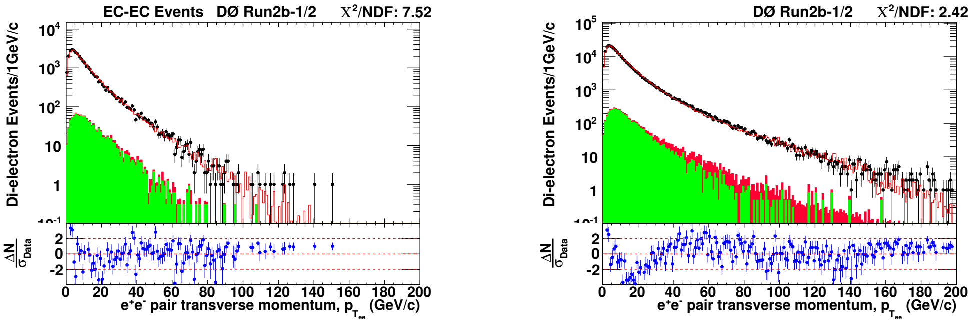

(c) EC-EC (d) All events

Figure A.55: Distributions of the reconstructed boson p_T for Run2b-12 data and MC.

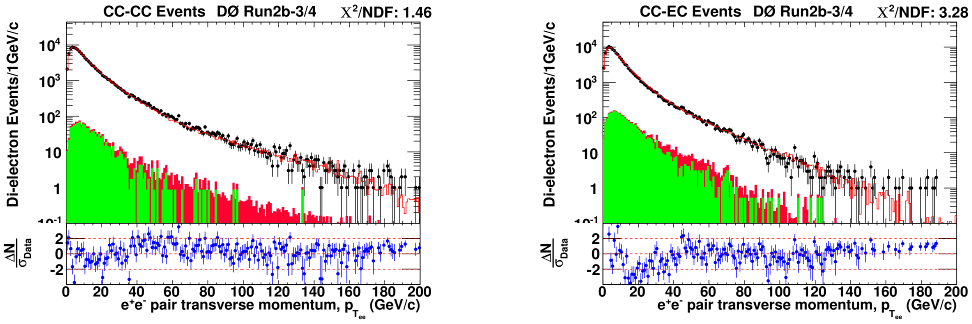

(a) CC-CC (b) CC-EC

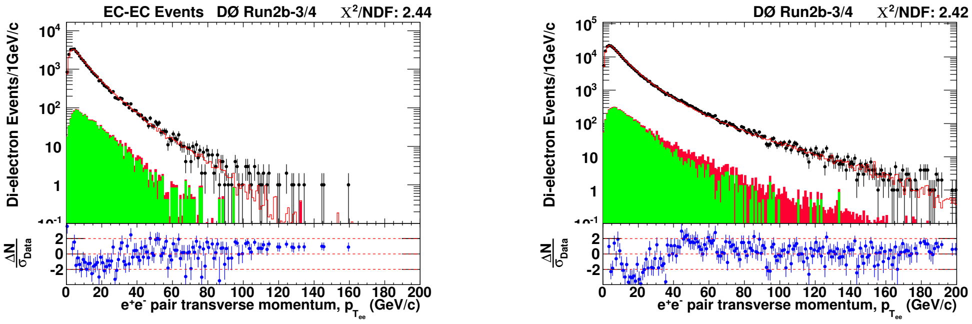

(c) EC-EC (d) All events

Figure A.56: Distributions of the reconstructed boson p_T for Run2b-34 data and MC.

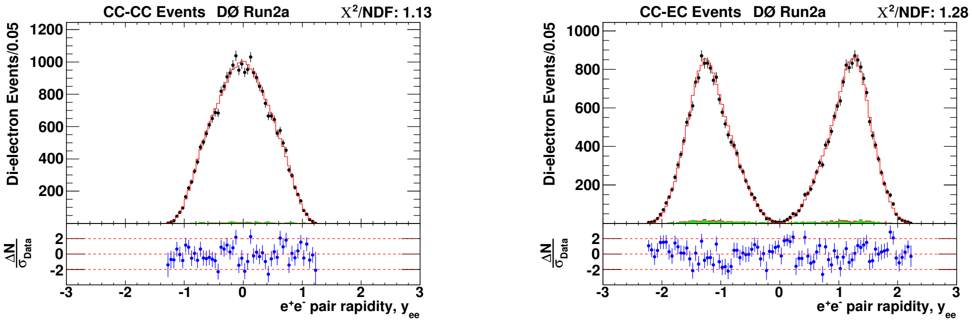

(a) CC-CC (b) CC-EC

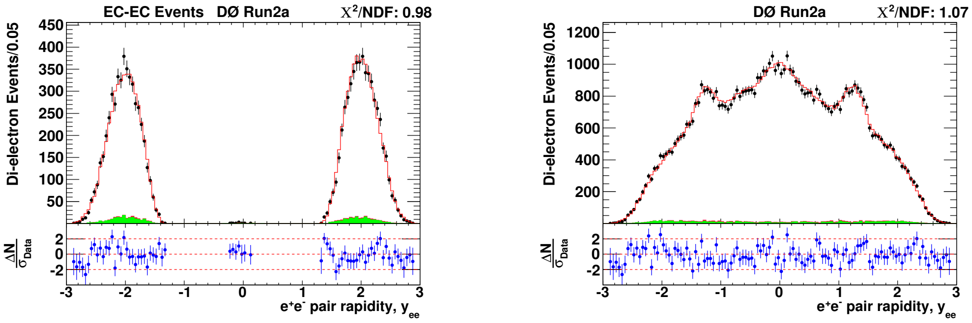

(c) EC-EC (d) All events

Figure A.57: Distributions of the reconstructed boson rapidity for Run2a data and MC.

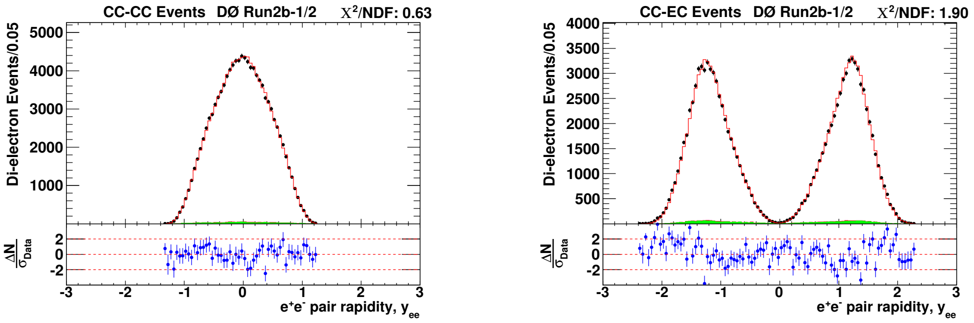

(a) CC-CC (b) CC-EC

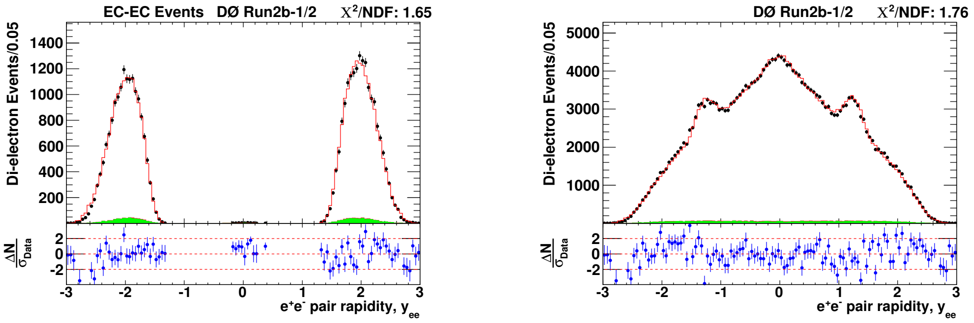

(c) EC-EC (d) All events

Figure A.58: Distributions of the reconstructed boson rapidity for Run2b-12 data and MC.

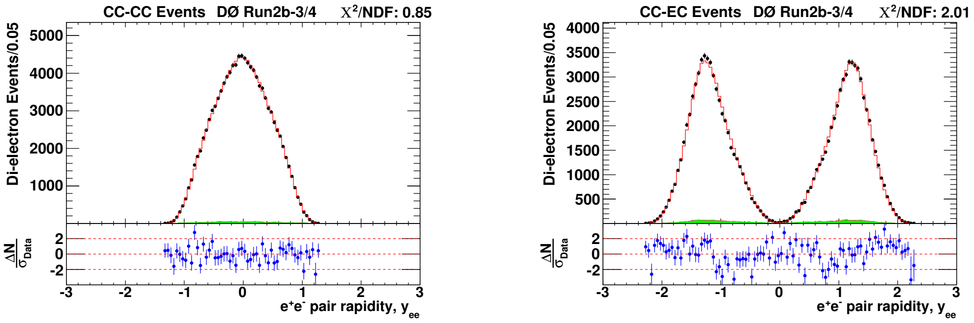

(a) CC-CC (b) CC-EC

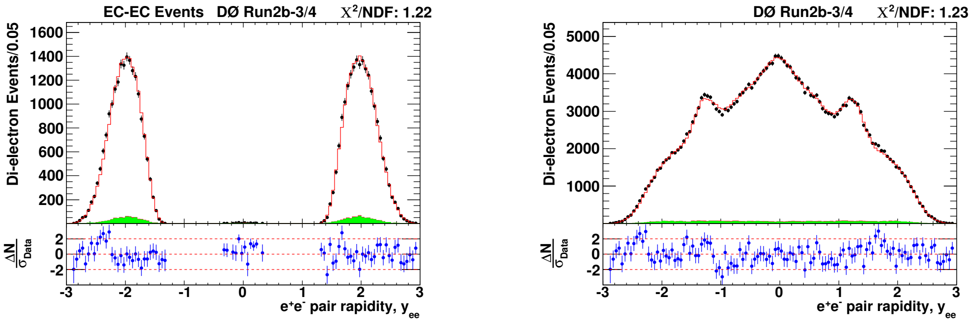

(c) EC-EC (d) All events

Figure A.59: Distributions of the reconstructed boson rapidity for Run2b-34 data and MC.

Appendix B

Supplementary tables

B.1 $\epsilon \times A$ in bins of y

y	$\epsilon\times$ A	δ(total)	$\delta(e^{-}s.f.)$		δ (E scale)	δ (PDF)	δ (y modeling)
			stat.	method			
-2.90	-	-	-	-	-	-	-
-2.8	0.1000	±0.0055	±0.0012	±0.0024	±0.0030	±0.0005	±0.0035
-2.65	0.1367	±0.0076	±0.0011	±0.0029	±0.0028	±0.0016	±0.0061
-2.55	0.1522	±0.0040	±0.0008	±0.0030	±0.0018	±0.0010	±0.0011
-2.45	0.1751	±0.0039	±0.0007	±0.0032	±0.0012	±0.0004	±0.0015
-2.35	0.2013	±0.0038	±0.0005	±0.0033	±0.0009	±0.0003	±0.0014
-2.25	0.2165	±0.0035	±0.0005	±0.0033	±0.0005	±0.0002	±0.0006
-2.15	0.2246	±0.0041	±0.0004	±0.0032	±0.0012	±0.0003	±0.0021
-2.05	0.2171	±0.0032	±0.0003	±0.0029	±0.0007	±0.0001	±0.0008
-1.95	0.2129	±0.0032	±0.0003	±0.0027	±0.0004	±0.0001	±0.0016
-1.85	0.2081	±0.0027	±0.0003	±0.0025	±0.0008	±0.0002	±0.0009
-1.75	0.2033	±0.0027	±0.0002	±0.0021	±0.0013	±0.0001	±0.0011
-1.65	0.2027	±0.0025	±0.0002	±0.0018	±0.0013	±0.0001	±0.0010
-1.55	0.2092	±0.0021	±0.0002	±0.0017	±0.0010	±0.0001	±0.0007
-1.45	0.2326	±0.0027	±0.0002	±0.0017	±0.0006	±0.0001	±0.0020
-1.35	0.2526	±0.0025	±0.0002	±0.0017	±0.0012	±0.0001	±0.0012
-1.25	0.2564	±0.0029	±0.0002	±0.0017	±0.0011	±0.0001	±0.0020
-1.15	0.2409	±0.0023	±0.0002	±0.0015	±0.0007	±0.0001	±0.0014
-1.05	0.2239	±0.0022	±0.0001	±0.0013	±0.0010	±0.0001	±0.0013
-0.95	0.2135	±0.0018	±0.0001	±0.0011	±0.0009	±0.0000	±0.0009
-0.85	0.2136	±0.0019	±0.0001	±0.0009	±0.0006	±0.0001	±0.0013
-0.75	0.2207	±0.0020	±0.0001	±0.0008	±0.0009	±0.0001	±0.0013
-0.65	0.2267	±0.0018	±0.0001	±0.0008	±0.0010	±0.0001	±0.0011
-0.55	0.2336	±0.0017	±0.0001	±0.0008	±0.0010	±0.0001	±0.0008
-0.45	0.2401	±0.0023	±0.0001	±0.0008	±0.0012	±0.0001	±0.0017
-0.35	0.2485	±0.0021	±0.0001	±0.0009	±0.0013	±0.0000	±0.0011
-0.25	0.2613	±0.0019	±0.0001	±0.0009	±0.0009	±0.0001	±0.0012
-0.15	0.2723	±0.0022	±0.0001	±0.0010	±0.0009	±0.0001	±0.0015
-0.05	0.2767	±0.0026	±0.0001	±0.0010	±0.0020	±0.0001	±0.0012

Table B.1: Contributions to the systematic uncertainty for $\epsilon \times A$ in each rapidity bin.

y	$\epsilon\times$ A	δ(total)	$\delta(e^{-}s.f.)$		δ (E scale)	δ (PDF)	δ (y modeling)
			stat.	method			
0.05	0.2770	±0.0024	±0.0001	±0.0010	±0.0005	±0.0001	±0.0019
0.15	0.2673	±0.0020	±0.0001	±0.0010	±0.0010	±0.0001	±0.0012
0.25	0.2537	±0.0022	±0.0001	±0.0009	±0.0009	±0.0001	±0.0015
0.35	0.2427	±0.0017	±0.0001	±0.0009	±0.0007	±0.0001	±0.0010
0.45	0.2316	±0.0019	±0.0001	±0.0008	±0.0011	±0.0001	±0.0011
0.55	0.2252	±0.0023	±0.0001	±0.0008	±0.0008	±0.0001	±0.0018
0.65	0.2160	±0.0015	±0.0001	±0.0007	±0.0011	±0.0000	±0.0001
0.75	0.2100	±0.0022	±0.0001	±0.0008	±0.0009	±0.0001	±0.0018
0.85	0.2044	±0.0019	±0.0001	±0.0009	±0.0013	±0.0001	±0.0008
0.95	0.2074	±0.0027	±0.0001	±0.0010	±0.0018	±0.0001	±0.0015
1.05	0.2211	±0.0017	±0.0001	±0.0012	±0.0009	±0.0001	±0.0005
1.15	0.2432	±0.0024	±0.0002	±0.0015	±0.0009	±0.0001	±0.0015
1.25	0.2561	±0.0028	±0.0002	±0.0016	±0.0012	±0.0001	±0.0019
1.35	0.2483	±0.0029	±0.0002	±0.0016	±0.0016	±0.0001	±0.0017
1.45	0.2231	±0.0022	±0.0002	±0.0016	±0.0010	±0.0001	±0.0011
1.55	0.2020	±0.0024	±0.0002	±0.0016	±0.0006	±0.0001	±0.0016
1.65	0.1977	±0.0024	±0.0002	±0.0017	±0.0010	±0.0001	±0.0012
1.75	0.2014	±0.0024	±0.0002	±0.0020	±0.0007	±0.0001	±0.0010
1.85	0.2081	±0.0030	±0.0003	±0.0023	±0.0009	±0.0002	±0.0015
1.95	0.2166	±0.0029	±0.0003	±0.0026	±0.0003	±0.0002	±0.0011
2.05	0.2228	±0.0031	±0.0003	±0.0029	±0.0007	±0.0002	±0.0006
2.15	0.2299	±0.0039	±0.0004	±0.0031	±0.0005	±0.0002	±0.0021
2.25	0.2221	±0.0036	±0.0005	±0.0033	±0.0012	±0.0003	±0.0006
2.35	0.2087	±0.0042	±0.0006	±0.0034	±0.0021	±0.0003	±0.0011
2.45	0.1852	±0.0039	±0.0007	±0.0033	±0.0016	±0.0003	±0.0007
2.55	0.1497	±0.0039	±0.0009	±0.0029	±0.0021	±0.0006	±0.0006
2.65	0.1313	±0.0045	±0.0011	±0.0028	±0.0026	±0.0006	±0.0017
2.8	0.0939	±0.0051	±0.0013	±0.0023	±0.0034	±0.0008	±0.0024
2.90	-	-	-	-	-	-	

Table B.2: Contributions to the systematic uncertainty for $\epsilon \times A$ in each rapidity bin.

B.2 Results of fractional differential cross section in bins of y

B.2 Results of fractional differential cross section in bins of y

y	$\frac{1}{\sigma} \times \frac{d\sigma}{dy} \pm stat. \pm syst.$	Candidate events	Background events	$\epsilon \times A$
-2.90	-	-	-	-
-2.8	$0.0030 \pm 0.0003 \pm 0.0002$	156	3.3 ± 1.8	0.1000 ± 0.0055
-2.65	$0.0093 \pm 0.0005 \pm 0.0005$	325	11.5 ± 3.5	0.1367 ± 0.0076
-2.55	$0.0218 \pm 0.0008 \pm 0.0006$	850	25.7 ± 7.6	0.1522 ± 0.0040
-2.45	$0.0379 \pm 0.0010 \pm 0.0009$	1,698	50.3 ± 12.2	0.1751 ± 0.0039
-2.35	$0.0540 \pm 0.0011 \pm 0.0011$	2,784	81.2 ± 18.9	0.2013 ± 0.0038
-2.25	$0.0718 \pm 0.0012 \pm 0.0012$	3,978	123.6 ± 16.4	0.2165 ± 0.0035
-2.15	$0.0868 \pm 0.0013 \pm 0.0016$	4,992	193.7 ± 9.6	0.2246 ± 0.0041
-2.05	$0.1114 \pm 0.0015 \pm 0.0017$	6,187	217.9 ± 17.0	0.2171 ± 0.0032
-1.95	$0.1277 \pm 0.0016 \pm 0.0019$	6,961	252.2 ± 11.9	0.2129 ± 0.0032
-1.85	$0.1473 \pm 0.0017 \pm 0.0020$	7,845	269.6 ± 13.3	0.2081 ± 0.0027
-1.75	$0.1643 \pm 0.0018 \pm 0.0022$	8,551	245.1 ± 17.7	0.2033 ± 0.0027
-1.65	$0.1818 \pm 0.0019 \pm 0.0023$	9,436	256.3 ± 20.6	0.2027 ± 0.0025
-1.55	$0.1984 \pm 0.0020 \pm 0.0020$	10,623	247.2 ± 20.8	0.2092 ± 0.0021
-1.45	$0.2066 \pm 0.0019 \pm 0.0025$	12,298	275.3 ± 30.8	0.2326 ± 0.0027
-1.35	$0.2216 \pm 0.0019 \pm 0.0022$	14,327	288.5 ± 21.1	0.2526 ± 0.0025
-1.25	$0.2263 \pm 0.0019 \pm 0.0026$	14,846	298.1 ± 18.8	0.2564 ± 0.0029
-1.15	$0.2355 \pm 0.0020 \pm 0.0023$	14,520	304.9 ± 11.0	0.2409 ± 0.0023
-1.05	$0.2400 \pm 0.0021 \pm 0.0024$	13,750	286.4 ± 18.2	0.2239 ± 0.0022
-0.95	$0.2453 \pm 0.0022 \pm 0.0021$	13,406	270.8 ± 21.5	0.2135 ± 0.0018
-0.85	$0.2505 \pm 0.0022 \pm 0.0023$	13,696	263.1 ± 26.6	0.2136 ± 0.0019
-0.75	$0.2580 \pm 0.0022 \pm 0.0023$	14,572	292.3 ± 25.6	0.2207 ± 0.0020
-0.65	$0.2658 \pm 0.0022 \pm 0.0022$	15,422	262.0 ± 14.0	0.2267 ± 0.0018
-0.55	$0.2705 \pm 0.0022 \pm 0.0021$	16,172	256.1 ± 28.4	0.2336 ± 0.0017
-0.45	$0.2677 \pm 0.0021 \pm 0.0026$	16,449	261.5 ± 18.3	0.2401 ± 0.0023
-0.35	$0.2728 \pm 0.0021 \pm 0.0023$	17,351	241.8 ± 17.8	0.2485 ± 0.0021
-0.25	$0.2741 \pm 0.0021 \pm 0.0020$	18,332	256.1 ± 17.9	0.2613 ± 0.0019
-0.15	$0.2744 \pm 0.0020 \pm 0.0022$	19,128	235.6 ± 25.2	0.2723 ± 0.0022
-0.05	$0.2769 \pm 0.0020 \pm 0.0027$	19,614	227.1 ± 22.9	0.2767 ± 0.0026

Table B.3: Summary of the measurement of $\frac{1}{\sigma}\frac{d\sigma}{dy}$ per rapidity bin for $Z/\gamma^* \rightarrow e^+e^-$events with mass $66 < M_{ee} < 116$ GeV.

B.2 Results of fractional differential cross section in bins of y

y	$\frac{1}{\sigma} \times \frac{d\sigma}{dy} \pm stat. \pm syst.$	Candidate events	Background events	$\epsilon \times A$
0.05	$0.2722 \pm 0.0020 \pm 0.0023$	19,303	226.1 ± 22.2	0.2770 ± 0.0024
0.15	$0.2739 \pm 0.0020 \pm 0.0021$	18,737	223.5 ± 23.0	0.2673 ± 0.0020
0.25	$0.2732 \pm 0.0021 \pm 0.0024$	17,742	257.7 ± 18.8	0.2537 ± 0.0022
0.35	$0.2726 \pm 0.0021 \pm 0.0020$	16,933	249.6 ± 30.6	0.2427 ± 0.0017
0.45	$0.2692 \pm 0.0022 \pm 0.0022$	15,961	259.7 ± 18.5	0.2316 ± 0.0019
0.55	$0.2666 \pm 0.0022 \pm 0.0027$	15,371	265.1 ± 14.2	0.2252 ± 0.0023
0.65	$0.2718 \pm 0.0023 \pm 0.0020$	15,027	253.6 ± 25.8	0.2160 ± 0.0015
0.75	$0.2560 \pm 0.0022 \pm 0.0028$	13,761	264.4 ± 23.7	0.2100 ± 0.0022
0.85	$0.2531 \pm 0.0023 \pm 0.0024$	13,244	278.6 ± 13.0	0.2044 ± 0.0019
0.95	$0.2438 \pm 0.0022 \pm 0.0032$	12,947	258.5 ± 34.6	0.2074 ± 0.0027
1.05	$0.2428 \pm 0.0021 \pm 0.0020$	13,736	289.1 ± 21.6	0.2211 ± 0.0017
1.15	$0.2341 \pm 0.0020 \pm 0.0023$	14,568	301.6 ± 14.5	0.2432 ± 0.0024
1.25	$0.2254 \pm 0.0019 \pm 0.0025$	14,774	266.1 ± 14.4	0.2561 ± 0.0028
1.35	$0.2162 \pm 0.0019 \pm 0.0026$	13,745	286.7 ± 20.4	0.2483 ± 0.0029
1.45	$0.2060 \pm 0.0020 \pm 0.0021$	11,762	256.6 ± 20.2	0.2231 ± 0.0022
1.55	$0.1954 \pm 0.0020 \pm 0.0023$	10,104	258.7 ± 17.4	0.2020 ± 0.0024
1.65	$0.1819 \pm 0.0020 \pm 0.0022$	9,203	246.2 ± 17.9	0.1977 ± 0.0024
1.75	$0.1668 \pm 0.0019 \pm 0.0020$	8,598	260.1 ± 16.2	0.2014 ± 0.0024
1.85	$0.1460 \pm 0.0017 \pm 0.0021$	7,774	249.9 ± 13.2	0.2081 ± 0.0030
1.95	$0.1272 \pm 0.0016 \pm 0.0017$	7,051	247.3 ± 6.9	0.2166 ± 0.0029
2.05	$0.1100 \pm 0.0014 \pm 0.0015$	6,271	212.5 ± 6.6	0.2228 ± 0.0031
2.15	$0.0874 \pm 0.0013 \pm 0.0015$	5,142	182.2 ± 7.6	0.2299 ± 0.0039
2.25	$0.0719 \pm 0.0012 \pm 0.0012$	4,088	131.5 ± 18.7	0.2221 ± 0.0036
2.35	$0.0539 \pm 0.0010 \pm 0.0012$	2,878	82.8 ± 19.9	0.2087 ± 0.0042
2.45	$0.0372 \pm 0.0009 \pm 0.0008$	1,763	49.0 ± 15.9	0.1852 ± 0.0039
2.55	$0.0223 \pm 0.0008 \pm 0.0006$	856	21.2 ± 10.5	0.1497 ± 0.0039
2.65	$0.0118 \pm 0.0006 \pm 0.0004$	398	9.0 ± 2.9	0.1313 ± 0.0045
2.8	$0.0032 \pm 0.0003 \pm 0.0002$	155	4.4 ± 2.4	0.0939 ± 0.0051
2.90	-	-	-	-

Table B.4: Summary of the measurement of $\frac{1}{\sigma}\frac{d\sigma}{dy}$ per rapidity bin for $Z/\gamma^* \rightarrow e^+e^-$events with mass $66 < M_{ee} < 116$ GeV.

Appendix C

Additional cross checks of the HoR method

C.1 Performance of the HoR discriminant in RunIIb-2 data

C.1.1 Performance of the HoR discriminant in the CC

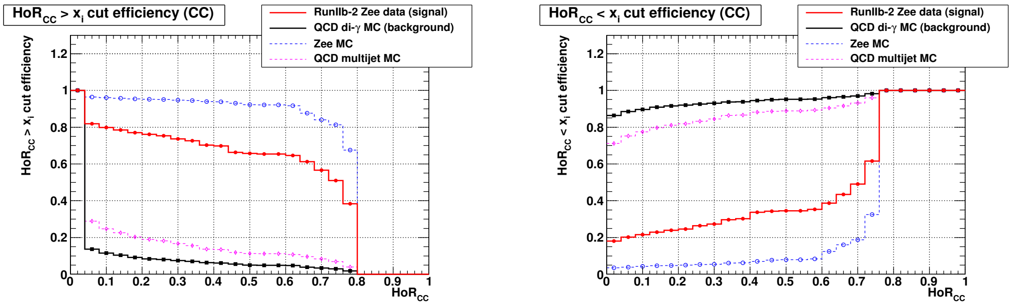

(a) Efficiencies of $\mathrm{HoR}_{CC} > x_i$ for electron identification (b) Efficiencies of $\mathrm{HoR}_{CC} < x_i$ for photon identification

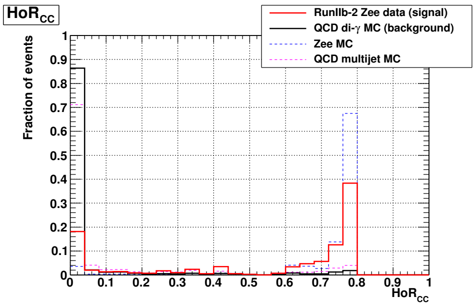

(c) HoR_{CC}

Figure C.1: Efficiencies of HoR_{CC} cuts and distributions of HoR_{CC}.

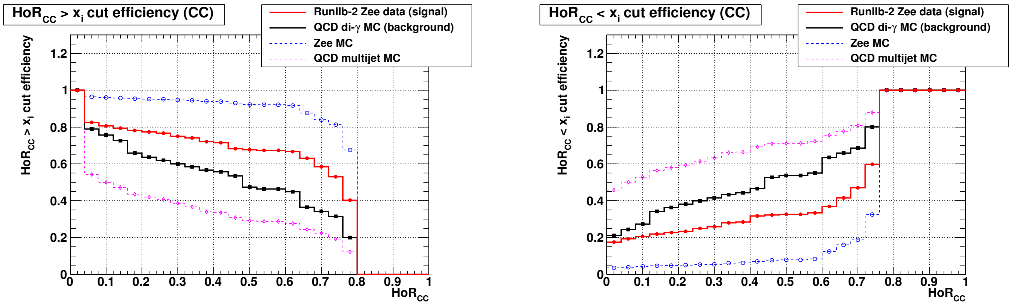

(a) Efficiencies of HoR$_{CC} > x_i$ for electron identification

(b) Efficiencies of HoR$_{CC} < x_i$ for photon identification

Figure C.2: Efficiencies of HoR$_{CC}$ cuts for CC EM objects with $P_{trk} > 0.0$.

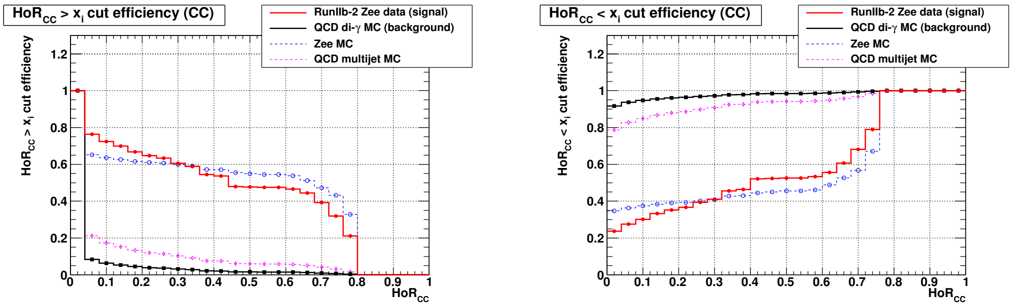

(a) Efficiencies of HoR$_{CC} > x_i$ for electron identification

(b) Efficiencies of HoR$_{CC} < x_i$ for photon identification

Figure C.3: Efficiencies of HoR$_{CC}$ cuts for CC EM objects with $P_{trk} < 0.0$.

C.1.2 Performance of the HoR discriminant in the EC

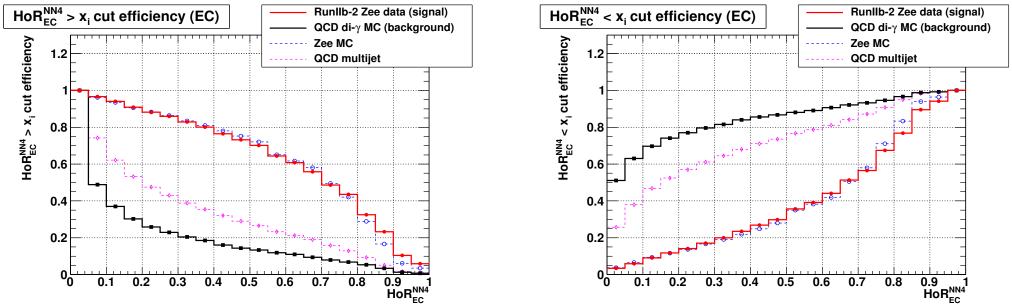

(a) Efficiencies of $\mathrm{HoR}^{NN4}_{EC} > x_i$ for electron identification (b) Efficiencies of $\mathrm{HoR}^{NN4}_{EC} < x_i$ for photon identification

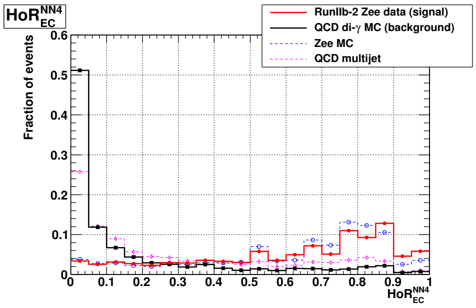

(c) HoR^{NN4}_{EC}

Figure C.4: Efficiencies of HoR^{NN4}_{EC} cut and distribution of HoR^{NN4}_{EC}.

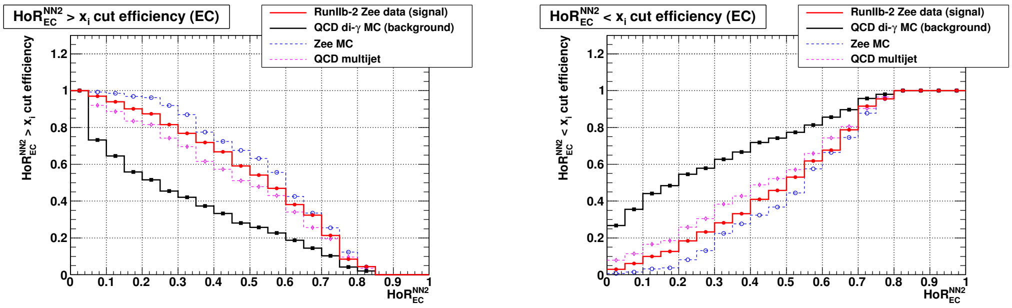

(a) Efficiencies of HoR$_{EC}^{NN2}$ $> x_i$ for electron identification

(b) Efficiencies of HoR$_{EC}^{NN2}$ $< x_i$ for photon identification

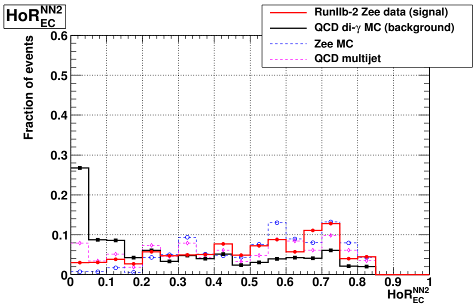

(c) HoR$_{EC}^{NN2}$

Figure C.5: Efficiencies of HoR$_{EC}^{NN2}$ cut and distribution of HoR$_{EC}^{NN2}$.

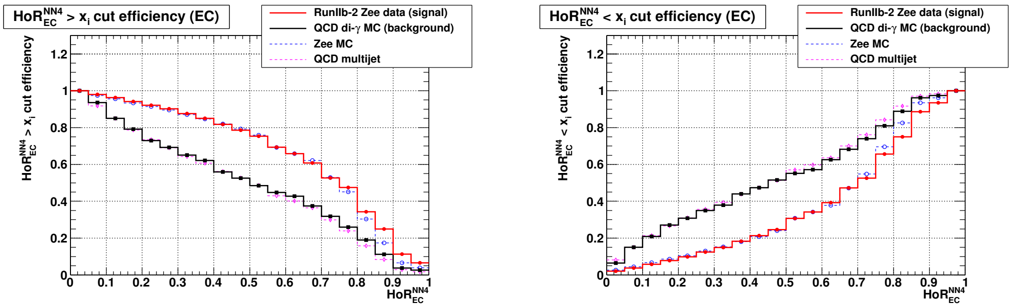

(a) Efficiencies of HoR$_{EC}^{NN4} > x_i$ for electron identification

(b) Efficiencies of HoR$_{EC}^{NN4} < x_i$ for photon identification

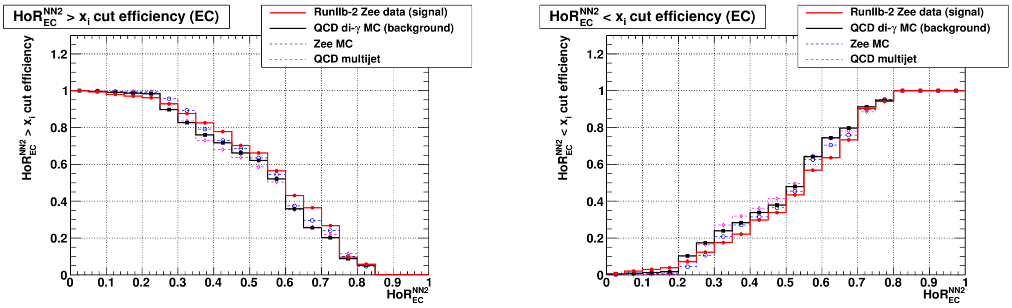

(c) Efficiencies of HoR$_{EC}^{NN2} > x_i$ for electron identification

(d) Efficiencies of HoR$_{EC}^{NN2} < x_i$ for photon identification

Figure C.6: Efficiencies of HoR$_{EC}^{NN4}$ and HoR$_{EC}^{NN2}$ cuts for EC EM objects with $P_{trk} > 0.0$.

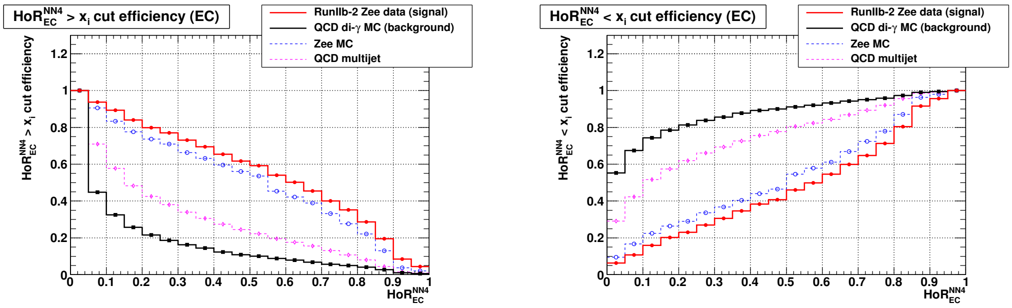

(a) Efficiencies of $\text{HoR}_{EC}^{NN4} > x_i$ for electron identification (b) Efficiencies of $\text{HoR}_{EC}^{NN4} < x_i$ for photon identification

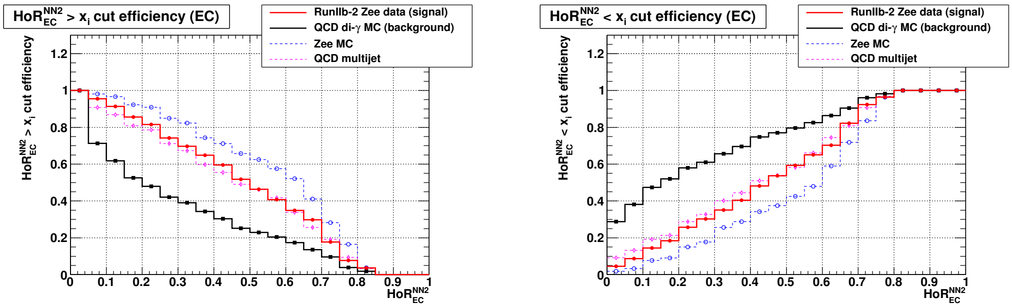

(c) Efficiencies of $\text{HoR}_{EC}^{NN2} > x_i$ for electron identification (d) Efficiencies of $\text{HoR}_{EC}^{NN2} < x_i$ for photon identification

Figure C.7: Efficiencies of HoR_{EC}^{NN4} cuts for EC EM objects with $P_{trk} < 0.0$.

C.2 Performance of the HoR discriminant for random noise in the EC

To study the performance of HoR$_{EC}^{NN4}$ and HoR$_{EC}^{NN2}$ for random noise in the EC, we define a road which has an equal distance in ϕ and η to both the tag and probe electrons selected from Z $\rightarrow$ ee data events. We do not expect the electrons to leave any activities in the tracking detector along the direction of this road. Thus hits found along this road are supposed to be random noise in the detector.

Similar to Figure 4.28 and Figure 4.29, Figure C.8 and Figure C.9 show the cut efficiencies of HoR$_{EC}^{NN4}$ and HoR$_{EC}^{NN2}$ for the random noise together with that for Z $\rightarrow$ ee data/MC events, and that for QCD di-γ events.

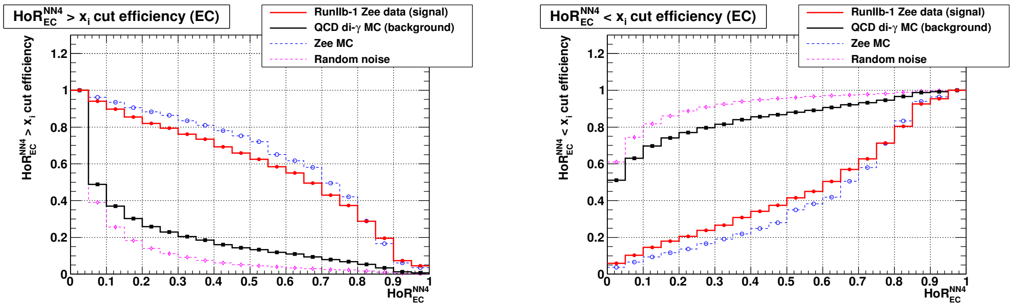

(a) Efficiencies of HoR$_{EC}^{NN4}$ $> x_i$ for electron identification

(b) Efficiencies of HoR$_{EC}^{NN4}$ $< x_i$ for photon identification

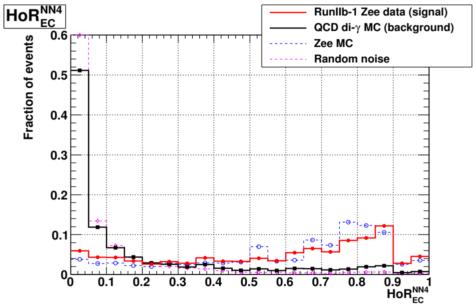

(c) HoR$_{EC}^{NN4}$

Figure C.8: Efficiencies of HoR$_{EC}^{NN4}$ cut and distribution of HoR$_{EC}^{NN4}$.

Similar to Figure 4.33, Figure C.10 show the HoR$_{EC}^{NN4}$ (HoR$_{EC}^{NN2}$) cut efficiencies for EC EM objects with $P_{trk} \geq 0.0$ and $P_{trk} < 0.0$, respectively.

Figure C.11 and Figure C.12 show the HoR$_{EC}^{NN4}$ > 0.2 and HoR$_{EC}^{NN2}$ > 0.2 cut efficiencies as a function of E_T, η_{det}, ϕ_{det} and instanteneous luminosity. Please note that the distributions are made for EM objects with $P_{trk} < 0.0$ since the HoR$_{EC}^{NN4}$ and HoR$_{EC}^{NN2}$ are recommended to be used on those EM objects. As expected, the HoR discriminant for random noise behaves exactly the same as

C.2 Performance of the HoR discriminant for random noise in the EC

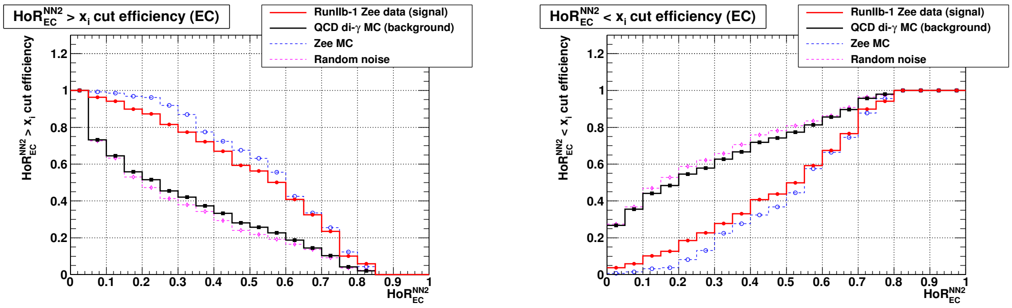

(a) Efficiencies of HoR$_{EC}^{NN2}$ $> x_i$ for electron identification

(b) Efficiencies of HoR$_{EC}^{NN2}$ $< x_i$ for photon identification

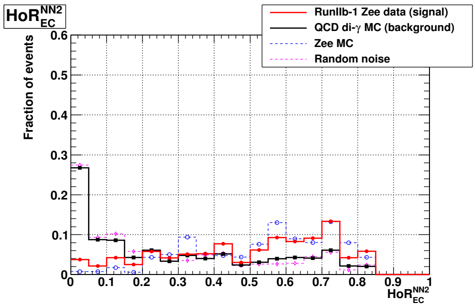

(c) HoR$_{EC}^{NN2}$

Figure C.9: Efficiencies of HoR$_{EC}^{NN2}$ cut and distribution of HoR$_{EC}^{NN2}$.

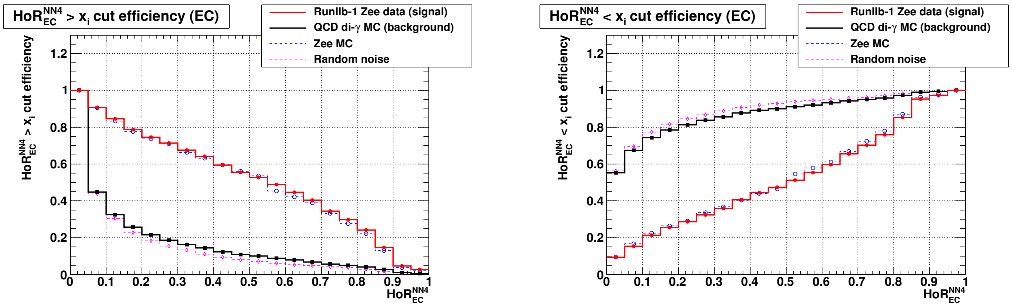

(a) Efficiencies of HoR$_{EC}^{NN4}$ $> x_i$ for electron identification

(b) Efficiencies of HoR$_{EC}^{NN4}$ $< x_i$ for photon identification

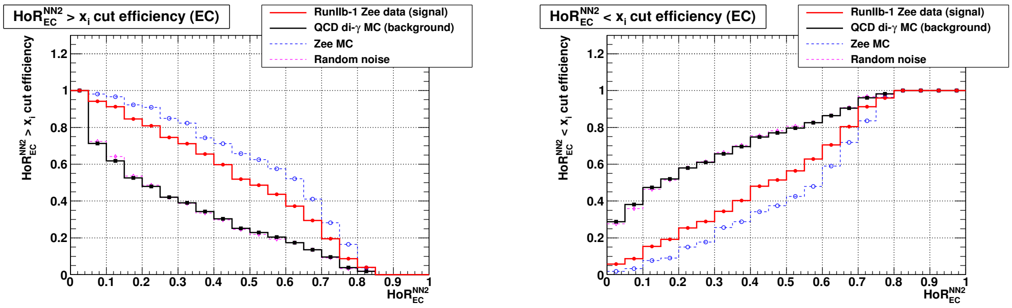

(c) Efficiencies of HoR$_{EC}^{NN2}$ $> x_i$ for electron identification

(d) Efficiencies of HoR$_{EC}^{NN2}$ $< x_i$ for photon identification

Figure C.10: Efficiencies of HoR$_{EC}^{NN4}$ cuts for EC EM objects with $P_{trk} < 0.0$.

for photons.

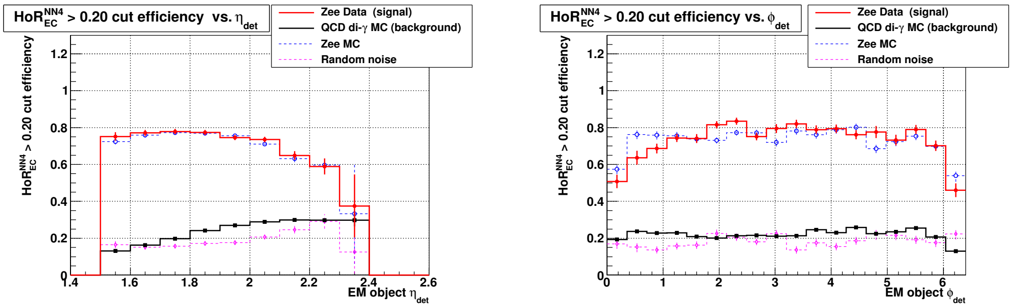

(a) Eff. vs. η_{det}

(b) Eff. vs. ϕ_{det}

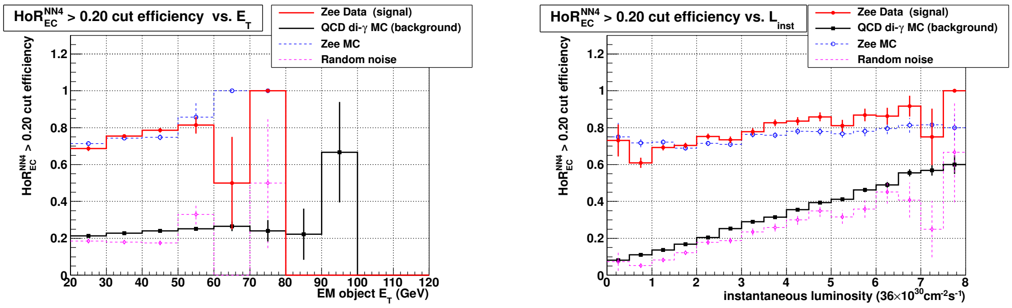

(c) Eff. vs. E_T

(d) Eff. vs. instanteneous luminosity

Figure C.11: HoR$_{EC}^{NN4}$ > 0.2 cut efficiences as functions of E_T, η_{det}, ϕ_{det} and instantaneous luminosity for EM objects with $P_{trk} < 0.0$.

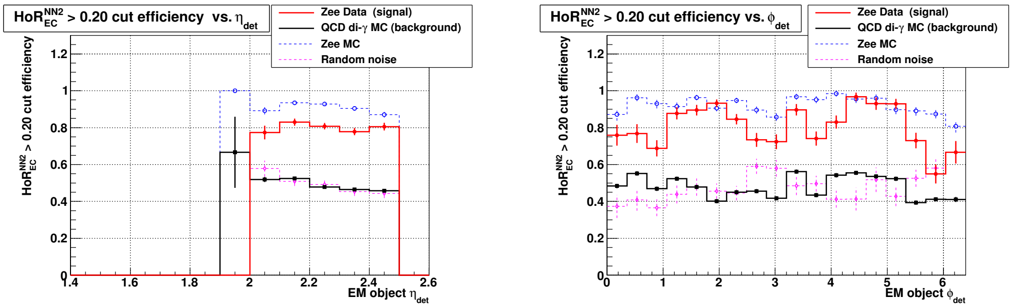

(a) Eff. vs. η_{det}

(b) Eff. vs. ϕ_{det}

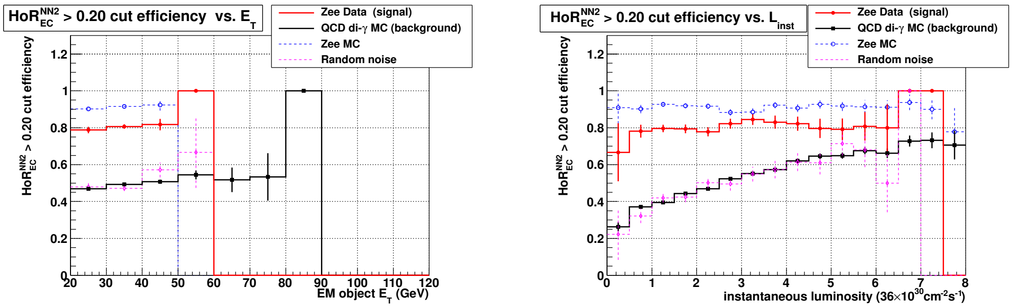

(c) Eff. vs. E_T

(d) Eff. vs. instanteneous luminosity

Figure C.12: HoR$_{EC}^{NN2}$ $>$ 0.2 cut efficiences as functions of E_T, η_{det}, ϕ_{det} and instantaneous luminosity.

Appendix D

Studies of online SMT clustering algorithm

In the online SMT clustering algorithm, four major steps are taken to form an cluster from the readout of detector.

1. Unpacking the SMT raw data, applying the off-line threshold (pedestal + 8 ADC counts) for every strip and apply an occupancy veto on a sensor chip (denote as sensor hereafter) basis.

2. Calculating the energy deposit (dE) in each strip and removing the dead or noisy strips;
   dE = (X - P) × G, where X is the readout ADC count of the considered strip (in the unit of ADC count), P is the pedestal for that channel (in the unit of ADC count) and G is the gain factor (G = 0 for dead or noisy channels, and G = 0.00353567 MeV per ADC count) for all the other channels).

3. Reconstructing 1D clusters using signal captured by single-sided sensors and those by each side of double-sided sensors. 1D clusters are reconstructed by several adjacent strips or one isolated single strip if the total energy deposit of the adjacent strips (or the single isolated strip) exceeds the cluster threshold, which is equivalent to 8 ADC count

4. Reconstructing 2D clusters based on the 1D clusters which have been reconstructed in one side of the double-sided sensors. (The 2-D clusters are made by any possible combinations of 1D cluster from n-side and p-side on the sensor chip basis.)

We operated the SMT in a “read-all” mode. Raw signals captured by the SMT were recorded to tape directly without any online processing in this mode. The online clustering algorithm was then studied offline by using these record raw signals. Raw signals taken under low instantaneous luminosity and high instantaneous luminosity are studied separately.

To study the performance of the clustering algorithm, we examine the reconstructed clusters in the following groups:

1. all of the reconstructed clusters (detailed plots can be found in Section D.1);
2. clusters which have been used in reconstructing a track with relatively good quality;
3. clusters which have been used in reconstructing a track with relatively poor quality (detailed plots can be found in Section D.2).

These clusters are denoted as “all clusters”, “good track clusters” and “poor track cluster” in this chapter hereafter.

The SMT clusters from different sensors are grouped in various levels:

1. 1. clusters from the same kind of sensors;
2. 2. clusters from the same layer of a SMT barrel;
3. 3. clusters from the same F-disk or H-disk.

Due to the large amount of SMT sensor, only plots of the clusters from the same kind of sensors are included. Plots for the second and third group can be found through the link `http://www-clued0.fnal.gov/~dingpf/Main_257601v5.php`.

We looked at the following properties of cluster during the examination :

1. the cluster width, which is reflected by the number of strips (N_{strips}) used in the cluster reconstruction;
2. the cluster charge (E_{pulse}), which is the energy deposit;
3. the difference of cluster width (ΔN_{strips}) and cluster charge (ΔE_{pulse}) between the sub-clusters in a 2D cluster (two 1D cluster for each side of a 2D sensor).

As learned from these extensive examinations, several proposals to improve the clustering algorithm had been made:

1. an additional algorithm, which identifies certain type of errors caused by pattern recognition, to remove noisy strips before cluster construction;
2. using a sensor based cluster thresholds, instead of a constant threshold which was used previously in the clustering algorithm;
3. introducing a cut on ΔE_{pulse} and ΔN_{strips} during the combination of 1D clusters for 2D clusters reconstruction (2D clusters were previously made by using all the possible combinations of 1D clusters found on each side of a double-sided sensor, ambiguity become large when multiple hits are captured by the sensor at the same time).

The performance of these new algorithms had been evaluated by reconstructing the K_{short} mass spectra in the tracking detector. The number of events enter into the peak region of in the mass spectra, as well as the width and significance of the peak is compared.

Modifications of the online clustering algorithm based on the studies had been implemented for data taking. The second and third proposal requires the tuning of the sensor based cut value. Since the overall performance of the SMT varies in difference instantaneous environment, The tuning of these cut values need to be studied extensively and carefully for high and low instantaneous luminosity environment. Also due to the aging of SMT sensors, these cut values need to be justified time-to-time.

Further information on this study can be found in Reference [43].

The following conclusions can be made from the plots provided in this Section D.1 to Section D.2:

- Clusters made of two strips take the larges fraction of all the clusters in layer 0; single strip clusters take the larges fraction of all the clusters in other sensors. This situation is caused by the high occupancy of layer 0 sensors.
- There are two peaks for the E_{pulse} distribution of the clusters from some sensors. This two-peak structure is much less obvious for the clusters which have been used in a successful reconstruction of a good track. Thus the clusters entered before the second peak are mainly noisy clusters, and should might be removed by a proper choice of pedestal threshold and/or cluster threshold.
- 2D clusters with large ΔN_{strips} or ΔE_{pulse} are found in certain sensors. Since we expect that the "real" 2D cluster made by a track should have

> similar cluster width and cluster charge in both n-side and p-side of the sensor, these 2D clusters with large ΔN_{strips} or ΔE_{pulse} are likely to be a wrong combination of the 1D clusters, thus the hit which may generate these 2D clusters does not physically exist. This is confirmed by looking at the clusters from good tracks. The width of the distributions for these two variables are much smaller in this case.

These leads to the proposals we made for the improvement of SMT clustering algorithm.

D.1 Properties of all clusters

D.1.1 Plots of N_{strips} for all clusters

Figure D.1 to Figure D.6 shows the plots of N_{strips} for all the reconstructed clusters.

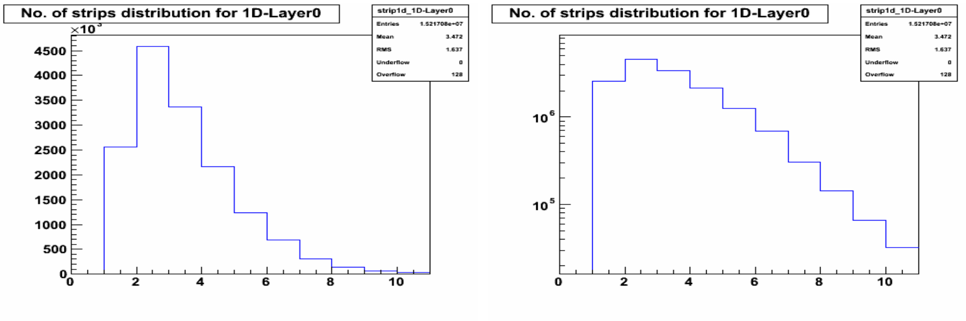

Figure D.1: N_{strips} for layer 0 clusters.

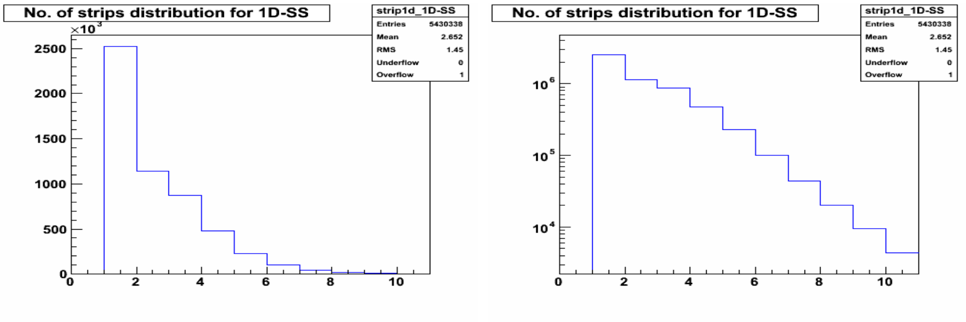

Figure D.2: N_{strips} for the clusters from SS sensors in layer 1 and layer 3.

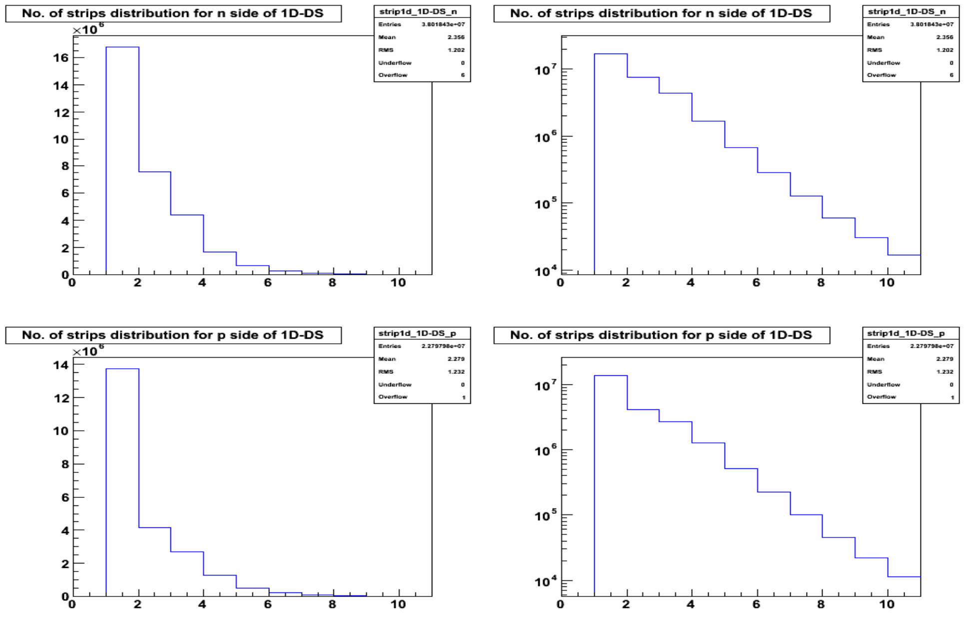

Figure D.3: N_{strips} for the clusters from the barrel DS sensors.

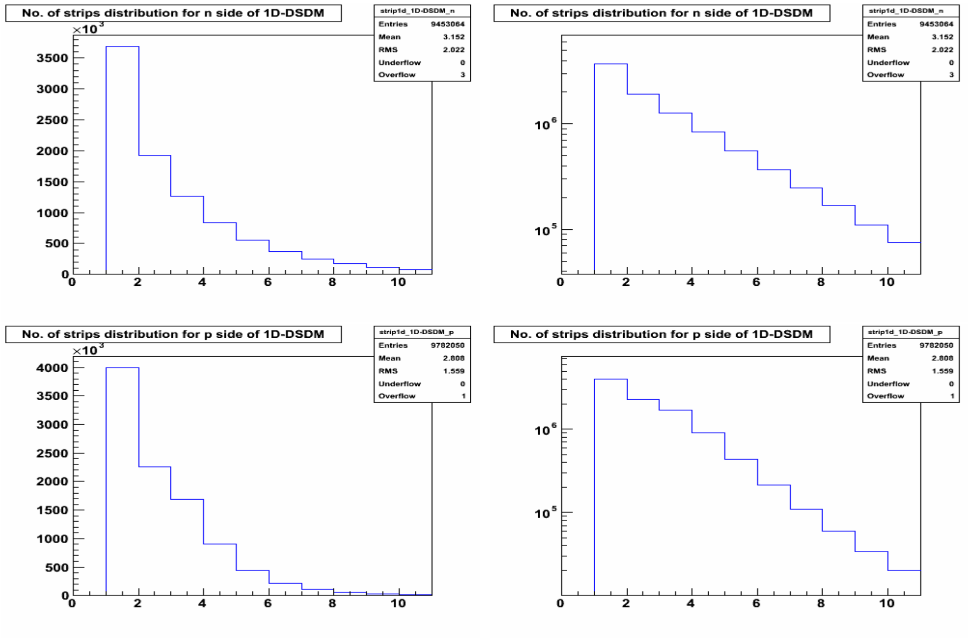

Figure D.4: N_{strips} for the clusters from the barrel DSDM sensors.

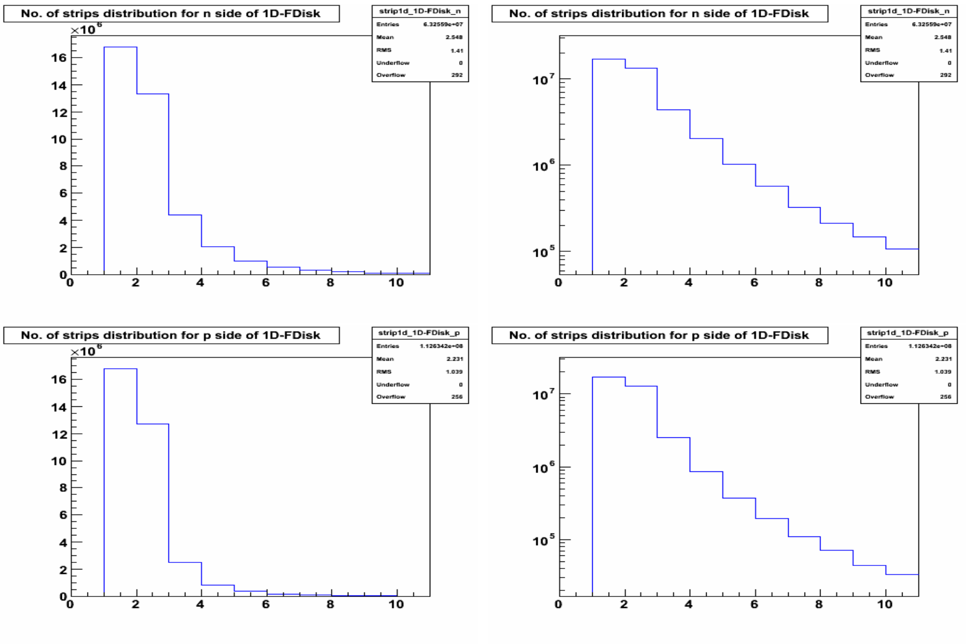

Figure D.5: N_{strips} for the clusters from F-disks.

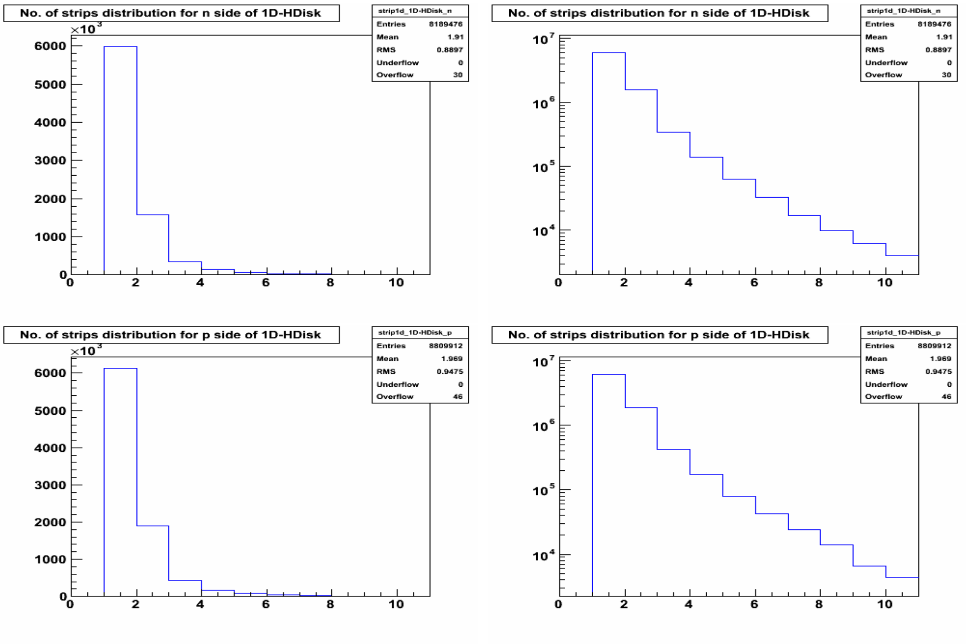

Figure D.6: N_{strips} for the clusters from the H-disks.

D.1.2 Plots of E_{pulse} for all clusters

Figure D.7 to Figure D.12 show the plots of E_{pulse} for all the reconstructed clusters.

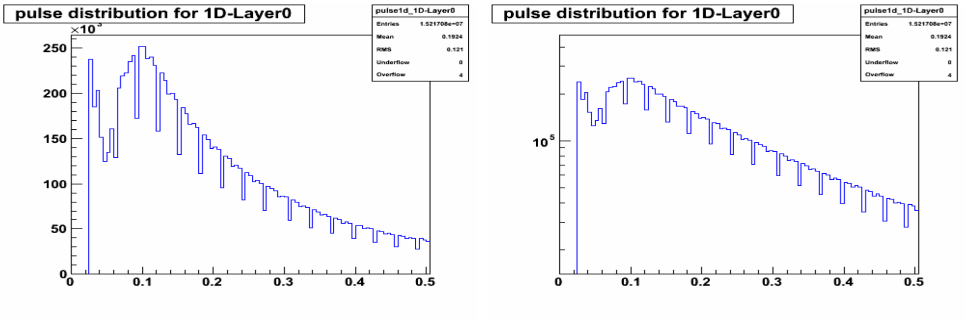

Figure D.7: E_{pulse} for layer 0 clusters.

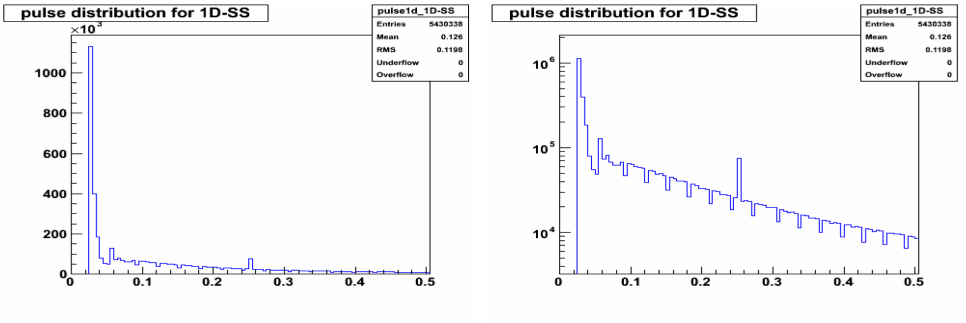

Figure D.8: E_{pulse} for the clusters from SS sensors in layer 1 and layer 3.

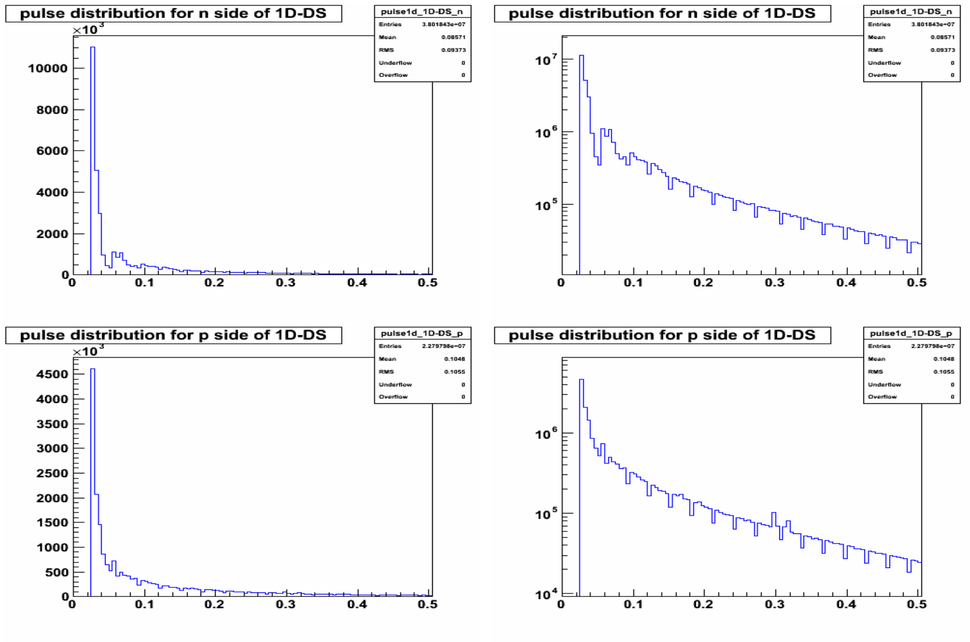

Figure D.9: E_{pulse} for the clusters from the barrel DS sensors.

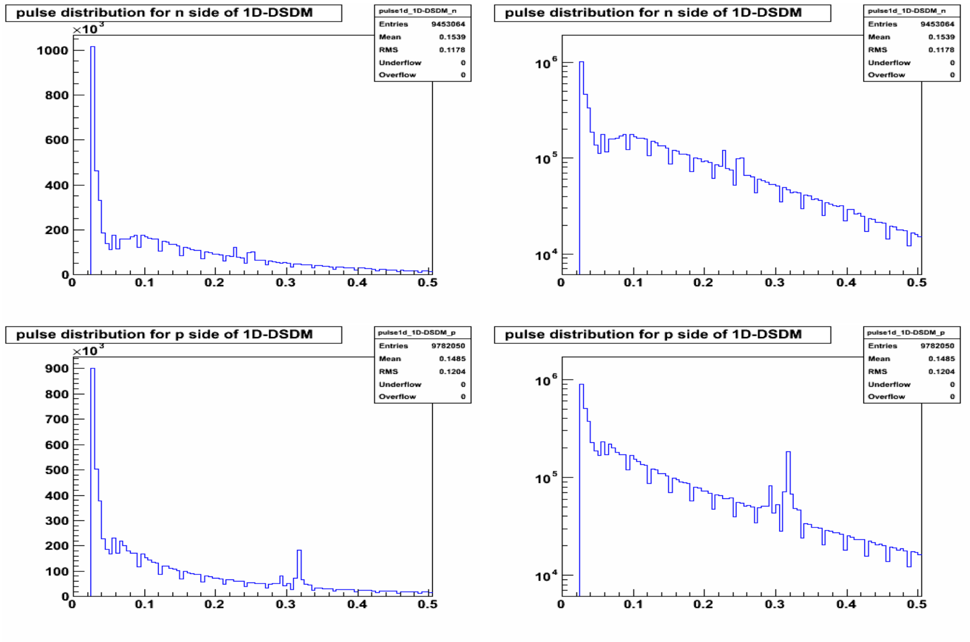

Figure D.10: E_{pulse} for the clusters from the barrel DSDM sensors.

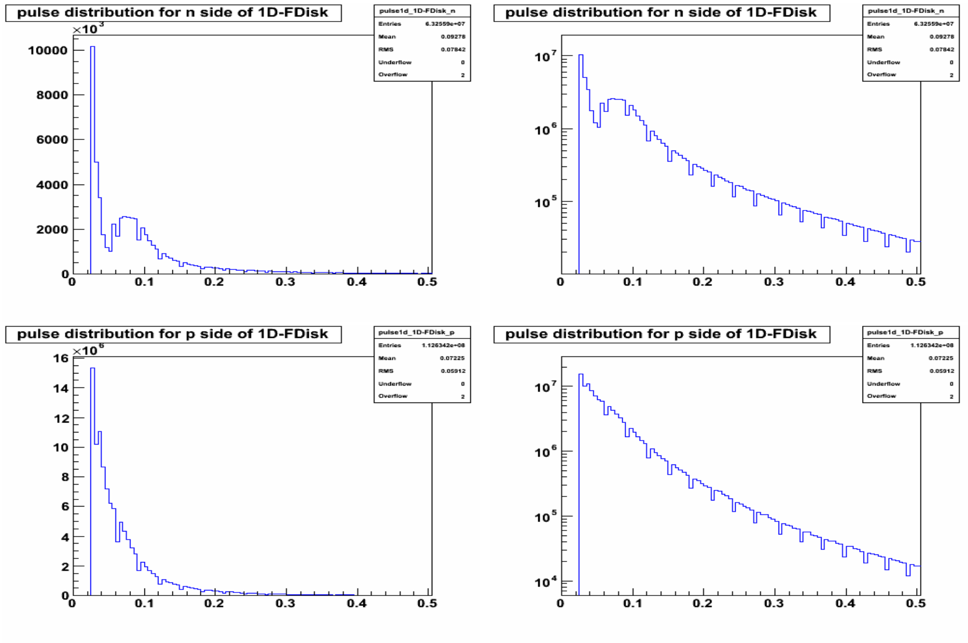

Figure D.11: E_{pulse} for the clusters from F-disks.

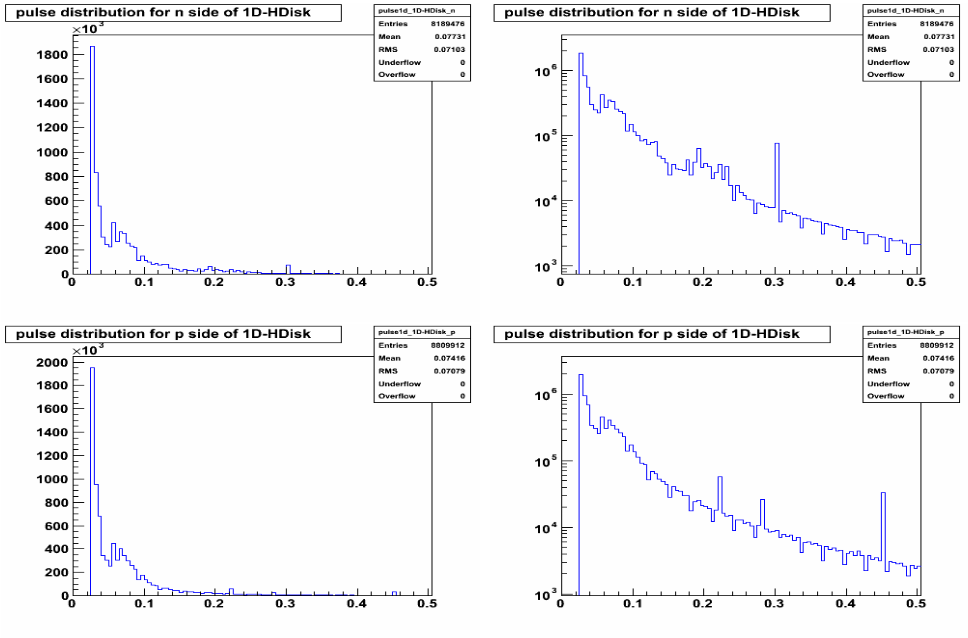

Figure D.12: E_{pulse} for the clusters from H-disk.

D.1.3 Plots of ΔN_{strips} for all the reconstructed 2-D clusters

Figure D.13 to Figure D.16 show the plots of ΔN_{strips} for all the reconstructed 2-D clusters.

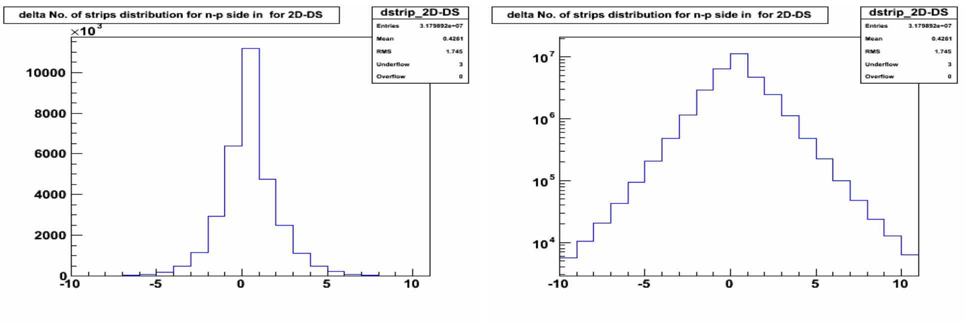

Figure D.13: ΔN_{strips} for the clusters from the barrel DS sensors.

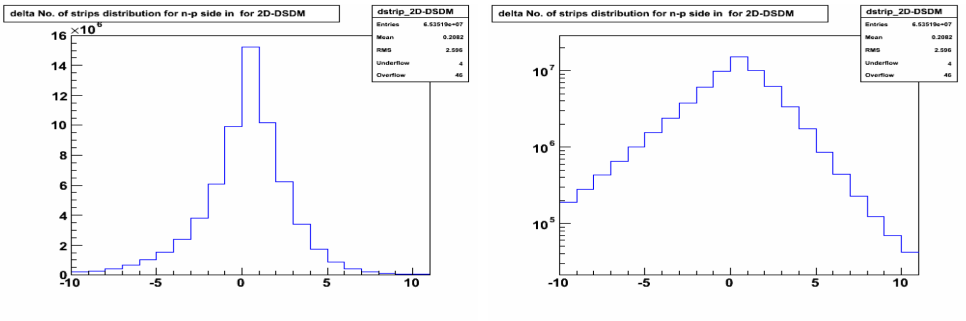

Figure D.14: ΔN_{strips} for the clusters from the barrel DSDM sensors.

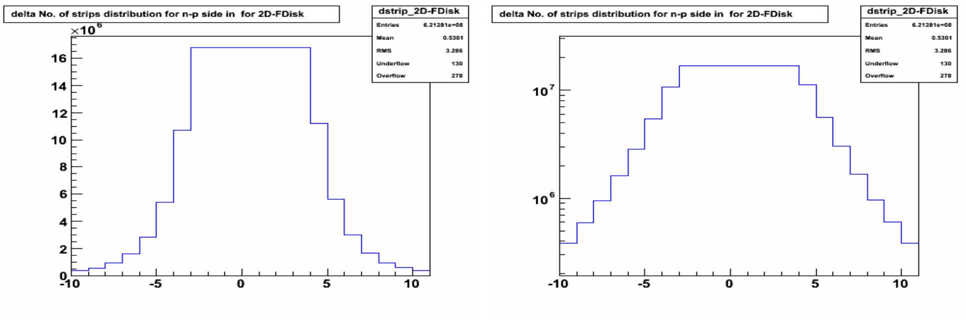

Figure D.15: ΔN_{strips} for the clusters from F-disks.

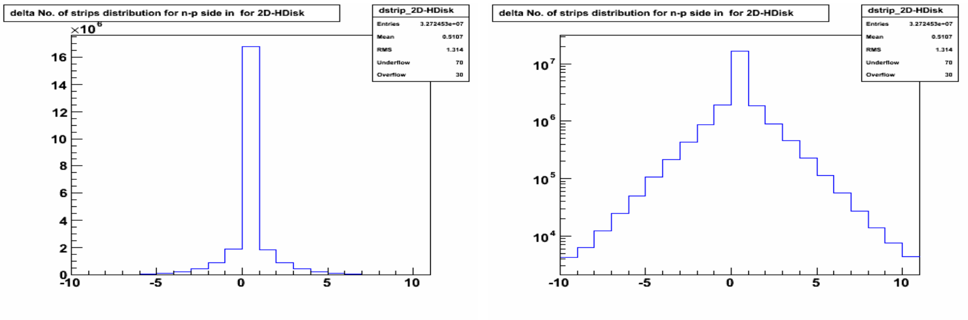

Figure D.16: ΔN_{strips} for the clusters from H-disks.

D.1.4 Plots of ΔE_{pulse} for all the reconstructed 2-D clusters

Figure D.17 to Figure D.20 show the plots of ΔE_{pulse} for all the reconstructed 2-D clusters.

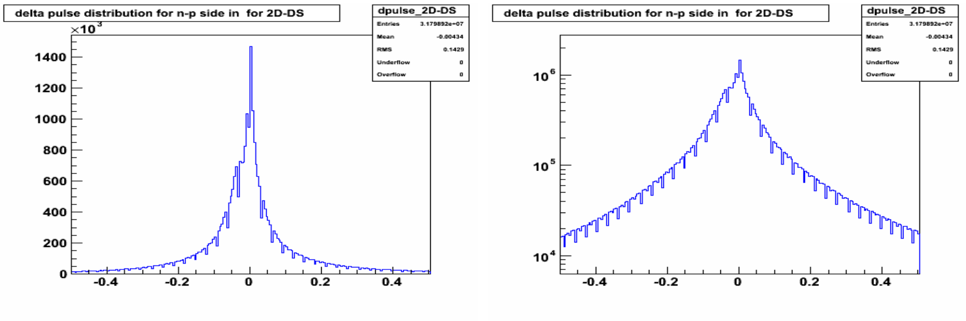

Figure D.17: ΔE_{pulse} for the clusters from the barrel DS sensors.

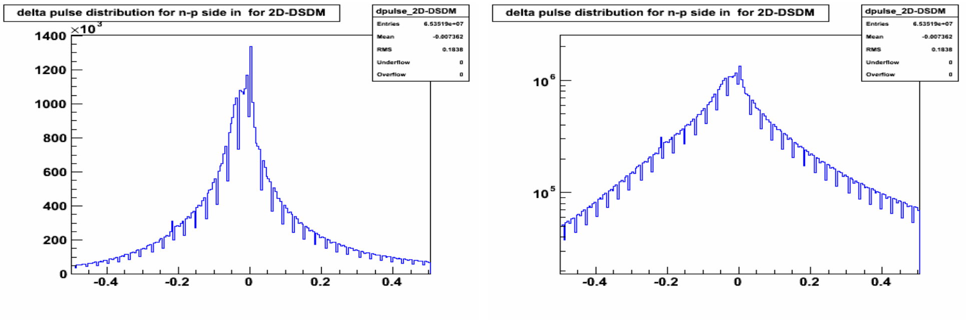

Figure D.18: ΔE_{pulse} for the clusters from the barrel DSDM sensors.

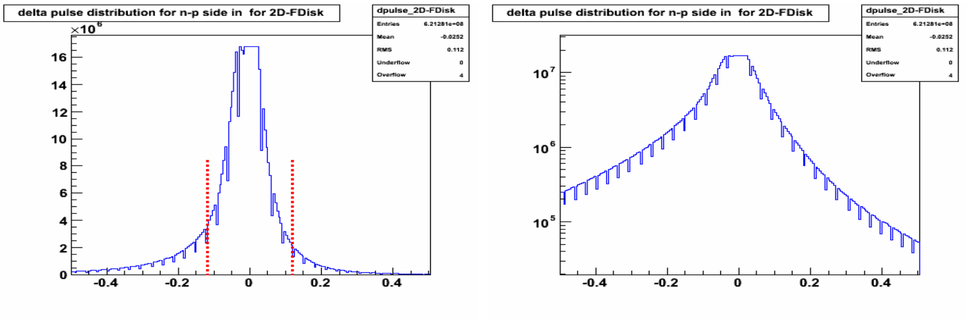

Figure D.19: ΔE_{pulse} for the clusters from F-disks.

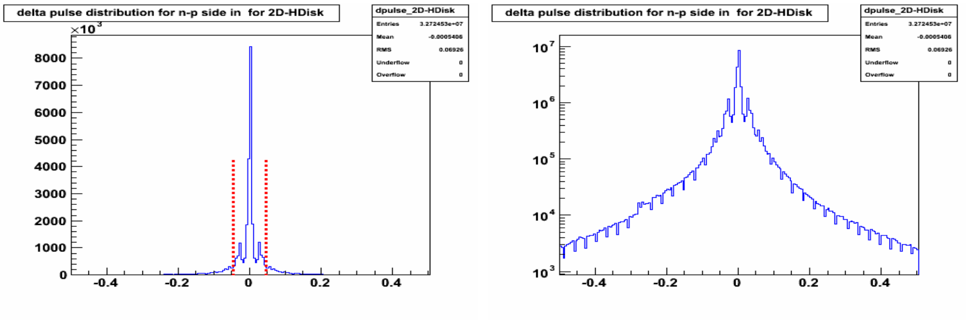

Figure D.20: ΔE_{pulse} for the clusters from H-disks.

D.2 Properties of good and bad track clusters

By looking at the plots for all the clusters in Section D.1, we found that there are certain fraction of noisy clusters with small E_{pulse} or large ΔE_{pulse} and ΔN_{strips}. We found these clusters are mainly noisy clusters or clusters which are wrongly reconstructed, thus do not represent a physical hit in the SMT caused by charged particles.

Clusters from tracks with relatively good and bad qualities are compared in this section. Good separation is obtained with proper selection criteria of the tracks (an example shown in Figure D.21 as an example).

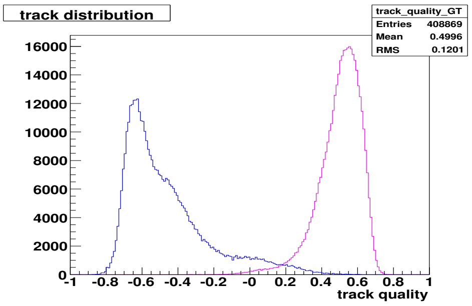

Figure D.21: The fake-track-killer discriminant for good (pink) and bad (blue) tracks. The distribution of bad tracks are normalized to that of good tracks.

Plots of N_{strips} for the clusters of good and bad tracks

Figure D.22 to Figure D.27 shows the plots of N_{strips} for the clusters from good and bad tracks.

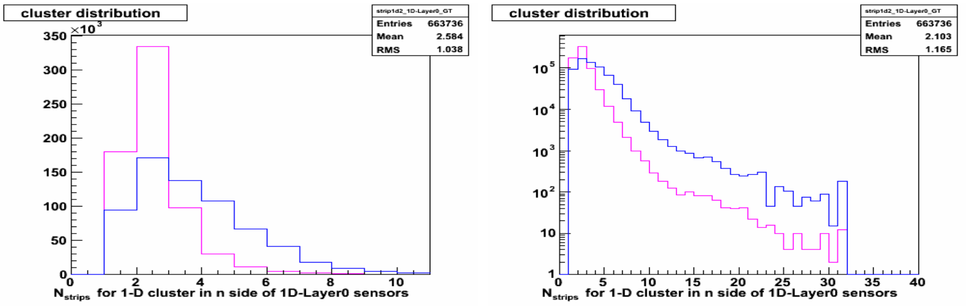

Figure D.22: N_{strips} for layer 0 clusters.

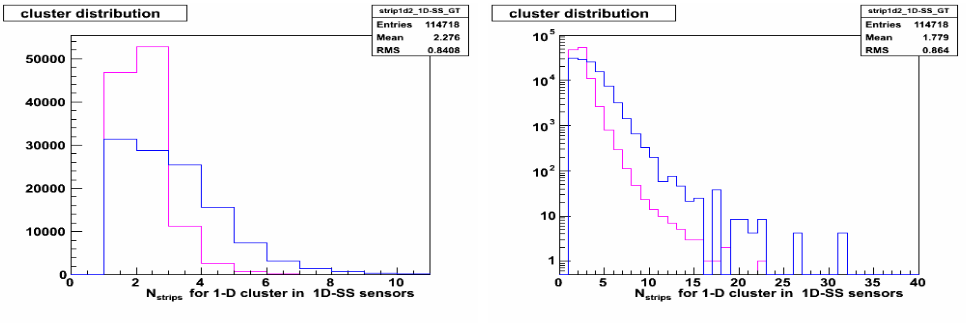

Figure D.23: N_{strips} for the clusters from SS sensors in layer 1 and layer 3.

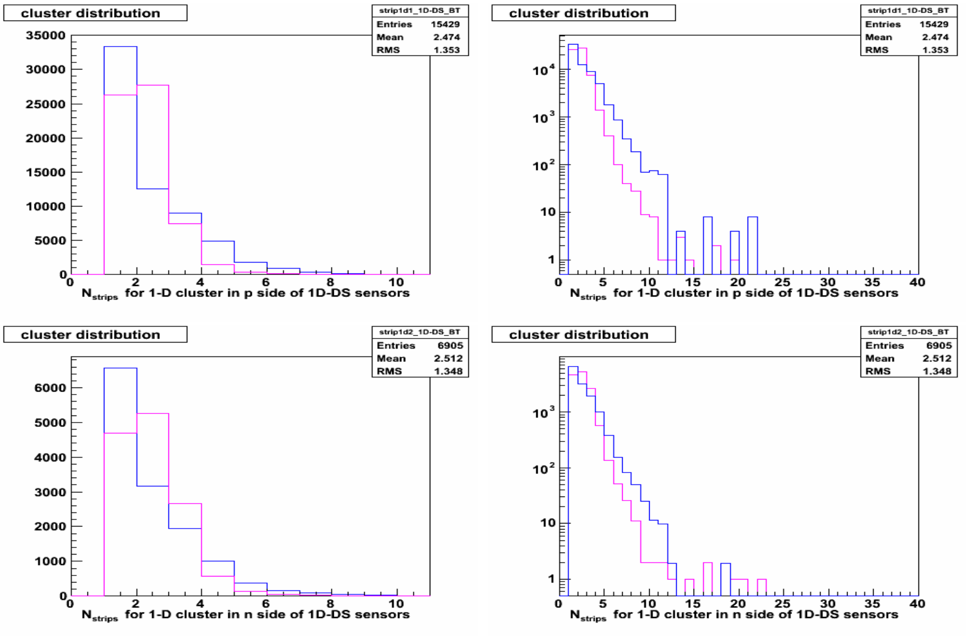

Figure D.24: N_{strips} for the clusters from the barrel DS sensors.

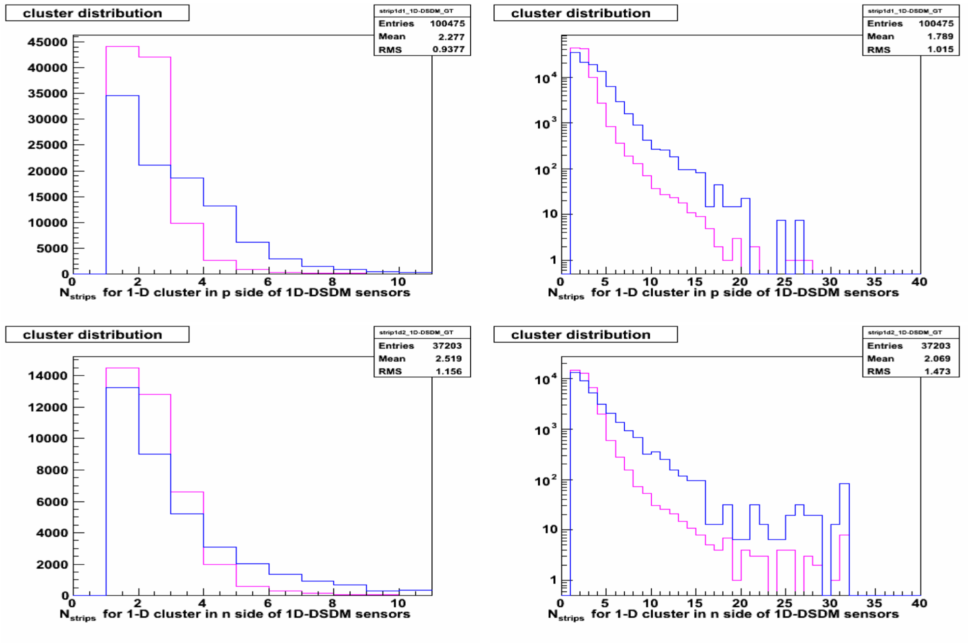

Figure D.25: N_{strips} for the clusters from the barrel DSDM sensors.

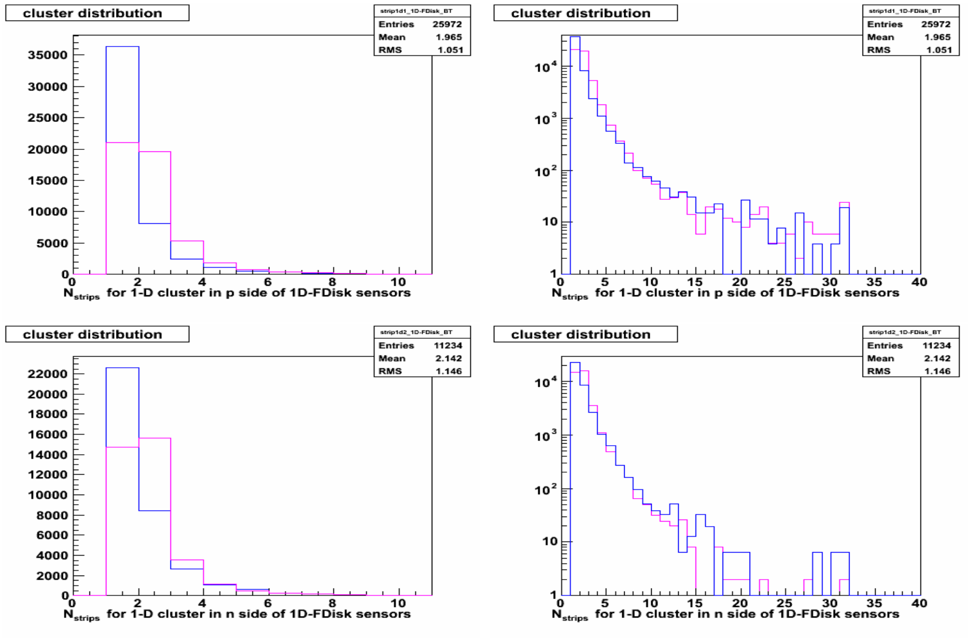

Figure D.26: N_{strips} for the clusters from F-disks.

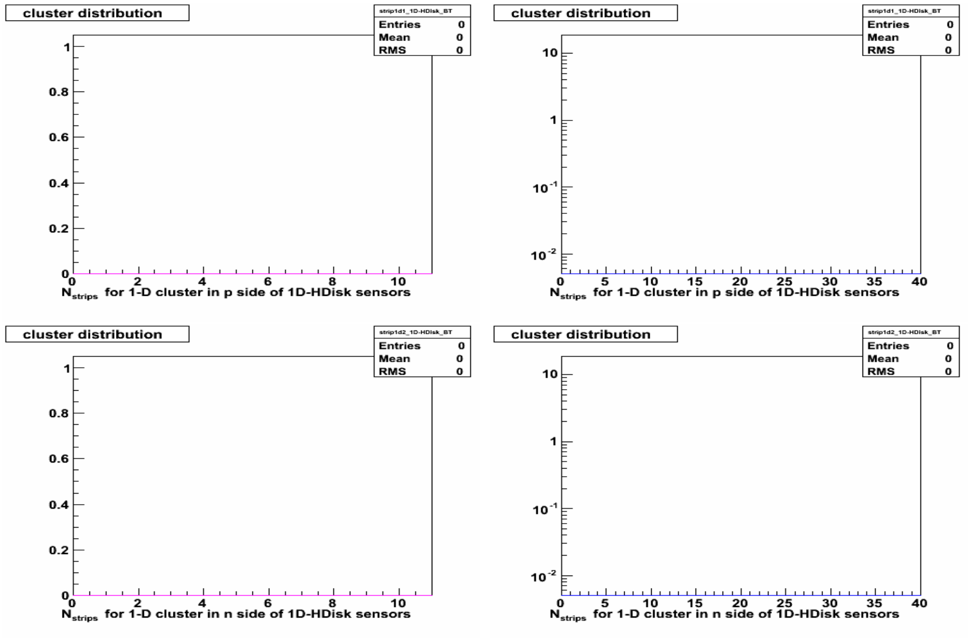

Figure D.27: N_{strips} for the clusters from the H-disks.

Plots of E_{pulse} for the clusters of good and bad tracks

Figure D.28 to Figure D.33 show the plots of E_{pulse} for the clusters from good and bad tracks.

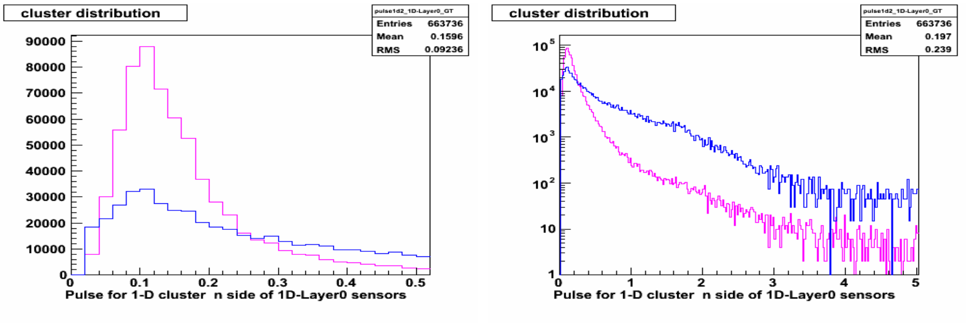

Figure D.28: E_{pulse} for layer 0 clusters.

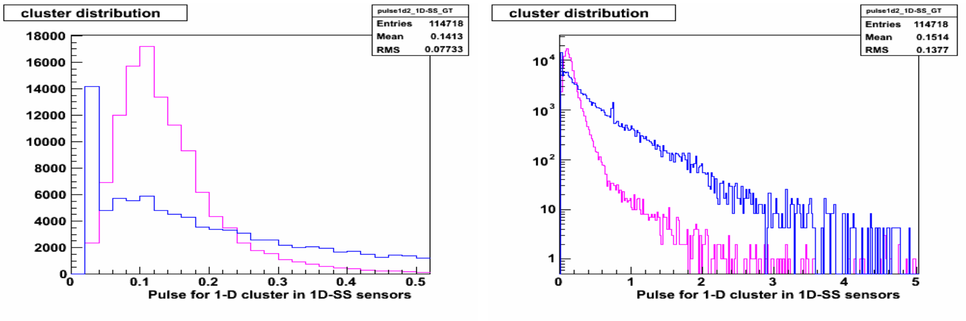

Figure D.29: E_{pulse} for the clusters from SS sensors in layer 1 and layer 3.

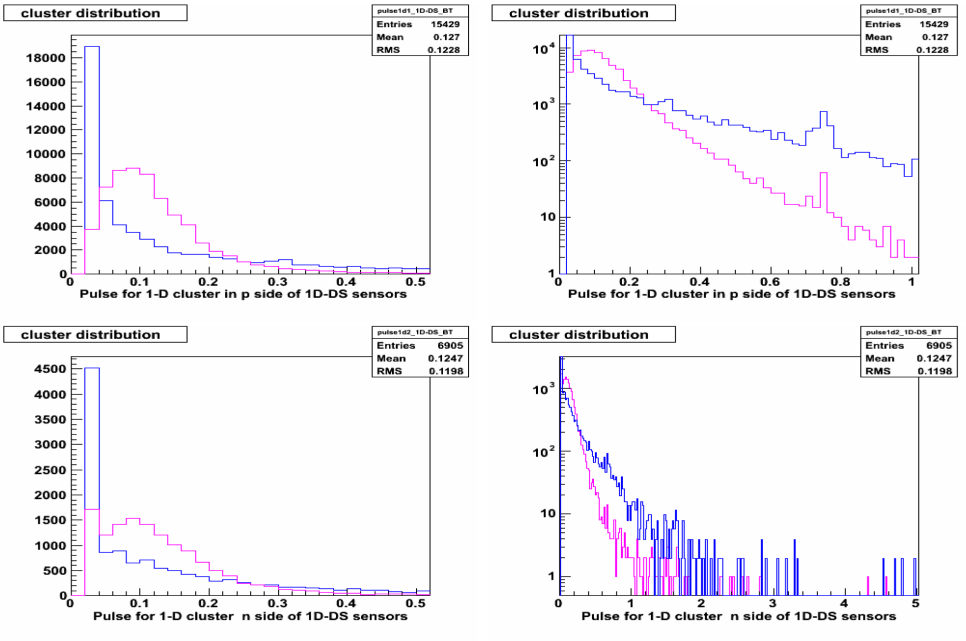

Figure D.30: E_{pulse} for the clusters from the barrel DS sensors.

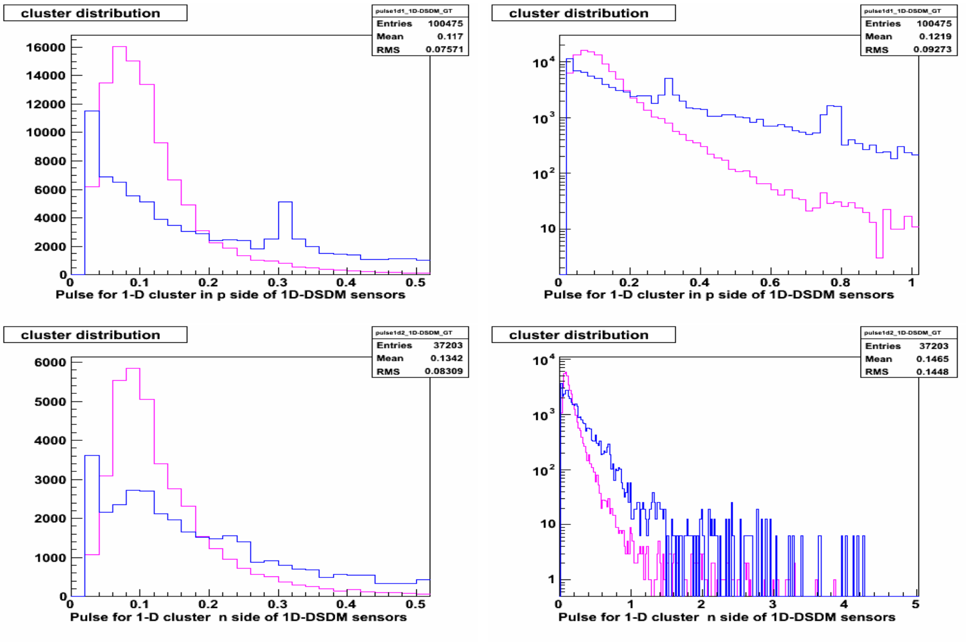

Figure D.31: E_{pulse} for the clusters from the barrel DSDM sensors.

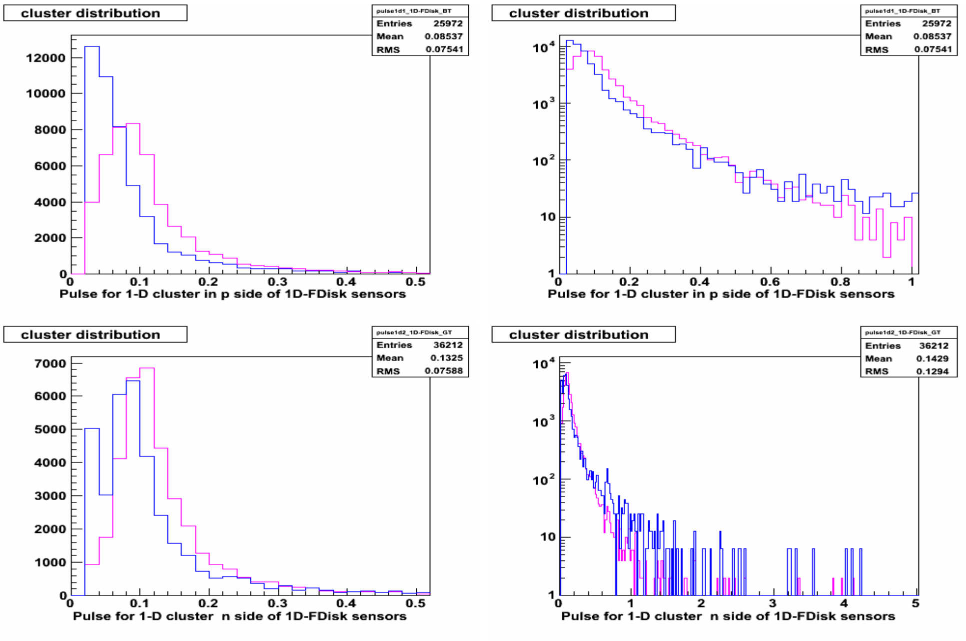

Figure D.32: E_{pulse} for the clusters from F-disks.

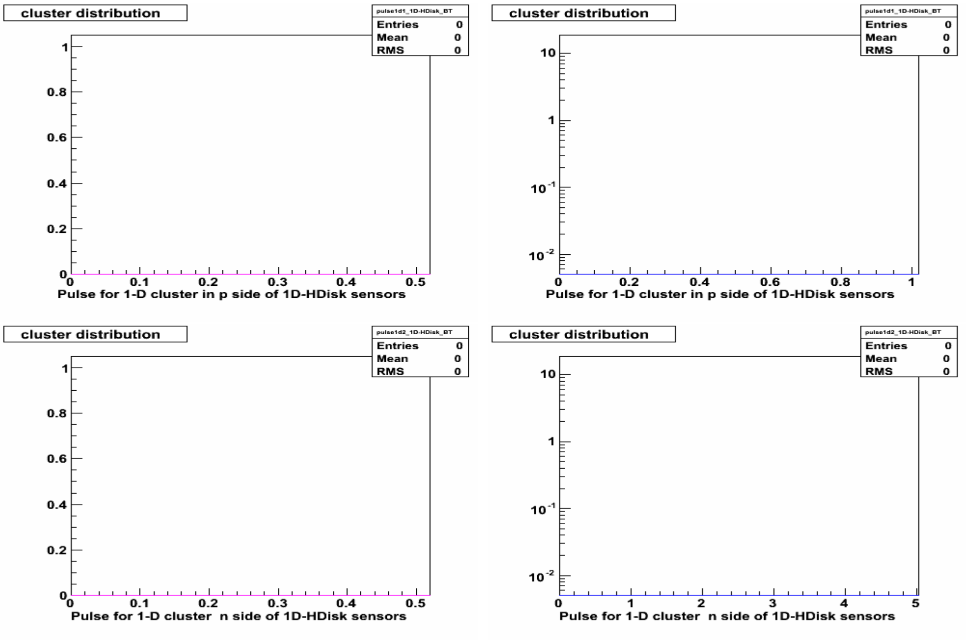

Figure D.33: E_{pulse} for the clusters from H-disk.

Plots of ΔN_{strips} for the clusters of good and bad tracks

Figure D.34 to Figure D.37 show the plots of ΔN_{strips} for 2-D clusters from good and bad tracks.

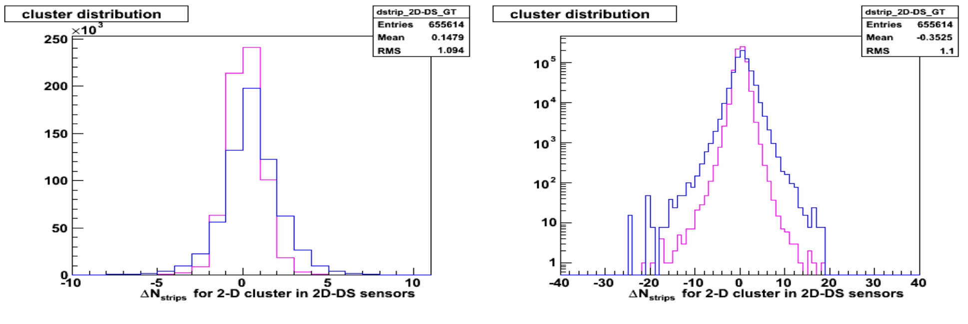

Figure D.34: ΔN_{strips} for the clusters from the barrel DS sensors.

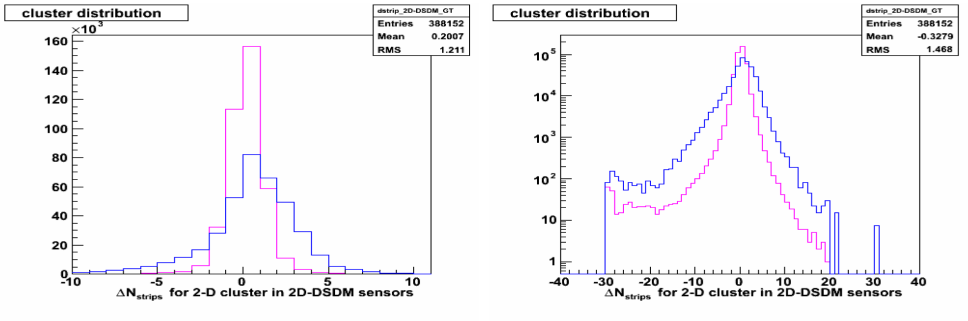

Figure D.35: ΔN_{strips} for the clusters from the barrel DSDM sensors.

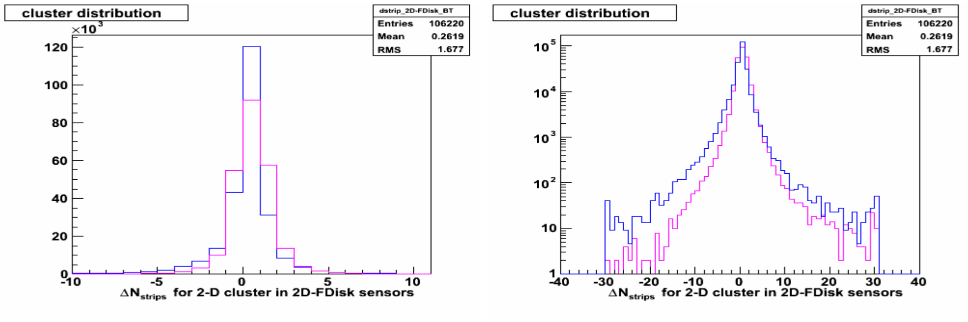

Figure D.36: ΔN_{strips} for the clusters from F-disks.

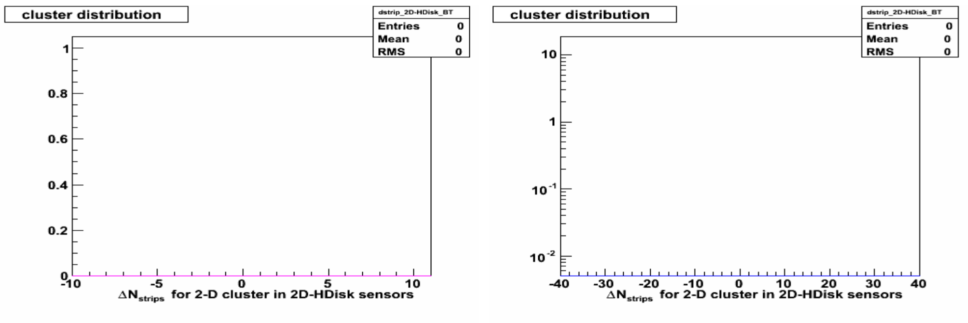

Figure D.37: ΔN_{strips} for the clusters from H-disks.

Plots of ΔE_{pulse} for the clusters of good and bad tracks

Figure D.38 to Figure D.41 show the plots of ΔE_{pulse} for 2-D clusters from good and bad tracks.

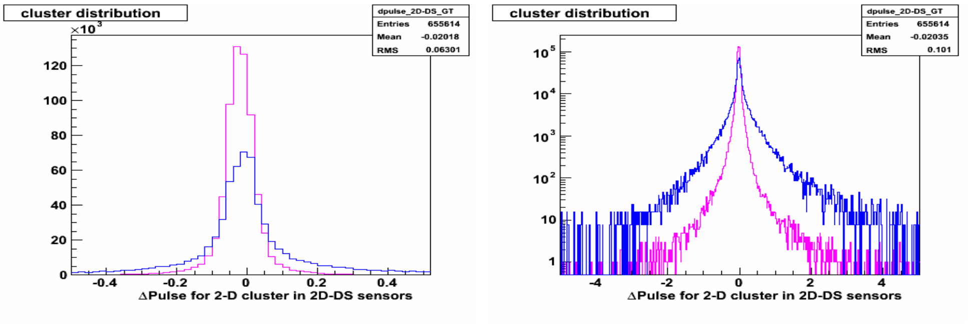

Figure D.38: ΔE_{pulse} for the clusters from the barrel DS sensors.

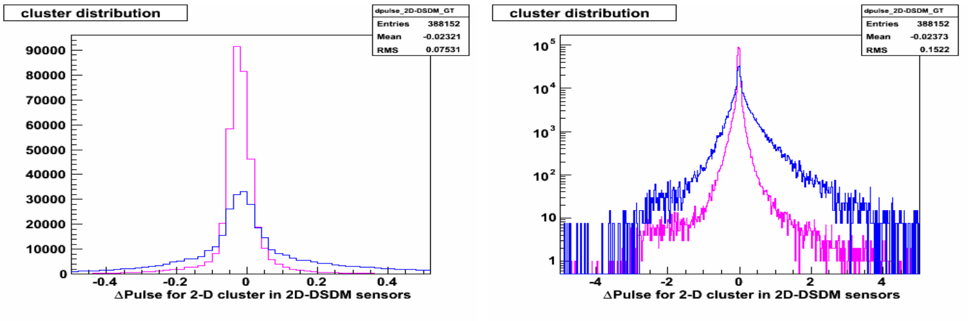

Figure D.39: ΔE_{pulse} for the clusters from the barrel DSDM sensors.

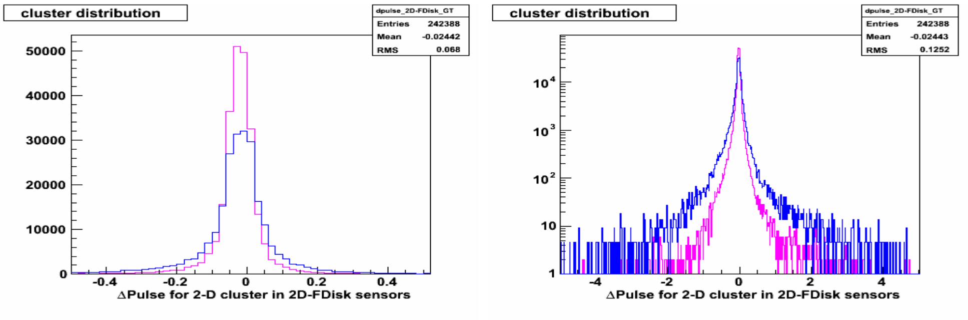

Figure D.40: ΔE_{pulse} for the clusters from F-disks.

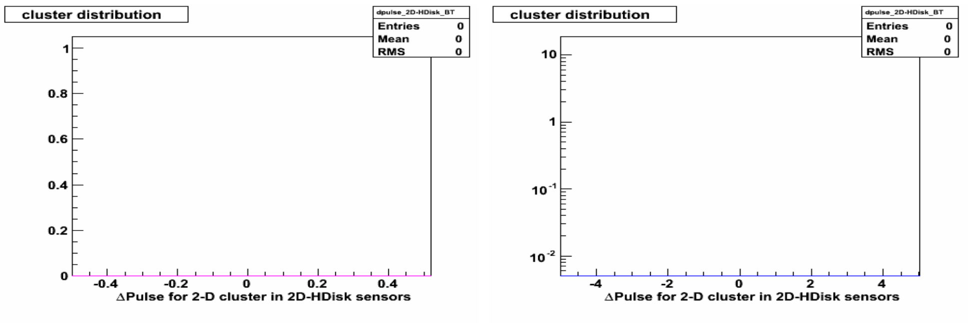

Figure D.41: ΔE_{pulse} for the clusters from H-disks.

Bibliography

[1] S.L. Glashow, Nucl. Phys. **22, 579** (1961); S. Weinberg, Phys. Rev. Lett. **19, 1264** (1967); A. Salam, in Elementary Particle Theory, edited by N. Svartholm (Almquist and Wiksells, Stockhlom, 1968).

[2] O.W. Greenberg, Phys. Rev. Lett. **13, 598** (1964).

[3] F. Abe et al., (D0 Collaboration), Phys. Rev. Lett. **74, 2626** (1995).

[4] S. Abachi et al., (CDF Collaboration), Phys. Rev. Lett. **74, 2632** (1995).

[5] ALEPH, DEPHI, L3, and OPAL Collaborations, Electroweak parameters of the Z0 resonance and the Standard Model, Phys. Lett. **B276, 247** (1992).

[6] UA1 Collaboration, GTJ Arnison et al., Phys. Lett. B **122** (1983) 103-116; UA1 Collaboration, GTJ Arnison et al., Phys. Lett. B **126** (1983) 398-410; UA2 Collaboration, M. Banner et al., Phys. Lett. B **122** (1983) 476-485; UA2 Collaboration, M. Banner et al., Phys. Lett. B **129** (1983) 130-140.

[7] Quadt, A. Top quark physics at hadron colliders. Eur. Phys. J. C 48, 835-1000 (2006)

[8] T. Wyatt, NATURE Vol **448** Page: 274-280 (2007)

[9] The Tevatron Run II Handbook," D. McGinnis, http://www-bd.fnal.gov/runII/index.html.

[10] V. M. Abazov et al., (D0 Collaboration), Nucl. Instrum. Methods A **565**; **hep-physics/0507191**.

[11] S. Abachi et al., Nucl. Instrum. Methods Phys. Res. A **338**, 185 (1994).

[12] H. Greenlee0, D0 Note **4303**, (2004).

[13] A. Khanov, D0 Note **3778**, (2000).

[14] S. Abachi et al. (D0 Collaboration), Nucl. Instrum. Meth. Phys. Res., Sect. A **324**, 53 (1993).

[15] O. Atramentov and Y. Maravin, D0 Note **4444**, (2004).

[16] X.B. Bu, D0 Note **5764**, (2008).

[17] P.F. Ding, D0 Note **6200**, (2011).

[18] EMID group, D0 Note **6116**, (2010).

[19] EMID group, D0 Note **6004**, (2009).

[20] F. Abe *et al.*, Nucl. Instrm. Methods Phys. Res. Sec.A **271**, 387 (1998).

[21] V. M. Abazov *et al.* (D0 Collaboration), Phys. Rev. **D76**, 012003 (2007).

[22] T. Aaltonen *et al.* (CDF Collaboration), Phys. Lett. **B692**:232-239, (2010).

[23] F. Abe *et al.*, Phys. Rev. **D59**, 052002 (1999).

[24] T. Sjöstrand *et al.*, Comput. Phys. Commun. **135** (2001) 238.

[25] D. bandurin, M. Hohlfeld and K. Kaadze, Electron trigger efficiencies in Common Analysis Framework for RunII Data, DØ note 5911.

[26] J. Pumplin *et al.*, JHEP 0207:012(2002), hep-ph/0201195

[27] M. Mangano *et al.*, ALPGEN arXiv:hep-ph/0206293, JHEP**0307** (2003) 001, version 2.05.

[28] R. Brun and F. Carminati, CERN Program Library Long Writeup W5013,1993 (unpublished).

[29] R. Hamberg, W. L. van Neerven, and T. Matsuura, Nucl. Phys. B **359**, 343 (1991).

[30] J. M. Campbell and R. K. Ellis, Phys. Rev. D **60**, 11306 (1999).

[31] M. Cacciari, *et al.*, J. High Energy Phys. **0404**, 068 (2004).

[32] V.M. Abazov *et al.*, (D0 Collaboration), Phys. Rev. Lett. **103**, 161801 (2009).

[33] F. Landry *et al.*, Phys. Rev. **D67**, 073016 (2003).

[34] V.M. Abazov *et al.*, (D0 Collaboration), Phys. Rev. Lett. **106**, 122001 (2011).

[35] J.C Collins and D.E.Soper, Phys. Rev. D **16**, 2219 (1977). No. W5013, 1993.

[36] S. Frixione and B.R. Webber, JHEP 0206 **029** (2002).

[37] J. Pumplin, D.R. Stump, J. Huston, H.L. Lai, Pavel M. Nadolsky, W.K. Tung, JHEP 0207 **012** (2002).

[38] M Paterno, "Calculating efficiency and their uncertainties", `http://home.fnal.gov/~paterno/images/effic.pdf` (2003).

[39] P.M.Nadolsky, H.-L.Lai, Q.-H.Cao, J. Huston, J.Pumplin, D.Stump, W.-K.Tung and C.-P.Yuan, Phys. Rev. D **78** (2008).

[40] H.-L.Lai, M.Guzzi, J. Huston, Z.Li, P.M.Nadolsky, J.Pumplin and C.-P.Yuan, Phys. Rev. D **82** (2010).

[41] A.D. Martin, W.J. Stirling, R.S. Thorne and G. Watt, Eur. Phys. J. **C63** (2009).

[42] D. Stump, J. Pumplin, R. Brock, D. Casey, J. Huston, J. Kalk, H.L. Lai, W.K. Tung, Phys. Rev. D **65**, 014012 (2001).

[43] P.F. Ding, D0 Note **6201**, (2011).